Two aspects of fluid dynamics in planetary cores

Maylis Landeau

Institut de Physique du Globe de Paris **Sorbonne Paris Cité**
Ecole doctorale des Sciences de la Terre

THÈSE de DOCTORAT

présentée par

Maylis LANDEAU

pour obtenir le titre de

Docteur de l'Institut de Physique du Globe de Paris

Spécialité : Géophysique

Deux aspects de la dynamique des fluides des noyaux planétaires

---

Soutenue le 30 septembre 2013 devant le jury composé de :

Édouard Kaminski	Président du Jury
Philippe Cardin	Rapporteur
Frédéric Moisy	Rapporteur
Peter Olson	Examinateur
Maurice Rossi	Examinateur
Julien Aubert	Directeur de thèse

Two aspects of fluid dynamics in planetary cores

by

Maylis LANDEAU

Institut de Physique du Globe de Paris, Sorbonne Paris Cité
Ecole doctorale des Sciences de la Terre

Remerciements

Tout d'abord, je remercie chaleureusement Julien Aubert, qui m'a accompagnée pendant cette thèse, en étant toujours très disponible et accessible. L'indépendance et la confiance qui m'ont été offertes ont joué un rôle essentiel durant mon apprentissage de jeune chercheuse. Je remercie également Peter Olson pour m'avoir accueillie dans son équipe pendant trois mois et Renaud Deguen pour m'avoir aidée à monter un projet expérimental. J'ai beaucoup appris en travaillant avec vous trois et j'espère que d'autres occasions d'apprendre à vos côtés se présenteront.

Je remercie Philippe Cardin et Frédéric Moisy pour avoir pris le temps (pendant les deux mois d'été !) de lire et commenter mon manuscrit. Je remercie également Peter Olson, Maurice Rossi et Édouard Kaminski pour leur présence à ma soutenance et pour leurs questions qui ont alimenté une riche discussion. Merci à tous les conseillers de ce manuscrit (Julien, Alexandre, Renaud, Élodie, Fotini, Charles) et merci à ceux et celles qui ont contribué à l'amélioration de la présentation orale.

En plus de Julien et Renaud, je tiens à remercier tout particulièrement Maurice Rossi, Alexandre Fournier, Claude Jaupart, Angela Limare, Olivier Devauchelle, Thibaut Putelat et Anne Davaille pour m'avoir conseillée à des moments clés de ma thèse ou de mes recherches de contrat post-doctoral. Les discussions scientifiques orales ou écrites avec Paul Roberts, François Pétrélis, Dominique Jault, Guillaume Carazzo, Marie-Charlotte Renoult, Philippe Cardin et Nathanaël Schaeffer ont beaucoup apporté au travail présenté dans ce manuscrit.

L'ambiance au sein de l'équipe DFG est à la fois très dynamique et extrêmement conviviale ; un cadre idéal pour y faire sa thèse ! L'IPGP est un endroit particulièrement favorable aux rencontres enrichissantes et j'ai beaucoup profité des discussions passionnées et engagées, scientifiques ou non scientifiques, près d'un tableau blanc ou autour d'une bière, avec vous : Olivier, Fanny, Morgane, Alexis, Fotini, Angela, Guillaume C, Guillaume LH, Cinzia, Éric, Clément, François, Alex, Gauthier, Erwan, Antoine, Maud, Clémentine, Sabrina, Ingrid, Boris, Frédéric, Samuel, Édouard, Hélène, Pierre, Hugo, Laure, Grégoire, John, Gaurav, Adrien, Kenny, Alberto, Florence, Geneviève, Loïc, Benoît, Emmanuella, Sylvie, Thierry, Stéphanie, Francis, Florian, Elske et bien d'autres. Je garde également un excellent souvenir des trois mois passés à Baltimore et Renaud y est pour beaucoup: les discussions passionnantes le midi, les fous rires dans le labo, les barbecues du vendredi. L'enthousiasme et la motivation régnaient pendant ces trois mois (même le tensiomètre Du Noüy n'a pas réussi à nous démotiver !). Merci également à Élisabeth, Erika, Floriane pour m'avoir encouragée à différents moments de ma thèse, et cela jusqu'à la soutenance.

Ce besoin d'apprendre, de comprendre, puis d'expliquer a été nourri par quelques professeurs et enseignants particulièrement rigoureux, exigeants et passionnés: Mme Barbe, Claire Santoni, Lionel Le Penven, Maurice Rossi et bien d'autres.

Merci à mon père et à ma mère. Pendant toute ma scolarité vous avez su encourager et nourrir mon envie de construire mes projets et de m'y engager avec passion, de rechercher l'essence en se débarrassant du superflu. Merci à ma soeur Noémie et à ma famille pour m'avoir entourée pendant mes études.

Merci à mes amis. Ces dernières années ont été alimentées en rires et en moments forts grâce à vous. Alexis et Fotini, vous me manquerez ; à quand ce voyage en Grèce ?

Les quelques week-ends randonnées, skis, raquettes (parfois raquettes sans raquettes, ou ski sur feuilles) ont été des moments riches en émotions, et j'ai adoré les partager avec vous: Maïa, Élodie, Anne-Sophie, Benoît, Laurent, Fotini, et d'autres. Sans oublier les moments culturels à Paris avec Maë, Morgane, Fanny, Maud. Merci aussi à celles que je vois moins souvent, mais avec toujours autant de plaisir : Amandine, Audrey, Clémentine B, Pauline, Laure, Claudia.

Charles, tu as coloré chaque moment de notre quotidien ces dernières années !

Contents

Abstract

This manuscript presents two independent studies on the fluid dynamics of planetary interiors.

The first part of this manuscript is a numerical study of thermal convection and magnetic field generation driven by internal heating in rotating spheres; a configuration appropriate for planetary cores prior to inner-core nucleation. For sufficiently vigorous convection, we find that the flow becomes strongly asymmetric with respect to the equator; this result contrasts with previously published studies of convection in spherical shells (i.e. with an inner core) where the flow is essentially symmetric. An antisymmetric and axisymmetric (EAA) mode then strongly influences the total flow and conflicts with the Taylor-Proudman theorem. We show that this spontaneous emergence of antisymmetric flow components induces localized magnetic fields with up to 90% of the total magnetic energy contained in a single hemisphere. Our results suggest a parsimonious scenario to explain the hemispherical crustal magnetic field of Mars.

In the second part of this manuscript, we present experiments on the instability and fragmentation of blobs of a heavy liquid released into a lighter immiscible liquid. These processes likely occurred on a massive scale during the formation of the Earth and its core, when dense liquid metal blobs were released within deep molten silicate magma oceans. During the fragmentation process, we observe deformation of the released fluid, formation of filamentary structures, capillary instability, and eventually drop formation. We find that, at low and intermediate Weber number (which measures the importance of inertia versus surface tension), the fragmentation regime results from the competition between a Rayleigh-Taylor instability and the roll-up of a vortex ring. At sufficiently high Weber number (the relevant regime for core formation), the large-scale flow behaves as a turbulent vortex ring or a turbulent thermal: it forms a coherent structure with self-similar shape during the fall and grows by turbulent entrainment of ambient fluid. An integral model based on the entrainment assumption, and adapted to buoyant vortex rings with initial momentum, is consistent with our experimental data. Such results provide the relevant framework for the development of geochemical core formation models that incorporate fluid dynamic constraints.

Keywords: geophysical fluid dynamics, planetary core dynamics, planetary core formation, magma ocean, rotating convection, dynamo, liquid-liquid fragmentation, numerical simulations, laboratory experiments, regime characterization, scaling.

Résumé de la thèse

Cette thèse contient deux études portant sur la dynamique des fluides des noyaux planétaires.

La première partie de ce manuscrit est une étude numérique de la convection thermique et de la génération de champ magnétique dans une sphère pleine en rotation; une configuration qui est appropriée pour étudier la dynamique d'un noyau planétaire sans graine. Quand la vigueur de la convection est suffisamment élevée, nous obtenons des écoulements fortement asymétriques par rapport à l'équateur, contrastant avec les écoulements essentiellement symétriques obtenus en présence d'une graine dans les études précédentes. Un mode antisymétrique et axisymétrique (EAA), brisant la contrainte de Taylor-Prouman, influence alors fortement l'écoulement total. Nous montrons que l'émergence spontanée de ces écoulements fortement asymétriques induit un champ magnétique localisé dans un hémisphère. Ces résultats suggèrent un scénario parcimonieux pour expliquer l'asymétrie du champ magnétique crustal de Mars.

Dans la seconde partie, nous présentons des expériences sur la déstabilisation et la fragmentation d'un volume de fluide dense dans un autre liquide non-miscible. De tels processus ont eu lieu à grande échelle lors des impacts qui ont formé la Terre et son noyau : le métal liquide de l'impactant était alors relâché dans un océan de magma moins dense. Pendant le processus de fragmentation, nous observons la déformation du fluide dense, la formation de structures filamentaires, et finalement la formation de gouttes. Pour des nombres de Weber (rapport des forces d'inertie et de tension de surface) suffisamment faibles, le régime de fragmentation résulte de la compétition entre une instabilité de Rayleigh-Taylor et la formation d'un anneau de vorticité. Pour des nombres de Weber suffisamment élevés (le régime pertinent pour la formation du noyau), l'écoulement grande échelle se comporte comme un thermique turbulent : il forme une structure cohérente et autosimilaire qui croit par entraînement de fluide ambiant. Un modèle basé sur l'hypothèse d'entraînement turbulent, et adapté au cas d'un anneau de vorticité ayant une inertie initial, est en accord avec nos résultats expérimentaux. Cela démontre que le concept d'entraînement turbulent peut être appliqué à une interface séparant des fluides non-miscibles. Ces résultats fournissent le cadre général nécessaire à l'insertion de contraintes physiques dans les modèles chimiques de formation du noyau.

Mots-clés : dynamique des fluides géophysiques, dynamique des noyaux planétaires, formation des planètes, océan de magma, convection en rotation, dynamo, fragmentation liquide-liquide, simulations numériques, expériences analogiques, caractérisation des régimes, loi d'échelle.

Chapter 1

Introduction

1.1 Research background

In this section, we introduce background material related to the state (structure, composition, temperature) and dynamics of planetary cores and their evolution through time, which is especially useful to understand the geophysical context (planetary core formation and convection in fully-liquid cores) that has inspired the two fluid mechanics problems addressed in this manuscript. This section also aims at giving some physical insights into the regime of flow motions in liquid portions of planetary cores.

1.1.1 Present state of planetary cores

1.1.1.1 Structure of Earth's core

Most of what we know about the layers of the Earth's interior (illustrated in figure 1.1(a)) comes from seismology, the study of elastic waves that travel through the Earth and of free oscillations. From the study of wave travel times as a function of the distance from the wave source, Oldham (1906) postulated the existence of a major discontinuity in physical properties within the Earth, separating two layers called the mantle and the core. Later, Gutenberg (1914) determined the location of the core-mantle boundary (CMB) by identifying waves reflected at the CMB (at radius ≈ 3500 km). Comparisons between the Earth's rigidity from solid Earth tides and the mantle's rigidity deduced from seismology supported the existence of a liquid core (Jeffreys, 1926). Later, Lehmann (1936) identified compressional waves in a region where they were not expected with a homogeneous core model, indicating the presence of a discontinuity inside the core: the inner core and the inner-core boundary (ICB) were discovered. Physical arguments were given by Jacobs (1953) in support of a solid inner core, a result later confirmed by the study of the free oscillations of the Earth (Dziewonski & Gilbert, 1971). Then, several models describing the structure of the Earth, including its core, were successively published; the reference model for a radially homogenous Earth is the Preliminary Reference Earth Models (PREM) by Dziewonski & Anderson (1981), which is illustrated in figure 1.1(b).

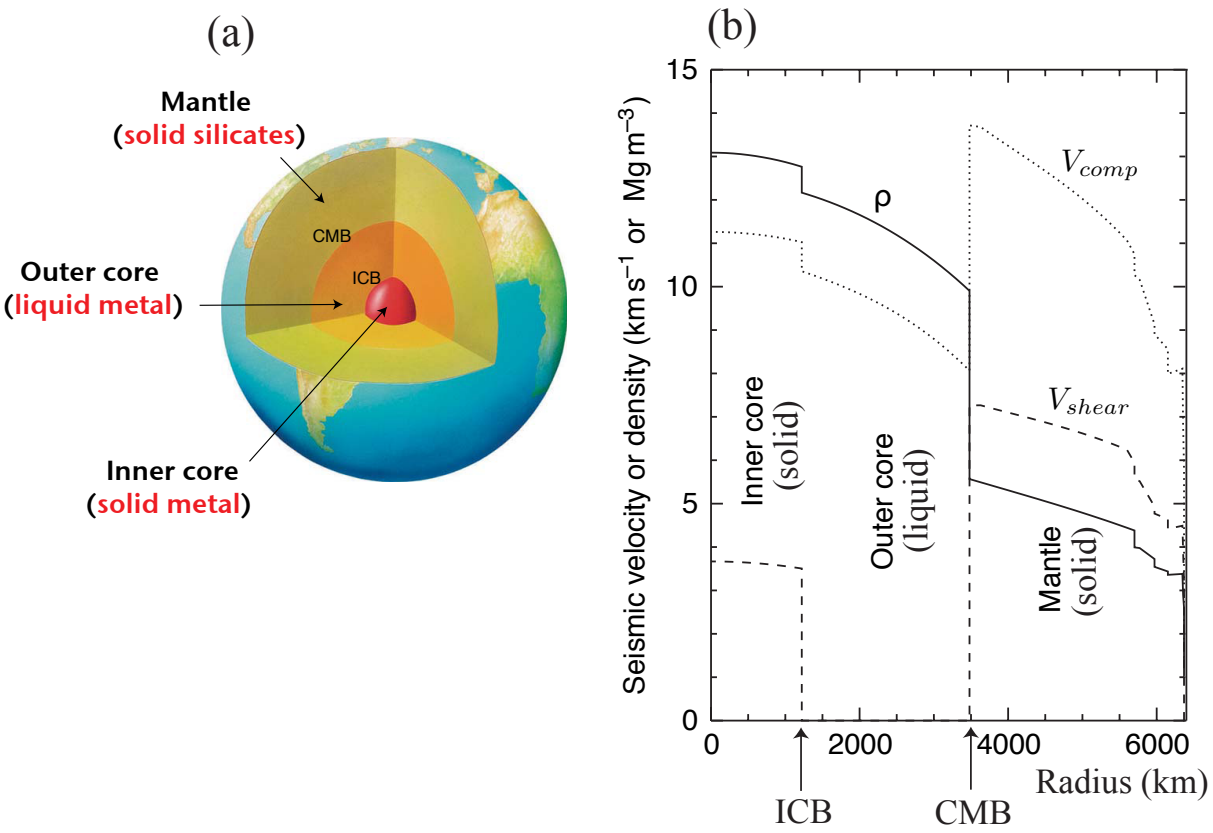

Figure 1.1: (a) Cutaway view showing the main layers of the Earth's interior (modified from Olson (2007)). (b) PREM model for the evolution of the shear wave velocity (V_{shear}), the compressional wave velocity (V_{comp}) and the density (ρ) as a function of the Earth's radius (modified from Olson (2007), after Dziewonski & Anderson (1981)).

1.1.1.2 Composition of Earth's core

Using experiments at high pressure and high temperature, Birch (1952) showed that properties of the Earth's core (deduced from compressional and shear wave velocity measurements) suggest that it is made of iron, plausibly alloyed with lighter elements, although the precise composition in light elements is highly controversial (Poirier, 1994). Other metals, as nickel, might also be present.

The value of the density contrast at the ICB (figure 1.1(b)) (Dziewonski & Anderson, 1981; Masters & Gubbins, 2003; Cao & Romanowicz, 2004) can not be accounted for by a phase change alone, indicating that the outer core is enriched in light elements compared to the inner core.

1.1.1.3 Thermal state of Earth's outer core

The presence of an inner core in the Earth provides a major constraint on its thermal structure since the ICB has to be at the melting temperature. The melting temperature of iron at the ICB pressure is estimated to be in the range $5500 - 6700$ K from high-pressure experiments (Ma *et al.*, 2004; Anzellini *et al.*, 2013) and ab-initio calculations

(Alfe *et al.*, 2002, 2003; Alfe, 2009), and Alfe *et al.* (2003) estimates that the presence of light elements in the core lowers this temperature by ~ -700K.

Given its value at the ICB, a temperature profile can be calculated throughout the outer core assuming that the latter is vigorously convecting, hence "well-mixed" and isentropic. The temperature gradient of an isentropic and hydrostatic system, also called *adiabatic temperature* gradient, is given by

$$\frac{\partial T_a}{\partial r} = -\frac{\alpha g T_a}{C_P}, \tag{1.1}$$

where α is the thermal expansion coefficient, g the gravitational acceleration, and C_P the specific heat capacity under constant pressure. Equation (1.1) means that the temperature of a liquid parcel advected upwards in the outer core, without exchanging heat with its surrounding, decreases as a result of pressure variations. The adiabatic temperature gradient (1.1) is significant in systems with large pressure variations, as in planetary cores or in the atmosphere. In such systems, a considerable portion of the total heat flux is conducted along the adiabat and does not contribute to drive convection.

The first term in the expansion of g is a linear function of r and it corresponds to the gravitational acceleration of a self-graviting sphere of constant density. Assuming constant values for α and C_P, equation (1.1) can be integrated and the temperature in a "well-mixed" core is given by (Labrosse *et al.*, 2001):

$$T_a = T_i \exp \frac{(r_i^2 - r^2)}{D^2} \quad \text{where} \quad D = \sqrt{\frac{3C_P}{2\pi\alpha\rho_c G}}, \tag{1.2}$$

where T_i is the temperature at the ICB, ρ_c the density at Earth's center, r_i the radius of the inner core and G is the gravitational constant.

1.1.1.4 Structure and composition of other planetary cores

From the knowledge of the Earth's structure, we expect other terrestrial* planets to have a silicate mantle and a metallic core separated by a CMB. Planetary cores can be entirely liquid, entirely solid or formed of an innermost solid core and an outermost liquid core. In the absence of seismological data, the main constraints on the state and size of planetary cores come from estimations of their mean density and their axial moment of inertia, which is closely related to the mass distribution inside the planet. The mean density is estimated from the mass and volume of the planet, its mass being deduced from satellite trajectories. The axial moment of inertia can be inferred from the planet gravitational field if the body is in hydrostatic equilibrium, from the precession of the rotation axis or from forced oscillations, called *librations*, of its rotation rate. Forced librations and tides are particularly sensitive to the presence of a liquid outer core. Finally, the presence of a magnetic field of internal origin at the surface of a terrestrial body (Earth, Jupiter's satellite Ganymede and Mercury) is most commonly interpreted as a result of convection and dynamo action within a liquid outer core. Usually, the above data are not all available for a single planetary object and other sources of information may be used on a case-by-

*A terrestrial planet is essentially composed of silicates and metal.

case basis (see Sohl & Schubert, 2007, for detailed information concerning the structure of every terrestrial object of the solar system).

Constraints on the composition of terrestrial cores are obtained from the analysis of meteorites that sample a planet mantle, whose compositions are then subtracted to that of undifferentiated meteorites, called chondrites, which are used as models for the global composition of that planet (this method is also used for the Earth's core).

1.1.1.5 Other physical properties

High-pressure and high-temperature laboratory experiments, using piston-cylinder presses, diamond anvil cells or shock waves have provided important data concerning the physical properties (thermal conductivity, electric conductivity, viscosity, ...) of liquid and solid metal at planetary pressure and temperature. More recently they have been complemented by ab-initio calculations, based on first-principles (see Price, 2007, and the subsequent chapters for a review on geophysical applications of mineral physics).

1.1.2 State of planetary cores in the past

We have introduced the main constraints concerning the present state of planetary cores. How and when was this state (structure, composition, temperature) acquired?

1.1.2.1 Core formation and planetary accretion

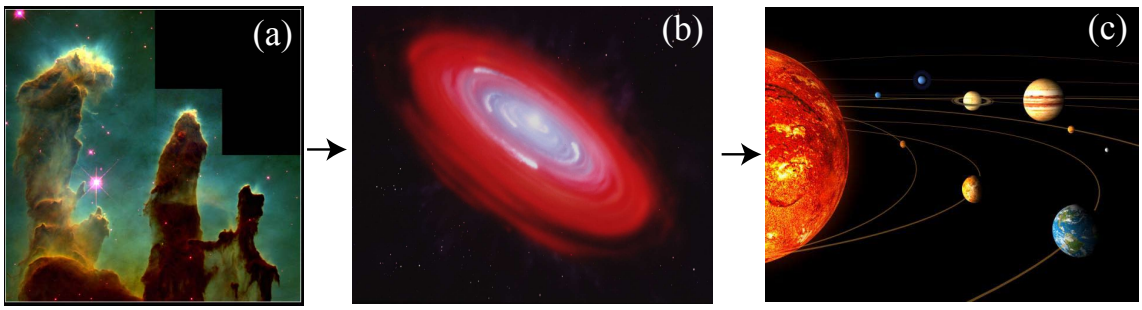

Figure 1.2: (a) Color image of the Eagle Nebula, constructed from data obtained by the Hubble Space Telescope (NASA). (b) Artistic view of a protoplanetary disk (NASA). (c) Artistic view of the present solar system (NASA).

The most widely accepted model of solar system formation involves the collapse of a fairly homogeneous cloud of dust and gas, called nebula (figure 1.4(a)), resulting in a disk-shaped structure, called protoplanetary disk (figure 1.4(b)), from which the planets and the sun were formed (figure 1.4(c)). Such a hypothesis is especially supported by astronomical observations of newborn stars (Beckwith *et al.*, 1990). In the planetesimal theory (reviewed in Chambers, 2004), dust grains would gather within the protoplanetary disk to form kilometer-sized bodies, called *planetesimals*. The mechanisms involved at this stage remain controversial, but gravitational instabilities, turbulence-induced gradients in dust concentration or *grain sticking* after low-speed collisions have been mentioned in

the literature. Once objects larger than a few kilometers are formed, they can interact gravitationally during close approaches (since their escape velocity is not small compared to their mean velocity), causing collisions and net accretion, and forming larger and larger planetesimals, eventually resulting in planet-sized bodies.

Numerical simulations of planetary collisions predict that Moon or Mars-sized embryos can be formed in $0.1 - 1$ Myrs (Weidenschilling *et al.*, 1997) whereas the complete formation of Earth-sized planets would take $10 - 100$ Myrs (Chambers & Wetherill, 1998; Agnor *et al.*, 1999). Comparison between these values and the characteristic timescale of core formation inferred from radiochronology for the parent bodies of iron meteorites ($\leq$ 1.5 Myr, Schersten *et al.*, 2006), for Mars' core ($\sim$ 10 Myrs, Yin *et al.*, 2002) and for Earth's core ($\sim 30 - 100$ Myrs, Yin *et al.*, 2002; Rudge *et al.*, 2010) indicates that core formation and planetary accretion were simultaneous processes. They correspond to a rather brief period compared to the 4.5 billion years of the planets' history. The above age for iron meteorites also suggests that the main structure of present terrestrial planets (metallic core and silicate mantle) was already acquired in early planetesimals.

The global composition of the core and the mantle were set during planetary accretion and the thermal state resulting from accretion can be regarded as the initial condition for planetary thermal evolution on geological timescales. Heat was accumulated during planetary formation as a result of (1) impacts, (2) release of gravitational potential energy and (3) radioactive decay of short-lived isotopes (see Breuer & Moore, 2007). It was then evacuated on geological timescales through a process called *secular cooling*, which essentially involves conduction and convection in terrestrial bodies with a solid or partially solid mantle.

1.1.2.2 Thermal evolution models

As a result of secular cooling, the temperature of the Earth's core progressively decreases, inducing solidification of the outer core and growth of the solid inner core. As the present state of the Earth's core is relatively well constrained, thermal evolution models can be integrated backwards in time to provide estimations of the age of the inner core. From the energy balance within the core it can be shown that (Gubbins *et al.*, 2003)

$$Q_o = \mathcal{B}\frac{dT_o}{dt} + Q_R, \tag{1.3}$$

where Q_o is the total heat flux at the CMB, T_o the core temperature below the CMB, Q_R the contribution from radioactive decay and $\mathcal{B}$ is a function that includes contributions from secular cooling, gravitational energy release, and latent heat release at the ICB due to inner core solidification. When the core temperature at the ICB, T_i, decreases, the inner core grows in size at a rate which depends on the difference between the adiabatic temperature gradient and the melting temperature gradient $\partial T_m/\partial r$ such that

$$\frac{dT_i}{dt} = \left[\frac{\partial T_m}{\partial r} - \frac{\partial T_a}{\partial r}\right]\frac{dr_i}{dt}, \tag{1.4}$$

as it can be intuited from figure 1.3. At leading order $dT_i/dt = T_i/T_o \cdot dT_o/dt$ (Gubbins *et al.*, 2003). Thus, by combining the latter equation with equations (1.4) and (1.3) one can obtain an evolution equation for dr_i/dt once models for $Q_o(t)$ and Q_R are prescribed.

The history of the total heat flux $Q_o(t)$ is not well constrained but end-member scenarios can be given from parametrized models of heat transfer within the mantle, or from the requirement that a dynamo has been active during the last 3 Gyrs as indicated by measurements of remanent magnetizations in rocks at the Earth's surface (Tarduno *et al.*, 2010).

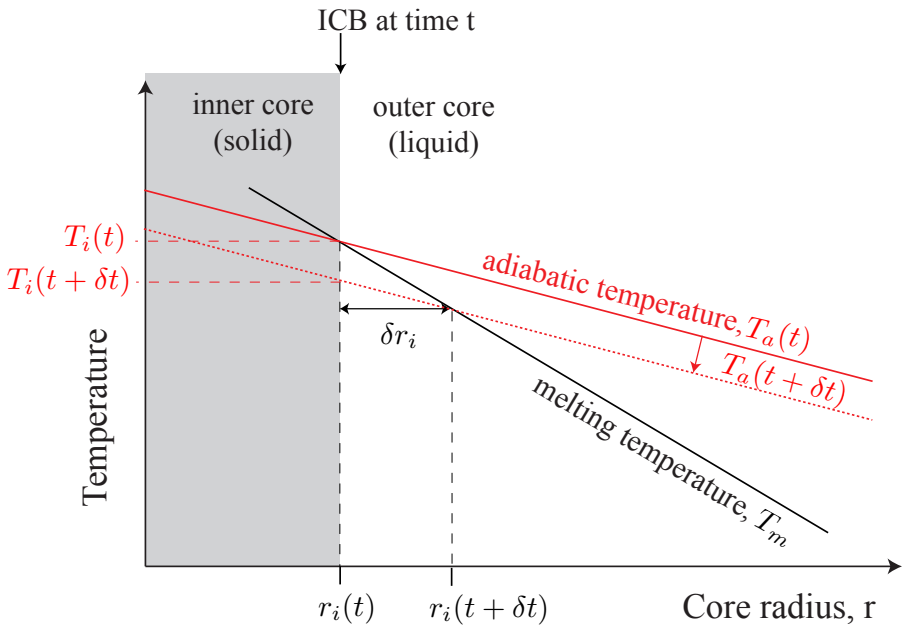

Figure 1.3: Schematic representation of inner core growth. The outer core temperature T_a (adiabatic temperature) decreases between times t and $t+\delta t$ as a result of secular cooling, inducing an increase of the inner core radius r_i equal to δr_i, the distance between the intersections of the melting temperature T_m and the outer core temperature T_a at times t and $t+\delta t$.

The present thermal state of planets other than Earth is poorly constrained. In this case, global thermal evolution models, this time integrated forward using plausible values for the initial (i.e. post-accretion) temperature, give insights into the present thermal state of these planets and its evolution through time, allowing for additional constraints on their internal structure (e.g. Stevenson *et al.*, 1983). The cooling rate of a planet is mainly controlled by its mantle, and global evolution models involve parameterizations of convective heat transfer in the planet mantle as a function of known quantities (e.g. temperature difference across the mantle).

1.1.3 Fluid dynamics implications

1.1.3.1 Convective regimes

The cooling of planetary cores after their formation on geological timescales can drive convection through two different processes. First, purely thermal convection can be driven in fully-liquid cores prior to inner-core solidification, if the total heat flux extracted from the core by the mantle at the CMB exceeds the heat flux conducted along the adiabatic temperature (equation (1.2)). Second, inner-core solidification drives convective instabilities

through the release of light elements (we have already mentioned that the concentration in light elements is lower in the inner core than is the outer core) and through the release of latent heat. Therefore, the convective regime in a given planetary core depends mainly on (1) the presence or absence of a solid inner core and (2) the values of the total and adiabatic heat fluxes at the CMB.

In the present Earth's core, the total heat flux at the CMB can be estimated by extrapolating the mantle temperature down from the near-surface and the core temperature up from the ICB, assuming that the temperature follows an adiabatic profile (equation (1.1)) in both layers. This gives an estimation of the temperature contrast across the mantle thermal boundary layer, whose thickness can be deduced from seismological observations. The resulting total heat flux is in the range $5 - 13$ TW (e.g. Buffett, 2003)*. Common cited estimates for the adiabatic heat flux at the CMB are between 5 and 8 TW (Lay *et al.*, 2008), although recent ab-initio calculations (Pozzo *et al.* 2012; de Koker *et al.* 2012) suggest larger values in the range $13 - 22$ TW (as a result of a thermal conductivity three times larger than previous estimates). Such values indicate two possible convective regimes for the Earth's core: either the upper layer of the outer core is presently thermally stable and convection is mainly driven by inner-core solidification, or the adiabatic heat flux at the CMB exceeds the total heat flux and convection is driven by both thermal and compositional effects. On the contrary, before Earth's inner core nucleation ($\sim 2.5 - 1$ Gyrs ago, Labrosse *et al.* 2001), convection was necessarily driven by purely thermal instabilities.

For other planets, the convective regime can be inferred from global thermal evolution models that provide constraints on (1) the structure of the core (fully-liquid or not) and (2) the total heat flux at the CMB.

1.1.3.2 Regime of flow motions

Compared to silicate mantles whose kinematic viscosity is extremely high (in the range $10^{15} - 10^{18} \mathrm{m}^2 \cdot \mathrm{s}^{-1}$), liquid metal has a very low viscosity of about $10^{-6\pm1}$ $\mathrm{m}^2 \cdot \mathrm{s}^{-1}$ at core pressures (Funakoshi, 2010; de Wijs *et al.*, 1998, and references within), similar to the viscosity of water. Hence, the Reynolds number, which measures the relative importance of inertial and viscous forces, is much lower than 1 in convecting solid mantles and the flow is very viscous†. On the contrary, high Reynolds numbers are easy to reach in liquid portions of planetary cores and flow motions are almost systematically turbulent. For instance, a characteristic velocity of convective motions near the Earth's outer core surface is $5 \cdot 10^{-4} \mathrm{m} \cdot \mathrm{s}^{-1}$ (obtained by inverting time-variations of the geomagnetic field, Bloxham & Jackson, 1991), which gives a Reynolds number larger than $5 \cdot 10^7$.

*Such values are in agreement with recent estimations that are based on double-crossing of a phase transition (perovskite to post-perovskite) in the Earth's mantle, which yields a global CMB heat flux in the range $7 - 15$ TW (Hernlund *et al.*, 2005).

†assuming a typical length of 1000km and a typical velocity of 1cm per year for the velocity of plates at the Earth's surface, we obtain a Reynolds number smaller than 10^{-19}.

1.2 Two independent projects, a common methodology

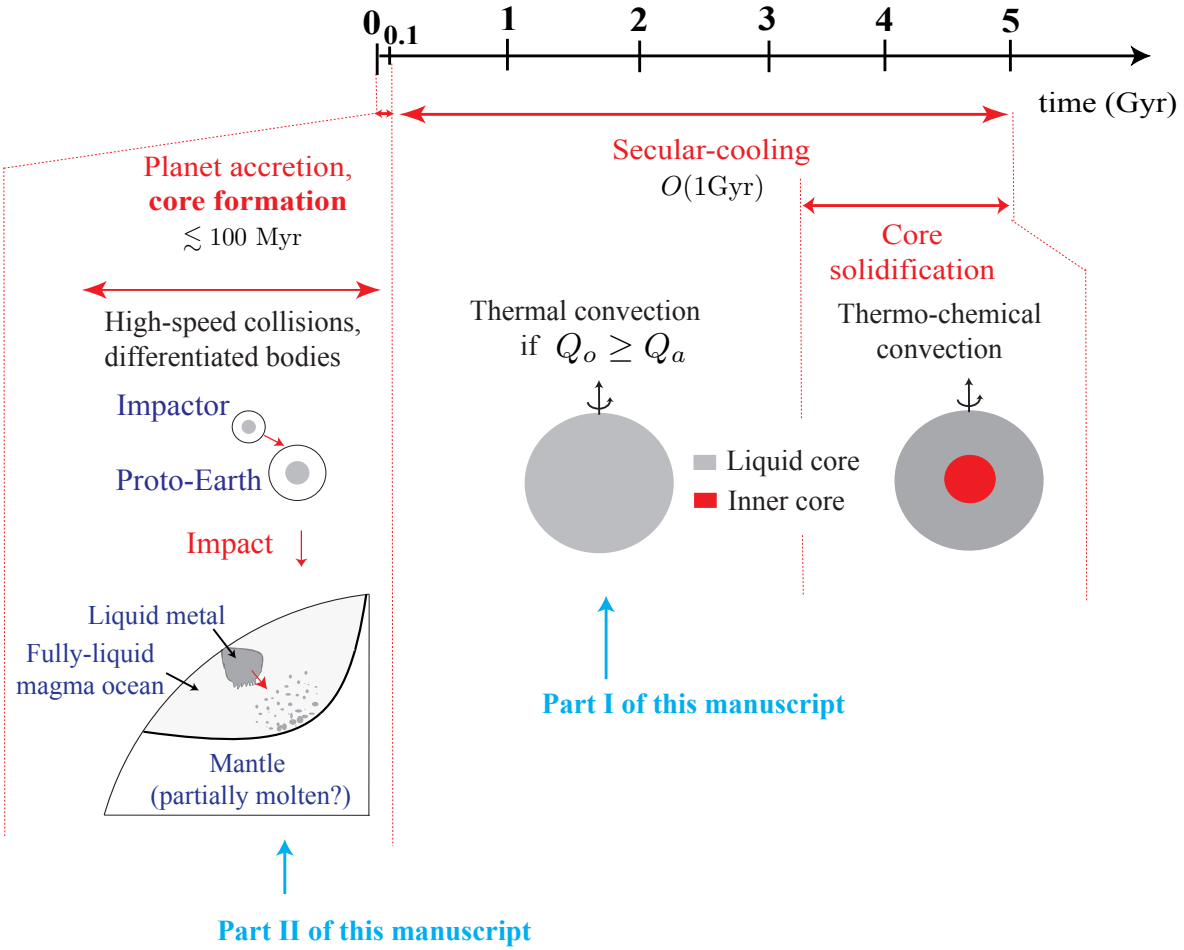

Figure 1.4: Typical history of the core of a terrestrial planet. Q_i and Q_a are the total and adiabatic heat fluxes at the CMB, respectively. The time scale is only indicative and the absolute values vary from one planet to the other. The studies presented in Part I and Part II of this manuscript are related to the stages indicated by blue arrows.

Figure 1.4 summarizes the typical history of a planet as deduced from the background material given in section 1.1 and locates the geophysical contexts that motivate the studies presented in Part I and Part II of this manuscript.

In the first part of this manuscript, a study on thermal convection and magnetic field generation driven by internal heating in rotating full spheres is presented. This configuration is appropriate to study the dynamics of planetary cores prior to inner core solidification and subsequent to core formation (figure 1.4). This study was conducted in IPGP* with Julien Aubert using numerical simulations.

The second part of this manuscript goes back in time and aims at better understanding the fluid dynamics of the last stages of core formation (figure 1.4), during which much of

*Institut de Physique du Globe de Paris

the Earth mass was formed as a result of high-speed collisions between planetary embryos that consisted of a silicate mantle and a metallic core (Melosh, 1990; Yoshino *et al.*, 2003; Schersten *et al.*, 2006; Ricard *et al.*, 2009). Energy release during each of these impacts induced widespread melting, creating an environment in which dense liquid metal blobs fell within deep molten silicate magma oceans (Tonks & Melosh, 1993; Pierazzo *et al.*, 1997). As liquid metal and liquid silicates are immiscible, liquid metal fragmented into smaller blobs during its fall. Inspired from this context, we study buoyancy-driven fragmentation of a liquid into another immiscible liquid using laboratory experiments. This project has been conducted with Renaud Deguen and Peter Olson and it involved a three-month stay in Johns Hopkins University that resulted from a personal initiative and during which laboratory experiments were designed and performed.

Although the two studies presented in this manuscript deal with the fluid mechanics of planetary cores, their specific geophysical motivations are not related. From a fluid mechanics perspective, there is another significant distinction: rotation plays a major role in the convective dynamics of planetary cores and in the study presented in Part I, whereas rotation is expected to have only a second-order effect on the fragmentation of liquid metal in magma oceans and it is not considered in the experiments presented in Part II of this manuscript. Nonetheless, the reader will notice that the scientific approach, which is summarized in figure 1.5, is very similar in these two projects.

First, both projects start from a fluid mechanics system (box 2 in figure 1.5) inspired from geophysical considerations (box 1 in figure 1.5). We emphasize that, in both cases, we do not aim at providing realistic visualizations of geophysical flows by accurately reproducing the geophysical context in our simulations or experiments. Such an objective is often not reachable given the complexity of geophysical systems, which involve numerous competing mechanisms and a wide range of time scales and length scales. Thus, we rather simplify the geophysical systems as much as possible, focusing on specific and well-defined processes and deliberately excluding others. This approach enables us to isolate understandable fluid mechanics problems. In summary, the geophysical contexts of interest and the studied fluid mechanics problems are associated with two different and separate stages in the general methodology (figure 1.5).

Second, in both projects the main questions can be stated as follows:

- What are the different flow or dynamo regimes, characterized by velocity or magnetic field patterns, when varying the different control parameters?
- Can we account for the dynamics observed in these regimes from theoretical arguments (time scales, length scales, velocity, oscillating behaviors, evolution with time,...)?
- What are the implications for the geophysical system of interest? In particular, can we infer the flow or dynamo regime in the geophysical system?

These questions illustrate that both studies are *exploratory*: initially, there is no precise competing or contradicting hypotheses, and the objective is rather to conduct a systematic exploration of the parameter space, reaching regions that have not been studied before.

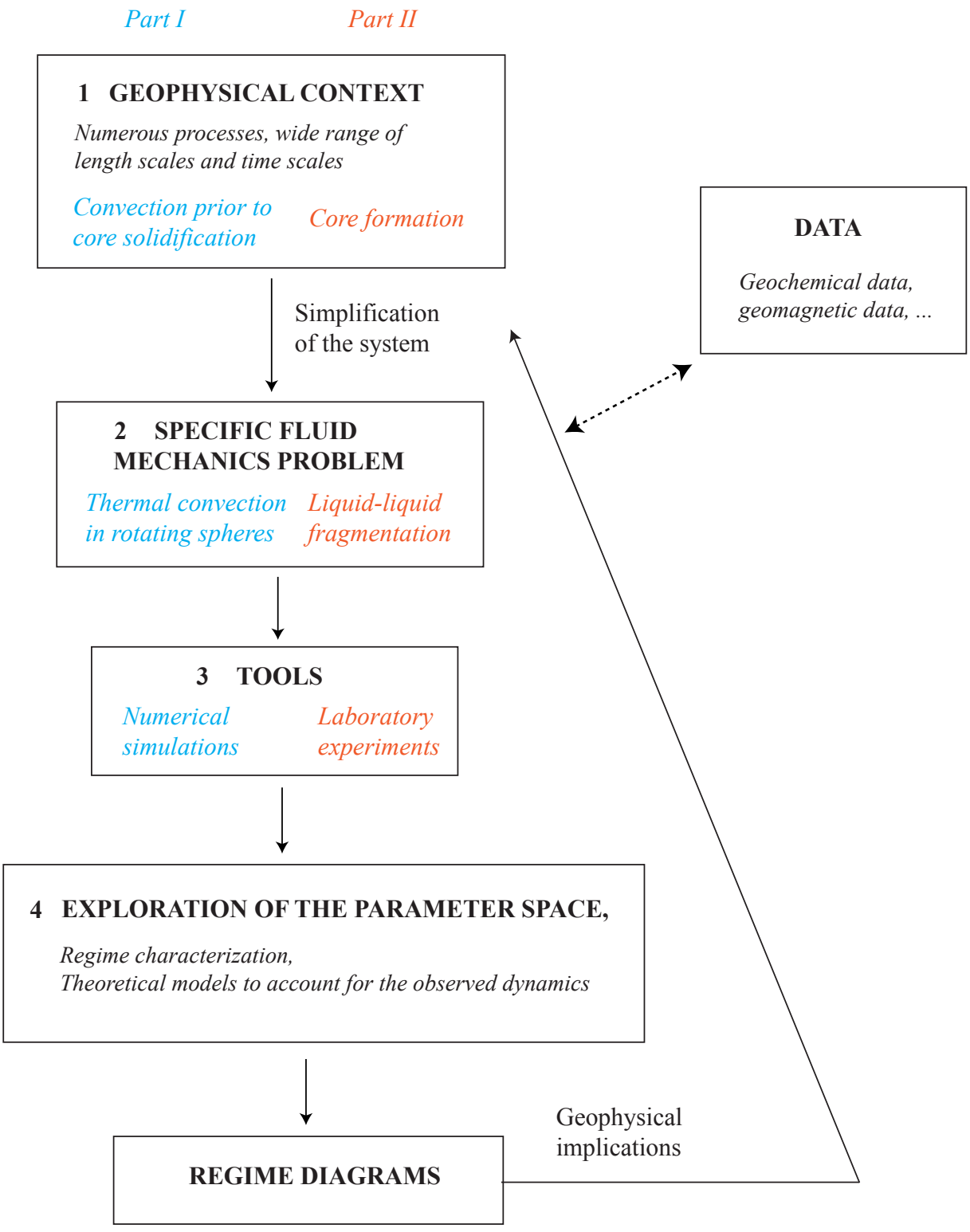

Figure 1.5: Schematic representation of the general methodology used in the two projects conducted during this PhD. The text in blue refers to the study presented in the first part of this manuscript while the text in orange refers to the second part. The dashed line refers to a direction which is less explored in the present manuscript, although it is an important guideline, affecting the choice of output quantities extracted from numerical or experimental data.

Part I

Numerical modeling of thermal convection and dynamo action in rotating spheres

Chapter 2

Context and background

2.1 Introduction

It is widely accepted that the Earth's magnetic field originates from convective motions in its outer core, involving both thermal and compositional effects (as mentioned in the main introduction of this manuscript). Most published studies on core convection and dynamo action have focused on configurations that model thermo-chemical convection in the Earth's core, i.e. considering a rotating spherical shell with a rather large inner core and using boundary conditions that ensure that the buoyancy flux is non-zero at the inner sphere (figure 2.1(c)). On the contrary, convection and dynamo action in entirely liquid cores prior to inner core solidification (figure 2.1(b)) has received little attention until now, and yet this configuration is simpler first because of its geometry (sphere rather than spherical shell) and second because the driving of convection is of thermal origin alone (i.e. no double-diffusive processes need to be considered).

Several convective dynamos in our solar system have probably operated in such a full-sphere configuration (figure 2.1(a)). First, paleomagnetic data indicate that the Earth's dynamo was active at least ~ 3.4 Gyr ago (Tarduno *et al.*, 2010; Biggin *et al.*, 2011), consistently with the results obtained by combining thermal evolution models with velocity scaling laws from dynamo simulations (Aubert *et al.*, 2009). Commonly cited values for the age of the inner core are in the range $0.5 - 2.5$ Gyr (Labrosse *et al.*, 2001)*, implying that the dynamo is likely to have operated prior to the nucleation of the inner core.

Second, an early dynamo in a convective core subject to secular cooling (Nimmo & Stevenson, 2000) is the most plausible hypothesis to explain the strong magnetizations measured on Mars' crust by the Mars Global Surveyor mission, although elliptical instabilities excited by tidal forces of large asteroids have been proposed (Arkani-Hamed, 2009). The former scenario is considered in the present study. The timing of the martian dynamo is debated but can be constrained using ages of the different crust regions, estimated from the method of crater counts (Hartmann & Neukum, 2001). Acuna *et al.* (1999) argue that large impact basins, believed to be ~ 4 Gyr old, are not magnetized,

*Although recent high values found for the thermal conductivity (Pozzo *et al.*, 2012; de Koker *et al.*, 2012) widen the range of plausible values for the inner core age. Indeed, either higher radiogenic heating or larger cooling rate may be required to power the geodynamo when increasing the thermal conductivity (Gubbins *et al.*, 2003). Larger radiogenic heating would imply a lower cooling rate and therefore an increased inner-core age while increasing the cooling rate results in a reduced inner core age.

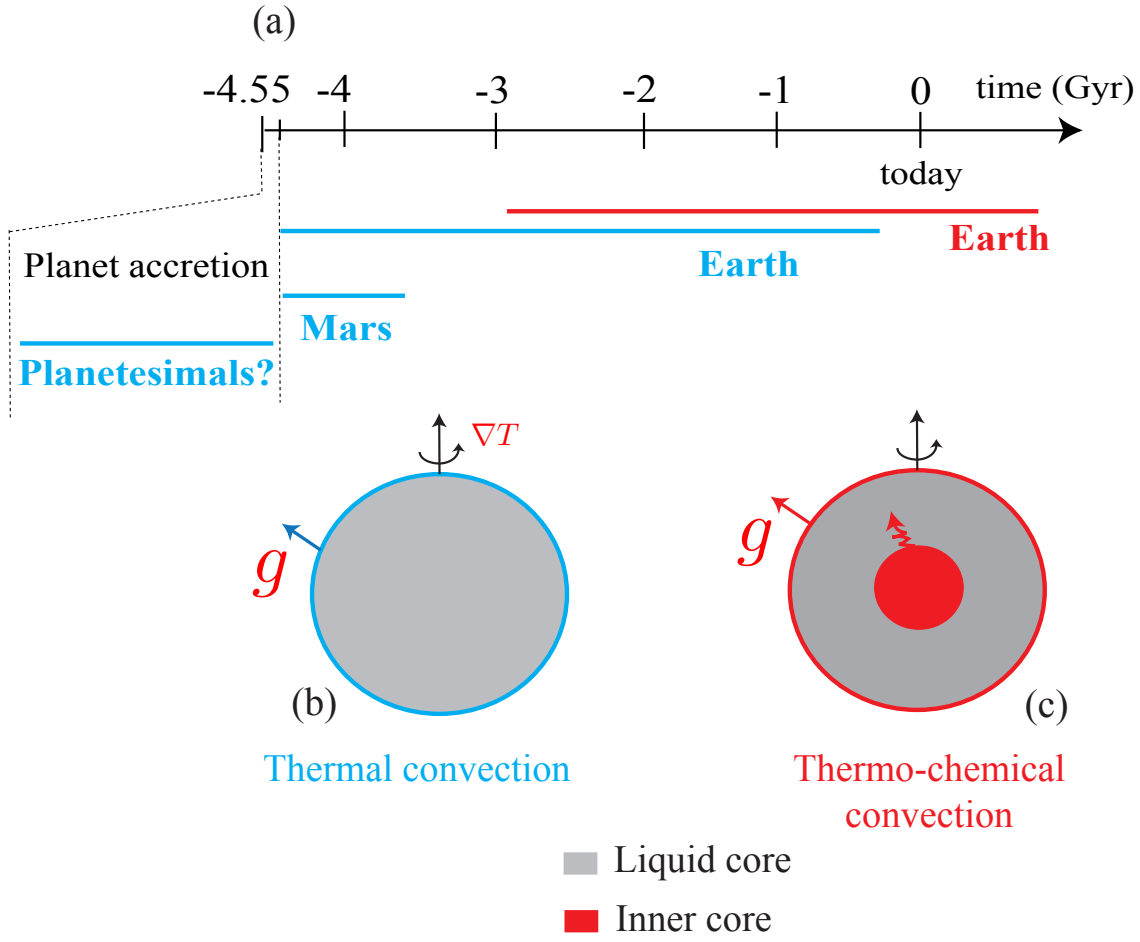

Figure 2.1: (a) Periods where dynamo action forced by purely thermal convection (blue) or by themo-chemical convection (red) is plausible in the Earth's core or in Mars. Besides, purely thermal convection and dynamo action might have been widespread during planet accretion, when heating due to both collisions and decay of short-life isotopes allowed global melting. (b) Configuration for purely thermal convection in an entirely liquid core, as considered in this study. Q represents the heat flux at the CMB. (c) Relevant configuration for the present Earth's core: convection and dynamo action forced by both thermal and compositional effects (release of light-elements at the ICB).

suggesting that the dynamo would have been active in the early history of Mars, between 4.5 Gyr and 4 Gyr, whereas other published studies (e.g. Milbury & Schubert, 2010; Milbury *et al.*, 2012) argue in favor of a later dynamo cessation. Several studies (Longhi *et al.*, 1992; Lodders & Fegley, 1997; Sanloup *et al.*, 1999) have compared sulphur contents of martian meteorites with those of other primitive meteorites and estimated a high sulphur content in Mars' core: from 10.6% to 16.2%. Stewart *et al.* (2007) performed experiments on iron-sulfur and iron-nickel-sulfur systems at high pressure and obtained the corresponding phase diagrams at fixed pressure. They showed that, considering such high sulphur contents and using plausible values for the present core temperature (as deduced from thermal evolution models), Mars' core is likely to be presently entirely liquid. Other geophysical constraints argue in favor of a presently entirely liquid core: solar tidal deformation of Mars indicates that its core is presently partially liquid (Yoder *et al.*, 2003) and, if metal solidification was presently occurring in Mars' core, a magnetic field of in-

ternal origin would be likely since compositional convection is a very efficient mechanism for dynamo generation (Labrosse, 2003; Lister, 2003; Gubbins *et al.*, 2004).

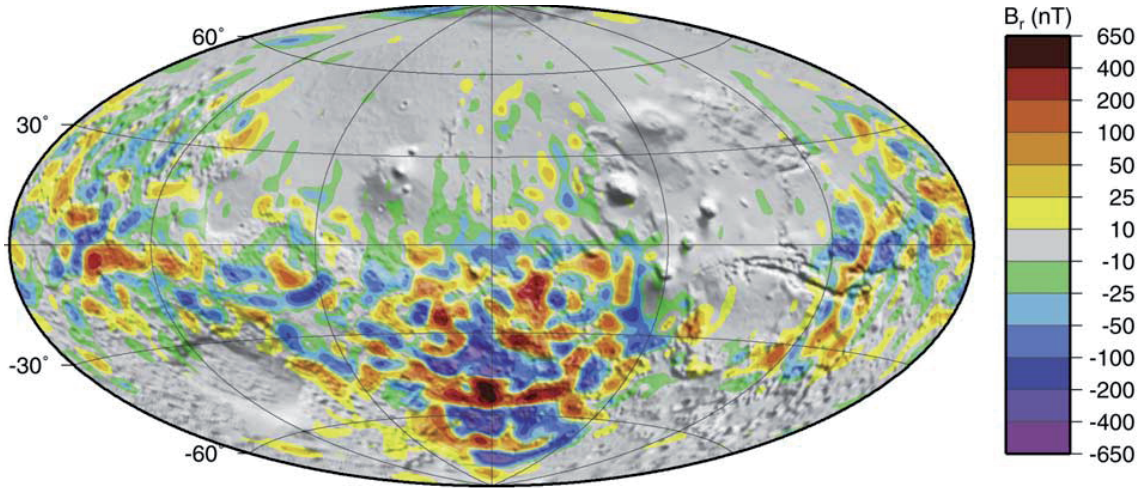

Figure 2.2: Predicted radial magnetic field at 200*-km altitude (modified from Langlais* et al.*, 2004)*

Hence, the crustal magnetic field of Mars may provide clues concerning the field generated by a full-sphere convective dynamo. The Mars Global Surveyor mission revealed a very unexpected feature for Mars' crust: intense crustal magnetizations were measured in the southern hemisphere, whereas the northern hemisphere contains only weak fields (figure 2.2) (Acuna *et al.*, 1999; Langlais *et al.*, 2004). Dynamo models do not easily explain this hemispherical crustal magnetic field. Since Mars is a terrestrial planet with a size comparable to that of the Earth, we could have expected a similar dynamo regime as in the Earth, characterized by a dipole dominated magnetic field with similar strength in both hemispheres. For this reason it has first been proposed that the asymmetry of the crustal magnetic field was due to partial demagnetization of the crust in the northern hemisphere by exogenic processes, such as volcanic resurfacing (Connerney *et al.*, 2005), several large impacts (Frey & Schultz, 1988) or a single giant impact (Andrews-Hanna *et al.*, 2008; Marinova *et al.*, 2008; Nimmo *et al.*, 2008; Citron & Zhong, 2012). More recently, Stanley *et al.* (2008) have explored the possibility that hemispherical magnetizations of Mars' surface have been caused by a dynamo process, influenced by a hemispherical pattern in the heat flux extracted by the mantle at the core-mantle boundary (CMB).

Inspired from the geophysical context mentioned above, we study thermal convection in rotating spheres, with and without dynamo action. The main questions investigated in this study are: What flow and magnetic field structures dominate in convecting rotating spheres? Are they identical to those found in previously published studies on convection in rotating spherical shells?

2.2 Prerequisites on rotating flows and magnetohydrodynamics

Before getting to the heart of the matter, we introduce a few fundamental notions that will be useful to understand the results presented in this manuscript.

In a reference frame that rotates at a constant rate Ω about the axis $\hat{z}$, the momentum equation for an electrically conducting newtonian fluid is given by

$$\rho\frac{\partial \mathbf{u}}{\partial t} + \rho\mathbf{u}\cdot\nabla\mathbf{u} \;=\; -2\rho\left(\mathbf{\Omega}\times\mathbf{u}\right) - \nabla P + \rho\boldsymbol{g} + \frac{1}{\mu}\left(\nabla\times\mathbf{B}\right)\times\mathbf{B} + \rho\nu\Delta\mathbf{u}, \qquad (2.1)$$

where $\mathbf{\Omega} = \Omega\hat{z}$, $\mathbf{u}$ is the velocity field, P the pressure field, ν the kinematic viscosity of the fluid, ρ the density, $\mathbf{B}$ the magnetic induction (usually called magnetic field), $\mathbf{g}$ the gravity field and μ the magnetic permeability of free space. The first right-hand side (RHS) term is a fictitious force called the Coriolis force. It is fictitious in the sense that it has no physical origin: a straight motion in the non-rotating frame appears deflected in the rotating frame, *as if* the motion was driven by such a force. The fourth RHS term in (2.1) corresponds to the Lorentz force.

2.2.1 The Taylor-Proudman theorem

In a stationary rapidly rotating flow where the Lorentz, viscous and inertial forces are small compared to the Coriolis force and where other body forces (e.g. buoyancy forces) are weak, equation (2.1) becomes, at leading order,

$$2\rho\mathbf{\Omega}\times\mathbf{u} = -\nabla P. \qquad (2.2)$$

Taking the curl of equation (2.2) leads to a result known as the Taylor-Proudman theorem (or Taylor-Proudman constraint):

$$\frac{\partial \mathbf{u}}{\partial z} = \mathbf{0}, \qquad (2.3)$$

where the z axis is directed along the rotation axis. Hence, the velocity field is invariant under translation along the rotation axis. The Taylor-Proudman theorem was first derived by J. Proudman in 1916 and demonstrated experimentally by G.I. Taylor later on (see figure 2.3 for examples of laboratory demonstrations).

2.2.2 Baroclinic flows and thermal winds

In a rapidly rotating flow, departures from the Taylor-Proudman constraint (2.3) can be caused by baroclinicity. Taking the curl of the momentum equation (2.1) while assuming a stationary flow and neglecting the viscous, Lorentz and inertial forces, we obtain:

$$-2\rho\Omega\frac{\partial \mathbf{u}}{\partial z} = \nabla\rho\times\mathbf{g}. \qquad (2.4)$$

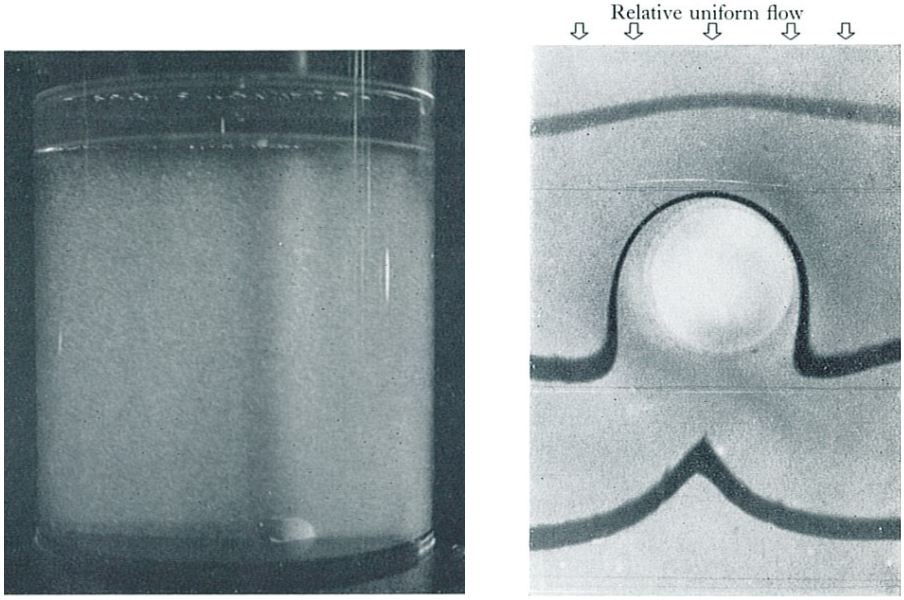

Figure 2.3: Visualizations obtained when a small obstacle is fixed at the bottom of a rotating cylinder. The system is first put into a state of solid body rotation and, then, the rotation rate is slightly changed, inducing flow motions inside the tank. (a) Side-view of a fluid column aligned with the rotation axis and attached to the obstacle. (b) Top-view, the dye lines lie in a plane well above the obstacle. In the absence of rotation, a dye line remains horizontal as it passes over the body. Figures modified from Greenspan (1968).

Equation (2.4) indicates that a shear flow, called *baroclinic flow*, is generated when density gradients are not aligned with gravity. This flow is perpendicular to the plane that includes density gradients and gravity, as illustrated in figure 2.4.

When density gradients are caused by temperature gradients, baroclinic flows are referred to as *thermal winds*.

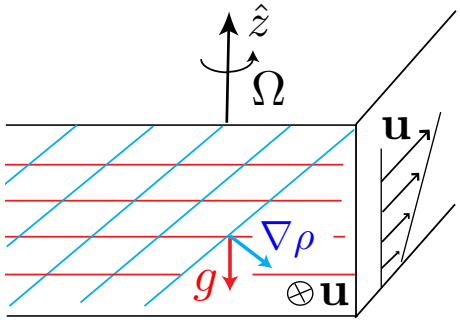

Figure 2.4: Generation of baroclinic flows. Red and blue lines represent equipotentials of the gravity field $\boldsymbol{g}$ and iso-density lines, respectively, in a xz-plane. Black arrows represent the resulting velocity field in a yz-plane.

2.2.3 Induction equation and the dynamo effect

In the context of magnetohydrodynamics (MHD), which studies the dynamics of electrically conducting fluids, the term *dynamo effect* refers to the ability of a flow to amplify small magnetic field perturbations and then maintain a magnetic field of finite amplitude.

At this stage, it is useful to introduce the induction equation, which governs the dynamics of the magnetic field within the framework of the MHD approximation (demonstrated in appendix A) and which is given by

$$\frac{\partial \mathbf{B}}{\partial t} = \nabla \times (\mathbf{u} \times \mathbf{B}) + \eta \Delta \mathbf{B}, \tag{2.5}$$

where $\mathbf{B}$ is the magnetic induction (usually called magnetic field), and η the magnetic diffusivity. Making use of the continuity equation in an incompressible flow, equation (2.5) can be written as

$$\frac{\partial \mathbf{B}}{\partial t} + \mathbf{u} \cdot \nabla \mathbf{B} = \mathbf{B} \cdot \nabla \mathbf{u} + \eta \Delta \mathbf{B}. \tag{2.6}$$

The second term on the left-hand side (LHS) of equation (2.6) corresponds to the advection of $\mathbf{B}$ by the flow. The first RHS term corresponds to the stretching of $\mathbf{B}$ by the flow, meaning that velocity gradients may be responsible for an increase of $\mathbf{B}$, i.e. a dynamo effect. The second RHS term is a diffusion term.

We emphasize that $\mathbf{B} = \mathbf{0}$ is always a solution of equation (2.6) and a dynamo effect is possible only when this solution becomes unstable. Therefore, dynamo action is essentially an instability mechanism, which occurs when the ratio of the production term $\mathbf{B} \cdot \nabla \mathbf{u}$ to the diffusion term $\eta \Delta \mathbf{B}$ is large enough, as measured by the magnetic Reynolds number Rm. The value of the magnetic Reynolds number from which a magnetic field starts to be self-maintained is called *dynamo onset*. The main mechanisms of magnetic field generation, called the α and ω-effects, are introduced in appendix B. Once a magnetic field of finite amplitude has been generated, it acts back on the velocity field through the Lorentz force (fourth RHS term in equation (2.1)), which eventually leads to magnetic field saturation.

In the present study, the term *convective dynamo* will refer to simulations where a magnetic field of finite amplitude can be maintained by convective motions, in the absence of any imposed external magnetic field.

2.3 State of the art

This section provides a review of previously published studies on convection and dynamo action in rotating spheres and shells. This review is not exhaustive, we rather concentrate on aspects that will help interpreting our results and discuss their significance. In particular, we progressively introduce the different regime transitions indicated in figure 2.5 when increasing the forcing of convection. The reader is referred for instance to Busse (2002); Jones (2007); Christensen & Wicht (2007); Cardin & Olson (2007) for more complete reviews.

In planetary cores, the ratio of viscous (Funakoshi, 2010; de Wijs *et al.*, 1998) and

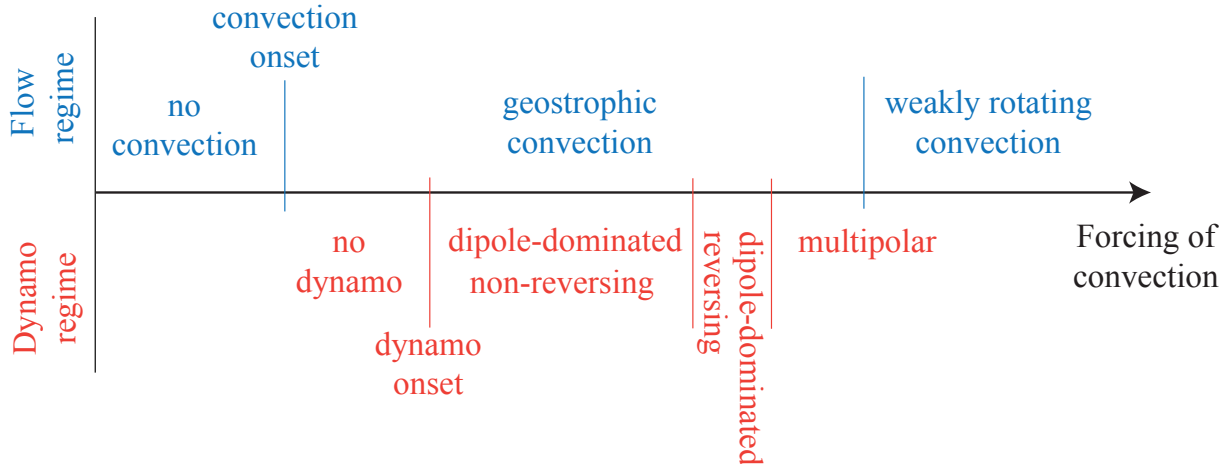

Figure 2.5: Different flow and dynamo regimes (progressively introduced in the text) found when increasing the forcing of convection, i.e. the Rayleigh number.

thermal (Olson, 2007; Pozzo *et al.*, 2012; de Koker *et al.*, 2012) diffusivities, called the Prandtl number Pr, is very poorly constrained and can take values in the range $10^{-3} - 1$. In the present study, and hence in the following review, we focus on the regime of Prandtl number of order unity. Such a choice facilitates comparisons with convection in spherical shells since most published studies have focused on this domain of parameter space. Yet, several authors have investigated the effect of lower Prandtl numbers (e.g. Zhang, 1992; Ardes *et al.*, 1997; Simitev & Busse, 2003, 2005).

2.3.1 Definitions and notations

The spherical shell or sphere is rotating at rate Ω around a vertical axis $\hat{z}$. We use spherical coordinates (r, θ, ϕ) and cylindrical coordinates (s, ϕ, z) as illustrated in figure 2.6(a). The terms *radial*, *axial* and *azimuthal* refer to projections along $\hat{r}$, $\hat{z}$ and $\hat{\phi}$, respectively. *Horizontal* and *meridional* components refer to projections in a $s\phi$-plane and a sz-plane, respectively.

Symmetric and antisymmetric fields

In the present study, it is understood that a *symmetric* vector or pseudovector field $\mathbf{u}$ is left unchanged by the operator Γ which describes mirror-reflection through the equatorial plane (in grey in figures 2.6(b,c)), i.e. $\Gamma\mathbf{u} = \mathbf{u}$, while an *antisymmetric* vector or pseudovector field is such that $\Gamma\mathbf{u} = -\mathbf{u}$. Examples of symmetric and antisymmetric flows (i.e. vector fields) are given in figures 2.6(b,c).

Any field $\mathbf{u}$ can be decomposed into a symmetric field $\mathbf{u}_S$ and an antisymmetric field $\mathbf{u}_A$. The equations of flow motions have equatorial reflection symmetry. Therefore, when the boundary conditions are also symmetric with respect to the equator, the solutions $\mathbf{u} = \mathbf{u}_S + \mathbf{u}_A$ and $\mathbf{u} = \mathbf{u}_S - \mathbf{u}_A$ are two equivalent solutions. Besides, it also follows that symmetric and antisymmetric modes are decoupled in the linearized equations and the flow at convection onset, just as any eigenvector, will be either symmetric or antisymmetric.

The product of a symmetric field by an antisymmetric field gives an antisymmetric

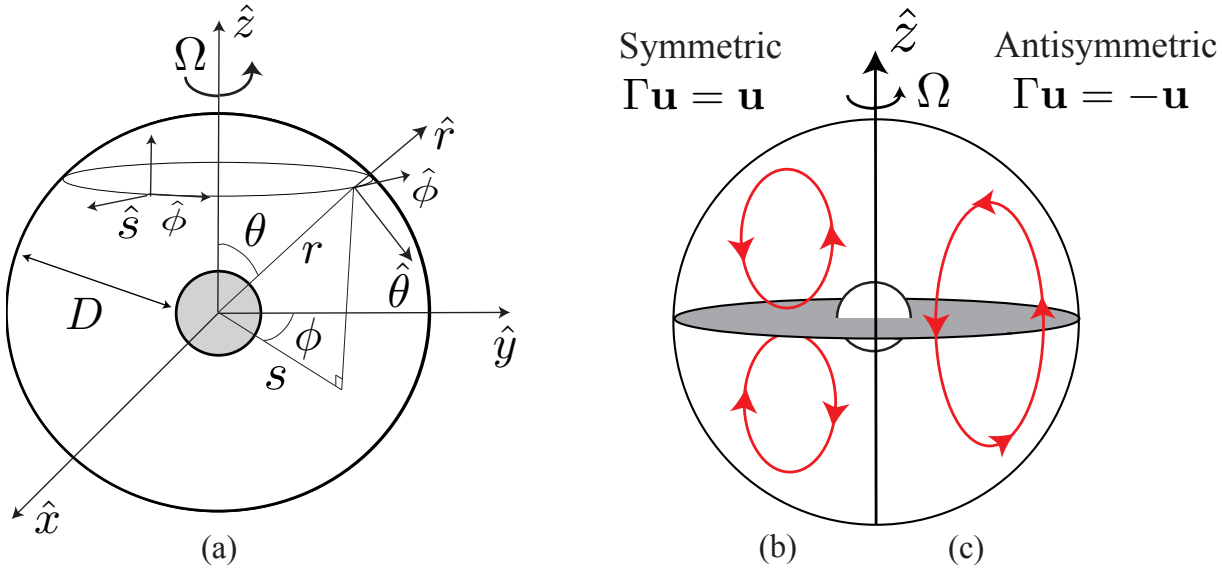

Figure 2.6: (a) Configuration and coordinate systems. The convecting fluid is located between the inner and outer sphere. (b,c) Examples of a symmetric (b) and antisymmetric (c) flow inside a spherical shell. Red lines represent the streamlines in a meridional plane (for a given value of ϕ) whereas the arrows indicate the direction of the flow. The equatorial plane is depicted in grey.

field, a symmetric field by a symmetric field gives a symmetric field and an antisymmetric field by an antisymmetric filed gives a symmetric field.

To avoid any confusion, the terms *symmetric* and *antisymmetric* will be used in this study to refer to equatorial symmetry properties of the flow, whereas the term *dipolar* and *quadrupolar* will be used to refer to equatorial symmetry properties of the magnetic field*.

Axisymmetric fields

In the following, an *axisymmetric* field is invariant under rotation about the vertical axis $\hat{z}$.

2.3.2 Different approaches

The results presented in the following subsections have been obtained using laboratory experiments, numerical simulations and theory. While theoretical studies have successful addressed the problem of the onset of convection and the weakly nonlinear regime (e.g. Roberts, 1968; Busse, 1970; Soward, 1977; Jones *et al.*, 2000), experimental and numerical studies have first confirmed theoretical predictions and then examined the fully-nonlinear regime of convection. In most of the experiments in rotating spherical shells, the centrifugal acceleration plays the role of gravity, while the shells is heated up at the outer boundary and cooled down at the inner boundary (e.g. Carrigan & Busse, 1983; Cardin

*The magnetic field is a pseudovector, therefore dipolar and quadrupolar components are symmetric and antisymmetric, respectively.

& Olson, 1994; Aubert *et al.*, 2001; Gillet *et al.*, 2007). Experimental configurations in which the effective buoyancy force has also a non-negligible component in the direction of the rotation axis, which better simulates the case of self-graviting spheres, have been conducted using a dielectric liquid in an imposed electrical field in a microgravity environment (Hart *et al.*, 1986) or using hemispherical shells rotating at intermediate rotation rate such that the Earth gravitational acceleration (parallel to the rotation axis) is of the same order of magnitude as the centrifugal acceleration (perpendicular to the rotation axis) (Cordero & Busse, 1992; Cordero, 1993; Sumita & Olson, 2000, 2003). The magnetic Reynolds number that can be reached in laboratory experiments is several orders of magnitude smaller than its critical value for dynamo onset and, therefore, the study of convective dynamos requires the use of numerical simulations, which have been fairly successful in reproducing self-sustained magnetic fields that exhibit dynamical and morphological similarities with fields observed on planets (e.g. Glatzmaier & Roberts, 1995; Christensen *et al.*, 1999; Olson *et al.*, 1999; Christensen & Aubert, 2006).

2.3.3 Onset of convection

Problems of convection in rotating systems can be divided into two categories. The first category corresponds to systems where the buoyancy force is aligned with the rotation axis, as in the case of a horizontal fluid layer heated from below (figure 2.7(a)) (Chandrasekhar, 1961, part III, chapter 2). The second category gathers systems where the buoyancy force is perpendicular to the rotation axis, as in the case of the rotating annulus (figure 2.7(b)) (e.g. Busse, 1970; Busse & Carrigan, 1974; Busse, 1986). In a self-graviting rotating sphere or spherical shell, the buoyancy force is along $\mathbf{r}$ and these two categories are represented: near the equatorial plane the buoyancy force is perpendicular to $\mathbf{\Omega}$ whereas it is parallel to $\mathbf{\Omega}$ near the rotation axis. Thus, it can be anticipated that the rotating plane layer (figure 2.7(a)) exhibits a dynamics somewhat similar to the dynamics near the axis in a rotating sphere or inside a cylinder tangent to the inner sphere, called *tangent cylinder*, in a spherical shell (figure 2.7(c)). Similarly, the rotating annulus is expected to give insights into the dynamics further away from the axis (outside the tangent cylinder in a shell, provided that the inner sphere is sufficiently large). The above analogies help to provide a physical understanding of convection patterns in rotating spheres or shells and, more specifically, they have inspired successive studies of the onset of convection in rotating spheres.

The first attempts to solve the onset of thermal convection in rotating spheres focused on axisymmetric modes (Chandrasekhar, 1957*a*,*b*; Bisshopp, 1958; Roberts, 1965; Bisshopp & Niiler, 1965). Scaling laws for the threshold of instability of these modes could be extracted from Bisshopp (1958) but the asymptotic theory in the limit of small Ekman number (measuring the relative importance of viscous and Coriolis forces) was simultaneously developed by Roberts (1965) and Bisshopp & Niiler (1965), inspired from the study of the onset of convection in a rotating plane layer by Niiler & Bisshopp (1965). They showed that the onset of axisymmetric convection takes the form of a meridional cell centered on the rotation axis (figure 2.7(d)) and of thickness $O(E^{1/3}D)$, where D is the sphere radius or the shell thickness. Exactly as in a rotating plane layer (figure 2.7(a)), heat is carried away along the rotation axis by the axial velocity component u_z. However, the non-penetration condition on the upper and lower boundaries prevents u_z

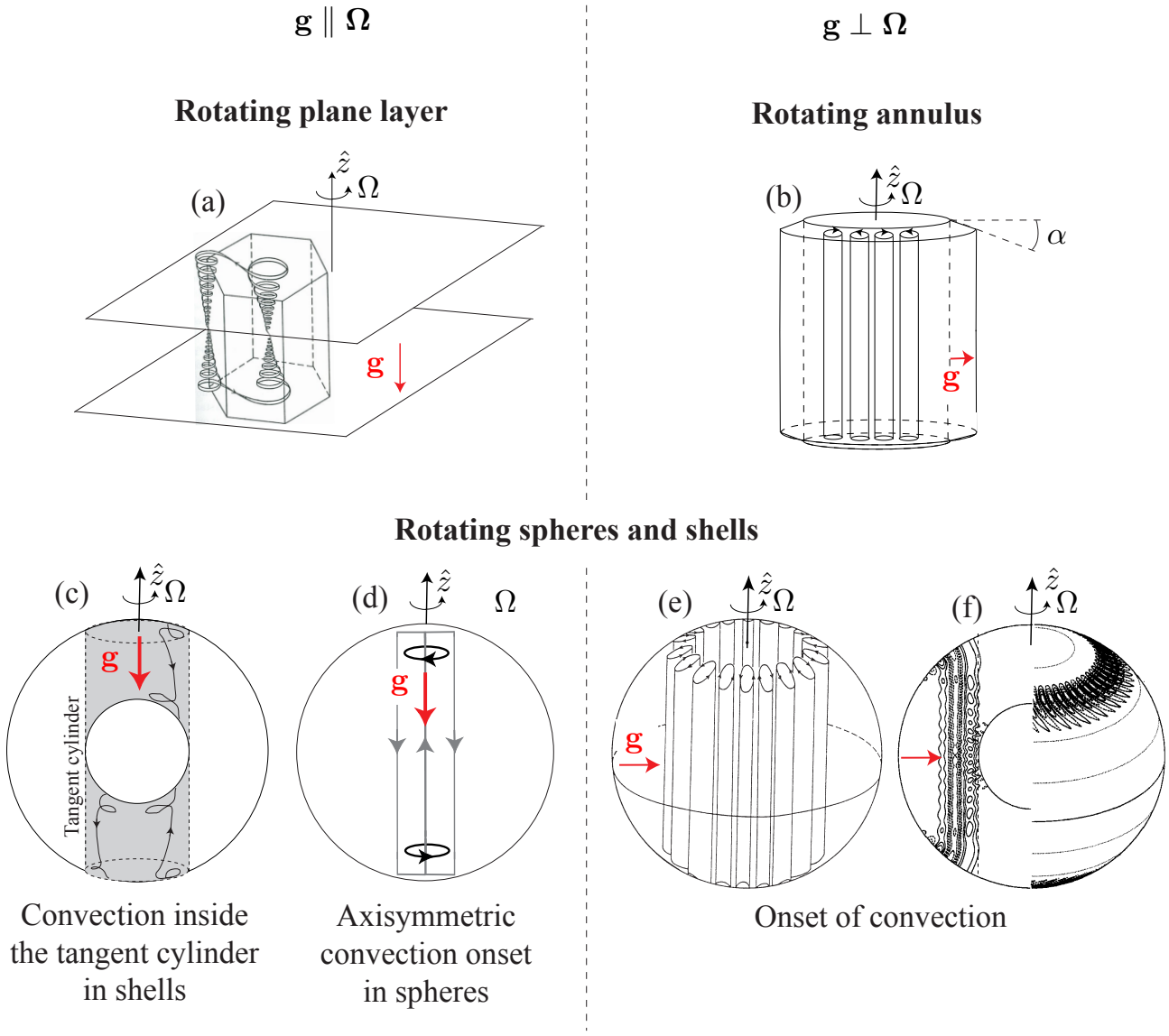

Figure 2.7: Convective motions in different rotating systems, the direction of the buoyancy force is represented by red arrows (also indicating the direction of the imposed temperature gradient and the dominant acceleration). (a) Rotating plane layer, with a sketch of the pathline in a hexagonal cell at onset, modified from Chandrasekhar (1961, part III, chapter 2). (b) Rotating annulus where the centrifugal acceleration dominates over gravity (the fluid is located between the two cylinders) and artistic view of convective motions at onset. (c,d,e,f) Rotating shells and spheres. (c) Artistic view of convection inside the tangent cylinder in spherical shells. (d) Schematic representation of the flow at axisymmetric convection onset in spheres. (e) Schematic representation of the onset of convection in rotating spheres, modified from Busse (1970). (f) Numerical results for the onset of convection in rotating shells with stress-free boundary conditions, modified from Zhang (1992). The left panel in (f) shows contours of the cylindrically radial component of the velocity field, u_s, in a meridian plane whereas the right panel shows streamlines of the toroidal flow on the outer surface.

to be z-invariant and the Taylor-Proudman constraint has to be broken by viscosity for convection to start, creating a small horizontal length scale of order $E^{1/3}D$.

Roberts (1968) was the first to recognize that non-axisymmetric modes become unstable at a lower forcing (measured by the Rayleigh number Ra) than axisymmetric modes. He predicted that, when the Prandtl number is of order unity, the critical Rayleigh number Ra_c at which convection starts evolves as $E^{-4/3}$ while motions take the form of waves with an azimuthal wavelength $O(E^{1/3}D)$, localized within an annulus of thickness $E^{2/9}D$. However, Roberts concentrated his efforts on antisymmetric modes, in the wake of his 1965 study (Roberts, 1965) where he found that the linearly most unstable axisymmetric mode of convection had this parity. Busse (1970) subsequently showed that the dominant structures at onset are not only non-axisymmetric but also symmetric with respect to the equator, corresponding to the famous illustration of vortices parallel to the axis of rotation and localized in the vicinity of a fixed radius in cylindrical coordinates (figure 2.7(e)). As noticed by Roberts (1968), non-axisymmetric modes carry heat away in a direction perpendicular to the rotation axis, as do convective motions in a rotating annulus. The latter analogy was developed by Busse (1970) to show that the slope at the outer sphere boundary is responsible for much of the dynamics of non-axisymmetric modes*, which take the form of Rossby waves (the Rossby-wave mechanism is qualitatively illustrated in figure 2.8).

The scaling $Ra_c \propto E^{-4/3}$ and the decrease of the azimuthal wavelength $O(E^{1/3}D)$ with the Ekman number, have been confirmed by laboratory experiments (Carrigan & Busse, 1983). However, Soward (1977) pointed out that, although the Roberts-Busse local theory provides a satisfactory understanding of the onset of convection, it results in an underestimated critical Rayleigh number†. The numerical results of Zhang (1992) for the onset of convection in rapidly rotating shells (figure 2.7(f)) confirmed a leading order discrepancy ($O(25\%)$) with the results predicted by the Roberts-Busse local theory. The first correct asymptotic solution for rapidly rotating full spheres was given by Jones *et al.* (2000) using global theory, with very good agreement with Zhang (1992)'s numerical results. The same theory was used by Dormy *et al.* (2004) for rapidly rotating shells.

To summarize, columnar symmetric Rossby waves with small azimuthal wavelength $O(E^{1/3})$ (figure 2.7(e,f)) are the first unstable convective modes at sufficiently low Ekman numbers in both spherical shells and spheres and at Prandtl numbers of order unity. We mention that another type of convective modes, corresponding to modified inertial modes, becomes the preferred form of convection at sufficiently low Prandtl numbers and

*Indeed, when the top and bottom boundary are purely horizontal in a rotating annulus ($\alpha = 0$ in figure 2.7(b)), two-dimensional horizontal convective rolls meet the non-penetration condition at the top and bottom boundaries. In the limit $E \to 0$, the leading order flow satisfies the Taylor-Proudman theorem in the annulus interior, resulting in a large azimuthal wavelength of the same order as the annulus thickness, just as in non-rotating Rayleigh-Bénard convection. On the contrary, when a finite slope is added on the boundaries ($\alpha \neq 0$), horizontal convective rolls do not meet the non-penetration conditions, which forces a z-dependent axial flow within the whole annulus interior. In the latter case, the onset of convection only occurs when the Taylor-Proudman constraint is broken by viscosity through Rossby waves of small ($O(E^{1/3})$) dimensionless azimuthal wavelength.

†When solving the problem in the real $s-$plane (local theory), one ends up with a non-zero phase mixing $\partial\sigma_i/\partial s$, where σ_i is the angular frequency. Phase mixing acts as a radial shear on the perturbations, stretching them in the azimuthal direction and reducing their s-length scale. Eventually, the enhanced viscous dissipation leads to the decay of the initially growing perturbations. For those reasons, the problem has to be solved using global theory (Huerre & Monkewitz, 1990) in the complex s-plane.

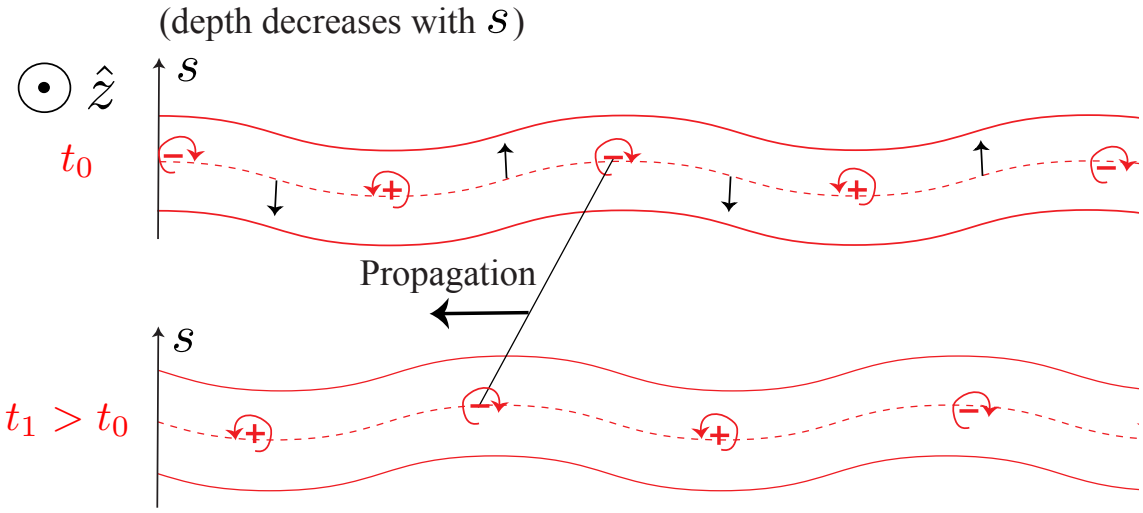

Figure 2.8: Schematic illustration of the mechanism for Rossby-waves, which are typical features of any rotating system with changing depth (Greenspan, 1968). The red lines and red symbols represent material lines and vorticity perturbations, respectively, while black arrows depict the velocity perturbations resulting from the vorticity perturbations. When a fluid tube aligned with the rotation axis (perpendicular to the plane depicted in the present figure) is displaced in the direction of decreasing depth (larger s values), mass conservation requires an increase of its horizontal section area. Therefore, its local vorticity decreases owing to Kelvin's circulation theorem (conservation of the circulation around a material tube in an inviscid fluid), inducing negative vorticity perturbations (clockwise motions). Similarly, displacements in the direction of increasing depth are associated with positive vorticity perturbations (anticlockwise motions). The induced velocity perturbations cause a leftward propagation between times t_0 and t_1. Translated into a rotating sphere or spherical shell, this mechanism leads to an eastward propagation.

sufficiently large Ekman numbers (Zhang, 1994, 1995; Busse & Simitev, 2004), although this regime is not in the scope of the present study.

2.3.4 Supercritical convection

Nonlinear convection and dynamo action in a rotating spherical system has been essentially studied in shells. The results obtained in such a geometry are instructive since they provide a physical intuition of the flow and magnetic field structures that are expected in rotating spheres.

2.3.4.1 Geostrophic (or rotationally dominated) regime

In its rigorous sense, a *geostrophic* flow is characterized by a balance between the Coriolis force and the pressure gradient in the leading-order momentum equation (Greenspan, 1968). If the geostrophic balance (2.2) is exactly satisfied, the Taylor-Proudman constraint (2.3) holds and, therefore, the term *geostrophic* often refers to flows that are invariant along the rotation axis (Cardin & Olson 2007, Christensen & Wicht 2007). In a less restrictive view, flows resulting from thermal wind mechanisms are usually referred to as geostrophic winds in the literature of atmosphere or ocean dynamics (Kundu & Cohen, 1990), although they cause departures from the Taylor-Proudman constraint. Even more

generally, the terms *geostrophic* or *rotationally dominated* refer to flows in which the dynamics is clearly influenced by rotation, i.e. the Coriolis force is involved in the leading order force balance, and the latter definition will be retained in the present study.

For a flow to be rotationally dominated, both the Ekman number E, which measures the relative importance of the viscous and Coriolis forces, and the Rossby number Ro, which measures the relative importance of inertial to Coriolis forces, have to be small compared to unity. A transition from a geostrophic regime to a *weakly rotating regime*, in which the flow becomes three dimensional and heat transfer satisfies the same laws as in non-rotating systems, is found when increasing the forcing of convection in simulations and experiments for various geometries (rotating plane layers, cylinders or rotating shells) (King *et al.*, 2009; Schmitz & Tilgner, 2009; Zhong *et al.*, 2009; Schmitz & Tilgner, 2010; King *et al.*, 2010, 2012). The parameter controlling this transition has been a controversial topic and remains a subject of debate*.

In the presence of dynamo action, the Lorentz force may also cause departures from geostrophy. This is quantified by the Elsasser number, which measures the relative importance of the Lorentz and Coriolis forces. Several definitions of the Elsasser number have been proposed in the literature (Christensen *et al.*, 1999; Soderlund *et al.*, 2012) and whether the Lorentz force affects the flow dynamics in simulations or in planetary cores remains an unsolved question†.

2.3.4.2 Dynamics outside the tangent cylinder

Columnar flow structures

Above the onset of convection, with increasing forcing, the flow experiences a series of transitions which finally leads to chaotic convection. In the fully nonlinear regime at intermediate Prandtl numbers, the flow remains dominated by symmetric columnar structures aligned with the rotation axis, forming either a set of drifting vortex pairs inherited from the onset of convection at intermediate forcing of convection (figure 2.9(c,d)) (e.g. Simitev & Busse, 2003; Soderlund *et al.*, 2012) or plumes at higher forcing (figure 2.9(a)) (e.g. Cardin & Olson, 1994; Sumita & Olson, 1999). In both cases, the axial vorticity, as well as the equatorial velocity, varies very slowly with z, appearing almost two-dimensional (figures 2.9(b,c,d)), indicating that those symmetric flows tend to satisfy the Taylor-Proudman theorem. Similar convective structures are also found in self-sustained dynamos (figure 2.9(e,f)) (e.g Olson *et al.*, 1999; Christensen *et al.*, 1999; Simitev & Busse, 2005; Kageyama *et al.*, 2008) with no major influence of the magnetic field (Soderlund *et al.*, 2012). Thus, antisymmetric modes always play a secondary role outside the tangent cylinder in previously published studies of nonlinear convection in rotating spherical shells, with or without dynamo action.

*King *et al.* (2009) and King *et al.* (2012) argue that this transition occurs when the thickness of the thermal boundary layer, which decreases with the forcing of convection, matches the thickness of the viscous boundary layer. This boundary layer control is especially difficult to reconcile with the absence of any $O(E^{1/2})$ layer in the the free-slip simulations of Schmitz & Tilgner (2010), while a transition in heat transfer is obtained at similar parameter values as in no-slip simulations.

†e.g. Soderlund *et al.* (2012) report a weak influence of the magnetic field on the flow whereas the flow morphology is strongly affected by the magnetic field in the numerical study by Hori & Wicht (2013).

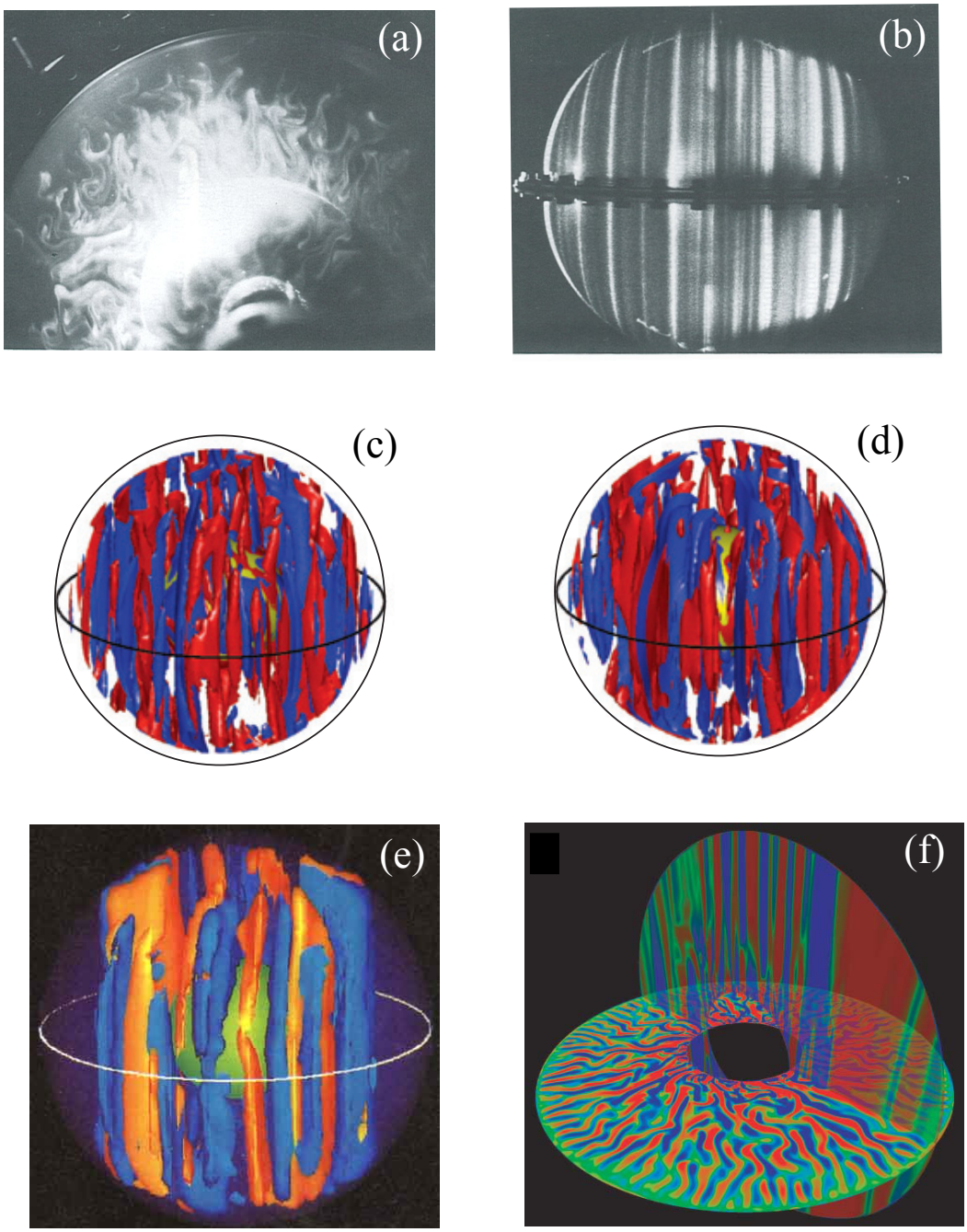

Figure 2.9: Flow snapshots for supercritical convection in rotating shells in (a,b) laboratory experiments, (c,d) hydrodynamic simulations and (e,f) self-sustained dynamo simulations. (a,b) Experiments at $E = 2.5 \times 10^{-6}$, $Ra \approx 50 Ra_c$ *where* Ra *is the Rayleigh number and* Ra_c *the critical Rayleigh number. (a) Side view (using flakes inside the fluid) and (b) top view (using fluorescein dye) of convection patterns (Cardin & Olson, 1994). (c,d) Isosurfaces of axial vorticity,* $E = 10^{-4}$, $Ra = 4.9 Ra_c$ *and* $Ra = 5.6 Ra_c$, *respectively (Soderlund* et al., *2012). (e) Isosurfaces of axial vorticity,* $E = 10^{-4}$, $Ra \approx 10 Ra_c$ *(Olson* et al., *1999). (f) Equatorial and meridional cross-sections of the axial component of the vorticity,* $E = 5.2 \times 10^{-6}$ *(Kageyama* et al., *2008).*

The weak influence of antisymmetric modes is widely admitted and has plaid an important role in the modeling of convection in rotating spherical shells. From the observation that the flow is dominated by symmetric and almost two-dimensional motions in the fully nonlinear regime, simplified models, called *quasigeostrophic* models, have been developed (e.g. Cardin & Olson, 1994; Aubert *et al.*, 2003; Gillet & Jones, 2006; Gillet *et al.*, 2007), and were inspired from models of convection in a rotating annulus (Busse, 1970, 1986; Busse & Or, 1986; Or & Busse, 1987). Quasigeostrophic models compute a two-dimensional flow within the equatorial plane, assuming that the axial vorticity is invariant along the rotation axis while the leading order axial velocity is parametrized to satisfy the non-penetration condition. Such models are rigorously exact in the limit of small slope at the upper and lower boundaries in a rotating annulus, but can not be mathematically justified in rotating shells or spheres where the large slope at the outer spherical boundary forces a leading order z-varying flow (see Gillet & Jones, 2006, for further discussions of the validity of quasigeostrophic models). Despite this limitation, the quasigeostrophic approximation is very convenient to reach low Ekman numbers that are not accessible with three-dimensional simulations.

Zonal flows

Nonlinear interactions between columnar structures drive axisymmetric (i.e. invariant in ϕ-direction) azimuthal flows, also called *zonal flows*, through either Reynolds stresses (Aubert *et al.*, 2001; Christensen, 2001, 2002; Gillet *et al.*, 2007) or thermal wind mechanisms (Aurnou & Olson, 2001). The former arise from nonlinear coupling in the Navier-Stokes equations when the azimuthal and cylindrically radial components of the columnar structures are correlated. The latter results from non-homogeneous heat transfer by columnar convection, which carries heat away preferentially in a plane perpendicular to the rotation axis. This induces mean temperature gradients along lines of constant effective acceleration (gravitational or centrifugal), and therefore shear flows in the azimuthal direction through a thermal-wind mechanism.

The amplitude of the zonal flow relative to columnar structures varies with the boundary conditions and the control parameters, mainly the Ekman and Rayleigh numbers. At $Pr \gtrsim 1$, zonal flows generally contain between $10 - 20\%$ of the total kinetic energy for no-slip boundary conditions whereas they can dominate over columnar structures for stress-free boundary conditions (Christensen, 2001), inducing periodic vacillations of the non-axisymmetric columns (Simitev & Busse, 2003). Lower Prandtl numbers usually favor dominant zonal flows (Aubert *et al.*, 2001; Zhang, 1992).

In the absence of any magnetic field, zonal flows are mainly induced by Reynolds stresses at low Ekman numbers and are almost invariant in the direction of the rotation axis, satisfying the Taylor-Proudman constraint (figure 2.10(a)) (Christensen, 2002). When a large-scale magnetic field is maintained, the Taylor-Proudman constraint is relaxed and thermal winds dominate, causing a shear along $\hat{z}$ (figure 2.10(b)) (Aubert, 2005). In both cases, zonal flows are strongly symmetric with respect to the equator in previously published studies.

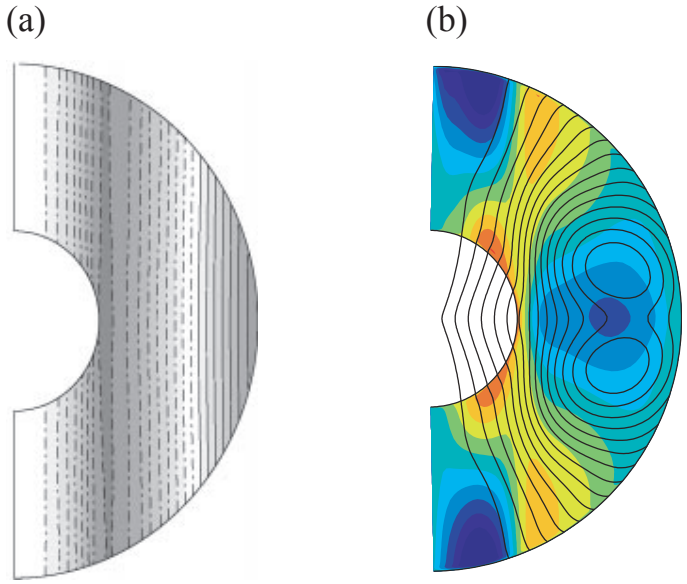

Figure 2.10: Zonal flows for convection (a) in the absence of magnetic field and (b) when a large-scale magnetic field is sustained. (a) Time-averaged zonal flow, $E = 10^{-5}$, $Ra \approx 40Ra_c$, $Pr = 1$, free-slip, dashed and solid lines indicate negative and positive values, respectively, while greyscale indicates absolute magnitude, (Christensen, 2002). (b) Structure of the time-averaged zonal flow (colors), $E = 10^{-4}$, $Ra \approx 11Ra_c$, $Pr = 1$, no-slip, black lines correspond to meridional magnetic field lines (Aubert, 2005).

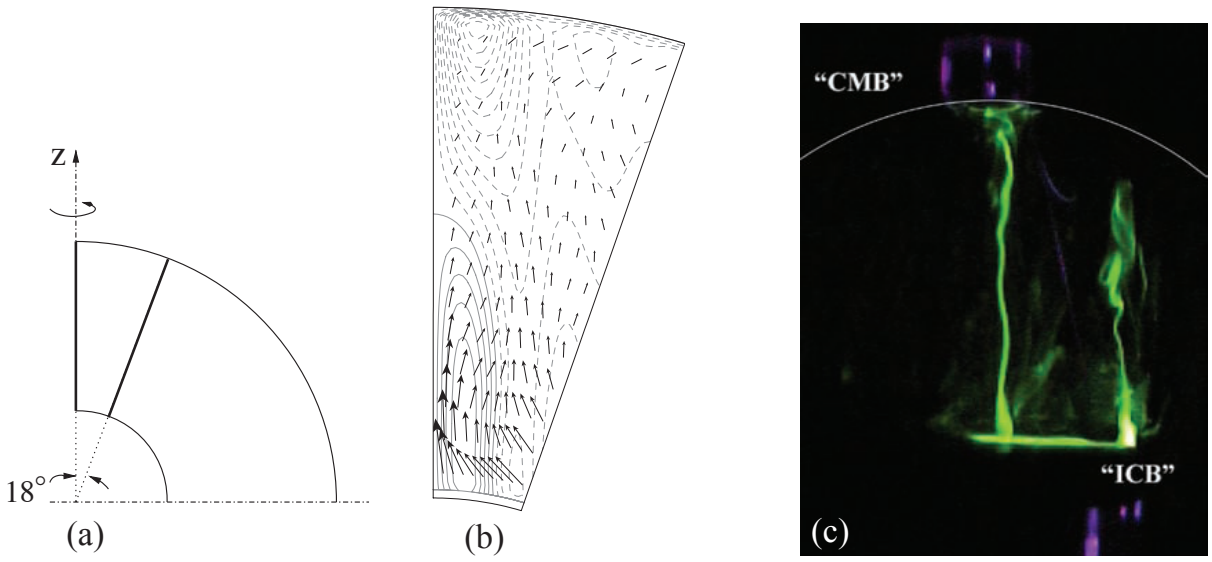

Figure 2.11: Numerical (a,b) and laboratory (c) models of convection inside the tangent cylinder, (a,b) when a magnetic field is sustained and (c) in the absence of any magnetic field. (b) Azimuthal flow (contours) and meridional flow (arrows) at a constant ϕ value, in a sector shown highlighted in (a), $E = 10^{-4}$, $Ra \approx 8Ra_c$, $Pr = 5$, (Sreenivasan & Jones, 2006a). (c) Two small-scale helical plumes marked with fluorescein dye, $E = 4.3 \times 10^{-5}$, $Pr = 7$, picture from Aubert et al. *(2008), further details in Aurnou* et al. *(2003).*

2.3.4.3 Dynamics inside the tangent cylinder

In the case of a radial gravity (such as in planetary cores), the rotation axis is almost parallel to gravity inside the tangent cylinder (excluding very thick of very thin spherical shells) and convective motions are dynamically similar to convection in a rotating plane layer (figure 2.7(a)) (Simitev & Busse, 2005). In the absence of any magnetic field, convection takes the form of thin axial plumes (figure 2.11(c)) (Aurnou *et al.*, 2003) whereas it is dominated by larger plumes if a sufficiently strong magnetic field is imposed or self-sustained (figure 2.11(b)) (Sreenivasan & Jones, 2006*a*). In both cases heat is carried away in the direction of the rotation, and the mean temperature inside the tangent cylinder is slightly different from the mean temperature outside*, inducing strong zonal flows through a thermal wind mechanism (Aurnou *et al.*, 2003; Sreenivasan & Jones, 2005, 2006*a*). The two polar regions inside the tangent cylinder are disconnected and, therefore, they are not tied together by the Taylor-Proudman constraint, possibly resulting in non-negligible antisymmetric components inside the tangent cylinder (Grote & Busse, 2001).

2.3.5 Dynamo regimes

Several types of magnetic field patterns have been reported in convective dynamos after the onset of dynamo action. The main and widely admitted categorization separates cases where a large-scale dipole magnetic field is observed, called the *dipole-dominated regime* (figure 2.12(a)), from cases where the magnetic field is dominated by higher multipoles, called the *multipolar regime* (figure 2.12(b)). A dipole component whose axis is aligned with the rotation axis is usually favored in the dipole-dominated regime (Olson *et al.*, 1999; Christensen *et al.*, 1999; Gubbins *et al.*, 2000), though magnetic field with a dipole axis located within the equatorial plane have been found in self-sustained dynamos (Ishihara & Kida, 2002; Aubert & Wicht, 2004). The transition from the dipole-dominated to the multipolar regime, which occurs when increasing the forcing of convection, has been studied systematically when varying the control parameters in rotating spherical shells (Kutzner & Christensen, 2002; Olson & Christensen, 2006; Christensen & Aubert, 2006; Yadav *et al.*, 2013). It remains unclear what competition controls this transition: It was first explained by a competition between inertial and Coriolis forces (Sreenivasan & Jones, 2006*b*; Christensen & Aubert, 2006; Olson & Christensen, 2006), whereas a recent study (Soderlund *et al.*, 2012) finds that the transition does not correlate with the breakdown of columnar flow structures and suggests that it is rather controlled by the ratio of inertial to viscous forces. Dipole-dominated dynamos in which the magnetic field undertakes reversals are usually found in a narrow region of parameter space, between non-reversing dynamos and multipolar dynamos.

Most commonly, in both dipole-dominated or multipolar dynamo regimes, the magnetic field pattern is such that the hemispheres located below and above the equatorial plane (northern and southern hemispheres) contain about the same magnetic energy. *Hemispherical dynamos* where the magnetic field is mainly localized in one hemisphere, and almost vanishes in the other, have been reported (Grote & Busse, 2000), but they correspond to a narrow domain in parameter space (Simitev & Busse, 2005).

*Since (1) heat transfer inside and outside the tangent cylinder involves motions that are somewhat disconnected and (2) the ratio of the outer to inner boundary area is different inside and outside the tangent cylinder, a temperature difference is maintained between the two regions.

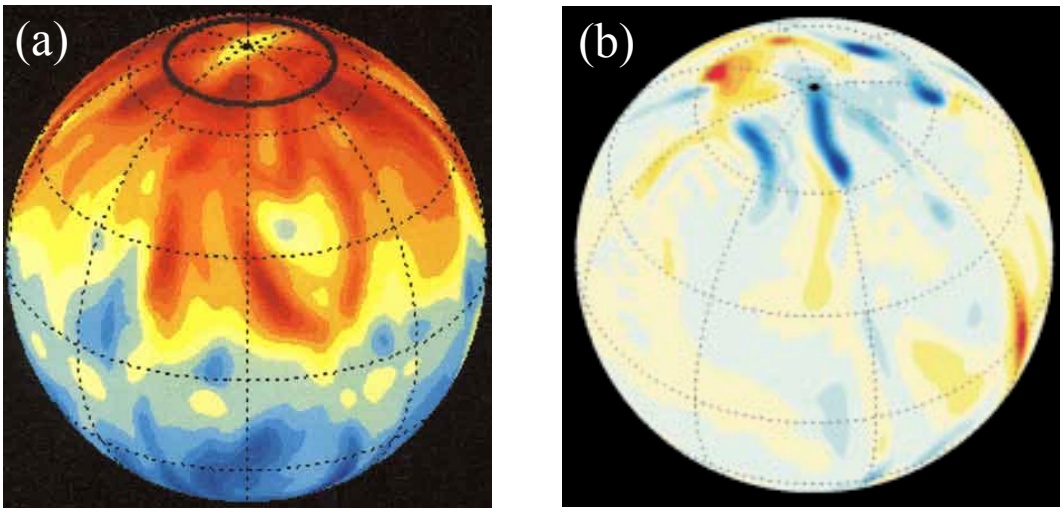

Figure 2.12: Most common radial magnetic field patterns in convective dynamos in rotating spherical shells. (a) Dipole-dominated magnetic field with dipole axis aligned with the rotating axis, $E = 10^{-4}$, $Ra \approx 11 Ra_c$, $Pr = 1$, $Pm = 1$ where Ra is the Rayleigh number, Ra_c the critical Rayleigh number and Pm the magnetic Prandtl number (ratio of viscous to magnetic diffusivities) (from Olson et al.*, 1999). (b) Multipolar magnetic field, $E = 10^{-3}$, $Ra \approx 14 Ra_c$, $Pr = 1$, $Pm = 4$ (from Christensen* et al.*, 1999).*

The fundamental mechanisms involved in magnetic field generation have been analyzed in dipole-dominated dynamos (Kageyama & Sato, 1997; Olson *et al.*, 1999) (appendix B). Those studies have shown that the axisymmetric axial magnetic field is essentially generated by columnar convection through an α-effect, while the axisymmetric azimuthal magnetic field can be induced either by an ω-effect involving thermal winds or by an α-effect involving columnar convection. Depending on what mechanism dominates the generation of azimuthal magnetic field, dynamos are classified as $\alpha\omega$-dynamos or α^2-dynamos.

2.3.6 Summary: What regimes and structures do we expect in rotating spheres?

Intuitively, the flow and dynamo regimes in rotating full-spheres are expected to be similar to those obtained in spherical shells, as summarized in figure 2.5. The flow in the geostrophic regime is expected to be formed by the superposition of columnar vortices, aligned with the rotation axis, and zonal flows, both being mainly symmetric with respect to the equator. The magnetic field is expected to be either dipole-dominated or multipolar, but most often of same strength in both hemispheres.

2.4 Recent approaches and current challenges

The main limitations when studying convection and dynamo action in planetary cores comes from the inability of any experiment or simulation to replicate core conditions, which correspond to extremely low Ekman numbers (typically $E \lesssim 10^{-12}$), high Rayleigh

numbers (typically $Ra \gtrsim 5000 Ra_c$) and turbulent flows (Reynolds numbers typically larger than 10^7). Therefore, it is disputable whether the dynamics isolated in laboratory experiments or numerical simulations is somewhat similar to convective flows in planetary cores.

To overcome this difficulty, two main approaches have been developed. The first one consists in using numerical approximations in order to reach lower Ekman numbers than in three-dimensional simulations, such as the previously mentioned quasigeostrophic approximation (e.g. Cardin & Olson, 1994; Aubert *et al.*, 2003; Gillet & Jones, 2006; Gillet *et al.*, 2007) or the $2 - 1/2$ dimensional approach in which only the axisymmetric component and one non-axisymmetric azimuthal wavenumber are retained in the calculation (Morrison & Fearn, 2000; Cupal *et al.*, 2002). The second approach consists in conducting systematic studies in which the parameter space is explored, allowing the characterization of regime transitions and the retrieval of various scaling laws that depict the behavior of output quantities as a function of control parameters (e.g. Christensen & Aubert, 2006; Olson & Christensen, 2006; Simitev & Busse, 2005; Christensen *et al.*, 2009; King *et al.*, 2010). The scaling laws and the regime transitions are then extrapolated to planetary values, leading to a better understanding of the dynamical regime in planetary cores.

Other studies have focused on the dynamics obtained in specific simulations, especially those studying statistical properties of magnetic field reversals (Driscoll & Olson, 2011; Olson *et al.*, 2013), those interested in isolated dynamical behaviors (Grote & Busse, 2000) or those computed at extreme parameters and requiring very high computational power (Sakuraba & Roberts, 2009; Kageyama *et al.*, 2008; Miyagoshi *et al.*, 2010). In this case, the simulations need to be located in a regime which is relevant for planetary dynamos for the numerical results to be of any geophysical significance. For example, recent efforts have been developed to isolate domains of the parameter space where simulations behave in a way that is compatible with observations of the Earth's magnetic field (Christensen *et al.*, 2010).

Despite recent efforts in characterizing regime transitions and scaling laws, further investigations are required in order to (1) identify new regime transitions (as achieved in the present study), (2) provide an improved understanding of the basic mechanisms responsible for presently known transitions (including dipole-dominated to multipolar dynamos and rotationally dominated to weakly rotating convection) and (3) investigate the influence of other effects (i.e. stratification, boundary conditions, ...) on those transitions.

2.5 This study

In this study, we use three dimensional direct numerical simulations to study convection in rotating full-spheres, with and without dynamo action, at Prandtl number of order unity and with uniform boundary conditions. We follow the second approach introduced in the previous section: we adopt a systematic approach which consists in exploring regions of parameter space in order to characterize the different dynamical regimes of convection and dynamo action in rotating full-spheres. Scaling laws for the regime boundaries are extracted. In addition to this systematic approach, a few simulations will be specifically analyzed in order to isolate particular dynamical behaviors and compare the numerical

results with existing theories.

The first part of this manuscript is organized as follows:

In chapter 3, we introduce the model. It includes: the different approximations leading to the final equations that are solved numerically, the different control parameters, the boundary conditions, the main output quantities that are analyzed in this study and the numerical methods.

In chapter 4, we vary the control parameters within the rotationally dominated regime and characterize the different flow and dynamo regimes. We especially focus on the secondary bifurcation that marks the emergence of antisymmetric modes. For sufficiently supercritical Rayleigh numbers, we find an unexpected hydrodynamic regime where the flow is strongly asymmetric with respect to the equator, and in which an equatorially antisymmetric and axisymmetric (EAA) mode strongly influences the total flow, in apparent conflict with the Taylor-Proudman theorem. This flow regime induces hemispherical dynamos, with a magnetic energy up to 9 times stronger in one hemisphere than in the other. This chapter contains most of the numerical results presented in the article "Equatorially asymmetric convection inducing hemispherical magnetic field in rotating spheres and implications for the past martian dynamos" published in 2011 in *Physics of the Earth and Planetary Interiors* (reproduced in appendix D), although the analysis has been improved in the present manuscript.

Chapter 5 provides a general discussion of numerical results and geophysical implications. In particular, we discuss the significance of our results with respect to the Taylor-Proudman constraint. We also discuss whether the hemispherical dynamos identified in chapter 4 can be comprehended within a theoretical framework based on interactions between two magnetic modes.

Finally, possible developments and further investigations are suggested in Chapter 6.

Chapter 3

Model and methods

We consider the configuration and coordinate system defined in the previous chapter and recalled in figure 3.1. A spherical shell of thickness $D = r_o - r_i$, where r_i is the inner radius and r_o the outer radius, rotates at a constant rate Ω. In this work, we are interested in entirely liquid planetary cores, corresponding to $r_i/r_o = 0$. Because of numerical considerations, a very small inner sphere of radius $r_i = 0.01 r_o$ was retained in our first calculations. Later numerical implementations (detailed in section 3.8) enabled us to completely remove the inner sphere ($r_i/r_o = 0$).

In the following, the symbol D/Dt denotes the material derivative (or Lagrangian derivative), which is equal to $\partial/\partial t + \mathbf{u} \cdot \nabla$ in Eulerian variables.

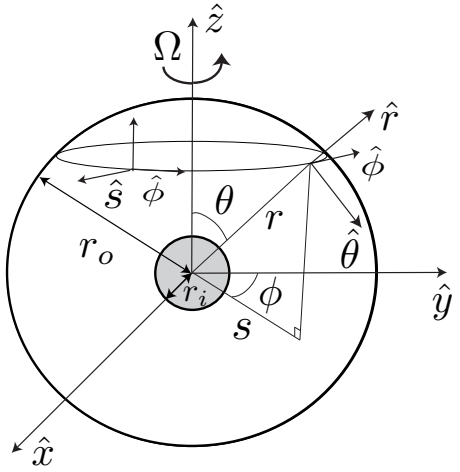

Figure 3.1: Configuration and coordinate systems. The electrically conducting fluid is located between $r = r_i$ and $r = r_o$.

3.1 Adiabatic reference state and Boussinesq approximation

We first consider a "well-mixed" (isentropic) and hydrostatic system, called the adiabatic reference state, which is given by

$$\frac{\partial T_a}{\partial r} = -\frac{T_a}{H_T} \quad ; \quad \frac{\partial P_a}{\partial r} = -\rho_a g \quad ; \quad \frac{\partial \rho_a}{\partial r} = -\frac{\rho_a}{H_\rho} \quad ; \quad S_a = const;$$
$$H_T = \frac{C_P}{\alpha g} \quad ; \quad H_\rho = \frac{C_P}{\alpha g \gamma}; \tag{3.1}$$

where the subscript $_a$ denotes the adiabatic reference state. T is a temperature field, P a pressure field, ρ a density field, S a specific entropy, α the thermal expansion coefficient, g the gravitational acceleration, γ the Grüneisen parameter and C_P the specific heat capacity under constant pressure. D/H_T, called the dissipation number (Schubert *et al.*, 2001), is the ratio of the core thickness to the characteristic length scale of adiabatic temperature variations whereas D/H_ρ is the ratio of the core thickness to the characteristic length scale of adiabatic density variations. The adiabatic temperature gradient $\partial T_a/\partial r$ is caused by hydrostatic pressure variations (see appendix C for the derivation of the first equation in (3.1)) and this gradient plays an essential role in planetary cores where a considerable portion of the total heat flux is conducted along the adiabat and does not contribute to convection driving (as already mentioned in the main introduction).

The total temperature $\mathcal{T}$, specific entropy $\mathcal{S}$ and pressure $\mathcal{P}$ of the real planetary system can be decomposed into an adiabatic reference state and fluctuations (T, S, P):

$$\mathcal{T} = T_a + T \quad ; \quad \mathcal{S} = S_a + S \quad ; \quad \mathcal{P} = P_a + P. \tag{3.2}$$

Fluctuations are assumed to be small compared to the adiabatic reference state, as expected in planetary cores.

The Boussinesq approximation is used in the present study. It consists in (1) neglecting the effect of adiabatic quantities gradients on convective motions, (2) neglecting density variations in the momentum equation except in the buoyancy force, (3) assuming that density fluctuations that drive motions result principally from thermal effects (as opposed to pressure) and (4) neglecting ohmic and viscous dissipations. The Boussinesq approximation especially requires D/H_ρ and the dissipation number D/H_T to be small compared to 1 (explicitly shown in section 3.2.1).

In the Earth's core D/H_ρ is of order 0.2 according to the Preliminary Reference Earth Model (Dziewonski & Anderson, 1981) and $D/H_T \approx 0.2 - 0.3$ (Anufriev *et al.*, 2005). Similar values hold for Mars'core and the Earth's core prior to inner core crystallization. Most published numerical studies of core convection and dynamo action have assumed that such values are small enough for fluctuations around the adiabatic system to be well approximated by a Boussinesq system (i.e. Olson *et al.* 1999, Christensen *et al.* 1999, Simitev & Busse 2005, Christensen & Aubert 2006). Though, models based on the anelastic approximation (formulated in Braginsky & Roberts 1995, Anufriev *et al.* 2005, benchmarked in Jones *et al.* 2011), have been used in a few numerical studies (Glatzmaier & Roberts, 1996).

3.2 Dimensional equations

3.2.1 Temperature equation

In this subsection, the temperature equation is derived from the energy equation and the different simplifications related to the Boussinesq approximation are explicitly given. Such a derivation is essential to understand the way secular cooling is modeled in the present study. For a more detailed derivation the reader is referred, for instance, to Anufriev *et al.* (2005).

In the general case, the energy equation can be written in a form involving the specific entropy $\mathcal{S}$ (Gubbins & Roberts 1987, Braginsky & Roberts 1995):

$$\rho\mathcal{T}\frac{D\mathcal{S}}{Dt} = -\nabla\cdot\mathbf{q}+s_I, \tag{3.3}$$

$$\mathbf{q} = -k\nabla\mathcal{T}, \tag{3.4}$$

where $\mathbf{q}$ is the heat-flux vector, k the thermal conductivity, ρ the total density field, and s_I the rate of internal generation of heat per unit volume. s_I includes radioactive sources, viscous dissipation and ohmic dissipation.

At this stage it is useful to isolate two time scales in the dynamics of convecting planetary cores. First, the time scale relevant for large scale convective motions t_{conv} is of the order of a few hundred years. Second, planetary cores cool down on a few hundred million year time scale t_{cool}, causing the adiabatic reference state to vary with time. The ratio t_{conv}/t_{cool} is much smaller than 1 in planetary cores.

Equations (3.2) and (3.4) are injected into (3.3). Only the leading-order terms are retained in the limit of small t_{conv}/t_{cool} values and of small fluctuations to the adiabatic reference state. Then, (3.3) becomes

$$\rho_a T_a\frac{DS_a}{Dt}+\rho_a T_a\frac{DS}{Dt} = \nabla\cdot(k\nabla T)+\nabla\cdot(k\nabla T_a)+s_I. \tag{3.5}$$

Making use of Maxwell's relations, the change in entropy is related to temperature variations through

$$d\mathcal{S} = \frac{C_P}{\mathcal{T}}d\mathcal{T}-\frac{\alpha}{\rho}d\mathcal{P}, \tag{3.6}$$

from which an expression for the entropy fluctuations can be deduced:

$$S = \frac{C_P}{T_a}T-\frac{\alpha}{\rho_a}P. \tag{3.7}$$

Pressure forces and buoyancy forces are expected to be of the same order of magnitude in planetary cores, implying that $P/r_o\sim\rho_a g\alpha T$ (when neglecting the effect of pressure on density fluctuations). Therefore,

$$\frac{\alpha}{\rho_a}P\sim\alpha T_a\frac{r_o}{H_T}\frac{C_P T}{T_a}. \tag{3.8}$$

Thus, in the limit of small $\alpha T_a r_o/H_T$ values, the second RHS term in equation (3.7) can be neglected compared to the first RHS term and we can write

$$S = \frac{C_P}{T_a}T. \tag{3.9}$$

Given that $\alpha = O(10^{-5})$ K^{-1} and $T_a = O(10^3)$ K, αT_a is always small compared to 1 in planetary cores and equation (3.9) is a good approximation even in cases where $D/H_T = O(1)$.

Injecting equation (3.9) in (3.5), assuming a constant value for C_P and retaining the leading-order terms as before (for $t_{conv}/t_{cool} \ll 1$ and small fluctuations) leads to the following temperature equation:

$$\rho_a C_P \frac{DT}{Dt} + \frac{\rho_a C_P T}{T_a}\mathbf{u}\cdot\nabla T_a = \nabla\cdot(k\nabla T) + \nabla\cdot(k\nabla T_a) + s_I - \rho_a T_a \frac{dS_a}{dt}, \tag{3.10}$$

where $\mathbf{u}$ is the velocity field. Making use of the first equation in (3.1), the second LHS term in (3.10) can be written as $\rho_a C_P u_r T/H_T$. Thus, the ratio of the second LHS to the first LHS term is of order D/H_T. Similarly, the ratio of the second RHS term to the first LHS term is of order $\max\left(Re^{-1}Pr^{-1}(D/H_T)^2, Re^{-1}Pr^{-1}(D^2/H_T H_\rho)\right)$, where $Re = \sqrt{\mathbf{u}^2}D/\nu$ is the Reynolds number and $Pr = \nu\rho C_P/k$ the Prandtl number. Since $Re^{-1}Pr^{-1} \ll 1$ in planetary cores, assuming that D/H_T and D/H_ρ are small compared to 1 and that the thermal diffusivity $\kappa = k/\rho C_P$ varies little with r gives the following leading-order temperature equation:

$$\frac{DT}{Dt} = \kappa\Delta T + \frac{s_I}{\rho_a C_P} - \frac{T_a}{C_P}\frac{dS_a}{dt}, \tag{3.11}$$

which is the final temperature equation within the Boussinesq approximation. The term s_I contains only radioactive heating in the Boussinesq equation (3.11) since viscous and ohmic dissipations are of order D/H_T (Anufriev *et al.*, 2005, see equation (7.5)). The third RHS term corresponds to the decrease of the adiabatic entropy due to core cooling on geological time scales (secular cooling) and it acts as a heat source in the evolution equation (3.11) for T.

Following Aubert *et al.* (2009), radioactive heating and secular cooling are modeled by a uniform distribution of internal heat sources s_T such that

$$\frac{DT}{Dt} = \kappa\Delta T + s_T. \tag{3.12}$$

3.2.2 Momentum and continuity equations

Within the Boussinesq approximation, the momentum equation (2.1) becomes:

$$\frac{\partial\mathbf{u}}{\partial t} + \mathbf{u}\cdot\nabla\mathbf{u} = -2\Omega\left(\hat{z}\times\mathbf{u}\right) - \frac{1}{\rho_0}\nabla P + \alpha g(r)T\hat{r} + \frac{1}{\rho_0\mu}\left(\nabla\times\mathbf{B}\right)\times\mathbf{B} + \nu\Delta\mathbf{u}, \tag{3.13}$$

where P is now a modified pressure field that incorporates centrifugal effects* and ρ_0 is the radial average of the adiabatic fluid density. In equation (3.13), the hydrostatic reference state (3.1) has been subtracted. The third RHS term in (3.13) corresponds to the buoyancy force that drives convective motions.

In the limit of small D/H_ρ ratio, the mass conservation equation can be written in its Boussinesq form as

$$\nabla \cdot \mathbf{u} \;=\; 0. \tag{3.14}$$

3.2.3 Final set of equations

Finally, if we incorporate the induction equation (2.5) into the set that includes the temperature, momentum and mass conservation equations (3.12), (3.13) and (3.14), we obtain the following set of equations, taking into account that $\mathbf{B}$ is a solenoidal vector field:

$$\frac{\partial \mathbf{u}}{\partial t} + \mathbf{u}\cdot\nabla\mathbf{u} + 2\Omega\,(\hat{z}\times\mathbf{u}) = -\frac{1}{\rho_0}\nabla P + \alpha g(r) T\hat{r} + \frac{1}{\rho_0\mu}\,(\nabla\times\mathbf{B})\times\mathbf{B} + \nu\Delta\mathbf{u}, \tag{3.15}$$

$$\frac{DT}{Dt} = \kappa\Delta T + s_T, \tag{3.16}$$

$$\frac{\partial \mathbf{B}}{\partial t} = \nabla\times(\mathbf{u}\times\mathbf{B}) + \eta\Delta\mathbf{B}, \tag{3.17}$$

$$\nabla\cdot\mathbf{u} = 0, \tag{3.18}$$

$$\nabla\cdot\mathbf{B} = 0. \tag{3.19}$$

Equations (3.15)-(3.19) admit the static solution

$$\mathbf{u}^{(s)} = 0 \;\;;\;\; \mathbf{B}^{(s)} = 0 \;\;;\;\; \frac{\partial P^{(s)}}{\partial r} = \rho_0\alpha g T^{(s)} \;\;;\;\; \kappa\Delta T^{(s)} = -s_T; \tag{3.20}$$

where $T^{(s)}$ is a function of r only in the present study. Subtracting the above static solution to (3.15-3.19) gives the following final set of equations for the perturbations $T' = T - T^{(s)}$, $P' = P - P^{(s)}$, $\mathbf{u}' = \mathbf{u}$ and $\mathbf{B}' = \mathbf{B}$:

*The centrifugal force is formed of two terms: $\rho_0\Omega\times(\Omega\times\mathbf{r})$ and $\alpha T\rho_0\Omega\times(\Omega\times\mathbf{r})$. The first term can be written as a gradient and incorporated in the pressure term. The second term is called *centrifugal buoyancy* (Lopez *et al.*, 2013) and it is small compared to the canonical buoyancy in planetary cores.

$$\frac{\partial \mathbf{u}}{\partial t} + \mathbf{u}\cdot\nabla\mathbf{u} + 2\Omega\,(\hat{z}\times\mathbf{u}) = -\frac{1}{\rho_0}\nabla P' + \alpha g(r) T'\hat{r} + \frac{1}{\rho_0\mu}\,(\nabla\times\mathbf{B})\times\mathbf{B} + \nu\Delta\mathbf{u}, \tag{3.21}$$

$$\frac{\partial T'}{\partial t} + \mathbf{u}\cdot\nabla T' + \mathbf{u}\cdot\nabla T^{(s)} = \kappa\Delta T', \tag{3.22}$$

$$\frac{\partial \mathbf{B}}{\partial t} = \nabla\times(\mathbf{u}\times\mathbf{B}) + \eta\Delta\mathbf{B}, \tag{3.23}$$

$$\nabla\cdot\mathbf{u} = 0, \tag{3.24}$$

$$\nabla\cdot\mathbf{B} = 0. \tag{3.25}$$

Solutions of equations (3.21)-(3.25) must also satisfy some boundary conditions, explicitly given in section 3.4.

3.3 Final set of dimensionless equations and control parameters

Equations (3.21) - (3.25) are non-dimensionalized using the following scales: $D = r_o - r_i$ for length, Ω^{-1} for time, $\rho_0 D^2\Omega^2$ for pressure, $\sqrt{\rho_0\mu}\Omega D$ for magnetic field and $Q/4\pi\rho_0 C_P \Omega D^3$ for temperature where Q is the static heat flux integrated over the surface at the external boundary, given by

$$Q = \int_{\Sigma_o} q^{(s)}\mathrm{d}s \quad ; \quad q^{(s)} = -k\frac{\partial T^{(s)}}{\partial r}, \tag{3.26}$$

where Σ_o is the outer boundary surface and $q^{(s)}$ the static heat flux. In the specific case of a full sphere ($r_i/r_o = 0$) with non-zero internal heating, Q is equal to $4/3\pi r_o^3\rho_0 C_P s_T$ and the temperature scale is then given by $s_T/3\Omega$.

We use the same notations for dimensional and dimensionless variables. To avoid confusions, only dimensionless variables are used hereafter and throughout Part I of this manuscript.

The acceleration due to gravity is assumed to be a linear function of the radius, as for a self-gravitating sphere of constant density. Then, the resulting set of dimensionless equations is

$$\frac{\partial \mathbf{u}}{\partial t} + \mathbf{u}\cdot\nabla\mathbf{u} + 2\hat{z}\times\mathbf{u} = -\nabla P' + Ra_Q\frac{\mathbf{r}}{r_o}T' + (\nabla\times\mathbf{B})\times\mathbf{B} + E\Delta\mathbf{u}, \tag{3.27}$$

$$\frac{\partial T'}{\partial t} + (\mathbf{u}\cdot\nabla)T' + (\mathbf{u}\cdot\nabla)T^{(s)} = \frac{E}{Pr}\Delta T', \tag{3.28}$$

$$\frac{\partial \mathbf{B}}{\partial t} = \nabla\times(\mathbf{u}\times\mathbf{B}) + \frac{E}{Pm}\Delta\mathbf{B}, \tag{3.29}$$

$$\nabla\cdot\mathbf{B} = 0, \tag{3.30}$$

$$\nabla\cdot\mathbf{u} = 0. \tag{3.31}$$

where dimensionless control parameters are:

- the modified Rayleigh number

$$Ra_Q = \frac{\alpha g_o Q}{4\pi\rho_0 C_P \Omega^3 D^4}, \tag{3.32}$$

- the Ekman number

$$E = \frac{\nu}{\Omega D^2}, \tag{3.33}$$

- the Prandtl number

$$Pr = \frac{\nu}{\kappa}, \tag{3.34}$$

- the magnetic Prandtl number

$$Pm = \frac{\nu}{\eta}, \tag{3.35}$$

where g_o is the acceleration due to gravity at the outer radius. Using this choice of dimensionless numbers, the canonical Rayleigh number

$$Ra = \frac{\alpha g_o Q D^2}{4\pi\rho_0 C_P \kappa^2 \nu}, \tag{3.36}$$

is given by $Ra = Ra_Q E^{-3} Pr^2$. Contrary to Ra, Ra_Q has the advantage of being independent of the thermal and viscous diffusivities, and is therefore the relevant parameter to study convection in the limit where diffusivities play a negligible role, at low Ekman and high Rayleigh numbers . Christensen & Aubert (2006) and Aubert *et al.* (2009) have shown that output quantities that characterize convective motions and dynamo properties can be expressed as a function of Ra_Q alone for sufficiently supercritical convection and for a given set of boundary conditions and geometry, suggesting that diffusive processes do not play a major role in dynamo simulations.

3.4 Boundary conditions

Temperature fluctuations in planetary cores are negligible with respect to (1) the adiabatic core temperature and (2) the possible temperature fluctuations within the above convecting mantle. Thus, the core adiabatic temperature at the CMB provides an isothermal boundary condition for the mantle. The resulting heat flux at the CMB, either related to thermal boundary layers in a convective mantle or to a conductive heat flux in a stagnant mantle, provides the thermal boundary condition for core convection. In most of our simulations, we thus impose $\partial T'/\partial r = 0$, together with a uniform static heat flux $q^{(s)} = k\partial T^{(s)}/\partial r$, at the surface of the sphere which represents the CMB. Convective motions in the solid mantle are much slower than in the core and the no-slip boundary condition at the CMB can approximated by imposing zero velocity at r_o. Finally, our modeled core is assumed to be surrounded by an electrically non-conducting mantle. In

summary, the boundary conditions at $r = r_o$ are

$$\mathbf{u} = 0 \quad ; \quad \nabla \times \mathbf{B} = 0 \quad ; \quad \frac{\partial T'}{\partial r} = 0. \tag{3.37}$$

For simulations with a small inner sphere ($r_i/r_o = 0.01$), boundary conditions (3.37) are also implemented at $r = r_i$, and $q^{(s)} = 0$ is imposed at $r = r_i$.

In the present model, we impose a time-invariant heat flux $q^{(s)}$ at the surface of the sphere, or equivalently a time-invariant distribution of heat sources s_T, such that the forcing of convection Ra_Q is time-invariant and a statically stationary regime is reached in our simulations. Such a model is suitable for core dynamics since the total heat flux, imposed by the planetary mantle, evolves on a time scale of order t_{cool}, much longer than the time scale of core convection t_{conv} as illustrated in figure 3.2. We note that T can be statically stationary in the present model because the heat budget of the sphere vanishes (internal heating balances the net heat flux at the sphere surface), which is again relevant for the dynamics of entirely liquid cores where the internal heating term and the decrease in adiabatic entropy balance the total heat flux at the CMB (as obtained by taking the time and volume average of equation (3.10)).

3.5 Initial conditions

In all our simulations, we initially impose infinitesimal perturbations on the static temperature field $T^{(s)}$ (all the spherical harmonics have initially the same infinitesimal amplitude).

We conduct *hydrodynamic simulations* (convection without dynamo action) in which the magnetic field is initially set to zero. $\mathbf{B} = 0$ is always a solution to equation (3.29) and, if the magnetic field is not initially perturbed, it remains equal to zero during the entire simulation. Then, the set of dimensionless equations reduces to equations (3.27), (3.28) and (3.31) with only three dimensionless parameters Ra_Q, Pr and E. In this framework, the onset of convection occurs when the static solution $(\mathbf{u}^{(s)}, T^{(s)}, P^{(s)})$ becomes unstable.

We also conduct *dynamo simulations* in which the initial magnetic field corresponds to a dipole of infinitesimal amplitude. The dynamo onset occurs when the solution $\mathbf{B} = 0$ becomes unstable, i.e. when the ratio of the shearing of $\mathbf{B}$ to the diffusion of $\mathbf{B}$, measured by the magnetic Reynolds number $Rm = UD/\eta$, becomes sufficiently high for amplification of magnetic field perturbations.

3.6 Reference models

Several simulations with $r_i/r_o = 0.35$ are used for comparison with a configuration relevant for the present Earth's core. They are our *reference models*. The boundary conditions (3.37) are used at the inner and outer sphere. A non-zero static heat flux $q_i^{(s)}$ is imposed at the inner boundary to model the release of light elements at the bottom of the Earth's outer core. The ratio of the buoyancy flux at the inner boundary to the same flux at the outer boundary is not well constrained in the Earth's core (Cardin & Olson 1992, Lister

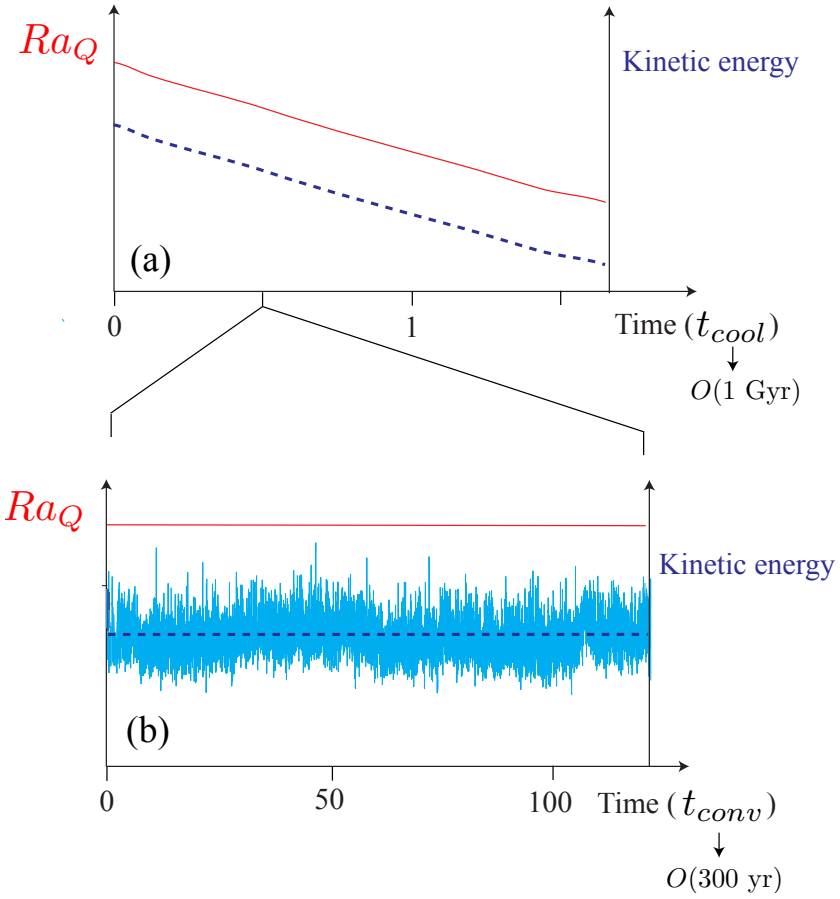

Figure 3.2: Schematic representations of the forcing of convection Ra_Q (red curve in (a,b)), mean kinetic energy (dashed blue curve in (a,b)) and kinetic energy (blue curve in (b)) as a function of time. (a) The forcing of convection varies on a time scale of order t_{cool}, which is imposed by mantle dynamics (a few hundred million years to a few billion years). (b) On a time scale of a few ten thousand years, which is much smaller than t_{cool} and much larger than the core convective time scale t_{conv} (a few hundred years), variations of heat flux and other volume-averaged variables (density, temperature, ...) are negligible. As a result, core dynamics can be approached as a succession of statistically stationary regimes in which kinetic energy and other volume-averaged variables vary around a constant mean.

& Buffett 1995). Following Aubert *et al.* (2009) we use $q_i^{(s)}/q_o^{(s)} = 1$ and $s_T = 0$, where $q_o^{(s)}$ is the static heat flux at the outer boundary.

3.7 Output dimensionless quantities

The dimensionless power generated by buoyancy forces, called convective power (Aubert *et al.*, 2009) or available energy flux (Christensen *et al.*, 2009), is equal to

$$p = Ra_Q \int_V T u_r \frac{r}{r_o} \mathrm{d}V. \tag{3.38}$$

For sufficiently supercritical convection, it can be shown that $p = \gamma Ra_Q$, where γ is a function of the shell aspect ratio r_i/r_o and the buoyancy ratio $q_i^{(s)}/q_o^{(s)}$ (Buffett *et al.* 1996, Aubert *et al.* 2009). The convective power p is a generalized measure of the power available for convective motions and dynamo action, it holds for any shell geometry or buoyancy distribution. It will be used in chapter 4 to compare full-sphere and bottom-driven reference models.

The time-averaged kinetic energy density K is defined as follows:

$$K = \frac{1}{2V_S} \left\langle \int_{V_S} \mathbf{u}^2 \mathrm{d}V \right\rangle, \tag{3.39}$$

where V_S is the shell volume and the angled brackets denote a time-averaging operator. Using this template, we additionally define:

- the time-averaged kinetic energy density contained in equatorially antisymmetric modes K_a,
- the time-averaged kinetic energy density contained in equatorially symmetric modes K_s,
- the time-averaged kinetic energy density contained in axisymmetric* flow components K_0,
- the time-averaged kinetic energy density contained in the equatorially antisymmetric, axisymmetric (EAA) flow component K_{0a}.

We define the Rossby number

$$Ro = 2K^{1/2}, \tag{3.40}$$

which measures the ratio of the rotation time scale to the advective time scale at scale D (we recall that K is a dimensionless quantity). Following Christensen & Aubert (2006) we also define the local Rossby number

$$Ro_l = \frac{Ro}{l_u}, \tag{3.41}$$

where l_u is the characteristic half-wavelength of the flow given by

$$l_u = 2\pi \frac{K}{\sum_l l K_l}, \tag{3.42}$$

where K_l is the time-averaged kinetic energy density contained in modes of spherical harmonic degree l. Ro_l measures the ratio of the rotation time scale to the advective time scale at scale l_u.

*Axisymmetric flow components corresponds to modes with $m = 0$, where m is the spherical harmonic order

The time-averaged magnetic energy density M at the external boundary of the model is given by:

$$M = \frac{1}{2\Sigma_o} \int_{\Sigma_o} \mathbf{B}^2 \mathrm{d}S, \tag{3.43}$$

where Σ_o is the outer surface (at the CMB). Using this template, we also define:

- the time-averaged CMB magnetic energy related to modes of dipole parity (odd $l+m$ in spherical harmonics) M_{dip},
- the time-averaged CMB magnetic energy related to modes of quadrupole parity (even $l+m$) M_{qua}.

Another output quantity f_{hem} is used to characterize the hemisphericity of the magnetic field at the CMB:

$$f_{hem} = \frac{\max[M^S, M^N]}{M}, \tag{3.44}$$

where M^S and M^N are the time-averaged magnetic energy densities contained in the Southern and Northern hemispheres. The hemisphericity factor f_{hem} is equal to 0.5 for a purely dipolar field and has the value 1 for a purely hemispherical field, i.e. entirely localized in one hemisphere.

3.8 Numerical method

3.8.1 PARODY numerical code

The PARODY code, developed by Emanuel Dormy and Julien Aubert, solves the MHD equations (3.27)-(3.31) in a rotating spherical shell. It has been validated in the benchmark study of Christensen *et al.* (2001) for a spherical shell configuration. The numerical implementation is detailed in Emmanuel Dormy's PhD manuscript (Dormy, 1997) and in Dormy *et al.* (1998). The main numerical approach is given below.

As any solenoidal field, $\mathbf{u}$ and $\mathbf{B}$ can be decomposed in the form

$$\mathbf{u} = \nabla \times \nabla \times (\mathcal{U}_p \mathbf{r}) + \nabla \times (\mathcal{U}_t \mathbf{r}), \tag{3.45}$$

$$\mathbf{B} = \nabla \times \nabla \times (\mathcal{B}_p \mathbf{r}) + \nabla \times (\mathcal{B}_t \mathbf{r}), \tag{3.46}$$

where the subscripts $_p$ and $_t$ denote the poloidal and toroidal fields respectively. $\mathcal{U}_p$, $\mathcal{U}_t$, $\mathcal{B}_p$, $\mathcal{B}_t$ and T' are then expanded in terms of spherical harmonics, i.e.

$$T' = \sum_{l=0}^{L} \sum_{m=0}^{l} T_{lm}(r) Y_{lm}(\theta, \Phi), \tag{3.47}$$

where Y_{lm} is the spherical harmonic function of degree l and order m. m is also called the azimuthal wavenumber.

In the radial direction a Finite Difference scheme is used on a grid that is refined in the vicinity of the boundaries. The number of grid points that is required to obtain accurate resolution is mainly enforced by the thickness of the viscous boundary layer which evolves as $E^{1/2}$. The minimum value of E below which simulations are not feasible (i.e. the computational time is too high) is of order 10^{-6} (Sakuraba & Roberts, 2009). Time integration involves a Crank-Nicolson scheme for diffusion terms and a second-order Adams-Bashforth scheme for other terms. Whereas the Crank-Nicolson scheme is unconditionally stable, the Adams-Bashforth scheme is explicit and therefore conditionally stable. To ensure numerical stability the time step is chosen as the minimum between the characteristic times of advection and Alfvén wave propagation in one grid (Christensen *et al.*, 1999).

Linear stability results are obtained using a linear version of PARODY. The equations (3.27)-(3.31) are linearized about the static solution ($\mathbf{u}^{(s)} = 0$, $\mathbf{B}^{(s)} = 0$, $T^{(s)}$, $P^{(s)}$) in order to get the corresponding perturbation equations. The algorithm used here is the same as in Dormy *et al.* (2004): it does not solve an eigenvalue problem but, for a given Ra_Q value, it integrates the equations in time until the system converges towards an eigenfunction of the form $F(r,\theta)\exp(\sigma t)\exp i(m\phi - \omega t)$ for each azimuthal wavenumber m. Then, we increase Ra_Q until the growth rate of a particular mode with azimuthal wavenumber m_c becomes positive.

3.8.2 Full-sphere configuration

Implementation

A few modifications had to be implemented in PARODY to conduct simulations with $r_i/r_o = 0$. The main modifications are detailed below.

First, the spherical coordinate system has a singularity in $r = 0$ since neither ϕ nor θ are uniquely defined. This singularity is not *real*, it does not exist in Cartesian coordinates*. One way to overcome this difficulty is to impose additional boundary conditions, in the numerical scheme, that force the solution $(\mathbf{u}, \mathbf{B}, T')$ and its derivatives to be regular at the center, i.e. they can be written as a Taylor series expansion near $r = 0$. As shown in Dormy (1997, chap.2, p.67), the highest order of the radial derivatives in the evolution equations for $\mathcal{U}_p$, $\mathcal{U}_t$, $\mathcal{B}_p$, $\mathcal{B}_t$, T' is 4, 2, 2, 2, 2, respectively. It corresponds to the total number of boundary conditions required in the numerical scheme. It can be shown that the boundary conditions (3.37) at $r = r_o$ become, in spectral space:

$$\mathcal{U}_{p,lm} = 0 \quad ; \quad \mathcal{U}_{t,lm} = 0 \quad ; \quad \frac{\partial \mathcal{U}_{p,lm}}{\partial r} = 0; \tag{3.48}$$

$$\frac{\partial}{\partial r}\mathcal{B}_{p,lm} + \frac{l+1}{r}\mathcal{B}_{t,lm} = 0 \quad ; \quad \mathcal{B}_{t,lm} = 0; \tag{3.49}$$

$$\frac{\partial T_{lm}}{\partial r} = 0. \tag{3.50}$$

Therefore, two additional boundary conditions are required for $\mathcal{U}_p$ and one boundary condition for each other field. The regularity of $\mathbf{u}$ and $\nabla \times \mathbf{u}$ (resp. $\mathbf{B}$ and $\nabla \times \mathbf{B}$)

*The singularity also exists at the poles ($\theta = 0$ and $\theta = \pi$, $r \neq 0$) where ϕ is not uniquely defined. However, the use of spherical harmonics to handle the derivatives in θ and ϕ directions has removed the singularity, which does not persist in spectral space.

requires that $\mathcal{U}_p = 0$ and $\mathcal{U}_t = 0$ (resp. $\mathcal{B}_p = 0$ and $\mathcal{B}_t = 0$) at the center of the sphere. To obtain the fourth required boundary condition on $\mathcal{U}_p$, we need to consider the regularity of $\Delta\mathbf{u}$, which forces

$$\mathcal{U}_{p,lm} \propto r^l, \tag{3.51}$$

where l is the spherical harmonics degree (derived in Gissinger 2009, chap.4, p.105). The regularity of $\Delta T'$ forces

$$T_{p,lm} \propto r^l. \tag{3.52}$$

Finally, the following boundary conditions have to be implemented at $r = 0$:

$$\mathcal{U}_{p,lm} = 0 \quad ; \quad \mathcal{U}_{t,lm} = 0 \quad ; \quad \frac{\partial \mathcal{U}_{p,lm}}{\partial r} = 0 \quad \text{for} \quad l \neq 1, \tag{3.53}$$

$$\mathcal{U}_{p,lm} = 0 \quad ; \quad \mathcal{U}_{t,lm} = 0 \quad ; \quad \frac{\partial^2 \mathcal{U}_{p,lm}}{\partial r^2} = 0 \quad \text{for} \quad l = 1, \tag{3.54}$$

$$\mathcal{B}_{p,lm} = 0 \quad ; \quad \mathcal{B}_{t,lm} = 0, \tag{3.55}$$

$$\frac{\partial T_{lm}}{\partial r} = 0 \quad \text{for} \quad l \neq 1, \tag{3.56}$$

$$T_{lm} = 0 \quad \text{for} \quad l = 1. \tag{3.57}$$

Second, the grid must not be stretched near $r = 0$. Contrary to the outer boundary, the velocity does not go to zero near $r = 0$ and the advective time scale, as well as the numerical time step, would become very small if the grid was stretched.

Difficulties

The integrated evolution equations (given in Dormy 1997, chap.2, p. 67) contain terms that incorporate the operator $1/r^2\partial^2/\partial r^2$. In PARODY the operator $\partial^2/\partial r^2$ is computed with an error $O(\delta_r^3)$, where δ_r is the grid spacing. Thus, the error on the operator $1/r^2\partial^2/\partial r^2$ is $O(\delta_r^3/r^2)$ which degenerates to $O(\delta_r)$ near the center of the sphere where $r = O(\delta_r)$. As a result, the numerical scheme is of order 2 everywhere except near the center where it decreases to 0. Because the numerical error becomes rather large at the center, it was important to benchmark our numerical code in a full sphere configuration.

3.8.3 Code validation

The modes emerging at axisymmetric convection onset, introduced in section 2.3.3, are well suited for the validation of PARODY in a full sphere configuration. Indeed, as shown in figure 3.3, these modes take the form of a convective cell centered on the rotation axis, which involves a strong axial flow through the sphere center, where the numerical error is the strongest. During my PhD, I dedicated some time to the comparison of theoretical and numerical results for the onset of axisymmetric convection, validating both the numerical code in a full-sphere configuration and the linear stability analysis conducted by Bisshopp (1958); Roberts (1965); Bisshopp & Niiler (1965). These results will be included and further detailed in a future publication. Figure 3.4 provides a summary of such results, illustrating the good agreement between theoretical and numerical results for the critical Rayleigh number Ra_{Q_0} that marks the onset of axisymmetric convection.

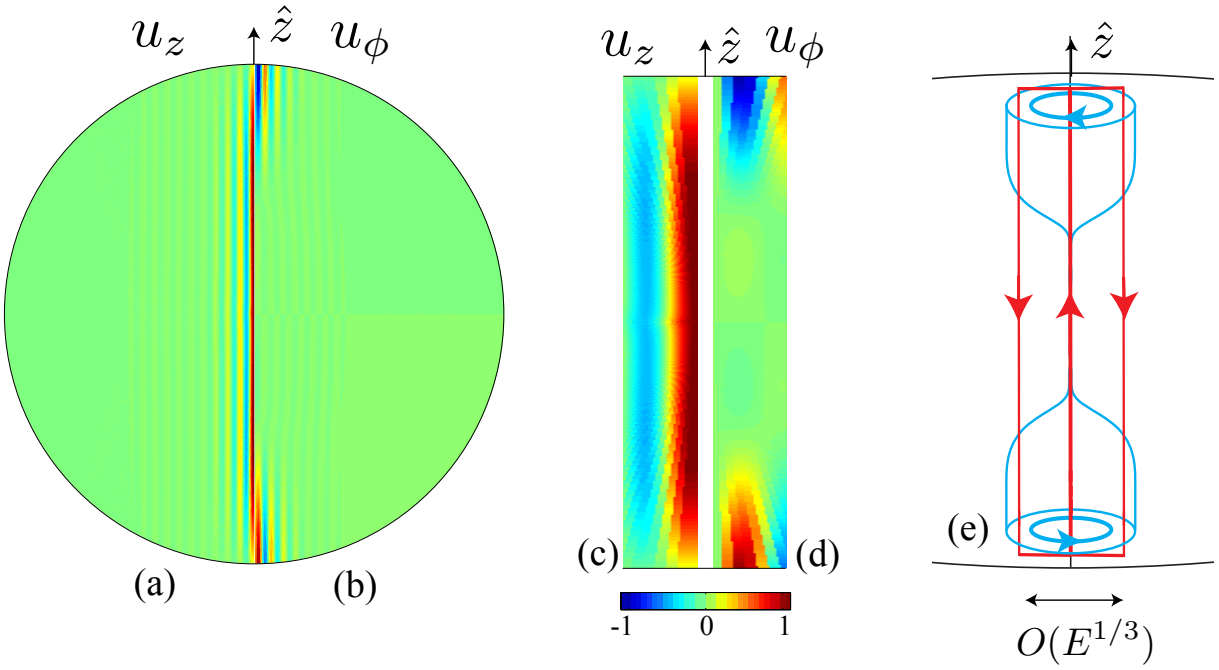

Figure 3.3: Velocity field at axisymmetric convection onset. (a,b,c,d) Numerical results for the vertical velocity (a,c) and azimuthal velocity (b,d). (c,d) are close-ups of (a,b) showing the velocity fields for $-1 \leq z \leq 1$ and $0 \leq s \leq 0.043$. (e) Sketch of the flow in an axial cell of thickness $O(E^{1/3})$ at axisymmetric onset where red (resp. blue) arrows represent the meridional (resp. azimuthal) circulation.

The simulations presented in chapter 4 have been conducted with $r_i/r_o = 0.01$. After the implementations detailed in §3.8.2, calculations with $r_i/r_o = 0$ were conducted and confirmed that the small inner sphere has a negligible impact on the results presented in 4. For this reason, the system is refered to as a rotating full sphere for both $r_i/r_o = 0.01$ and $r_i/r_o = 0$.

Finally, as the results presented in chapter 4 are rather unexpected, we also tested our numerical implementation PARODY against another implementation (the Christensen, Wicht, Glatzmaier MAG/MAGIC code, Christensen *et al.*, 2001) in a case where antisymmetric convection arises in the presence of an inner core, with the following parameters: $E = 10^{-4}$, $Ra_Q = 2 \cdot 10^{-4}$, $Pr = 1$, $Pm = 7$, $q_i^{(s)} = 0$ and an aspect ratio $r_i/r_o = 0.35$. We have checked that after equilibration, both codes yield the same results, with an equatorially asymmetric temperature profile outside the tangent cylinder.

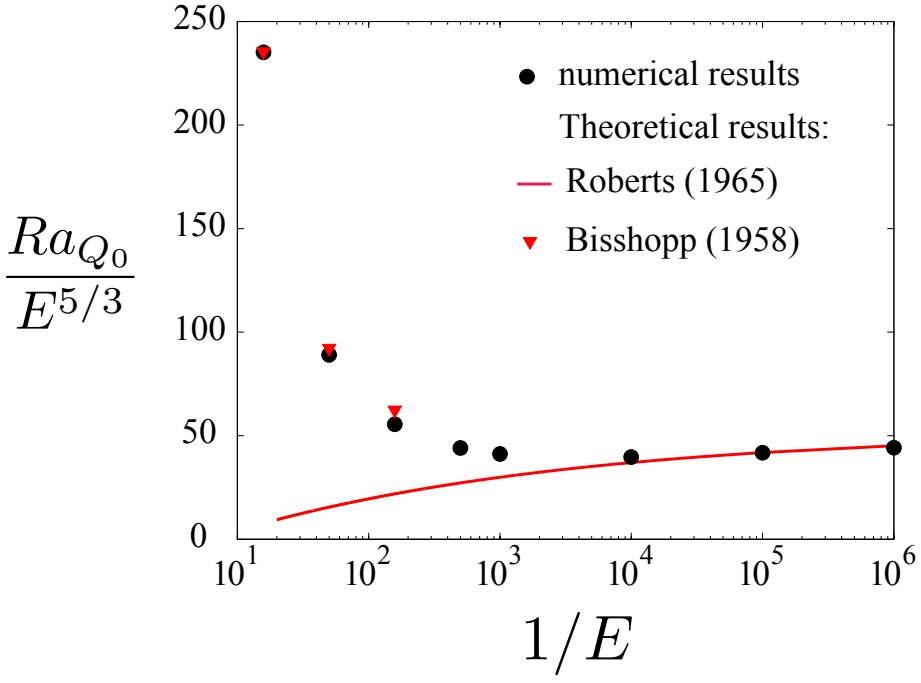

Figure 3.4: $Ra_{Q0}/E^{5/3}$ versus $1/E$ at $Pr = 1$, where Ra_{Q0} is the critical Rayleigh number for the onset of axisymmetric convection. Black circles: numerical results obtained using PARODY. Red triangles: theoretical results at intermediate Ekman numbers as obtained by Bisshopp (1958). Red curve: asymptotic behavior valid for sufficiently small Ekman numbers (or sufficiently large $1/E$ values) as obtained by Roberts (1965).

Chapter 4

Results

This chapter contains most of the numerical results presented in the article "Equatorially asymmetric convection inducing hemispherical magnetic field in rotating spheres and implications for the past martian dynamos" published in 2011 in *Physics of the Earth and Planetary Interiors* (reproduced in appendix D), although the analysis has been improved in the present manuscript.

In this chapter, we present numerical results when exploring the (E, Ra_Q) parameter space. The Prandtl and magnetic Prandtl numbers Pr and Pm are set to 1 and 5, respectively, in most simulations. The parameters of all the nonlinear simulations used are contained in Table 4.1 (hydrodynamic simulations) and Table 4.2 (dynamo simulations). The velocity and magnetic field structures are illustrated using a series of simulations named A, B, C, D, F, G, H, I whose parameters are reported in Table 4.1 and Table 4.2. The values of the diagnostic quantities that are given in this chapter correspond to the final statistically stationary regime of each simulation. We recall that the terms *symmetric* and *antisymmetric* are used in this study to refer to equatorial symmetry properties of the flow.

4.1 Convection without dynamo action

In this section, we investigate convection driven by internal heating in a rotating full-sphere without dynamo action. Starting from a non-convective stable state at low Rayleigh numbers, we introduce the main hydrodynamic transitions found when we progressively increase the forcing. This includes the onset of convection (section 4.1.1) and the secondary emergence of antisymmetric modes (section 4.1.2). Results from nonlinear full-sphere simulations are compared with those from reference models, i.e. with a rather large inner sphere and bottom driving, as detailed in section 3.6. Previous numerical studies (Aubert *et al.* 2009, Christensen *et al.* 2009) have found scaling laws in which output quantities that characterize convective motions and dynamo properties are expressed as functions of the convective power p alone. Such scalings hold for any set of shell geometry or buoyancy distribution. Accordingly, we compare velocity structures in full-sphere and bottom-driven reference models at similar convective powers.

	E	Ra_Q	K_s	K_a	K_{0a}	
	0.0001	1.5×10^{-5}	2.56×10^{-5}	3.10×10^{-15}	6.86×10^{-16}	Sym
	0.0001	1.7×10^{-5}	3.01×10^{-5}	1.13×10^{-12}	1.65×10^{-13}	Sym
	0.0001	1.8×10^{-5}	3.24×10^{-5}	1.46×10^{-9}	1.67×10^{-10}	Sym
	0.0001	2×10^{-5}	3.61×10^{-5}	1.45×10^{-6}	2.16×10^{-7}	Asym
	0.0001	2.2×10^{-5}	3.90×10^{-5}	3.98×10^{-6}	7.38×10^{-7}	Asym
	0.0001	2.5×10^{-5}	4.40×10^{-5}	6.44×10^{-6}	1.23×10^{-6}	Asym
	0.0001	4×10^{-5}	6.49×10^{-5}	2.63×10^{-5}	6.81×10^{-6}	Asym
	0.0001	4.5×10^{-5}	7.11×10^{-5}	3.25×10^{-5}	8.48×10^{-6}	Asym
	0.0001	5×10^{-5}	7.76×10^{-5}	3.88×10^{-5}	1.02×10^{-5}	Asym
	0.0001	6×10^{-5}	9.27×10^{-5}	5.15×10^{-5}	1.33×10^{-5}	Asym
	0.0001	7×10^{-5}	1.08×10^{-4}	6.13×10^{-5}	1.52×10^{-5}	Asym
	0.0001	9.75×10^{-5}	1.52×10^{-4}	9.20×10^{-5}	1.52×10^{-5}	Asym
	0.0003	1.8×10^{-5}	6.40×10^{-7}	9.28×10^{-18}	9.20×10^{-18}	Sym
	0.0003	4.5×10^{-5}	3.22×10^{-5}	3.13×10^{-16}	2.55×10^{-16}	Sym
	0.0003	7.2×10^{-5}	6.99×10^{-5}	9.22×10^{-12}	9.80×10^{-13}	Sym
A	0.0003	9×10^{-5}	9.11×10^{-5}	3.69×10^{-11}	7.79×10^{-12}	Sym
	0.0003	1.08×10^{-4}	1.15×10^{-4}	1.41×10^{-10}	1.00×10^{-11}	Asym
	0.0003	1.26×10^{-4}	1.28×10^{-4}	2.07×10^{-5}	6.29×10^{-6}	Asym
	0.0003	1.35×10^{-4}	1.38×10^{-4}	2.30×10^{-5}	6.33×10^{-6}	Asym
	0.0003	1.575×10^{-4}	1.49×10^{-4}	4.93×10^{-5}	1.78×10^{-5}	Asym
	0.0003	1.8×10^{-4}	1.66×10^{-4}	7.20×10^{-5}	2.81×10^{-5}	Asym
	0.0003	1.98×10^{-4}	1.73×10^{-4}	9.04×10^{-5}	3.59×10^{-5}	Asym
	0.0003	2.25×10^{-4}	1.92×10^{-4}	1.14×10^{-4}	4.56×10^{-5}	Asym
	0.0003	2.475×10^{-4}	2.02×10^{-4}	1.35×10^{-4}	5.37×10^{-5}	Asym
	0.0003	2.7×10^{-4}	2.15×10^{-4}	1.58×10^{-4}	6.36×10^{-5}	Asym
	0.0003	3.15×10^{-4}	2.45×10^{-4}	1.94×10^{-4}	7.56×10^{-5}	Asym
B	0.0003	3.6×10^{-4}	2.76×10^{-4}	2.34×10^{-4}	9.00×10^{-5}	Asym
	0.001	6.5×10^{-4}	3.70×10^{-4}	1.88×10^{-7}	7.60×10^{-8}	Asym
	0.001	7×10^{-4}	3.58×10^{-4}	5.98×10^{-5}	3.68×10^{-5}	Asym
	0.001	1×10^{-3}	4.17×10^{-4}	2.50×10^{-4}	1.59×10^{-4}	Asym
	0.001	3.14×10^{-3}	9.08×10^{-4}	1.77×10^{-3}	1.27×10^{-3}	Asym
	0.01	1.25×10^{-2}	3.40×10^{-5}	0	0	Sym
	0.01	1.3×10^{-2}	8.48×10^{-5}	0	0	Sym
	0.01	1.4×10^{-2}	2.25×10^{-4}	0	0	Sym
	0.01	1.55×10^{-2}	6.00×10^{-5}	2.08×10^{-4}	2.02×10^{-4}	Asym
	0.01	1.57×10^{-2}	1.29×10^{-6}	2.83×10^{-4}	2.83×10^{-4}	Asym
	0.01	1.6×10^{-2}	1.47×10^{-6}	3.35×10^{-4}	3.35×10^{-4}	Asym
	0.01	1.61×10^{-2}	1.60×10^{-6}	3.52×10^{-4}	3.52×10^{-4}	Asym
	0.01	1.62×10^{-2}	1.75×10^{-6}	3.69×10^{-4}	3.69×10^{-4}	Asym
	0.01	1.63×10^{-2}	1.92×10^{-6}	3.87×10^{-4}	3.87×10^{-4}	Asym
	0.01	1.65×10^{-2}	2.32×10^{-6}	4.21×10^{-4}	4.21×10^{-4}	Asym
	0.01	1.7×10^{-2}	3.30×10^{-6}	5.08×10^{-4}	5.08×10^{-4}	Asym
	0.01	1.8×10^{-2}	5.93×10^{-6}	6.80×10^{-4}	6.80×10^{-4}	Asym
	0.01	1.9×10^{-2}	9.30×10^{-6}	8.52×10^{-4}	8.52×10^{-4}	Asym
C	0.0003	1.8×10^{-4}	1.93×10^{-4}	2.64×10^{-5}	4.28×10^{-6}	Asym
D	0.0003	7.2×10^{-4}	6.30×10^{-4}	2.44×10^{-4}	3.41×10^{-5}	Asym

Table 4.1: Numerical models and results for hydrodynamic simulations. See chapter 3 for the definitions of input parameters and output quantities. In all simulations we impose $Pr = 1$*. The first column labels A, B, C, D tag runs which are specifically referred to in the text. All the calculations correspond to full-sphere simulations, except simulations C and D which are reference models (see section 3.6). Simulation A and B have about the same convective power as simulation C and D, equal to about* $3 \cdot 10^{-5}$ *and* $1.5 \cdot 10^{-4}$*, respectively. The last column characterizes the resulting flow regime: 'Sym' and 'Asym' for simulations which are in a symmetric and asymmetric regime, respectively (see section 4.1.2 for definitions).*

	E	Ra_Q	K_s	K_a	K_{0a}	M_{dip}	M_{qua}	
L	3×10^{-5}	4.5×10^{-5}	1.46×10^{-4}	6.07×10^{-5}	8.86×10^{-6}	1.94×10^{-7}	2.16×10^{-7}	Asym
	0.0001	2×10^{-5}	1.79×10^{-5}	3.61×10^{-6}	2.18×10^{-7}	1.65×10^{-5}	9.39×10^{-6}	Os
	0.0001	4×10^{-5}	3.67×10^{-5}	1.03×10^{-5}	6.05×10^{-7}	2.35×10^{-5}	1.66×10^{-5}	Os
	0.0001	6×10^{-5}	5.81×10^{-5}	1.84×10^{-5}	1.43×10^{-6}	2.43×10^{-5}	1.92×10^{-5}	Os
	0.0001	6.5×10^{-5}	6.16×10^{-5}	1.97×10^{-5}	1.47×10^{-6}	2.88×10^{-5}	2.25×10^{-5}	Os
	0.0001	7×10^{-5}	6.61×10^{-5}	2.26×10^{-5}	2.22×10^{-6}	2.85×10^{-5}	2.29×10^{-5}	Os
	0.0001	7.5×10^{-5}	7.26×10^{-5}	2.59×10^{-5}	3.17×10^{-6}	2.69×10^{-5}	2.23×10^{-5}	Os
	0.0001	8×10^{-5}	7.30×10^{-5}	3.44×10^{-5}	7.68×10^{-6}	2.72×10^{-5}	2.43×10^{-5}	Os
I	0.0001	9×10^{-5}	7.79×10^{-5}	5.19×10^{-5}	2.08×10^{-5}	2.54×10^{-5}	2.41×10^{-5}	Os
	0.0001	9.5×10^{-5}	8.11×10^{-5}	6.13×10^{-5}	2.75×10^{-5}	2.23×10^{-5}	2.16×10^{-5}	Asym
	0.0001	1.5×10^{-4}	1.32×10^{-4}	1.27×10^{-4}	5.50×10^{-5}	1.37×10^{-5}	1.40×10^{-5}	Asym
	0.0003	1.8×10^{-5}	6.40×10^{-7}	5.62×10^{-22}	5.57×10^{-22}	7.07×10^{-16}	1.13×10^{-22}	Sym
	0.0003	4.5×10^{-5}	3.26×10^{-5}	1.53×10^{-13}	1.26×10^{-13}	3.30×10^{-10}	7.48×10^{-17}	Sym
	0.0003	7.2×10^{-5}	6.85×10^{-5}	3.56×10^{-11}	1.48×10^{-11}	1.44×10^{-10}	5.17×10^{-14}	Sym
F	0.0003	9×10^{-5}	7.67×10^{-5}	2.33×10^{-6}	1.79×10^{-7}	1.59×10^{-5}	3.13×10^{-6}	Sym
	0.0003	1.08×10^{-4}	8.33×10^{-5}	7.16×10^{-6}	8.03×10^{-7}	2.65×10^{-5}	1.00×10^{-5}	Os
	0.0003	1.35×10^{-4}	1.14×10^{-4}	1.15×10^{-5}	1.27×10^{-6}	3.86×10^{-5}	2.00×10^{-5}	Os
	0.0003	1.8×10^{-4}	1.38×10^{-4}	2.40×10^{-5}	3.11×10^{-6}	2.97×10^{-5}	1.88×10^{-5}	Os
	0.0003	1.98×10^{-4}	1.38×10^{-4}	2.90×10^{-5}	3.73×10^{-6}	4.33×10^{-5}	2.72×10^{-5}	Os
H	0.0003	2.25×10^{-4}	1.58×10^{-4}	4.52×10^{-5}	1.23×10^{-5}	3.84×10^{-5}	2.80×10^{-5}	Os
	0.0003	2.48×10^{-4}	1.58×10^{-4}	4.74×10^{-5}	1.06×10^{-5}	5.59×10^{-5}	4.07×10^{-5}	Os
	0.0003	2.7×10^{-4}	1.48×10^{-4}	8.69×10^{-5}	4.42×10^{-5}	5.88×10^{-5}	5.12×10^{-5}	Os
	0.0003	2.925×10^{-4}	1.49×10^{-4}	1.31×10^{-4}	8.36×10^{-5}	5.05×10^{-5}	4.94×10^{-5}	Asym
	0.0003	3.15×10^{-4}	1.53×10^{-4}	1.65×10^{-4}	1.13×10^{-4}	4.76×10^{-5}	4.89×10^{-5}	Asym
G	0.0003	3.6×10^{-4}	1.75×10^{-4}	2.14×10^{-4}	1.51×10^{-4}	4.28×10^{-5}	4.37×10^{-5}	Asym
	0.0003	4.05×10^{-4}	1.92×10^{-4}	2.83×10^{-4}	2.05×10^{-4}	4.25×10^{-5}	4.43×10^{-5}	Asym
	0.0003	4.5×10^{-4}	2.15×10^{-4}	3.37×10^{-4}	2.40×10^{-4}	3.97×10^{-5}	4.12×10^{-5}	Asym
	0.001	6×10^{-4}	3.25×10^{-4}	2.50×10^{-8}	1.16×10^{-8}	3.34×10^{-11}	4.48×10^{-14}	Sym
	0.001	7×10^{-4}	3.88×10^{-4}	1.95×10^{-5}	9.15×10^{-6}	3.59×10^{-11}	8.83×10^{-12}	Asym
	0.001	7.5×10^{-4}	3.02×10^{-4}	9.33×10^{-5}	6.51×10^{-5}	1.23×10^{-5}	1.00×10^{-5}	Asym
	0.001	7.6×10^{-4}	3.11×10^{-4}	9.44×10^{-5}	6.56×10^{-5}	1.40×10^{-5}	1.12×10^{-5}	Asym
	0.001	7.7×10^{-4}	3.14×10^{-4}	1.10×10^{-4}	7.87×10^{-5}	1.09×10^{-5}	9.27×10^{-6}	Asym
	0.001	8×10^{-4}	3.17×10^{-4}	1.30×10^{-4}	9.29×10^{-5}	1.01×10^{-5}	9.02×10^{-6}	Asym
	0.001	8.2×10^{-4}	3.17×10^{-4}	1.39×10^{-4}	1.00×10^{-4}	1.35×10^{-5}	1.16×10^{-5}	Asym
	0.001	8.5×10^{-4}	3.27×10^{-4}	1.48×10^{-4}	1.05×10^{-4}	1.48×10^{-5}	1.31×10^{-5}	Asym
	0.001	8.7×10^{-4}	3.23×10^{-4}	1.63×10^{-4}	1.18×10^{-4}	1.65×10^{-5}	1.49×10^{-5}	Asym
	0.001	9×10^{-4}	3.25×10^{-4}	1.93×10^{-4}	1.41×10^{-4}	1.48×10^{-5}	1.37×10^{-5}	Asym
	0.001	9.5×10^{-4}	3.29×10^{-4}	2.16×10^{-4}	1.60×10^{-4}	2.15×10^{-5}	1.98×10^{-5}	Asym
	0.001	1×10^{-3}	3.29×10^{-4}	2.24×10^{-4}	1.66×10^{-4}	3.69×10^{-5}	3.41×10^{-5}	Asym
	0.001	3×10^{-3}	7.60×10^{-4}	1.73×10^{-3}	1.34×10^{-3}	7.18×10^{-6}	7.53×10^{-6}	Asym
	0.001	5×10^{-3}	1.31×10^{-3}	2.94×10^{-3}	2.21×10^{-3}	1.46×10^{-5}	1.51×10^{-5}	Asym

Table 4.2: Numerical models and results for dynamo simulations. See text for the definitions of input parameters and output quantities. In all simulations we impose $Pr = 1$ and $Pm = 5$, except in simulation L in which $Pm = 1$. The first column labels F to L tag runs which are specifically referred to in the text. The last column characterizes the flow regime: 'Sym', 'Os' and 'Asym' for simulations which are in a symmetric, oscillating and asymmetric regime, respectively (see section 4.1.2 and 4.2 for definitions).

E	Ra_{Qc}	m_c
10^{-6}	1.750×10^{-9}	37
3×10^{-6}	5.172×10^{-8}	26
10^{-5}	5.173×10^{-8}	17
3×10^{-5}	3.328×10^{-7}	12
5×10^{-5}	7.944×10^{-7}	10
10^{-4}	2.608×10^{-6}	7
3×10^{-4}	1.717×10^{-5}	5

Table 4.3: Critical Rayleigh number Ra_{Qc} (with 4 significant digits) and azimuthal wavenumber m_c for the linearly most unstable symmetric convection mode.

4.1.1 Linear stability results: the onset of convection

The first hydrodynamic transition corresponds to the onset of convection and occurs when the modified Rayleigh number reaches a first critical value Ra_{Qc}. For each value of the azimuthal wavenumber m and each value of the modified Rayleigh number, two growth-rates can be calculated using the linear version of the code PARODY: one for symmetric modes and one for antisymmetric modes. Indeed, these two families of modes are not coupled in the linearized equations.

The first unstable modes are symmetric, non-axisymmetric modes, as expected from previous theoretical studies (Busse 1970; Jones *et al.* 2000). Table 4.3 lists the critical Rayleigh number and azimuthal wavenumber for each studied value of the Ekman number. Figure 4.1 shows that $Ra_{Qc}/E^{5/3}$ converges towards an asymptote which is consistent with the value 10.3749 (≈ 10.4) obtained by Jones *et al.* (2000). It must be pointed out that Jones *et al.* (2000) used slightly different boundary conditions (fixed temperature and stress-free) at the external boundary, while we presently use a fixed flux condition for geophysical relevance and we consider rigid boundaries. However, the boundary conditions do not affect the leading order asymptotic results and the asymptote computed by Jones *et al.* (2000) should remain valid in our configuration, as confirmed by our numerical results. The asymptotic behavior of the critical modified Rayleigh number in the limit $E \to 0$ is thus approximated by:

$$Ra_{Qc} \approx 10.4 \times E^{5/3}. \tag{4.1}$$

In terms of critical canonical Rayleigh number Ra_c, this corresponds to the following asymptotic behavior: $Ra_c \approx 10.4 \times E^{-4/3}$. As introduced in section 2.3.3, the exponent value $-4/3$ is a robust feature of the onset of convection in rotating spheres or shells. Comparison of our results for Ra_{Qc} with values obtained using quasi-geostrophic simulations in a full-sphere with fixed temperature boundary condition (Guervilly, 2010) suggests that Ra_{Qc} converges more slowly towards (4.1) when imposing a fixed heat flux at the outer sphere rather than a fixed temperature.

As predicted by Busse (1970), the velocity structures at onset correspond to quasi-geostrophic Rossby waves that vary slowly in z-direction, forming a set of vortices aligned with the rotation axis (figure 4.2). The values we find for m_c are reported in Table 4.3

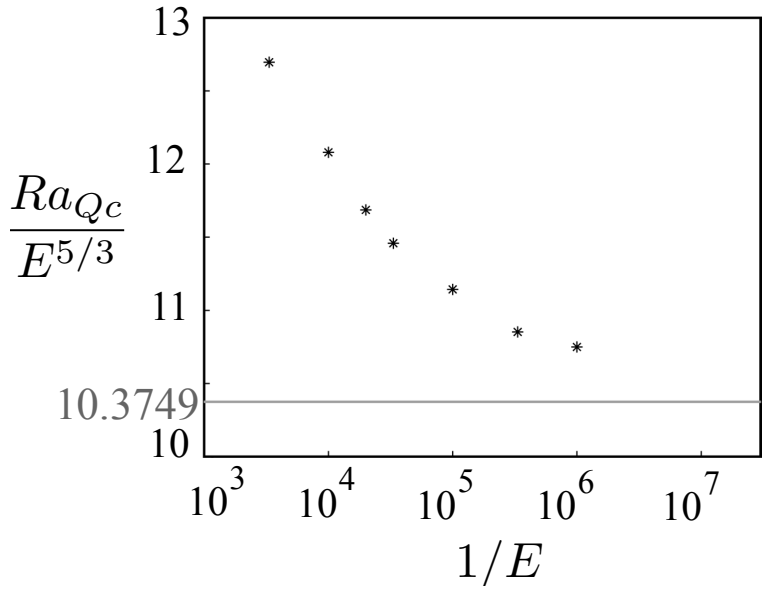

Figure 4.1: Convection onset. Stars: $Ra_{Qc}/E^{5/3}$ versus $1/E$ (logarithmic scale). The grey line is the asymptote predicted by the theory of Jones et al. *(2000) with slightly different boundary conditions (see text).*

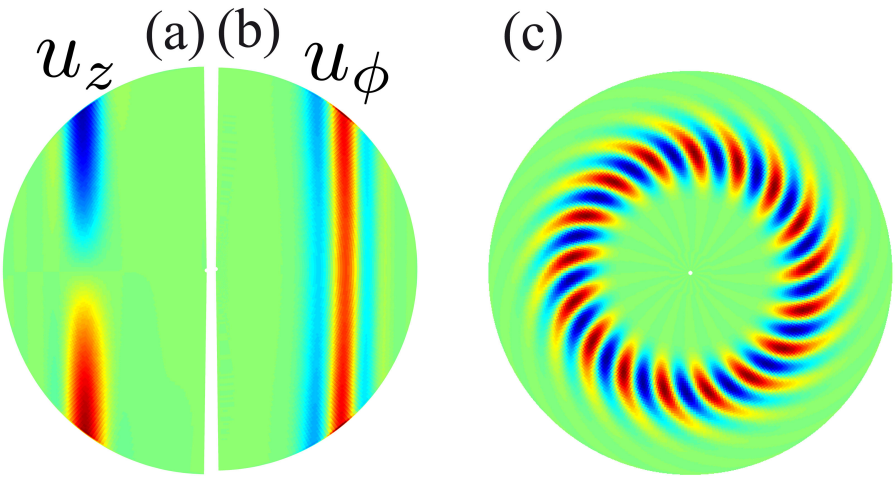

Figure 4.2: Velocity structures at onset for $E = 10^{-5}$ and $Pr = 1$. (a) Meridional section of the z-component of velocity. (b) Meridional section of the azimuthal velocity field. (c) Equatorial section ($\theta = \pi/2$) of the z-component of vorticity.

E	m_a	Ra_{Qa}	Ra_{Qt}
10^{-4}	1	8.34×10^{-6}	1.95×10^{-5}
3×10^{-4}	0	5.00×10^{-5}	1.07×10^{-4}
10^{-3}	0	3.34×10^{-4}	6.28×10^{-4}
10^{-2}	0	1.41×10^{-2}	1.41×10^{-2}

Table 4.4: Critical Rayleigh numbers Ra_{Qa} for the linear onset of antisymmetric convection, azimuthal wavenumber m_a of the most unstable antisymmetric modes and Ra_{Qt} for the nonlinear emergence of antisymmetric modes (see section 4.1.2).

and are in agreement with the expected trend $m_c \propto E^{-1/3}$ (Busse 1970; Jones *et al.* 2000).

A second family of convective modes is the antisymmetric family. As announced in chapter 2 and developed in the following section, antisymmetric modes acquire a crucial importance in our nonlinear simulations. We thus compute (Table 4.4) the linear threshold of instability for antisymmetric modes Ra_{Qa}. These results will be required in section 4.1.2 for comparison between Ra_{Qa} and the threshold for the emergence of antisymmetric modes in nonlinear simulations.

4.1.2 Nonlinear simulation results: emergence of antisymmetric modes

4.1.2.1 Bifurcation and regime diagrams

Figure 4.3(a) illustrates the different hydrodynamic transitions found at a fixed Ekman number equal to 3×10^{-4}. At the onset of convection ($Ra_{Qc} \approx 1.7 \times 10^{-5}$), symmetric modes become linearly unstable and the symmetric kinetic energy density K_s starts to grow. The flow is said to be in a *symmetric regime*. At $Ra_{Qt} \approx 1.07 \times 10^{-4}$, the symmetric solution looses stability and antisymmetric modes emerge through a secondary supercritical bifurcation (see the increase of the antisymmetric kinetic energy density K_a in figure 4.3(a)). For $Ra_Q \geq Ra_{Qt}$, the flow is said to be in an *asymmetric regime* since it results from the superposition of symmetric and antisymmetric modes.

At low Ekman numbers ($E \leq 10^{-3}$), Ra_{Qt} is located above the threshold Ra_{Qa} for linear instability of antisymmetric modes with respect to a static basic flow (Table 4.4), implying that the emergence of antisymmetric modes in nonlinear simulations cannot be explained by linear stability analysis for $E \leq 10^{-3}$. Thus, the asymmetric solution emerges from the symmetric solution, which has to be seen as the new basic state, and Ra_{Qt} corresponds to the threshold at which the purely symmetric solution becomes linearly unstable. Indeed, in a given simulation at $Ra_Q \geq Ra_{Qt}$, the flow first reaches the symmetric solution (such that $K_a \ll K_s$); then, this symmetric flow undergoes a secondary instability which leads to the emergence of antisymmetric modes and, eventually, to a statistically stationary asymmetric regime as depicted in figure 4.4.

The bifurcation at $E = 10^{-2}$ is a very isolated case since $Ra_{Qt} = Ra_{Qa}$ (Table 4.4). In this case the bifurcation can be described in terms of interactions between two linearly

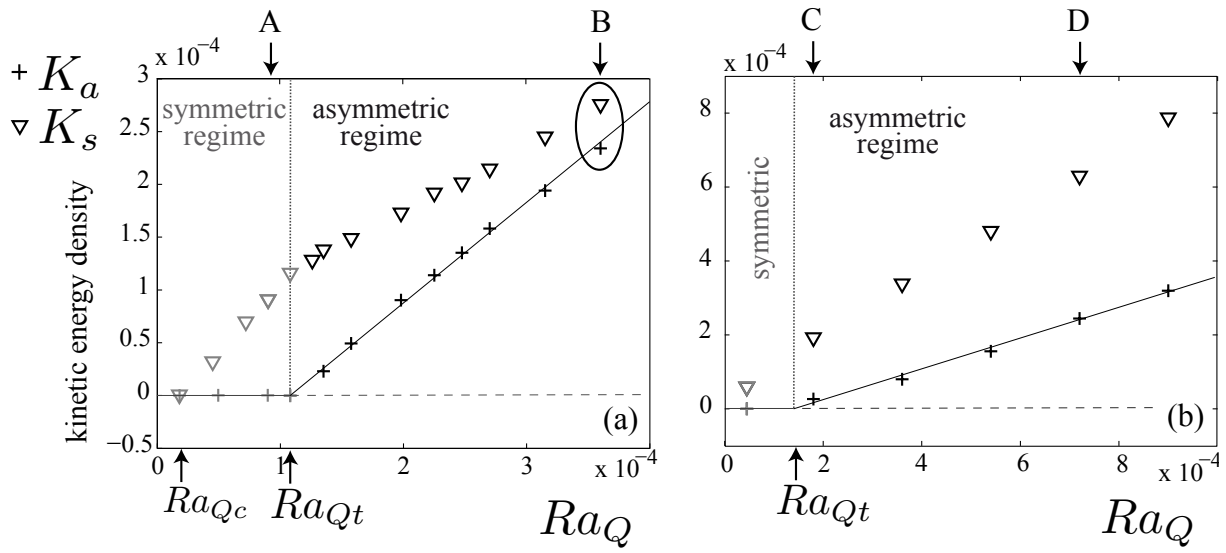

Figure 4.3: Bifurcation diagram for convection without dynamo action showing the antisymmetric kinetic energy density K_a (crosses) and the symmetric kinetic energy density K_s (triangles) versus the Rayleigh number Ra_Q at $E = 3 \times 10^{-4}$ in (a) full-sphere simulations and (b) bottom-driven reference models. We recall that kinetic energy densities are non-dimensionalized such that their square root is a Rossby number. Ra_{Qt} locates the emergence of antisymmetric modes. To estimate the value of Ra_{Qt} we look for Ra_{Qt} and the constant a such that K_a is best scaled (in the sense of the least squares) by $a(Ra_Q - Ra_{Qt})$ on the asymmetric branch. Symbols A, B, C, D denote simulations A, B, C, D that are shown in figures 4.6 and 4.7 (parameters reported in Table 4.1).

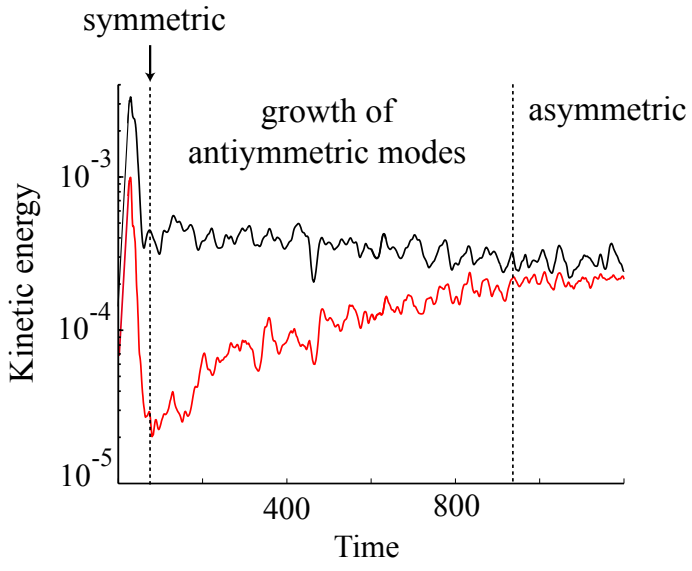

Figure 4.4: Instantaneous value of the symmetric (black) and antisymmetric (red) kinetic energy density as a function of time in simulation B (parameters reported in Table 4.1).

unstable modes: a symmetric mode of order $m = 1$ and an antisymmetric mode of order $m = 0$. Since we are looking for asymptotic behaviors in the limit $E \to 0$, we

do not consider the slowly rotating cases $E \geq 10^{-2}$ for the determination of the regime boundaries.

The different hydrodynamic transitions are summarized in a $(1/E, Ra_Q)$ parameter space (figure 4.5). Ra_{Qt} is best scaled (in the sense of the least squares) by:

$$Ra_{Qt} \approx 21.2 \times E^{1.51}. \tag{4.2}$$

Because the slope of the curve $K_a(Ra_Q)$ is larger than the slope of the curve $K_s(Ra_Q)$ in figure 4.3(a) for $Ra_Q \geq Ra_{Qt}$, we finally obtain $K_a \approx K_s \pm 15\%$ (simulation B). We expect the curves to cross at $Ra_Q \approx 4.5 \times 10^{-4}$ in figure 4.3(a). Simulations with $K_a \gtrsim K_s$ are also reached at $E = 10^{-2}$ and $E = 10^{-3}$ (Table 4.1). Such strongly asymmetric simulations are noteworthy since antisymmetric modes always play a secondary role in previous numerical studies of nonlinear rotation-dominated convection in spherical shells, with or without dynamo action (e.g. Olson *et al.* 1999; Grote & Busse 2001; Sakuraba & Roberts 2009). Indeed, although antisymmetric modes emerge in our spherical-shell reference models, the slope of $K_a(Ra_Q)$ is smaller than the slope of $K_s(Ra_Q)$ in the asymmetric regime (figure 4.3(b)) and a regime with $K_a \approx K_s$ will never be reached. Symmetric modes always contain more than 70% of the total kinetic energy in our reference models.

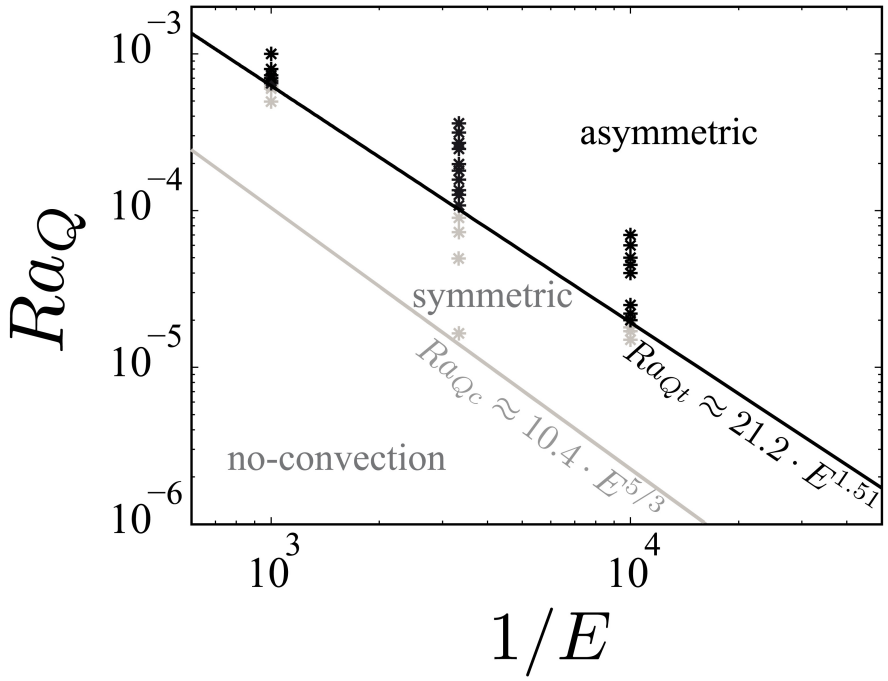

Figure 4.5: Hydrodynamic transitions in $(1/E, Ra_Q)$ space in the absence of dynamo action and for full-sphere models: from a non-convective state to the symmetric regime (light grey curve corresponds to the asymptotic behavior of Ra_{Qc} at low Ekman numbers according to equation (4.1)) and from the symmetric regime to the asymmetric regime (black curve), marking the emergence of antisymmetric modes. Light grey symbols: symmetric simulations. Black symbols: asymmetric simulations.

Then, the following question arises: Does the size of the inner sphere controls the growth of antisymmetric modes, accounting for the difference observed in reference mod-

els and full-sphere simulations? To investigate this question, we consider spherical-shell simulations with $r_i/r_o = 0.35$ as in our reference models, but we impose a zero heat flux at the inner sphere (i.e. no bottom driving) as in our full-sphere simulations. In such a configuration, strongly asymmetric simulations such that $K_a \approx K_s$ are found (results not reported here), indicating that the emergence of antisymmetric modes is controlled by the ratio between the inner and outer buoyancy flux rather than the inner-sphere size.

We emphasize that the dynamics of the strongly asymmetric simulations (including simulation B) is highly influenced by rotation since both the Rossby number and the local Rossby number remain much smaller than 1 ($Ro \leq 0.04$ and $Ro_l \leq 0.09$ in figure 4.3(a)). Thus, the emergence of strong antisymmetric modes in our simulations is not related to the breaking of the Taylor-Proudman constraint by inertia. We also checked that the emergence of antisymmetric modes does not correlate with a change in the scaling law for heat transfer. This suggests that convection remains rotationally dominated (or geostrophic) in the simulations presented in this section and that the emergence of antisymmetric modes in our simulations has no connection with the transition from a rotationally dominated to a weakly rotating regime (King *et al.*, 2009; Zhong *et al.*, 2009; King *et al.*, 2012)).

4.1.2.2 Flow structures

In this subsection, we study the flow morphology and dynamics in the unexpectedly asymmetric simulations (such that $K_a \gtrsim K_s$) that have been identified previously. The results are compared with those obtained in strongly symmetric simulations (such that $K_a \ll K_s$) and in bottom-driven reference models at similar convective powers.

The emergence of strong antisymmetric modes is correlated with major changes in the morphology of the flow in full-sphere simulations, as shown in figure 4.6, which compares flow structures in symmetric simulation A ($K_a \ll K_s$, see Table 4.1) to flow structures in asymmetric simulation B ($K_a \approx K_s$, see Table 4.1). Both simulations are located in the bifurcation diagram of figure 4.3(a). Although the flow is chaotic in simulation A, it shares strong similarities with the onset of convection: symmetric and columnar vortices, aligned with the rotation axis, are the main convective features (figures 4.6(a,c) and 4.8(a)). The temperature field is also highly symmetric (figure 4.6(e)). The change in flow morphology related to the emergence of antisymmetric modes is particularly pronounced when looking at the azimuthal flow field in simulation B. Indeed, this field is dominated by negative values in the northern (upper) hemisphere and positive values in the southern (lower) hemisphere (figures 4.6(b), 4.8(b)), indicating that (1) the azimuthal flow has a very strong antisymmetric component, and (2) this antisymmetric component is highly axisymmetric, i.e. dominated by modes of harmonic order $m = 0$. Thus, the azimuthal flow is strongly influenced by an equatorially antisymmetric and axisymmetric (EAA) component, which consists of two large-scale vortices, one in each hemisphere, with an axial vorticity of opposite sign in the two hemispheres (arrows in figure 4.6(b)), causing shear in the axial direction. Such an azimuthal flow contrasts with the symmetric flow of simulation A (figure 4.6(a)). The axial vorticity of the total flow (figure 4.6(d)) is still very columnar (i.e. stretched in the axial direction) in simulation B, confirming that the flow is still highly influenced by rotation, as previously anticipated. The vorticity columns are slightly tilted in figure 4.6(d) and the direction of the tilt is compatible with

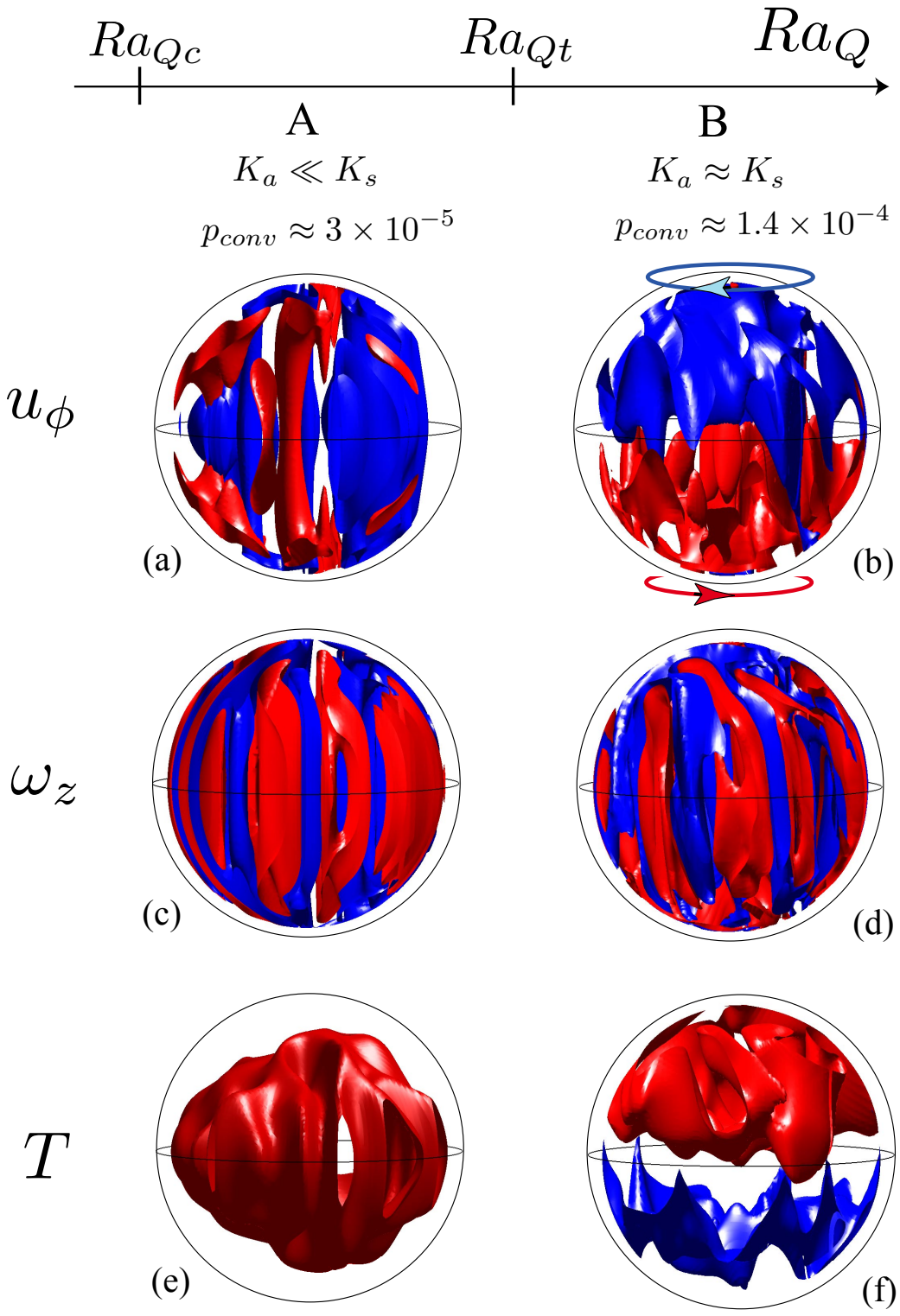

Figure 4.6: Isosurfaces of instantaneous (a,b) azimuthal velocity, (c,d) axial vorticity and (e,f) temperature for full-sphere simulations A and B (hydrodynamic simulations located in figure 4.3, parameters reported in Table 4.1) at convective power p_{conv} close to 3×10^{-5} and 1.5×10^{-4}, respectively. The $\hat{z}$-axis is vertical in these figures. The viscous boundary layer at the outer sphere has been excluded for clarity. (a,b,c,d) Red and blue indicate positive and negative values, respectively. The following isosurfaces are shown: (a) $|u_\phi| = 8.1 \times 10^{-3}$, (b) $|u_\phi| = 2.4 \times 10^{-2}$, (c) $|\omega_z| = 0.12$, (d) $|\omega_z| = 0.24$, (e) $T = -867$, (f) $T = -667$ (red) and $T = -933$ (blue).

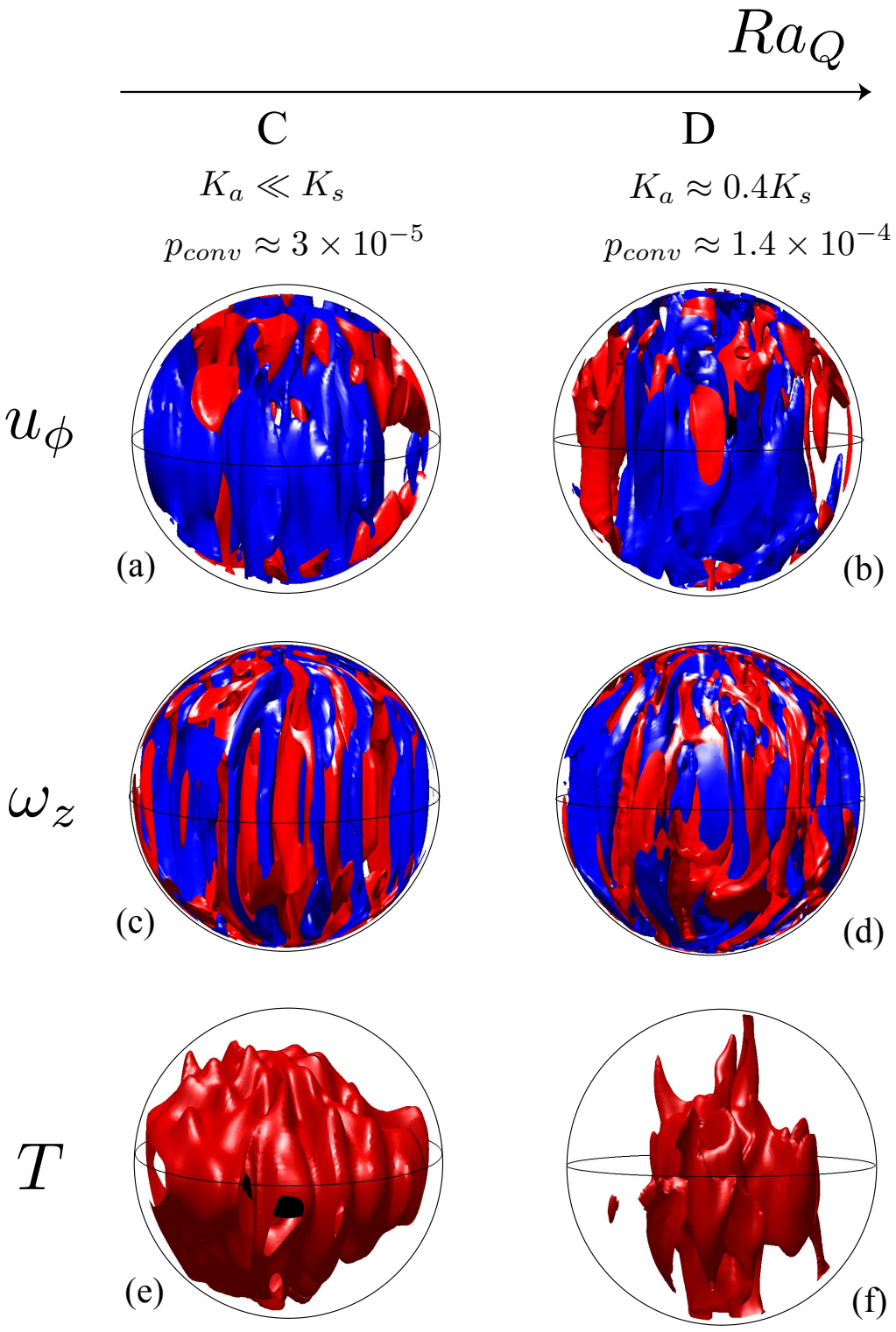

Figure 4.7: Isosurfaces of instantaneous (a,b) azimuthal velocity, (c,d) axial vorticity and (e,f) temperature for bottom-driven reference simulations C and D (hydrodynamic located in figure 4.3, parameters reported in Table 4.1), with the same convective power p_{conv} as in simulations A and B, respectively. The $\hat{z}$-axis is vertical in these figures. The viscous boundary layer at the outer sphere has been excluded for clarity. (a,b,c,d) Red and blue indicate positive and negative values, respectively. The following isosurfaces are shown: (a) $|u_\phi| = 9\times10^{-3}$, (b) $|u_\phi| = 3\times10^{-2}$, (c) $|\omega_z| = 0.15$, (d) $|\omega_z| = 0.36$, (e) $T = 1467$, (f) $T = 1500$.

the shear induced by the pair of EAA vortices (arrows in figure 4.6(b)). Because they are tilted, the vorticity columns are not entirely symmetric, which also contributes to the total antisymmetric kinetic energy. As seen in figure 4.6(f), the temperature field is also strongly asymmetric with respect to the equatorial plane in simulation B.

Figures 4.7 and 4.8(c,d) show the flow structures in bottom-driven reference models C and D, which are chosen such that the convective power p_{conv} is the same as in simulation A and B, respectively. Contrary to full-sphere models, no major morphological change is seen when increasing the forcing and the flow remains dominated by symmetric, columnar structures aligned with the rotation axis.

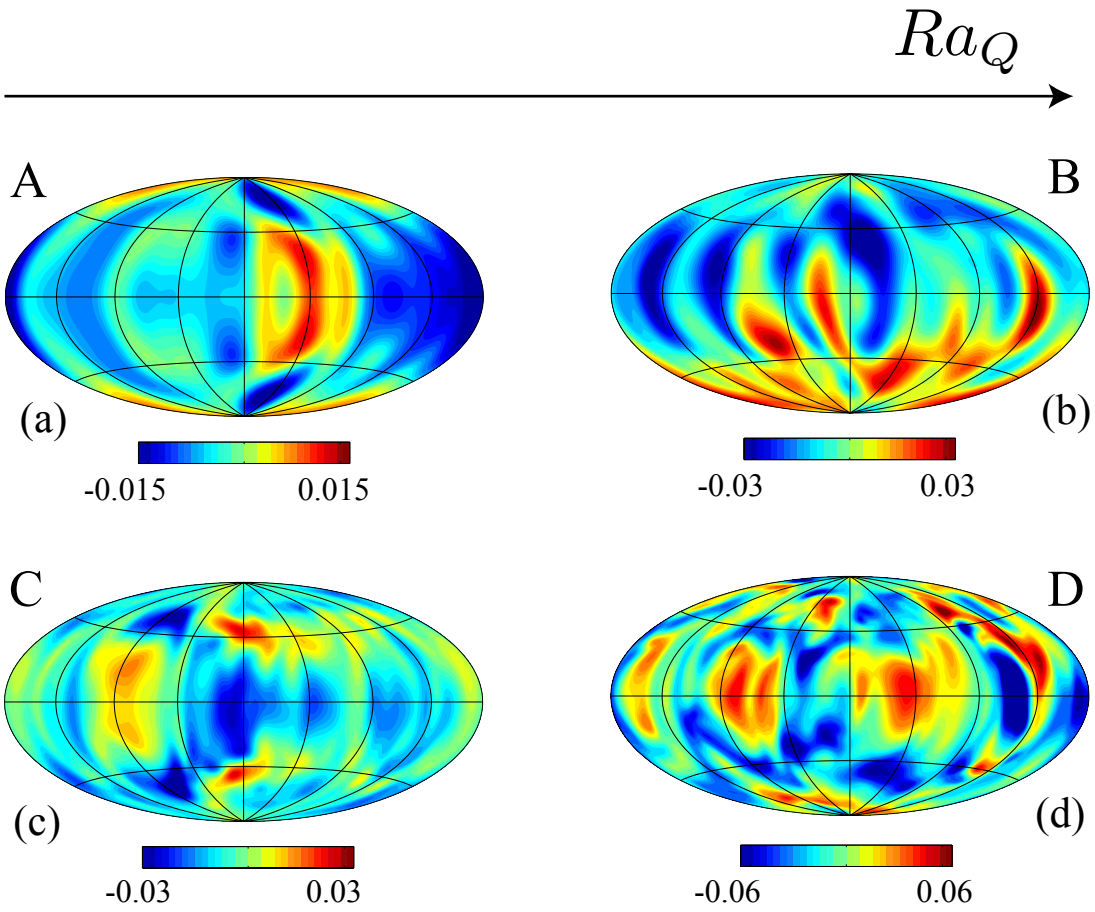

Figure 4.8: Instantaneous azimuthal velocity field at mid-shell (Hammer projection, the $\hat{z}$-axis is vertical) in hydrodynamic simulations: full-sphere simulations (top) and bottom-driven reference models (bottom) at $p_{conv} \approx 5 \times 10^{-5}$ (left) and $p_{conv} \approx 2 \times 10^{-4}$ (right). (a,b,c,d) Simulations A, B, C, D, respectively (parameters reported in Table 4.1).

When looking at kinetic energy spectra (figure 4.9), the most striking feature is the strong signature of antisymmetric modes of order $m = 0$ (referred to as EAA modes in this study) in simulation B (figure 4.9(b)). The kinetic energy contained in EAA modes is almost one order of magnitude higher than the antisymmetric kinetic energy contained in any single spherical harmonic order $m > 0$ and it is more than 3 times larger than the symmetric kinetic energy contained in $m = 2$, the most energetic symmetric modes.

In any single harmonic order $m > 0$, the antisymmetric energy is distinctly smaller than the symmetric energy, indicating that EAA modes are required to reach $K_a \approx K_s$ in simulation B. Although EAA modes are still the most energetic antisymmetric modes in reference simulation D (figure 4.9(c), same convective power as B), they contain 2 times less energy than symmetric modes of order $m = 4$.

EAA modes also have a major influence on the flow at $E = 10^{-2}$ and $E = 10^{-3}$ in strongly asymmetric simulations ($K_a \geq K_s$), where more than 70% of the total antisymmetric energy is contained in EAA modes (Table 4.1).

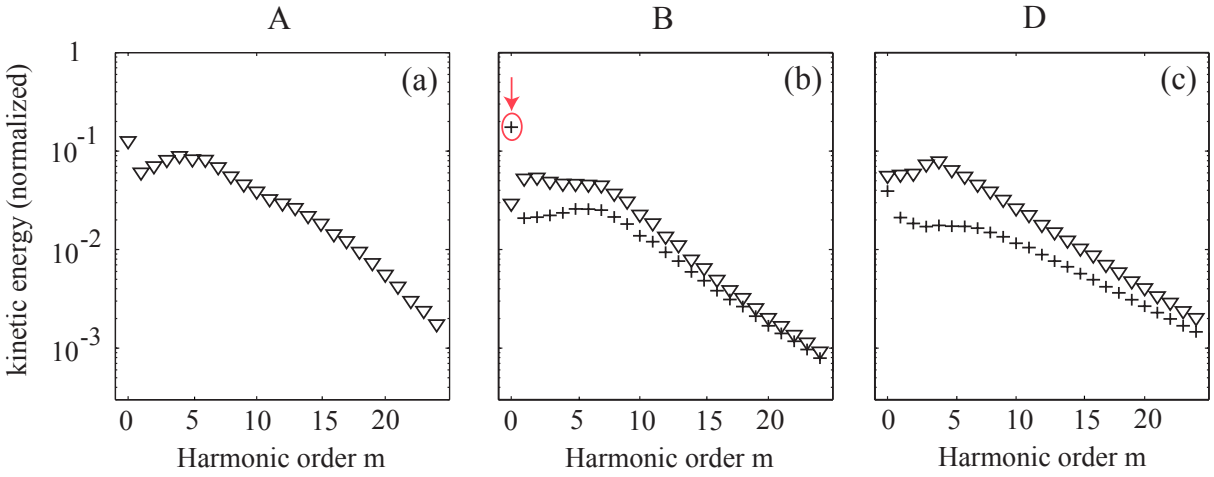

Figure 4.9: Time-averaged spectra of symmetric (crosses) and antisymmetric (triangles) kinetic energy as a function of harmonic order m (hydrodynamic simulations). We compare a strongly asymmetric simulation obtained in the full-sphere configuration ((b), simulation B, Table 4.1) with a symmetric full-sphere simulation ((a), simulation A, Table 4.1) and a bottom-driven reference model at similar convective power ((c), simulation D, Table 4.1). The spectra are normalized by the total kinetic energy. Note that no crosses appear in (a) because the antisymmetric kinetic energy is close to zero.

Time-averaged fields provide first insights into the EAA mode dynamics since they do not contain modes of order $m > 0$, which are drifting in the prograde azimuthal direction. Contrary to simulation A, the time-averaged temperature field is highly asymmetric in simulation B (figure 4.10(a,c)). This induces a strongly asymmetric zonal flow through a thermal wind mechanism, which is characterized by a balance between the Coriolis, pressure gradient and buoyancy forces. Taking the ϕ-component of the curl of the momentum equation, retaining only the above forces and assuming that the time-averaged flow is also axisymmetric, we have:

$$\left\langle \frac{\partial u_\phi}{\partial z} \right\rangle = \left\langle \frac{Ra_Q}{2r_0} \frac{\partial T}{\partial \theta} \right\rangle, \tag{4.3}$$

where the angled brackets denote the time-averaging operator. Figure 4.11 shows a high degree of similarity between the RHS and LHS terms of equation (4.3), confirming that equation (4.3) captures the flow dynamics inside the sphere (except near the boundaries where the viscous term cannot be neglected). The term $\langle \partial T/\partial \theta \rangle$ is negative almost everywhere in the sphere (figures 4.11(b) and 4.10(c)), inducing a negative $\langle \partial u_\phi/\partial z \rangle$ term

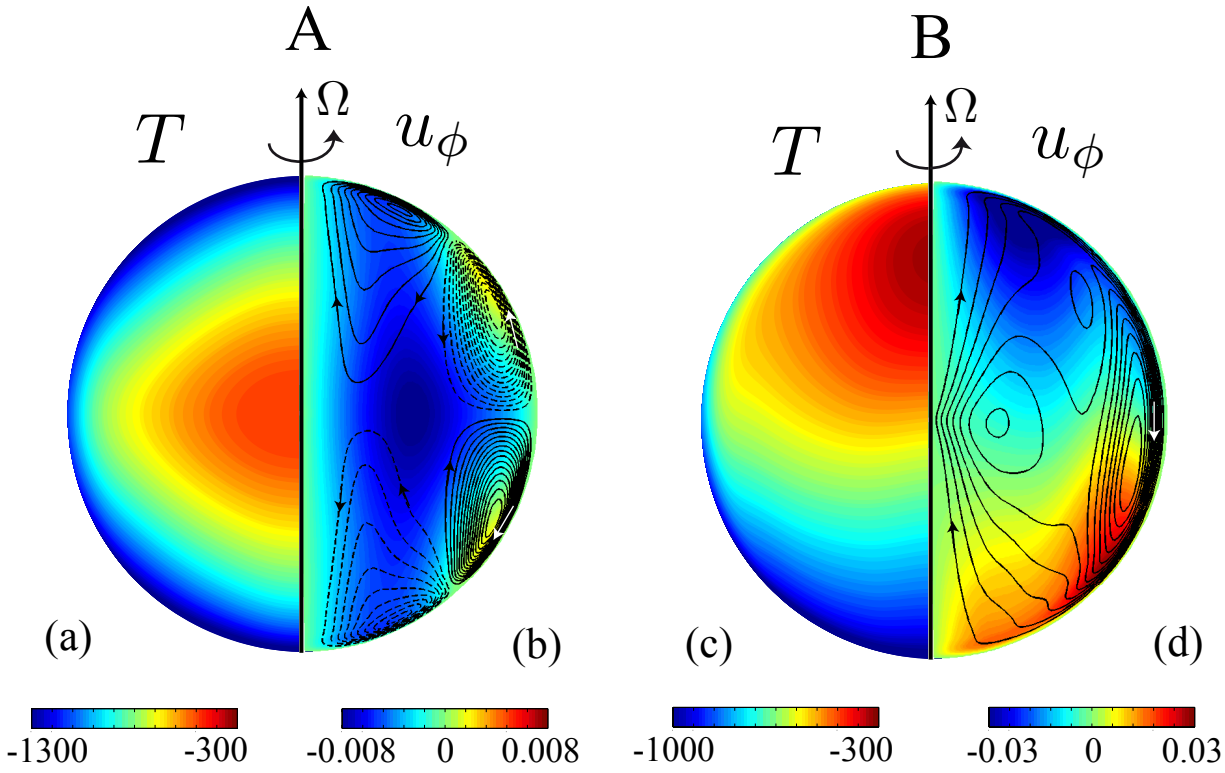

Figure 4.10: Meridional section (arbitrary azimuth) of (a,c) the time-averaged temperature field and (b,d) the time-averaged azimuthal velocity field in (left) symmetric simulation A and (right) asymmetric simulation B (hydrodynamic full-sphere simulations, parameters reported in Table 4.1). Contours in (b,d) show streamlines of the meridional circulation which rotates clockwise (solid lines) or anticlockwise (dashed lines).

according to equation (4.3). This is consistent with an antisymmetric zonal flow organized in a pair of large-scale vortices, as we find in simulation B (figures 4.10(b) and 4.6(b)).

The time-averaged azimuthal flow is also in equilibrium with the time-averaged meridional flow through Ekman pumping, which results from a differential rotation between the rigid boundary and the interior flow outside the viscous (or Ekman) boundary layer*. In the southern hemisphere in figure 4.10(d), the fluid is rotating faster than the external boundary, inducing a flow that converges towards the rotation axis in the viscous boundary layer. Conversely, the time-averaged meridional flow diverges from the rotation axis in the northern boundary layer. To ensure mass conservation, the flow from North to South in the viscous boundary layer has to be compensated by a net flow from the southern hemisphere to the northern hemisphere in the sphere interior, called Ekman pumping, which

*Ekman layers are viscous boundary layers that allow a rotating flow to meet the no-slip boundary condition and in which viscous forces are of the same order of magnitude as Coriolis and pressures forces. Two main features of an Ekman layer need to be mentioned here. First, the dimensionless thickness of an Ekman layer evolves as $E^{1/2}$. Second, a cyclonic columnar vortex near a rotating horizontal wall is associated with a converging flow inside the Ekman layer, while an anticyclonic vortex is associated with a diverging flow. Such converging or diverging flow has to be compensated by vertical motions in the fluid interior, called *Ekman pumping*, for mass conservation to be satisfied. The exact amplitude of the Ekman pumping for a horizontal rigid boundary is given by (Gubbins & Roberts, 1987) $u_z = -1/2E^{1/2}\boldsymbol{\omega}\cdot\mathbf{n}$, where u_z is the dimensionless velocity along the rotation axis, $\mathbf{n}$ the normal unit vector and $\boldsymbol{\omega}$ the dimensionless vorticity field.

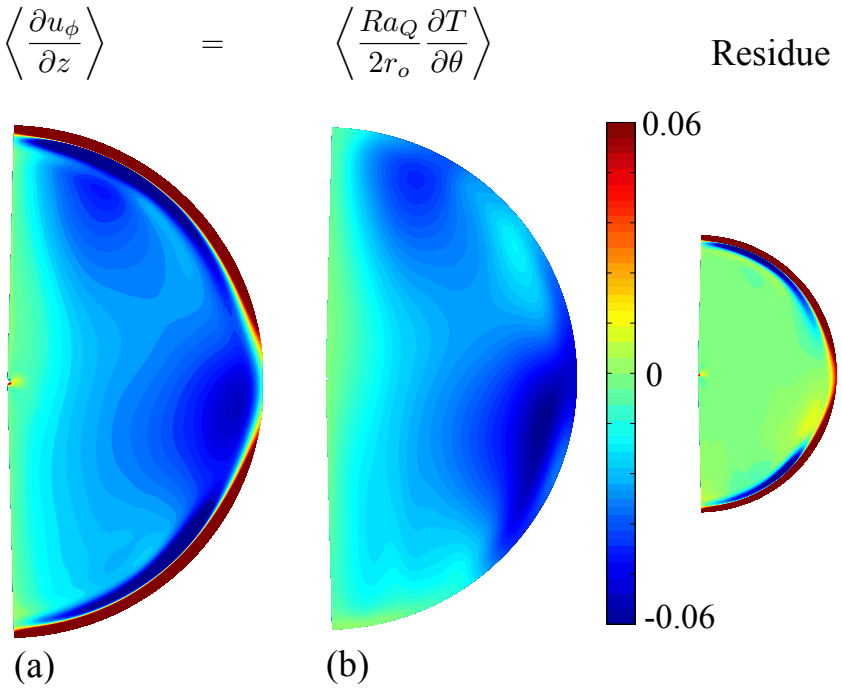

Figure 4.11: Comparison between (a) the LHS term of equation (4.3), and (b) the RHS term of the same equation. Results obtained using asymmetric simulation B (parameters indicated in Table 4.1).

tends to reinforce the antisymmetric temperature profile. If the above dynamics holds in our simulations then, U_z, the axial velocity averaged over the sphere interior (excluding the viscous boundary layer) and over time, is related to U_ϕ, the time-averaged azimuthal velocity close to the viscous boundary layer, such that $U_z = O(E^{1/2}U_\phi)$. The term U_ϕ is estimated by computing the square root of the kinetic energy contained in azimuthal components and averaged over a sphere surface located close to the viscous boundary layer. In simulations where the time-averaged flow is largely dominated by EAA modes, the ratio $U_z/E^{1/2}U_\phi$ remains of order 1 with a mean value equal to 2.76 and a standard deviation equal to 0.6, although the ratio U_z/U_ϕ varies between 0.02 and 0.2. This confirms that the time-averaged meridional flow partly results from an Ekman pumping mechanism. The time-averaged meridional circulation and the time-averaged temperature field (figures 4.10(c,d)) have some morphological similarities with the first linearly unstable mode of convection in non-rotating spheres (Chandrasekhar 1961, chap.6, see Fig.57). The latter consists of a unique large-scale meridional cell inducing an asymmetric temperature profile. However, the dynamics is very different here since the flow is highly influenced by rotation (Ekman boundary layers and thermal-wind balance).

Equations (3.27)-(3.28) and (3.31) and their boundary conditions have equatorial reflection symmetry. Consequently, if $A(t)$ is the amplitude of the antisymmetric flow $\mathbf{u}_A$ and $S(t)$ the amplitude of the symmetric flow $\mathbf{u}_S$, then $S\mathbf{u}_S + A\mathbf{u}_A$ and $S\mathbf{u}_S - A\mathbf{u}_A$ are two dynamically equivalent solutions. This means that the solution shown in figure 4.10(c,d) is dynamically equivalent to the solution obtained by taking the mirror-image of figure 4.10(c,d) with respect to the horizontal plane (with warm temperatures and negative azimuthal flows in the southern hemisphere). In our simulations we indeed find both

solutions. The system chooses one of the two and does not reverse towards the other.

4.2 Convection when allowing dynamo action

We now turn to the study of asymmetric convection in the presence of dynamo action. We first introduce the different flow regime transitions, which are compared to those found in section 4.1 without dynamo action. The associated changes in magnetic field morphology are then presented.

4.2.1 Hydrodynamic transitions

4.2.1.1 Bifurcation and regime diagrams

The results for the linear onset of convection at Ra_{Qc} are identical to what we found in section 4.1.1 (without dynamo action). This is due to the fact that the initial magnetic field is of infinitesimal amplitude and the Lorentz force, through which the magnetic field acts back on the flow, is a nonlinear term.

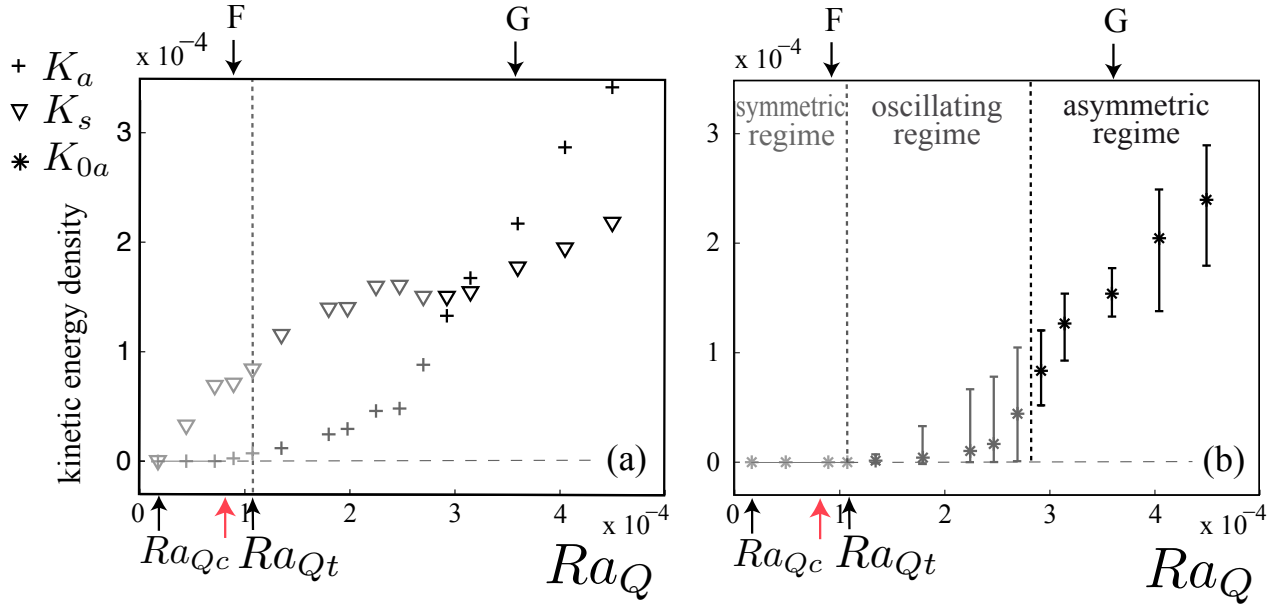

Figure 4.12: Bifurcation diagram for convection with dynamo action at $E = 3\times10^{-4}$ showing (a) the antisymmetric kinetic energy density K_a (crosses), the symmetric kinetic energy density K_s (triangles) and (b) the EAA kinetic energy density K_{0a} (stars), versus Ra_Q in full-sphere simulations. Vertical bars in (b) show the range of values taken by the instantaneous values of K_{0a}. Ra_{Qt} corresponds to the emergence of antisymmetric modes computed in the hydrodynamic study (section 4.1.2). Light grey, medium grey and black symbols correspond to symmetric, oscillating and asymmetric simulations respectively (see text). Vertical dashed lines denote flow regime transitions and the red arrow indicates the dynamo onset. Symbols F, G denote simulations shown in figure 4.18 (parameters reported in Table 4.2)

The flow undertakes successive regime transitions which are identified in the bifurcation diagrams of figure 4.12. The symmetric solution (such that $K_a \ll K_s$) becomes unstable and antisymmetric modes start to grow at a Rayleigh number close to Ra_{Qt} (computed in section 4.1.2), the threshold that marks the emergence of antisymmetric modes in hydrodynamic simulations (figure 4.3(a)). The main distinctive feature of convection with dynamo action is the emergence of an additional flow regime just above Ra_{Qt}, in which the instantaneous value of K_a oscillates in a chaotic manner between low values (weakly asymmetric state) and larger values (highly asymmetric state) as illustrated in figure 4.13. Oscillations in K_a are correlated with variations of the instantaneous value of the EAA kinetic energy K_{0a}, which oscillates between values close to 0 and larger values of order K_a (figures 4.13 and 4.12(b)). The flow is said to be in an *oscillating regime* (for Rayleigh numbers located just above Ra_{Qt}, we observe bursts towards the highly asymmetric state rather than oscillations, as shown in figure 4.13(a)). EAA mode reversals, during which the EAA mode amplitude changes sign, are observed between successive highly asymmetric states. Finally, when the forcing is strong enough ($Ra_Q \gtrsim 3 \times 10^{-4}$), the flow reaches the *asymmetric regime*, in which the instantaneous value of K_{0a} ceases to reach values close to zero and remains of order K_a (figure 4.12(b)). In the asymmetric regime, the flow remains in the highly asymmetric state and no longer oscillates between a weakly and highly asymmetric state.

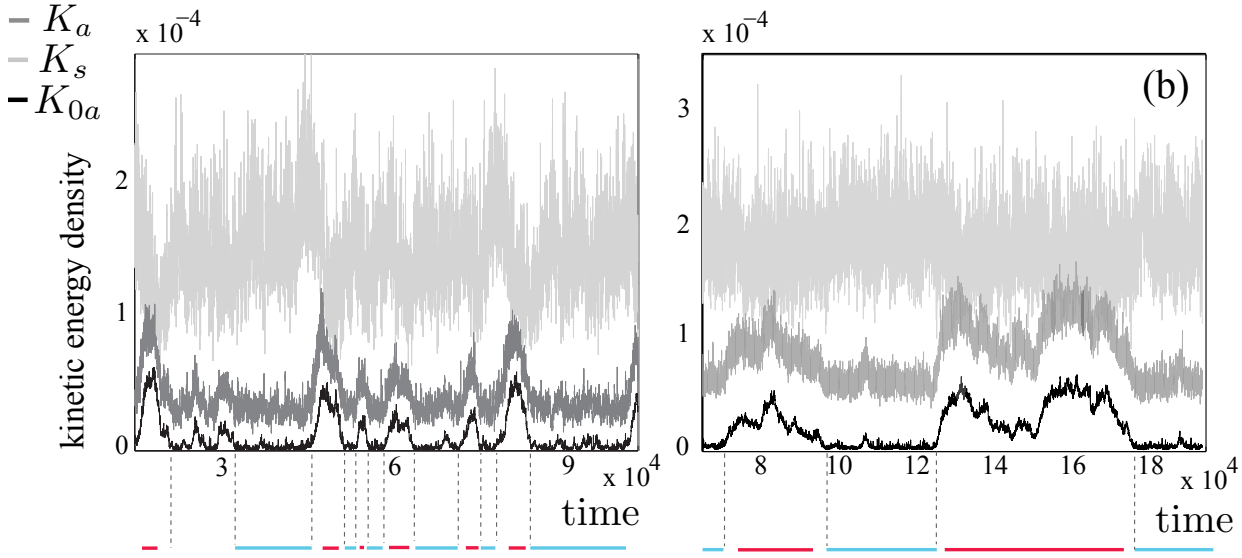

Figure 4.13: Instantaneous value of K_s (light grey curve), K_a (medium grey curve) and K_{0a} (black curve) as a function of time in (a) oscillating dynamo simulation H, in which Ra_Q is close to Ra_{Qt}, and (b) oscillating dynamo simulation I, in which Ra_Q is further away from Ra_{Qt} (Table 4.2). Red lines indicate the highly asymmetric state where K_a and K_{0a} take large values whereas blue lines indicate the weakly asymmetric state where K_{0a} is close to zero and K_a takes lower values.

We find a similar bifurcation diagram (with a symmetric, oscillating and asymmetric regime) at $E = 10^{-4}$. However, no oscillating simulations are obtained at $E \geq 10^{-3}$ because the dynamo onset is not overcome when Ra_Q reaches Ra_{Qt} at such Ekman numbers. Therefore, the bifurcation diagram is similar to the one obtained for convection without dynamo action if $E \geq 10^{-3}$. Similarly to figure 4.5, figure 4.14 summarizes the regime

boundaries in $(1/E, Ra_Q)$ space when dynamo action is allowed. We emphasize here again that the boundary between symmetric and oscillating regimes is set by $Ra_Q = Ra_{Qt}$, where Ra_{Qt} is the forcing at which the transition from the symmetric to the asymmetric regime occurs in the hydrodynamic case. Its location is thus given by equation (4.2).

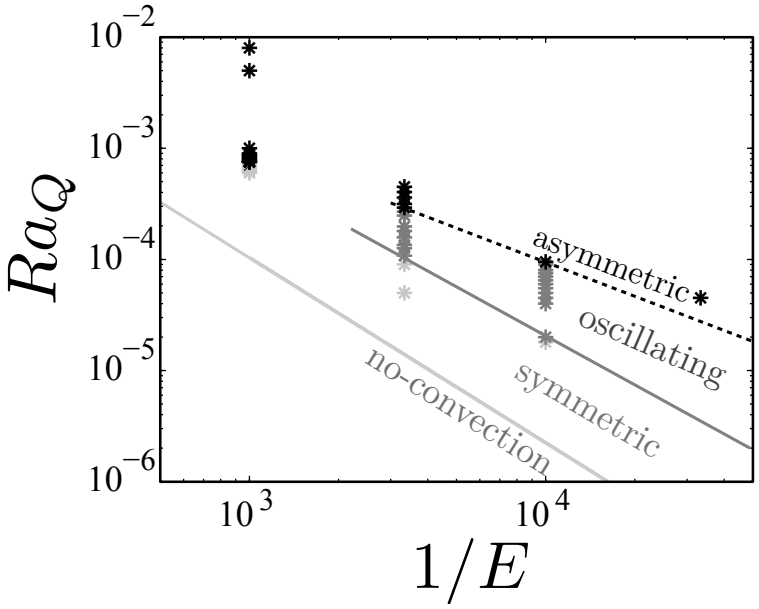

Figure 4.14: Flow regime diagram when allowing dynamo action. Light grey, medium grey and black symbols correspond to symmetric, oscillating and asymmetric simulations respectively. The light grey curve corresponds to the asymptotic behavior of Ra_{Qc} given by equation (4.1). The medium grey curve corresponds to the best fit (in the sense of the least squares) for Ra_{Qt}. The black dashed line corresponds to a tentative boundary regime between the oscillating and asymmetric regime.

From a phenomenological point of view, the appearance of the oscillating regime when allowing dynamo action can be seen as a consequence of Ferraro's law of corotation (Ferraro, 1937). This law states that the axisymmetric magnetic field lines tend to follow the isocontours of $\langle u_\phi/s \rangle_\phi$, where s is the cylindrical radius, in order to minimize the production of azimuthal magnetic field by the term $s\mathbf{B}\cdot\nabla(u_\phi/s)$ in the induction equation. The flow and magnetic fields organize themselves such that this principle is satisfied at first order in dipole-dominated dynamo simulations (Aubert, 2005). At the beginning of an oscillation towards the highly asymmetric state, the EAA flow component emerges because it is linearly unstable with respect to the symmetric solution (since $Ra_Q \geq Ra_{Qt}$). The EAA azimuthal flow distorts the isocontours of $\langle u_\phi/s \rangle_\phi$ which no longer follow the magnetic field lines and, therefore, induces an axisymmetric azimuthal magnetic field by stretching of the poloidal magnetic field (i.e. through an ω-effect, see appendix B). The induced azimuthal magnetic field causes a magnetic tension force* in the azimuthal direction that tends to oppose the EAA flow component and acts as a restoring force. If

*The dimensionless Lorentz force $(\nabla\times\mathbf{B})\times\mathbf{B}$ can be written as the sum of $\mathbf{B}\cdot\nabla\mathbf{B}$ and $-\nabla\mathbf{B}^2$. The former term is called *magnetic tension* and tends to straighten curved magnetic field lines. The latter term is called *magnetic pressure force* and arises when the magnetic energy varies in space.

the magnetic tension force becomes strong enough, the flow returns to its initial weakly asymmetric state that satisfies Ferraro's law of corotation.

As for the case of convection without dynamo action, K_a increases faster than K_s above Ra_{Qt} (figure 4.12(a)) and strongly asymmetric simulations in which $K_a \geq K_s$ are obtained for $Ra_Q \gtrsim 3 \times 10^{-4}$ at $E = 3 \times 10^{-4}$ (figure 4.12(a)), for $Ra_Q \gtrsim 1.5 \times 10^{-4}$ at $E = 10^{-4}$ (Table 4.2) and for $Ra_Q \gtrsim 3 \times 10^{-3}$ at $E = 10^{-3}$ (Table 4.2).

4.2.1.2 Flow structures

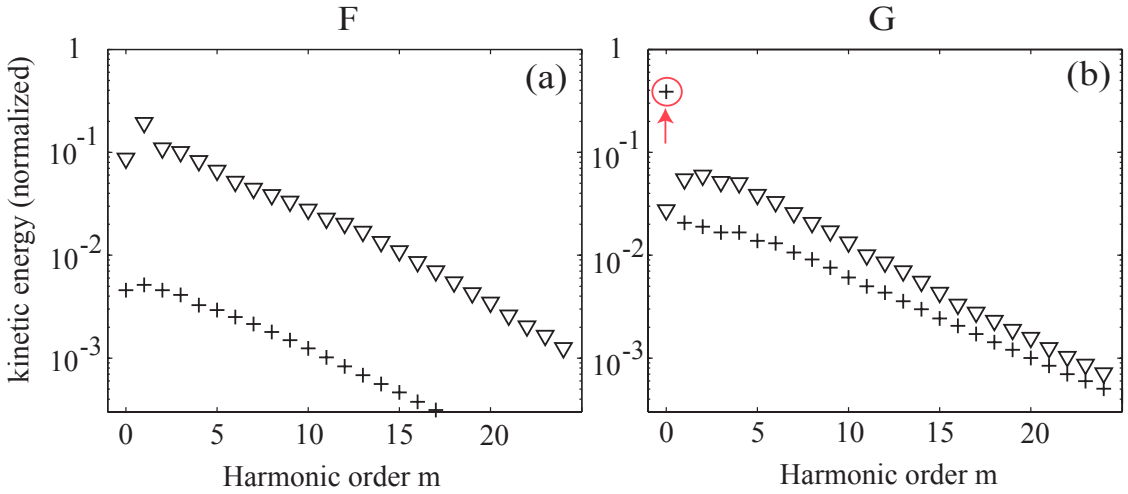

Figure 4.15: Time-averaged spectra of symmetric (crosses) and antisymmetric (triangles) kinetic energy as a function of harmonic order m in full-sphere dynamos, comparing (a) simulation F in which $K_a \ll K_s$ with (b) simulation G in which $K_a \approx 1.22 K_s$. The spectra are normalized by the total kinetic energy. Simulations F and G (Table 4.2), located in figure 4.12 and shown in figure 4.18, are computed at the same parameter values as hydrodynamic simulations A and B, respectively.

In terms of structure and dynamics of the flow, results obtained in hydrodynamic simulations (section 4.1.2) remain unchanged when allowing dynamo action. The flow in strongly asymmetric simulations ($K_a \geq K_s$) is highly influenced by EAA components, which are the most energetic modes (figure 4.15(b)) and the associated EAA azimuthal flow results from a thermal-wind balance (satisfying equation (4.3)) as shown in figure 4.16. The term $\langle \partial T / \partial \theta \rangle$ is positive almost everywhere in simulation G (figure 4.16(b)), which induces a positive $\langle \partial u_\phi / \partial z \rangle$ term, consistent with a clockwise zonal flow in the northern hemisphere and anti-clockwise in the southern hemisphere as seen in figure 4.18(b).

4.2.1.3 Scaling laws for the saturation of antisymmetric modes

The saturation amplitude of antisymmetric modes follows a similar trend in hydrodynamic and dynamo simulations that are located in the asymmetric regime (figure 4.17) and

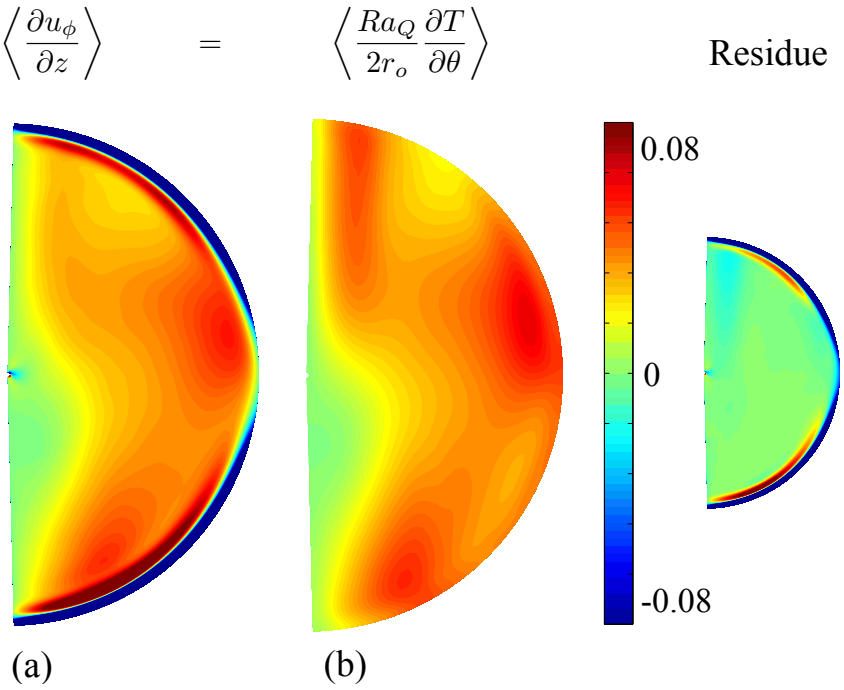

Figure 4.16: Comparison between (a) the LHS term of equation (4.3), and (b) the RHS term of the same equation. Results obtained using dynamo simulation G (Table 4.2).

scaling laws can be extracted. We obtain the following least square best fits:

$$K_a = b_1(Ra_Q - Ra_{Qt})^{a_1} \quad , \quad a_1 = 0.86 \pm 0.02 \quad , \quad b_1 = 0.24 \pm 0.04 \tag{4.4}$$

$$K_{0a} = b_2(Ra_Q - Ra_{Qt})^{a_2} \quad , \quad a_2 = 1.10 \pm 0.02 \quad , \quad b_2 = 1.0 \pm 0.3 \tag{4.5}$$

We note that our asymmetric simulations are located rather close to the threshold for antisymmetric mode emergence Ra_{Qt} and one has to be careful when extrapolating the above scalings to high $Ra_Q - Ra_{Qt}$ values. For instance, K_a and K_{0a} in dynamo simulations at $E = 3 \times 10^{-4}$ exhibit a slightly higher slope than in other simulations (figure 4.17(a,b)), which may be a local effect resulting from the proximity to Ra_{Qt}.

The value of the exponent $a_1 = 0.86 \pm 0.02$ for the evolution of the antisymmetric kinetic energy K_a (scaling (4.4)) is very close to values found for the evolution of the total kinetic energy as a function of Ra_Q in previous studies (Christensen & Aubert 2006, Aubert *et al.* 2009), suggesting that saturation mechanisms for symmetric and antisymmetric modes are similar. The value of the exponent a_2 for the evolution of the EAA kinetic energy K_{0a} is significantly higher than a_1 (scaling (4.5)) and close to 1, as predicted by dimensional analysis for a flow which is dominated by zonal components induced by a thermal wind mechanism (Aurnou *et al.*, 2003).

4.2.2 Magnetic field structures: hemispherical dynamos

Figure 4.18 compares magnetic field structures in simulation F in which $K_a \ll K_s$ and in simulation G in which the flow is strongly asymmetric. Contrary to simulation F in

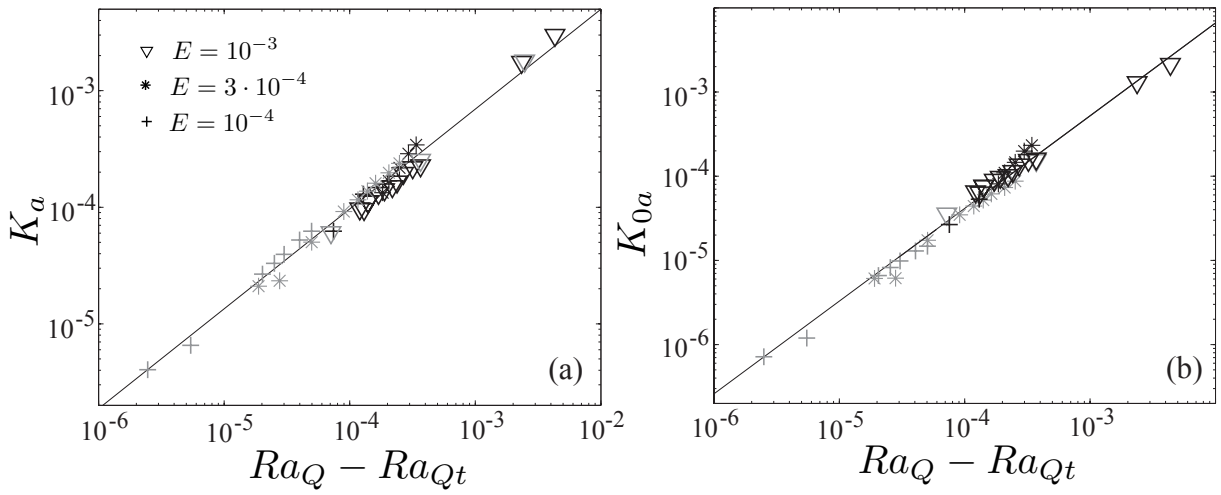

Figure 4.17: Saturation of hydrodynamic antisymmetric modes in hydrodynamic simulations (grey) and dynamo simulations (black) in the asymmetric regime. K_a (a) and K_{0a} (b) as a function of $Ra_Q - Ra_{Qt}$. The least square best fits $K_a = b_1(Ra_Q - Ra_{Qt})^{a_1}$ with $a_1 = 0.86 \pm 0.02$ and $b_1 = 0.24 \pm 0.04$ (a) and $K_{0a} = b_2(Ra_Q - Ra_{Qt})^{a_2}$ with $a_2 = 1.10 \pm 0.02$ and $b_1 = 1.0 \pm 0.3$ (b) are shown by black lines.

which the magnetic field is dipole-dominated and of similar strength in both hemispheres (figures 4.18(c)), the magnetic field of simulation G is hemispherical, with high intensities in one hemisphere and weaker in the other (figure 4.18(d)).

A phenomenological explanation for the hemispherical character of the radial magnetic field in strongly asymmetric simulations (such that $K_a = O(K_s)$) can be qualitatively captured using DMFI visualizations (Aubert *et al.*, 2008) as shown in figure 4.19. In symmetric simulation F, the surface magnetic flux is collected near the poles, where the meridional flow converges (figure 4.19(a)). Cold vertical plumes are generated close to the axis at the outer boundary where they detach from the thermal boundary layer; they are similar to vertical plumes generated in rotating cylinders (Aurnou *et al.*, 2003) or inside the tangent cylinder in spherical shells (Aubert *et al.*, 2008) where the buoyancy force is nearly aligned with the rotation axis. Those flow downwellings amplify the magnetic field that has been collected near the pole by stretching (through the term $B_r \partial u_r / \partial r$ in the induction equation), producing magnetic downwellings, which are similar to the magnetic upwellings described in Aubert *et al.* (2008) and which correspond to the radish-like structures located close to the rotation axis in figure 4.19(a). In strongly asymmetric simulations, the above mechanisms are active in only one hemisphere. Indeed, one hemisphere is stably stratified along the axis (southern hemisphere in figure 4.19(c)), which stops any cold plume, and thus any magnetic downwelling. In addition, in the same hemisphere, the magnetic flux is dispersed near the pole by a divergent meridional flow (figure 4.19(b)), limiting further the generation of strong radial magnetic field at the pole. As a consequence, the radial magnetic field at the sphere surface is much stronger near one pole than near the other pole (figure 4.18(d)).

In order to quantify the above morphological results, we compute the hemisphericity factor f_{hem} (defined in section 3.7). A dynamo is said to be hemispherical if $f_{hem} \geq 0.75$ which means that one hemisphere contains at least 75% of the CMB magnetic energy.

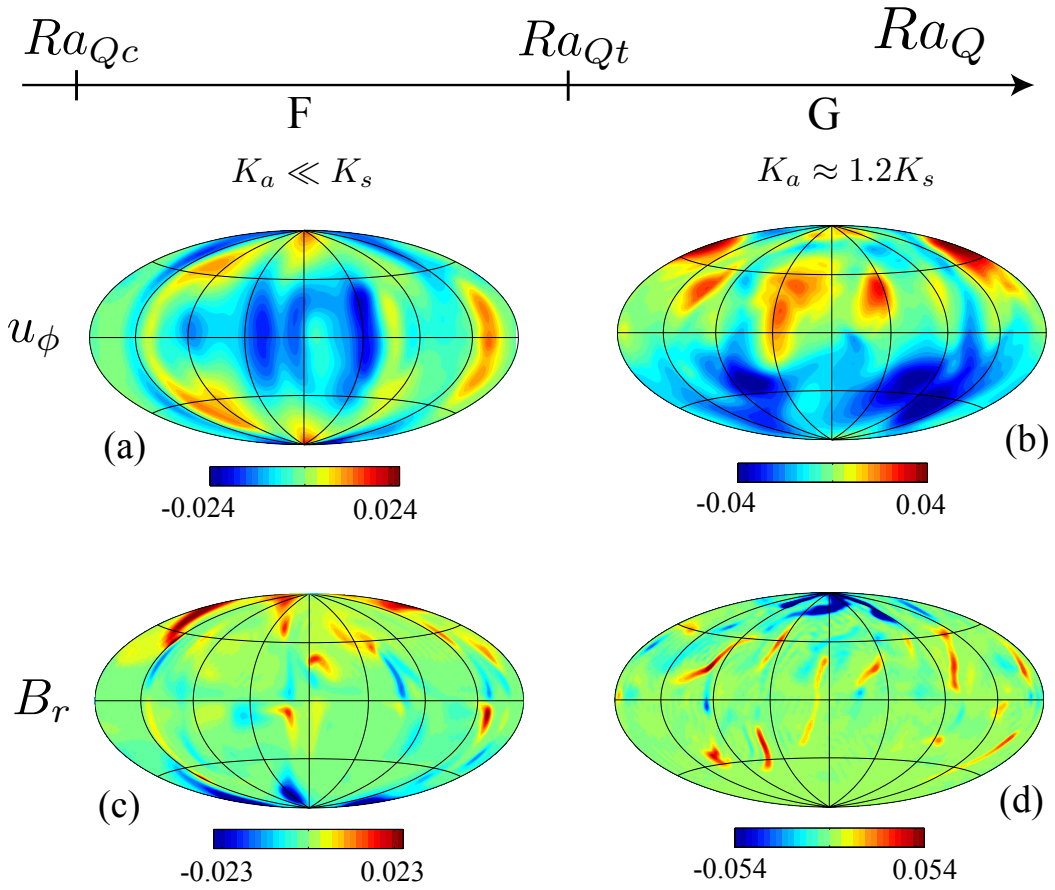

Figure 4.18: Instantaneous azimuthal velocity field at mid-shell (a,b) and instantaneous radial magnetic field at r_o (c,d) in dynamo simulations F (left) and G (right) (parameters reported in Table 4.2), which are computed at the same parameter values as hydrodynamic simulations A and B, respectively.

The ratio K_a/K_s, which measures the equatorial symmetry breaking of the flow, is a control parameter of the hemisphericity factor f_{hem}, as shown by the univariate behavior in figure 4.20(a). In symmetric simulations the flow is dominated by symmetric modes and K_a/K_s has low values. In these symmetric simulations the hemisphericity factor is very close to 0.5, indicating that the magnetic field is not hemispherical, as illustrated with figure 4.18(c). The progressive increase of the ratio K_a/K_s in asymmetric and oscillating simulations, from low (~ 0.2) to large values (~ 2.3), is associated with an almost linear increase of the hemisphericity factor f_{hem}, revealing that the transition from non-hemispherical to hemispherical dynamos is gradual. The hemisphericity factor reaches 0.75 when $K_a/K_s \approx 1$. Several hemispherical dynamos ($f_{hem} \geq 0.75$) are obtained, including the simulation shown in figures 4.18(b,d).

Figure 4.20(b) shows that the equatorial symmetry breaking of the flow K_a/K_s is also a control parameter of the magnetic field parity M_{qua}/M_{dip} at fixed Pm. Indeed, M_{qua}/M_{dip} increases with K_a/K_s and all the simulations are aligned on the same curve (with the exception of one simulation which has been obtained at a different value of Pm). When K_a/K_s reaches ~ 0.75, M_{qua}/M_{dip} saturates and remains close to 1: there is

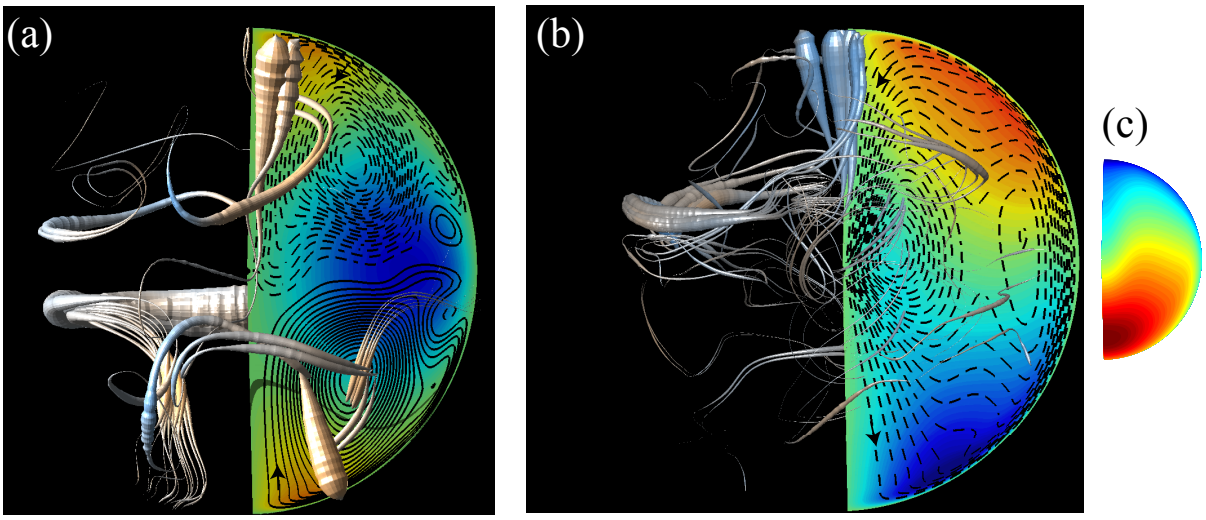

Figure 4.19: (a,b) DMFI visualizations of dynamo simulations F and G (Table 4.2). Magnetic field lines are displayed in grey, their thickness is proportional to $\boldsymbol{B}^2$ (for details see Aubert et al.*, 2008). The meridional cut shows the time-averaged azimuthal velocity field (red color for positive values and blue for negative values) and the streamlines of the meridional circulation which rotates clockwise (solid black lines) and anticlockwise (dashed black lines). (c) Meridional cut of the time-averaged temperature field, which varies between -1436 (dark blue) and -436 (dark red).*

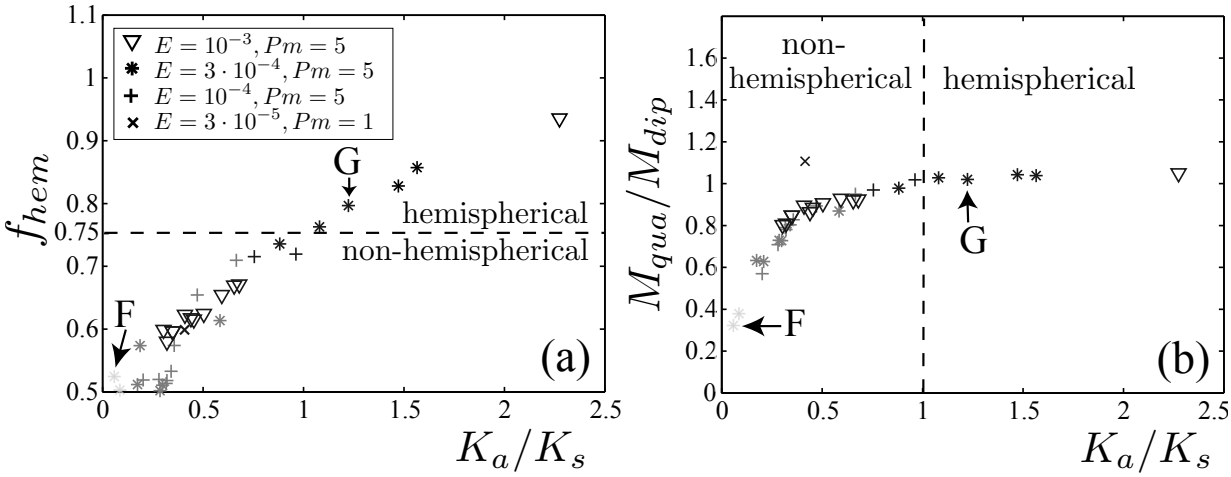

Figure 4.20: (a), Hemisphericity factor f_{hem} versus K_a/K_s. (b), Magnetic energy parity ratio M_{qua}/M_{dip} versus K_a/K_s. Light grey, medium grey and black symbols correspond to symmetric, oscillating and asymmetric simulations respectively. The dashed black line denotes the transition from non-hemispherical to hemispherical dynamos at $f_{hem} = 0.75$. The symbols F and G denote results obtained with simulations F and G respectively, which are illustrated in figure 4.18.

equipartition between magnetic energy contained in modes of dipole parity and magnetic energy contained in modes of quadrupole parity. We note that several simulations have reached the equipartition of magnetic energy even though they are not hemispherical (the magnetic field in those simulations is multipole-dominated).

The emergence of antisymmetric modes in our simulations is also correlated with changes in magnetic field generation. To measure the contribution of the ω-effect to the production of large-scale azimuthal magnetic field one can compute the ratio between the root mean square of $\overline{\mathbf{B}}\cdot\nabla\overline{u}_\phi$ in the sphere and the root mean square of the ϕ-component of the production term $\overline{\mathbf{B}\cdot\nabla\mathbf{u}}$, where the overline denotes the azimuthal-averaging operator. In symmetric simulation A, this ratio is equal to about 0.2, indicating that the ω-effect contributes weakly to magnetic field generation and the dynamo is of α^2-type (or $\alpha^2\omega$-type). In the strongly asymmetric simulation B, the same ratio is equal to about 0.6, meaning that the dynamo is of $\alpha\omega$-type. The enhanced ω-effect in simulation B is mainly due to the shear associated with the strong EAA zonal flows.

4.3 Summary

We have studied the systematic emergence of antisymmetric modes in the (Ra_Q, E) parameter space for full-sphere hydrodynamic simulations in regimes where the flow is strongly influenced by rotation (geostrophic). Contrary to bottom-driven simulations in which the flow remains dominated by symmetric modes (they always contain more than 70% of the total kinetic energy), antisymmetric modes become stronger than symmetric modes in our full-sphere simulations for sufficiently high Rayleigh numbers. The flow undertakes major morphological changes in these strongly asymmetric simulations. The most striking feature is a very energetic EAA mode, which is characterized by strong antisymmetric zonal flows resulting from a thermal wind mechanism.

A similar study was conducted while allowing dynamo action. In terms of flow features, results from dynamo simulations are very similar to those in hydrodynamic simulations: although the flow is geostrophic, unexpected simulations with $K_a \gtrsim K_s$ are systematically reached for sufficiently high Rayleigh numbers and the flow is strongly influenced by EAA modes. The unique difference with hydrodynamic simulations is the emergence of an additional flow regime, characterized by chaotic oscillations of the EAA kinetic energy between values close to zero and higher values of $O(K_s)$. In terms of magnetic field structures, we have shown that equatorial symmetry breaking, associated with antisymmetric mode emergence, controls the hemisphericity of the magnetic field. In strongly asymmetric simulations, we have found hemispherical dynamos, where more than 75% (and up to 90%) of the total magnetic energy is contained in a single hemisphere.

Figure 4.21 locates the different flow and dynamo regime transitions identified in this chapter in the regime diagram that were shown in chapter 2.

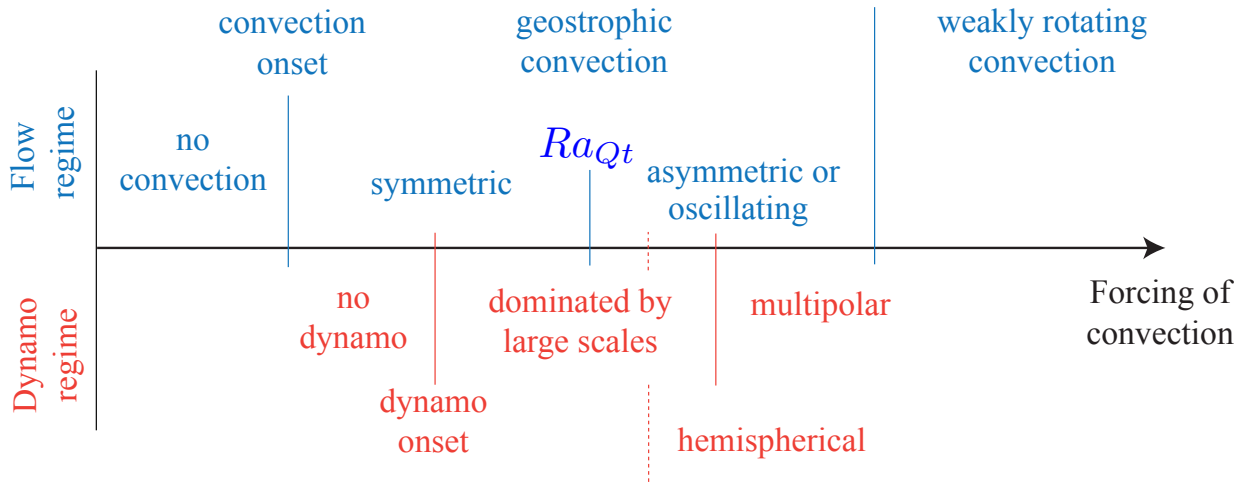

Figure 4.21: Schematic representation of the flow and dynamo regimes when increasing the forcing of convection; the transitions studied in this chapter have been added. The emergence of antisymmetric modes at $Ra_Q = Ra_{Qt}$ systematically occurs in the geostrophic regime of convecting spheres or shells. The transition from non-hemispherical to hemispherical dynamos (dotted line) is less systematic: it occurs only when antisymmetric flow components are of same strength as symmetric components and it may either precedes or follows the transition towards multipolar dynamos.

Chapter 5

Discussion and interpretation

5.1 Flow transitions

5.1.1 Symmetric and asymmetric regimes

We found that the emergence of antisymmetric modes, marking the transition from the symmetric to the asymmetric regime in hydrodynamic simulations and from the symmetric to the oscillating regime in dynamo simulations, occurs as a secondary bifurcation in the geostrophic regime, with no connection with the transition from a geostrophic to a weakly rotating regime (King *et al.* 2009, Zhong *et al.* 2009 and King *et al.* 2012). The Rayleigh number Ra_{Qt} for the nonlinear emergence of antisymmetric modes scales with the power 1.51 of the Ekman number (equation (4.2)), which is rather close to the value 5/3 that holds for the convection onset $Ra_{Qc} \propto E^{5/3}$.

The flow structures in the asymmetric regime highly depend on the saturation of antisymmetric modes when increasing the convection forcing. Indeed, these modes can grow either faster (figure 4.3(a)) or slower (figure 4.3(b)) than symmetric modes, resulting in strongly asymmetric or weakly asymmetric flows, respectively. The former situation is always encountered in rotating spheres at $E \geq 10^{-4}$, while the latter is found in bottom-driven spherical shells where the flow remains dominated by symmetric components when increasing the Rayleigh number.

Our results suggest that, at a given Ekman number, the main control parameters for the amplitude of antisymmetric modes are the forcing of convection Ra_Q, and the ratio between the buoyancy flux at the inner and outer boundary. Strongly asymmetric simulations have not been observed in previously published studies either because the forcing of convection was not sufficiently high, or because the ratio between the inner and outer buoyancy flux was not small enough.

5.1.2 From the perspective of the Taylor-Proudman constraint

We have shown that strongly asymmetric simulations such that $K_a \gtrsim K_s$ are reached in the rotationally dominated regime of convecting spheres at $E \geq 10^{-4}$, provided that the Rayleigh number is sufficiently large. Such a result is unexpected and in apparent conflict with the Taylor-Proudman constraint. Why is this constraint broken in this asymmetric,

but rotationally dominated regime?

In order to address this question, zonal and non-zonal flows need to be discussed separately. It is important to first stress that non-zonal flows always break the Taylor-Proudman constraint, regardless of their equatorial symmetry. Indeed they are affected by the condition of non-penetration $\mathbf{u} \cdot \mathbf{n} = 0$, where $\mathbf{n}$ is the unit vector normal to the external boundary, which imposes

$$u_z z = -u_s s \tag{5.1}$$

at the spherical boundaries. The non-penetration condition is non-dissipative (it holds for inviscid flows) and forces interior motions. Therefore, non-zonal horizontal flows with typical velocity scale U induce axial flows with the same order of magnitude. Since u_s and u_z have reversed symmetries, the z-varying flow component is necessarily of similar amplitude $O(U)$ as the z-independent component. However, breaking the Taylor-Proudman constraint does not prevent the flow from remaining geostrophic at leading order, as illustrated in the following example taken at convection onset.

Viscosity breaks the Taylor-Proudman constraint at convection onset (Roberts, 1968; Busse, 1970), leading to viscous and Coriolis terms with the same order of magnitude in the curl of the momentum equation (or vorticity equation), such that:

$$-2\frac{\partial \mathbf{u}}{\partial z} \sim E\Delta\boldsymbol{\omega} \tag{5.2}$$

where $\boldsymbol{\omega}$ is the vorticity field. If U is a typical velocity scale, δ_z a typical length scale in the axial direction and δ_ϕ a typical azimuthal length scale, the above balance leads to $\delta_\phi = O(E^{1/3}\delta_z)$. Comparing now the viscous force $E\Delta\mathbf{u}$ and the Coriolis force $2\hat{\boldsymbol{z}} \times \mathbf{u}$ in the momentum equation (not its curl), one sees that, owing to the small azimuthal wavelength, viscous forces $O(E^{1/3}U)$ are smaller than their contribution in the vorticity equation by an order $E^{1/3}$, while the Coriolis contribution is of same order of magnitude $O(U)$ in both equations since the curl of the Coriolis force does not involve any derivative in the azimuthal direction. Hence, viscous forces are smaller than the Coriolis force by an order $E^{1/3}$ and the classical geostrophic balance

$$2\hat{\boldsymbol{z}} \times \mathbf{u} = -\nabla P \tag{5.3}$$

is satisfied at leading order. Similar considerations hold in the supercritical convection regime, where inertia or viscous forces can break the Taylor-Proudman constraint while maintaining a leading order geostrophic balance (provided that the contribution of the Lorentz force is negligible in both the momentum equation and its curl).

In our simulations, non-axisymmetric antisymmetric motions can represent up to 60% of the total kinetic energy. From the above discussion, these structures are finally not unexpected and certainly not prohibited in the rotationally dominated regime. Indeed, their dynamics is similar to that of symmetric columns: the variation of the horizontal velocity with z is of order U/D, meaning that they break the Taylor-Proudman constraint, while meeting the geostrophic balance (owing to a small azimuthal wavelength, see figures 4.6(c,d)), just like symmetric columns. The viscous dissipation of antisymmetric columnar structures is probably slightly higher than that of symmetric columns, explaining why symmetric modes are the first to become unstable and are favored just above onset, but

this difference is small and may be overcome at sufficiently supercritical conditions.

Contrary to non-zonal flows, zonal flows are everywhere parallel to the boundaries and, therefore, are unaffected by the non-penetration condition. A viscous Ekman layer of small $O(E^{1/2})$ thickness then allows the zonal flow to meet the no-slip boundary condition, while the interior zonal flow can be rigorously z-invariant. The compliance of an equator-symmetric flow to the Taylor Proudman constraint can thus be total, while an antisymmetric flow necessarily involves departures from this constraint. Thus, the dynamics of symmetric and strongly asymmetric zonal flows is not equivalent. The emergence of a strong antisymmetric zonal flow in our simulations involves a particularly strong relaxation of the Taylor-Proudman theorem by buoyancy contributions, as a result of an asymmetric temperature profile (thermal wind balance (4.3)). The truly unexpected feature in our simulations is thus this strongly asymmetric temperature profile.

More generally, our results recall that strongly asymmetric flows are not prohibited in the rotationally dominated regime in convecting spheres or spherical shells and, at this stage, there is probably no immutable reasons for them to be of small amplitude compared to symmetric modes at small Ekman numbers, in particular at highly supercritical Rayleigh numbers as those reached in planetary cores. Therefore, the terms *geostrophic/ageostrophic* and *symmetric/asymmetric* refer to different properties of the flow that are not necessarily correlated in spheres and shells.

5.2 Hemispherical dynamos

Hemispherical dynamos have been found in other numerical simulations of convection and dynamo action in rotating shells, previously (Grote & Busse, 2000; Simitev & Busse, 2005; Stanley *et al.*, 2008) or subsequently (Amit *et al.*, 2011; Dietrich & Wicht, 2013) to the publication of the present results.

Fixed temperature and stress-free boundary conditions have been imposed in Grote & Busse (2000) and in Simitev & Busse (2005). Their hemispherical dynamos are located in a narrow domain of parameter space and do not result from the same mechanism as ours. Indeed, we found that the value of the antisymmetric kinetic energy remains low in their dynamo simulations ($K_a/K_s \approx 0.01$ at $Pr = 1$, $Pm = 2$, $E = 2 \times 10^{-4}$ and $Ra = 6.5 \times 10^5$) while it is exactly equal to zero in the corresponding hydrodynamic simulations.

As in our simulations, hemispherical dynamos result from the emergence of antisymmetric modes with strong EAA zonal flows in Stanley *et al.* (2008), Amit *et al.* (2011) and Dietrich & Wicht (2013), but we emphasize that EAA zonal flows are prescribed by a heterogeneous heat flux at the outer sphere in the latter studies while they spontaneously emerge in our study. In particular, the heat flux in the simulations by Stanley *et al.* (2008) is stabilizing in one hemisphere and destabilizing in the other, causing convective motions, and hence magnetic field generation, to be mainly located in one hemisphere, which necessarily results in a hemispherical magnetic field pattern. In agreement with our results, Dietrich & Wicht (2013) report an enhanced ω-effect in their forced asymmetric simulations, where the amplitude of the imposed symmetry breaking of the flow controls the transition from α^2 to $\alpha\omega$-type dynamos.

In the present study, the magnetic Prandtl number Pm is equal to 5 in most simula-

tions and equal to 1 in simulation L (Table 4.2). However, Pm is expected to be much smaller than unity in planetary cores and we anticipate that this might affect the dynamo regime. Unfortunately, it is difficult to investigate the effect of small magnetic Prandtl numbers on the generation of hemispherical dynamos. Indeed, the magnetic Reynolds number is equal to $Re \cdot Pm$ and, therefore, exceeding the dynamo onset requires higher Reynolds numbers Re when decreasing Pm. For $Pm < 1$, simulations conducted at similar forcing as the strongly hemispherical dynamos obtained in this study are below the onset of dynamo action.

5.3 Symmetry breaking of the flow and low-dimensional model

We have shown that the equatorial symmetry breaking of the flow, measured by K_a/K_s, controls the hemisphericity of the dynamo. If the energy contained in antisymmetric modes is strong enough (i.e. K_a/K_s is larger than ~ 1), then we obtain hemispherical dynamos in which at least 75% of the total magnetic energy at the CMB is localized in one hemisphere.

The idea that symmetry breaking of the flow can play an important role in the dynamics of magnetic field reversals had already emerged from previously published studies on dynamo action in convective spherical shells (Li *et al.*, 2002; Nishikawa & Kusano, 2008), in full-sphere with mechanical forcing on the boundaries (Gissinger *et al.*, 2010), or in the von Kármán Sodium dynamo experiment (Monchaux *et al.*, 2009). The results presented in chapter 4, combined with other recent results obtained in the von Kármán dynamo experiment (Gallet *et al.*, 2012) or in parametrized kinematic α^2-dynamo models (Gallet & Petrelis, 2009), show that symmetry breaking of the flow can also generates hemispherical dynamos in which the magnetic field is spatially localized. The above observations converge towards the more general idea that flow-symmetry breaking is a universal control parameter of dynamo regimes. Low-dimensional models, i.e. based on interactions between a few hydrodynamic or magnetic modes, are generally useful to account for the effect of symmetry breaking, as illustrated in what follows.

Gallet & Petrelis (2009) have introduced a model based on the interaction between two magnetic modes, predicting that equatorial symmetry breaking of the flow can induce hemispherical dynamos. This theoretical framework is satisfactory as it connects the results discussed in the previous sections: emergence of antisymmetric flow components and generation of hemispherical dynamos. First, it is assumed that the large-scale axisymmetric magnetic field $\overline{\mathbf{B}}$ can be written at first order as

$$\overline{\mathbf{B}} = d(t)\overline{\mathbf{D}}(\boldsymbol{r}) + q(t)\overline{\mathbf{Q}}(\boldsymbol{r}), \tag{5.4}$$

where $\overline{\mathbf{D}}$ and $\overline{\mathbf{Q}}$ are axisymmetric dipolar and quadrupolar components of amplitude $d(t)$ and $q(t)$, respectively. Sufficiently close to the dynamo threshold, the dynamics of the magnetic field is likely to be governed by interactions between the two first unstable magnetic modes and equation (5.4) is expected to hold.

Then, considering only linear interactions between magnetic modes (i.e. neglecting the back reaction of the magnetic field on the flow through the Lorentz force), we obtain

the following equations for the amplitudes d and q:

$$\dot{d} = \sigma_d d + \alpha_d q, \tag{5.5}$$
$$\dot{q} = \sigma_q q + \alpha_q d, \tag{5.6}$$

where σ_d and σ_q are the growth rate of the modes $\overline{\mathbf{D}}$ and $\overline{\mathbf{Q}}$ when the flow is purely symmetric, while coefficients α_d and α_q originate from the antisymmetric flow component, which couples dipolar and quadrupolar magnetic modes in the induction equation. Indeed, when comparing equations (5.5)-(5.6) with the induction equation (2.5), it becomes intuitive that (σ_d,σ_q) represents the effect of magnetic diffusion and induction of magnetic field by symmetric flow components, while (α_d,α_q) represents the effect of induction of magnetic field by antisymmetric flow components. Therefore, we expect that

$$\sigma_d = \sigma'_d S + \gamma'_d, \tag{5.7}$$
$$\sigma_q = \sigma'_q S + \gamma'_q, \tag{5.8}$$
$$\alpha_d = \alpha'_d A, \tag{5.9}$$
$$\alpha_q = \alpha'_q A, \tag{5.10}$$

where S is the amplitude of symmetric flow components, A the amplitude of antisymmetric flow components, σ'_d, σ'_q, α'_d, α'_q, γ'_d and γ'_q are constant coefficients. Writing $d + iq = a\exp(i\Theta)$, the following equation for Θ is deduced from equations (5.5) and (5.6):

$$\dot{\Theta} = \mu_i + \nu_i \cos(2\Theta) - \nu_r \sin(2\Theta) \tag{5.11}$$

where $\nu_r = 1/2(\sigma_d - \sigma_q)$ measures the difference of growth rates, and the coefficients $\mu_i = 1/2(\alpha_q - \alpha_d)$ and $\nu_i = 1/2(\alpha_q + \alpha_d)$ are proportional to A and, hence, originate from the symmetry breaking of the flow. If the antisymmetric flow components are such that $\mu_i \gg \nu_i$, a regime of magnetic field reversals is obtained for sufficiently large value of μ_i as can be deduced from equation (5.11) (Petrelis & Fauve, 2008). On the contrary, if $\nu_i \gg \mu_i$, two stable solutions for Θ always exist and the magnetic field remains stationary. In the latter case, when increasing the symmetry breaking, the solutions progressively converge towards $\Theta_c = (\pi/4, 3\pi/4)$ if $\nu_i \geq 0$ and $\Theta_c = (-\pi/4, -3\pi/4)$ if $\nu_i \leq 0$, or equivalently towards $\overline{\mathbf{B}} \propto \overline{\mathbf{D}} \pm \overline{\mathbf{Q}}$. Assuming that $\overline{\mathbf{D}}$ and $\overline{\mathbf{Q}}$ form a large-scale dipole and a large-scale quadrupole, respectively, both aligned with the rotation axis, the solution $\overline{\mathbf{B}} \propto \overline{\mathbf{D}} \pm \overline{\mathbf{Q}}$ corresponds to a hemispherical magnetic field that merely cancels near one pole and reaches strong values near the other. Therefore, the above low-dimensional framework predicts that equatorial symmetry breaking of the flow can either induce reversing or hemispherical magnetic fields, depending on the structure of the antisymmetric flow.

Are our numerical results compatible with the general framework of the above low-dimensional model? First, the magnetic field has to be large-scale and multipolar dynamos that emerge at sufficiently high forcing (Rm or Ra_Q) do not meet this condition. Second, the axisymmetric magnetic field needs to be satisfactorily described by a decomposition of the form (5.4), which is indeed the case at first order in our hemispherical dynamos at intermediate forcing. Third, nonlinear interactions involving the Lorentz force need to play a secondary role. We checked that that our hemispherical dynamos meet this condition: the axisymmetric magnetic field induced in a kinematic dynamo (i.e. where the Lorentz force is shut down) is almost identical to the field generated in a complete

dynamo simulation.

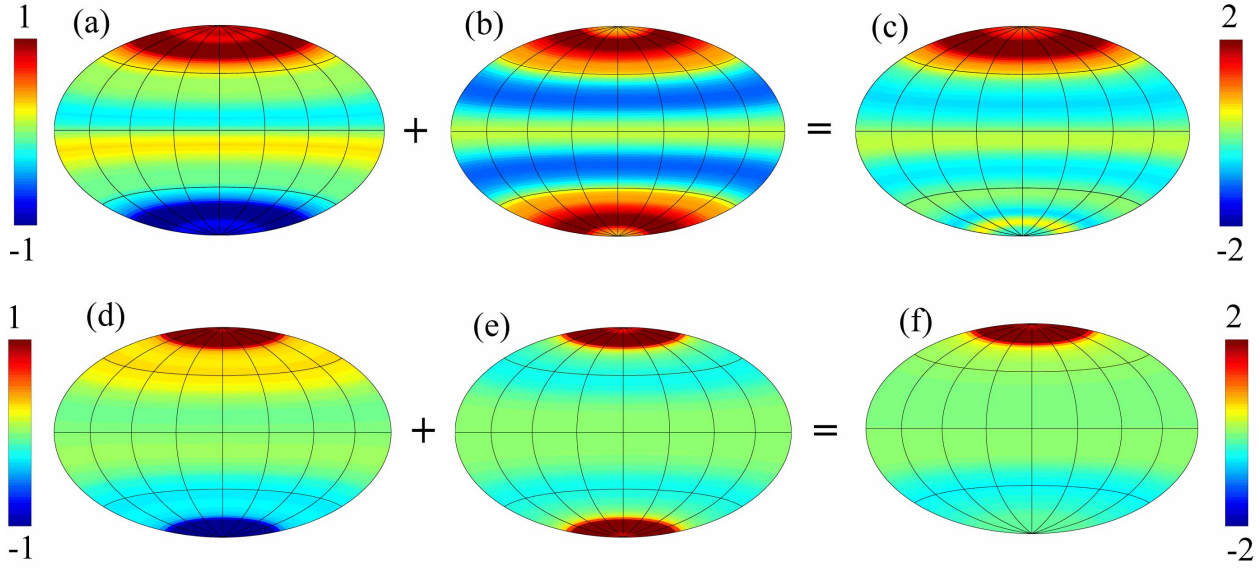

Figure 5.1: Axisymmetric radial magnetic field at the outer boundary and at a given time in (a,b,c) kinematic simulations where the Lorentz force is shut down and (d,e,f) a complete dynamo simulation at $E = 10^{-3}$, $Ra_Q = 10^{-3}$, $Pr = 1$, $Pm = 5$ (Hammer projections, fields are normalized by their root mean square at the outer boundary). (a) Most unstable dipolar magnetic field when the coupling between dipolar and quadrupolar modes is suppressed (for a purely symmetric flow). (b) Most unstable quadrupolar magnetic field. (c) Field resulting from the superposition of the normalized fields shown in (a) and (b). (d,e,f) Dipolar component, quadrupolar component and total field, respectively.

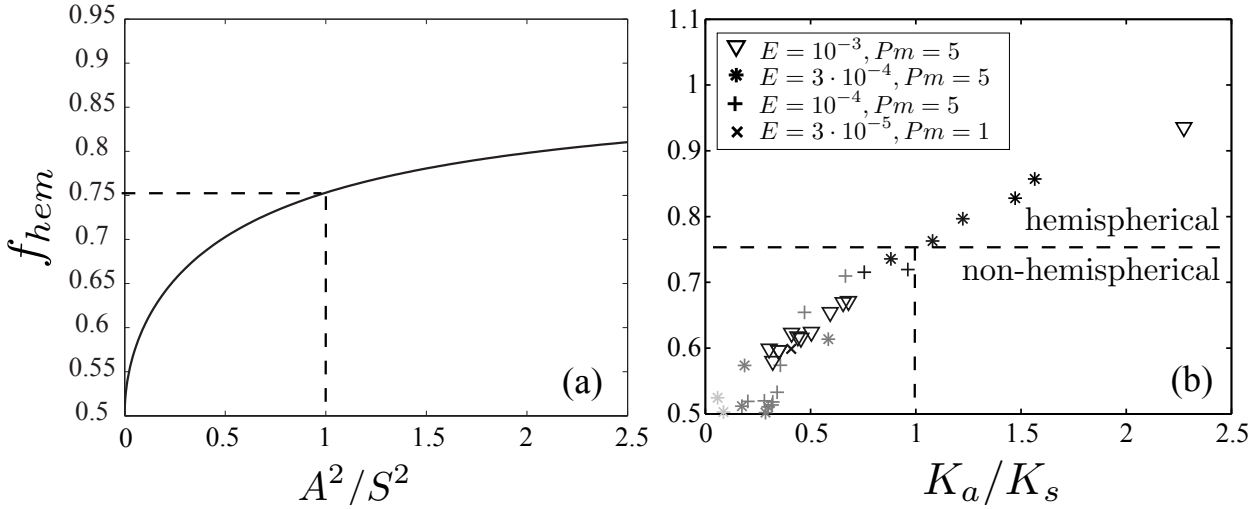

Figure 5.2: Hemisphericity factor f_{hem} as a function of the ratio of antisymmetric versus symmetric kinetic energy as predicted by the low-dimensional model (a) and in complete dynamo simulations (b). (a) Theoretical curves in the limit $\nu_i \gg \mu_i$ taking the modes $\overline{\boldsymbol{D}}$ and $\overline{\boldsymbol{Q}}$ shown in figure 5.1, for a constant value of the symmetric flow amplitude S, and with $\left[\alpha'_d + \alpha'_q\right] / \left[(\sigma'_d - \sigma'_q) + (\gamma'_d - \gamma'_q)/S\right] = 0.89$.

Considering a given hemispherical simulation that satisfies the above conditions, one can compute the most unstable magnetic modes induced by the purely symmetric flow component using kinematic dynamo simulations. In the example shown in figure 5.1, the axisymmetric components $\overline{\mathbf{D}}$ and $\overline{\mathbf{Q}}$ correspond to a large-scale dipole (figure 5.1(a)) and a large-scale quadrupole (figure 5.1(b)) whose superposition results in a hemispherical pattern (figure 5.1(c)), hence in qualitative agreement with the results from the corresponding complete dynamo simulation (figure 5.1(f)). In the limit $\nu_i \gg \mu_i$ (that eliminates reversing dynamos), the hemisphericity factor f_{hem} can be expressed as a function of A and S once $\overline{\mathbf{D}}$ and $\overline{\mathbf{Q}}$ are prescribed and for a given set of constant coefficients:

$$f_{hem} = \frac{1}{2} + \frac{2}{d/q + q/d} \int_{\Sigma_{ho}} \overline{\mathbf{Q}} \cdot \overline{\mathbf{D}} \mathrm{d}S \tag{5.12}$$

$$\text{where} \quad \frac{q}{d} = \tan\left[\frac{1}{2}\arctan\left[\frac{A}{S}\frac{\alpha'_q + \alpha'_d}{(\sigma'_d - \sigma'_q) + (\gamma'_d - \gamma'_q)/S}\right]\right] \tag{5.13}$$

where Σ_{ho} is the outer surface of the hemisphere with a stronger magnetic field. Figure 5.2(a) presents the evolution of the hemisphericity factor as a function of the equatorial symmetry breaking of the flow as predicted by (5.12)-(5.13) when using the most unstable modes $\overline{\mathbf{D}}$ and $\overline{\mathbf{Q}}$ shown in figures 5.1(a,b), assuming a constant value for S and when the value of the ratio $\left[\alpha'_d + \alpha'_q\right] / \left[(\sigma'_d - \sigma'_q) + (\gamma'_d - \gamma'_q)/S\right]$ is chosen such that $f_{hem} = 0.75$ for $(A/S)^2 = 1$. This figure illustrates both the advantages and limitations of the low-dimensional model: the main features of the numerical results (figure 5.2(b)) are reproduced since f_{hem} increases monotonically with $(A/S)^2$, although the detailed shape of the theoretical curve is not identical to that described by numerical results.

5.4 Geophysical implications

Our results indicate that hemispherical magnetic fields, at the CMB and at the surface of a Mars-like planet (figure 5.3), may be spontaneously induced by asymmetric convective flows in a rotating full-sphere, which represents the most plausible configuration for Mars' core when its dynamo was active. From such results, the most naive scenarios that can be proposed for the hemispherical magnetic field of Mars crust are depicted in figure 5.4: when the martian crust has formed and hence acquired its initial remanent magnetization, the Rayleigh number related to Mars' core was located in a region of parameter space where the flow was sufficiently asymmetric to generate hemispherical magnetic fields, which have been recorded on the martian crust. Two cases are possible: either the early crust formed before the cessation of the dynamo (figure 5.4(a)) or crust formation was active during the entire dynamo duration (figure 5.4(b)). In the latter situation the flow had to be sufficiently asymmetric at dynamo onset Rm_c for the dynamo to be hemispherical during its entire duration.

The above scenarios would be an attractive explanation for the hemispherical crustal magnetic field of Mars, satisfying the principle of parsimony since neither heterogeneous boundary conditions, as assumed by Stanley *et al.* (2008), Amit *et al.* (2011) and Dietrich & Wicht (2013), nor exogenic process responsible for partial demagnetization of the crust in the northern hemisphere, such as volcanic resurfacing (Connerney *et al.*, 2005), large impacts (Frey & Schultz, 1988) or a single giant impact (Andrews-Hanna *et al.*, 2008;

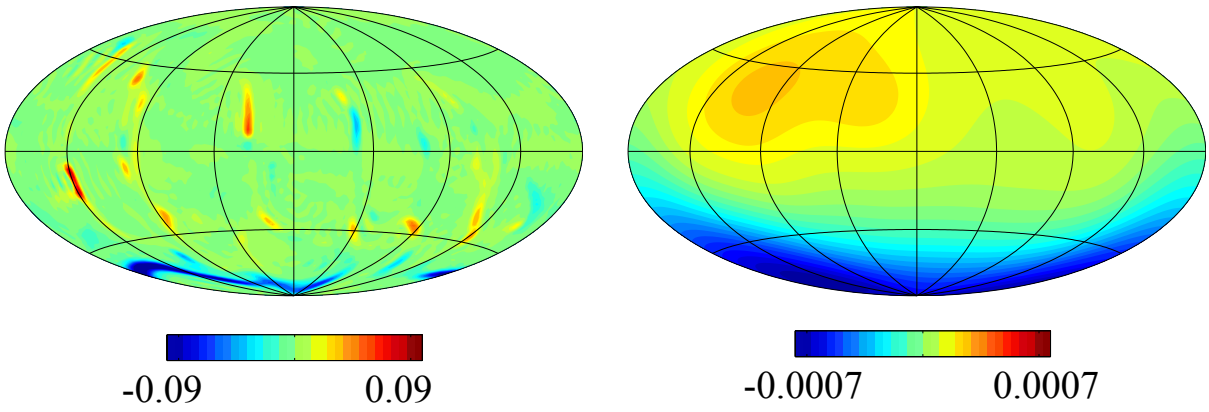

Figure 5.3: Snapshots of the radial magnetic field at the CMB (a) and at the surface of a Mars-like planet (b) obtained with the strongly asymmetric simulation G (parameters reported in Table 4.2, chapter 4) (Hammer projections).

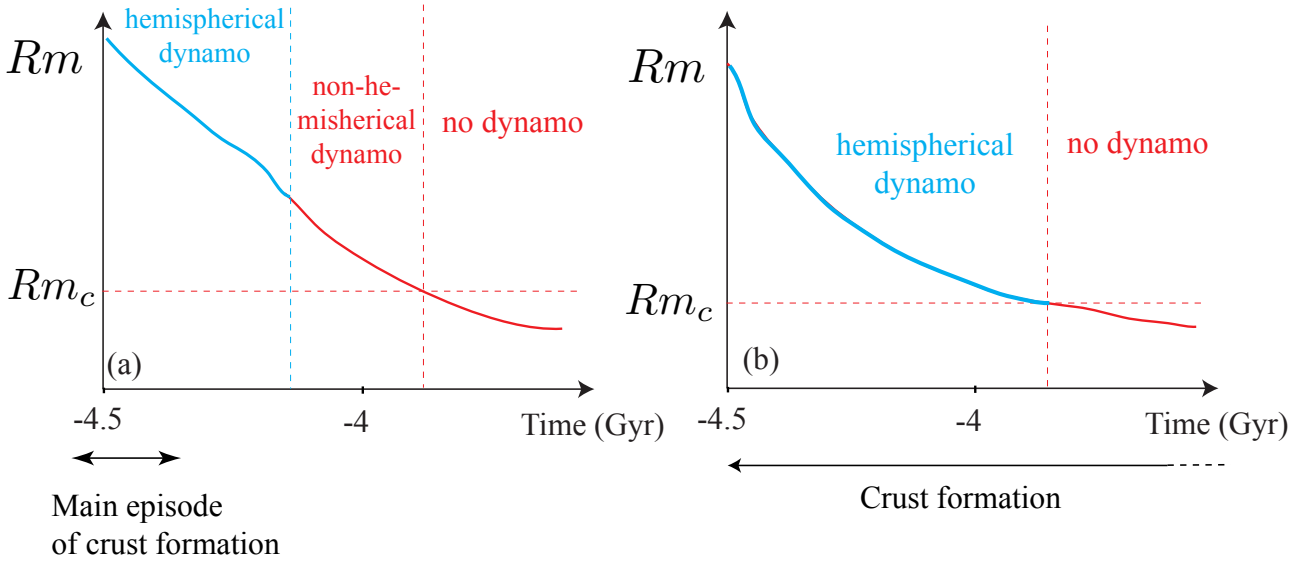

Figure 5.4: Qualitative scenarios that can be proposed to explain the hemispherical magnetic field of Mars crust: the flow was strongly asymmetric, inducing hemispherical dynamos (blue lines), during crust formation (black arrows). Rm is the magnetic Reynolds number and Rm_c its value at dynamo onset. (a) Much of the Mars crust formed before the cessation of the dynamo. (b) Crust formation lasted during the entire duration of the dynamo.

Marinova *et al.*, 2008; Nimmo *et al.*, 2008; Citron & Zhong, 2012), would be required. Below we discuss the applicability and limitations of the scenarios qualitatively depicted in figure 5.4.

For the specific mechanisms identified in the present study to be relevant to Mars' core, two conditions must be met: first, the past martian dynamo was in the asymmetric hydrodynamic regime (i.e. $Ra_Q \geq Ra_{Qt}$) and, second, flow-symmetry breaking K_a/K_s was sufficiently large to induce hemispherical dynamos.

The past martian dynamo may have reached the asymmetric regime if Ra_Q was at least larger than Ra_{Qt} when the dynamo was active. The scaling law (4.2) can be used to estimate Ra_{Qt} in Mars' core: considering plausible parameter values given in Table 5.1, we find that E is roughly within the range $5 \times 10^{-15} - 8 \times 10^{-14}$ in Mars' core and Ra_{Qt} within the range $5 \times 10^{-21} - 4 \times 10^{-19}$. Estimations of the past martian CMB heat flux highly depend on the mechanism of heat transfer which is considered. Considering a stagnant lid mantle convection the maximum heat flux is expected to be about 60 mW m^{-2} (Nimmo & Stevenson, 2000; Breuer & Spohn, 2003; Stevenson *et al.*, 1983) whereas if we consider an overturn after magma ocean crystallization it is about 600 mW m^{-2} (Elkins-Tanton *et al.*, 2005). Plate tectonics has been suggested for Mars but is not coherent with little remixing of crust and mantle as indicated by geochemistry. In addition Breuer & Spohn (2003) have shown that it is difficult to reconcile crust production required by geological constraints and the presence of a core-dynamo using a model that includes plate tectonics. We note that, in the case of plate tectonics, the maximum heat flux at the CMB would be of the same order as in the case of a stagnant lid regime ($\sim$ 100mW m^{-2}, Nimmo & Stevenson (2000)). It is important to underline that Ra_Q has to be estimated using the superadiabatic heat flux (the total heat flux minus the adiabatic heat flux). The adiabatic heat flux for Mars' core is estimated to be in the range 5-19 mW m^{-2} (Nimmo & Stevenson, 2000). Using the parameter values given in Table 5.1, one can estimate a plausible range of values for the maximum modified Rayleigh number Ra_{Qm}, in Mars' core. Considering convection underneath a single plate, Ra_{Qm} is within the range $2 \times 10^{-13} - 10^{-12}$ whereas with a model that supposes an overturn after magma ocean crystallization (Elkins-Tanton *et al.*, 2005), Ra_{Qm} is within the range $3 \times 10^{-12} - 10^{-11}$. These values are larger than Ra_{Qt} by more than seven orders of magnitude, suggesting that Mars' core could have been in the hydrodynamic asymmetric regime. Besides, in the case depicted in figure 5.4(b), another necessary condition is that $Ra_Q \geq Ra_{Qt}$ when $Rm = Rm_c$. Assuming that $Rm_c = O(100)$ (Christensen & Aubert, 2006), scalings laws for the dimensionless kinetic energy K as a function of Ra_Q (Christensen & Aubert, 2006; Aubert *et al.*, 2009) (discussed below) can be used to estimate the value of Ra_Q at dynamo onset (since $Rm = Pm \cdot K/E$). The resulting value is in the range $10^{-16} - 10^{-14}$, which is several orders of magnitude larger than Ra_{Qt}, indicating that the scenario depicted in figure 5.4(b) appears plausible.

In our numerical dynamo simulations, the CMB magnetic field is hemispherical if the equatorial symmetry breaking of the flow K_a/K_s is sufficiently large, typically larger than unity, and scaling laws for kinetic energies are useful at this stage in order to determine whether or not K_a/K_s was sufficiently high in Mars' core.
First, the scaling for the EAA kinetic energy $K_{0a} \propto Ra_Q$, in agreement with our numerical results, can be derived from dimensional analysis (Aurnou *et al.*, 2003). Thus,

Parameters	Plausible values for Mars
Acceleration due to gravity at the CMB, g_0 (m s^{-2})	~ 3
Core radius, r_o (km)	$1300 - 1700$
Density, ρ (kg m^{-3})	$7100 - 8300$
Thermal expansion coefficient, α (K^{-1})	$1.5 - 3 \times 10^{-5}$
Heat capacity, C_p (J kg^{-1}K^{-1})	$820 - 860$
Rotation rate (present), Ω (s^{-1})	7.1×10^{-5}
Kinematic viscosity, ν (m^2 s^{-1})	$\sim 10^{-7} - 10^{-5}$

Table 5.1: Plausible parameter values for Mars' core, after Nimmo & Stevenson (2000) and references therein for the first five parameters. The last parameter value is an estimation of ν in terrestrial cores (Funakoshi, 2010; de Wijs et al.*, 1998).*

it is expected to apply for Mars' core. Second, the validity of the viscosity-independent kinetic energy scaling ($\propto Ra_Q^{0.83\pm0.03}$) obtained from numerical simulations for the total kinetic energy K (Christensen & Aubert, 2006; Aubert *et al.*, 2009) or for the antisymmetric kinetic energy K_a (scaling (4.4)) is disputable since the Reynolds number does not exceed a few hundreds in numerical simulations*. However, a very similar scaling for non-axisymmetric flow components, such that kinetic energy is proportional to $Ra_Q^{0.8}$, is expected from theoretical arguments at large Reynolds numbers (the relevant regime for planetary cores), assuming that the Taylor-Proudman constraint is broken by inertia (e.g. Aubert *et al.* 2001; see also Jones (2011) for the derivation of this scaling).†

A few remarks can be drawn from the above reasonings:

- The ratio K_{0a}/K is proportional to $Ra_Q/Ra_Q^{0.8} \propto Ra_Q^{0.2}$, which is expected to be much smaller than unity in Mars' core with the plausible values listed above for Ra_{Qm}. Therefore, EAA modes were probably much weaker than other flow components in Mars' core and they could not be responsible for strong symmetry breaking as they are in our simulations. We emphasize that similar conclusions hold for EAA modes forced by heterogenous boundary conditions (Stanley *et al.*, 2008; Amit *et al.*, 2011; Dietrich & Wicht, 2013)‡.

- The ratio of the antisymmetric kinetic energy to the total kinetic energy K_a/K is expected to be independent of Ra_Q at sufficiently large forcing, meaning that

*King & Buffett (2013) have indeed shown that viscosity plays a significant role in simulations.

†An alternative scaling for the dimensional mean kinetic energy K in planetary cores is obtained by considering a balance between the Lorentz force, the buoyancy force and the Coriolis force (Starchenko & Jones, 2002), which predicts that $K \propto Ra_Q$. However, the latter scaling is not considered in the present discussion since the Lorentz force has a weak effect on kinetic energy in most published numerical dynamos (e.g. Christensen & Aubert, 2006; King & Buffett, 2013).

‡The scaling $K_{0a} \propto Ra_Q$ also holds in the presence of an asymmetric heat flux. One can show that the main difference will appear in the scaling prefactor which is expected to be a linear function of the ratio Q_a/Q_s, where Q_a and Q_s are the antisymmetric and symmetric heat flux, respectively. As the ratio Q_a/Q_s was not much larger than unity in Mars' core (Stanley *et al.*, 2008), EAA modes were likely to be weaks, even in the presence of an asymmetric heat flux at the CMB.

non-axisymmetric antisymmetric modes are not prevented from reaching large amplitude values, and hence allowing $K_a/K_s = O(1)$ at planetary parameter values. Unfortunately, giving the large uncertainties on the prefactor values in numerical scalings (Aubert *et al.*, 2009), or the proximity to the threshold Ra_{Qt} in the present study, no firm conclusion can be drawn concerning the value of K_a/K_s in Mars' core.

Finally, the above discussion has demonstrated that the specific dynamics that has been isolated in our dynamo simulations is not expected to dominate at planetary parameter values, although the general idea that spontaneous symmetry breaking of the flow can lead to hemispherical dynamos in planetary cores still holds and the scenarios depicted in figure 5.4 can not be ruled out. Similar limitations hold for asymmetric simulations forced by heterogeneous heat flux as in Stanley *et al.* (2008), Amit *et al.* (2011) or Dietrich & Wicht (2013). Although dynamo simulations are useful to explore dynamical regimes, retrieve scaling laws and isolate specific dynamical behaviors, quantitative comparisons of numerical results with geophysical data are not always legitimate giving the distance between planetary and simulation parameter values.

Chapter 6

Outlook

6.1 EAA circulation

EAA circulation deeply influences the flow in our strongly asymmetric simulations where it is the most energetic mode in the kinetic energy spectrum. It is also essential in the characterization of the oscillating and asymmetric flow regimes in dynamo simulations. Meanwhile, EAA flow components share the same symmetry properties as the most unstable modes at axisymmetric convection onset, as studied by Bisshopp (1958), Roberts (1965) and Bisshopp & Niiler (1965). Therefore, the following question arises: Are the EAA modes that emerge in our simulations somewhat inherited from the first unstable axisymmetric modes? In previously published studies of convection in spherical systems, heat is mainly carried away in a direction perpendicular to the rotation axis by modes inherited from the Rossby waves emerging at convection onset (Busse, 1970). On the contrary, the first unstable axisymmetric modes carry heat away along the rotation axis, which makes their dynamics somewhat analog to convection in a rotating plane layer or inside the tangent cylinder in spherical shells, as already mentioned in chapter 2 (see figure 2.7 and section 2.3.4.3). Hence, a closely related question to that mentioned above is whether modes carrying heat away along the rotation axis may play a significant role in the overall dynamics.

Besides, as discussed in section 5.1.2, the truly unexpected feature of our simulations is the strongly asymmetric temperature profile, with high temperature in one hemisphere and lower temperature in the other, responsible for strong EAA zonal flows that break the Taylor-Proudman constraint. Hence, another question related to EAA modes is: How does this strongly asymmetric EAA temperature profile arise?

A study dedicated to EAA circulation is currently underway in order to address the above questions. Our preliminary results show that, at sufficiently high Ekman numbers, the nonlinear EAA modes are identical to the first unstable axisymmetric modes (figure 6.1), whereas, at lower Ekman numbers, the EAA circulation is dominated by large-scale zonal flows that are dynamically different from the first unstable axisymmetric modes (figure 6.2). Then, we write the heat budget of the lower hemisphere to isolate the different terms that contribute to the net production of large-scale EAA temperature in nonlinear simulations. We find that the meridional EAA flow, which involves components inherited from the first unstable axisymmetric modes, is responsible for much of the production of

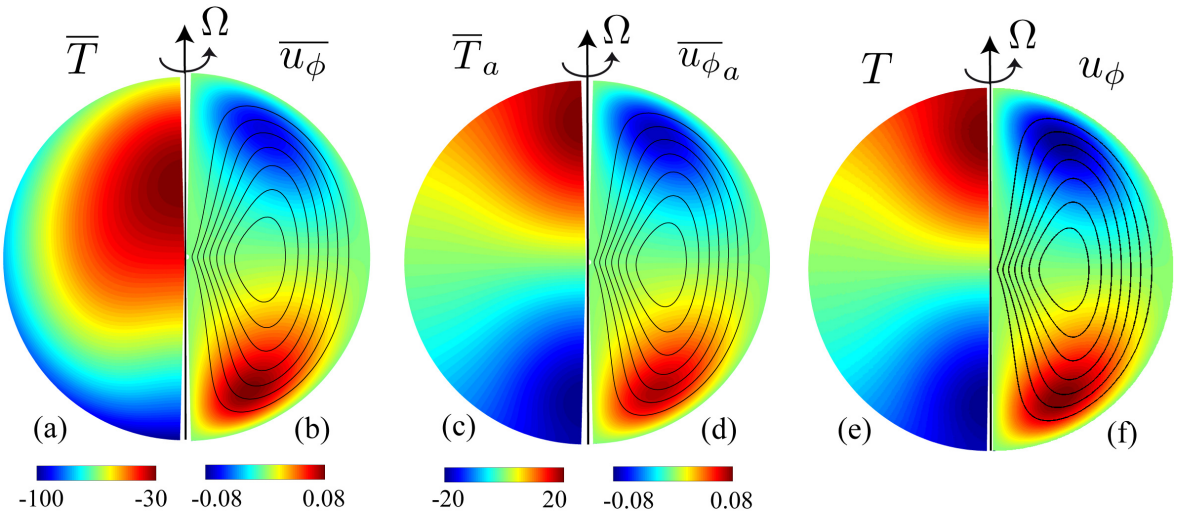

Figure 6.1: (a,b,c,d) Snapshots of (a) axisymmetric temperature (colors), (b) axisymmetric azimuthal velocity, (c) EAA temperature, and (d) EAA azimuthal velocity in a full-sphere nonlinear simulation at $E = 10^{-2}$, $Ra_Q \approx 1.5 Ra_{Qc}$. (e,f) Patterns of (e) temperature and (f) azimuthal velocity at axisymmetric convection onset at $E = 10^{-2}$ (same boundary conditions as in the nonlinear simulation). Solid lines in (b), (d) and (f) show the meridional circulation that rotates clockwise. The amplitude of the meridional circulation in (b) varies between 0 and 0.08.

EAA antisymmetric temperature in all our asymmetric simulations.

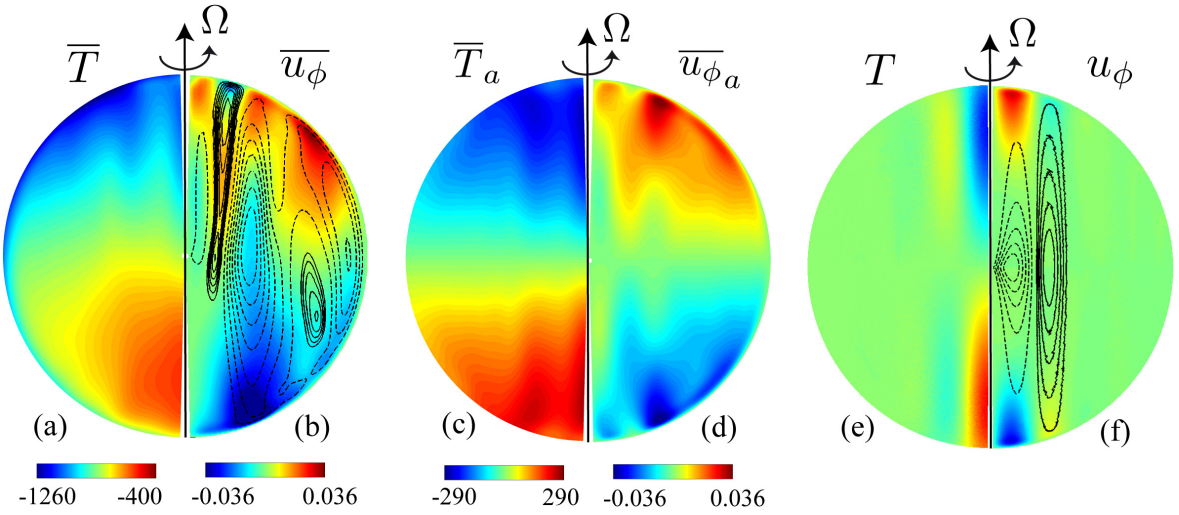

Figure 6.2: (a,b,c,d) Snapshots of (a) axisymmetric temperature (colors), (b) axisymmetric azimuthal velocity, (c) EAA temperature, and (d) EAA azimuthal velocity in a full-sphere nonlinear simulation at $E = 3 \times 10^{-4}$, $Ra_Q \approx 21 Ra_{Qc}$. (e,f) Patterns of (e) temperature and (f) azimuthal velocity at axisymmetric convection onset at $E = 3 \times 10^{-4}$ (same boundary conditions as in the nonlinear simulation). Solid and dashed lines in (b) and (f) show the meridional circulation that rotates clockwise and anticlockwise, respectively. The amplitude of the meridional circulation in (b) varies from values close to 0.01 near the axis in the northern hemisphere or in the Ekman boundary layer to values of order 0.003 in the rest of the sphere.

6.2 Towards an understanding of dynamical regimes and transitions

6.2.1 Emergence of antisymmetric modes

Up to know, we focused on the statistically stationary regime of our simulations. A possible development would be to investigate in more detail the secondary instability mechanism associated with the emergence of antisymmetric flows at $Ra_Q = Ra_{Qt}$ in order to recover, from theoretical reasoning, the scaling law (4.2) obtained numerically for Ra_{Qt} as a function of E. In particular, we have noticed that, in a given simulation, antisymmetric modes start to grow on the symmetric basic state after a few advective time scales, only when the pattern of EAA temperature and, hence, of EAA zonal flow start to be large-scale. The so-called $2-1/2$ dimensional approach would be adapted to study the secondary destabilization mechanism and especially the role played by large-scale EAA modes. Indeed, in this approach, only the axisymmetric component $m = 0$ and one non-axisymmetric azimuthal wavenumber are retained in the calculation (Morrison & Fearn, 2000; Cupal *et al.*, 2002), allowing for reduction of the system complexity while retaining essential ingredients.

At parameter values corresponding to the strongly asymmetric simulation B used in chapter 4 (parameters reported in Table 4.1), the ratio K_a/K_s is equal to about 0.16 when a free-slip boundary condition is imposed rather than no-slip. This value is significantly lower than in simulation B where $K_a/K_s \approx 0.85$, suggesting that free-slip boundary conditions favor strongly symmetric flows. However, we find that the absolute values of K_{0a} and K_a are very similar in both simulations. The main difference arises from the amplitude of symmetric zonal flows, which are about three times stronger in the free-slip simulation, where they contain about 70% of the total kinetic energy, whereas they represent only 30% of the total energy in the no-slip simulation B. The symmetric zonal flows are strongly z-independent in this free-slip simulation and we therefore hypothesize that the low K_a/K_s value is due to particularly strong Reynolds stresses-induced zonal flows rather than diminished antisymmetric flow components. Further investigations with free-slip boundary conditions are required, in particular to obtain scaling laws for the different energy contributions.

At similar convective power as in simulation B but with a lower Prandtl number equal to 0.1, the ratio K_a/K_s is equal to about 0.15, again a value significantly lower than in simulation B. This suggests that low Prandtl numbers favor strongly symmetric convection, although no firm conclusion can be drawn at this stage. Besides, in planetary cores that have nucleated an inner core, as the Earth, the Prandtl number associated with compositional convection is expected in the range $100-1000$ (Poirier, 1988; Vocadlo *et al.*, 2000). Therefore, a systematic investigation of the role of the Prandtl number on the emergence of antisymmetric modes in rotating shells and spheres would probably be legitimate.

6.2.2 Other regimes and transitions

We have shown in chapter 4 that the equatorial symmetry breaking of the flow controls the emergence of hemispherical dynamos and the equipartition in dipolar and quadrupolar

magnetic energy in our simulations (figure 4.20). We have also discussed in chapter 5 the significance of this result with respect to other recent experimental, numerical and theoretical results, which converge towards the general idea that symmetry breaking of the flow is a main control parameter of dynamo regimes. However, the role of symmetry breaking of the flow has received less attention in the geophysics community and it can be hypothesized that other properties of the magnetic field in dynamo simulations are controlled by equatorial symmetry breaking of the flow.

- First, it remains to be tested whether the emergence of antisymmetric modes may control the transition from dipole-dominated dynamos to multipolar dynamos. A systematic numerical study using adapted output quantities would test this scenario in a straightforward way.

- Second, the low-dimensional framework introduced by Gallet & Petrelis (2009) predicts that symmetry breaking of the flow can alternatively induce hemispherical dynamos or magnetic field reversals, depending on the structure of the antisymmetric flow. Thus, investigating the role played by antisymmetric flow components in reversing numerical dynamos would be a natural development to the present numerical study. It has been shown that the breaking of the equatorial symmetry of the flow is indeed connected with reversals (Li *et al.*, 2002) and controls the reversal frequency (Gissinger *et al.*, 2012) in some isolated direct numerical simulations of convection and dynamo action in shells, a result which can be predicted by low-dimensional models (Petrelis & Fauve, 2008; Petrelis *et al.*, 2009; Gissinger *et al.*, 2012). Meanwhile, Petrelis *et al.* (2011) have suggested that geomagnetic reversal frequency has been correlated with equatorial symmetry of continent distribution during the past 300 Myrs. Continent location is intimately related to the heat flux pattern at the CMB, known to affect the reversal frequency in dynamo simulations (e.g. Glatzmaier *et al.*, 1999; Olson *et al.*, 2010, 2013). Investigating the following questions could help to bridge the gap between paleomagnetic, numerical and low-dimensional results:
  Is the equatorial symmetry of the CMB heat flux a universal control parameter of reversal frequency in convective dynamos or does it affect reversal frequency only in a narrow region of parameters space? Does the geometry of the antisymmetric CMB heat flux affects the reversal frequency? Was reversal frequency influenced by equatorial symmetry of CMB heat flux in the past 300 Myrs?
  A systematic numerical study can be combined with more specific simulations of the geodynamo driven by mantle convection to investigate the above questions.

We have already mentioned that it remains controversial whether the Lorentz force may cause departures from geostrophy in self-sustained dynamos and what parameter would control this transition. Such a regime would strongly affect the flow pattern and amplitude and, therefore, would have major implications for the dynamics of planetary cores. King & Buffett (2013) showed that the kinetic energy is rather injected at a viscous scale in most numerical simulations, suggesting that the Taylor-Proudman constraint is broken by viscosity rather than Lorentz force, in agreement with the weak influence of magnetic field on the flow reported by Soderlund *et al.* (2012). More recently, Hori & Wicht (2013) studied convection and dynamo action in a configuration that favors strongly asymmetric flows (small inner sphere and zero buoyancy flux at the inner boundary), and

they demonstrated the existence of a *strong field* solution branch on which the magnetic field has a first order impact on the flow structure: the strongly asymmetric flow is suppressed by the presence of a strong self-sustained magnetic field, while the dominant flow length scales are influenced by the Lorentz force. We checked that this strong field branch is also reached in the full-sphere configuration considered in the present study when starting the simulation from a strong initial magnetic field. Therefore, a systematic study that includes full-sphere simulations located on the strong field branch could be used to investigate the role of the Lorentz force in dynamo simulations and, more precisely, to identify the relevant paramater controlling the transition towards a regime where the Taylor-Proudman constraint is broken by the Lorentz force.

6.3 Low-dimensional models

Taking the example of hemispherical dynamos, we have demonstrated in section 5.3 that low-dimensional models can satisfactorily account for the main dynamical behaviors obtained in direct numerical simulations at intermediate forcing, although detailed features will not be recovered. Therefore, direct numerical simulations and low-dimensional models are two complementary approaches: the former is used to obtain complete solutions of the fundamental equations while the latter may help to comprehend specific dynamical behaviors identified in numerical simulations and suggest relevant directions for the analysis of numerical results. Below, we introduce two possible investigations that aim at further exploring the advantages and limitations of low-dimensional models in the context of core dynamics.

The oscillating regime, characterized by chaotic oscillations and reversals of the EAA flow component (chapter 4), can possibly be accounted for by a low-dimensional analysis. Indeed, we have already identified the series of events involved in a given oscillation: emergence of an EAA zonal flow, generation of an azimuthal magnetic field that breaks Ferraro's law of corotation, growth of a magnetic tension force that tends to oppose the EAA flow component and eventually restores the initial symmetric state. Inspired from such a scenario, one could formulate a parametrized model formed of several amplitude equations, one for each field involved in an oscillation, and making use of their symmetry properties to simplify the equations. Then, the detailed study of the resulting dynamical system could help understanding the dynamics observed in our numerical simulations. In particular: Does the resulting model predict that an oscillating regime should first appear at $Ra_Q = Ra_{Qt}$, while eventually disappearing at higher convection forcing?

We have shown that, as soon as the magnetic field is dominated by large scales, hemispherical dynamos can be satisfactorily accounted for by the low-dimensional model introduced by Gallet & Petrelis (2009). However, this low-dimensional model becomes irrelevant at sufficiently high forcing of convection, especially in the multipolar regime where the magnetic field is dominated by small scales. Similarly, reversals are spatially and temporally complex in some convective dynamos (Aubert *et al.*, 2008), suggesting that numerous magnetic and hydrodynamic modes are involved in the dynamics, whereas other simulations at high magnetic Prandtl numbers and intermediate Ekman numbers (as in Olson *et al.* (2010) or Driscoll & Olson (2009)) appear to involve fewer modes. Petrelis *et al.* (2009) and Gissinger *et al.* (2010) argue that low magnetic Prandtl numbers favor low-dimensional behaviors in self-sustained dynamos. The magnetic Reynolds

number is also expected to be a main control parameter since the number of unstable magnetic modes increases with Rm.
Therefore, quantifying the transition from low to high-dimensional behaviors and identifying the main control parameters for this transition, could provide important information concerning the dimensionality of planetary dynamos and the ability of low-dimensional models to reproduce the dynamics of geomagnetic reversals.

6.4 Other geophysical applications?

6.4.1 Earth

Thermal evolution models integrated backward in time provide constraints on the age of the inner core, but the resulting range of plausible values is broad, owing to the large uncertainties on the total heat flux at the CMB and on the amount of radiogenic heating in the Earth's core. In the absence of radioactive elements, the inner core age is in the range $0.5-1.5$ Gyr (Labrosse *et al.*, 2001), or even smaller as suggested by the high values recently found for the thermal conductivity in the core (Pozzo *et al.*, 2012; de Koker *et al.*, 2012) which may require a higher cooling rate to power the geodynamo. This age can be extended to 3 Gyr if radioactive elements are present (Labrosse *et al.*, 2001). Meanwhile, inner core nucleation is likely to have occurred at a time covered by paleomagnetic data (Tarduno *et al.*, 2010; Biggin *et al.*, 2011). Then, the following question arises: May paleomagnetic data carry a signature of inner-core nucleation?
To investigate this question, one may use spherical-shell simulations in a region of Earth-like dynamo behavior (Christensen *et al.*, 2010) and then progressively decrease the inner sphere size to a full-sphere configuration as used in the present manuscript. Then, diagnostic quantities that can be extracted from paleomagnetic data would be computed. The study by Aubert *et al.* (2009) suggests that magnetic field intensity is not a relevant indicator of inner core nucleation but the frequency of reversals, as deduced from the Geomagnetic Polarity Time Scale for the first few hundred years (Ogg, 2012) or indicated by the percentages of paleomagnetic studies showing reversals for more distant times (Roberts & Piper, 1989), might be affected by the absence or presence of an inner core.

6.4.2 Mercury

Recent data from the MESSENGER spacecraft suggest that the internal magnetic field of Mercury is substantially hemispherical: it can be describe by the superposition of an axial dipole and an axial quadrupole, such that $g_2^0/g_1^0 \approx 0.4$ (Anderson *et al.*, 2011) where g_1^0 and g_2^0 are the Gauss coefficients measuring the amplitude of the axisymmetric dipole and quadrupole components, respectively. Other observations that need to be accounted for by dynamo models are the weak amplitude of Mercury's magnetic field (100 times weaker than on the Earth, Connerney & Ness, 1988) and a tilt smaller than 3% (Anderson *et al.*, 2011). Besides, thermal evolution models predict that Mercury's core is thermally stratified, implying that the dynamo is necessarily powered by compositional convection associated with metal solidification (Christensen, 2006; Hauck *et al.*, 2004).

A multipolar compositional dynamo generated below a stratified layer (Christensen, 2006; Christensen & Wicht, 2008) explains the weakness of Mercury's field while, in a given simulation, the dipole tilt and the ratio g_2^0/g_1^0 vary continuously between zero and high values, as a result of the multipolar nature of the magnetic field. This scenario implies that the small dipole tilt and the strong quadrupole component measured at Mercury's surface are one possible transient state explored by the core dynamo. Inspired from the numerical results presented in this manuscript, on can look for an alternative scenario in which a large-scale (i.e. non-multipolar) hemispherical magnetic field would be generated by strongly asymmetric flows in Mercury's core. In this case, the small dipole tilt and the strong value for g_2^0/g_1^0 may be permanent features in a given simulation, in contrast with the model of Christensen (2006) and Christensen & Wicht (2008). Solidification of metal at the ICB, as in the Earth's core, favors strongly symmetric flows as shown in the present manuscript. However, a snowing core regime, where dense iron-rich solids nucleate at specific depth in the outer core and sink towards the center due to gravity, has been suggested for Mercury (Chen *et al.*, 2008). The effect of such a regime has been investigated using a rather larger inner core in Vilim *et al.* (2010), where it is shown that a state with two snow layers (the most likely scenario according to Chen *et al.* 2008) generates weak magnetic fields compatible with those observed on Mercury. A similar model, combined with a small or absent inner core as in the present manuscript, could produce weak hemispherical magnetic fields, with permanently small dipole tilt and strong g_2^0/g_1^0 ratio. However, the latter scenario requires a very specific structure and solidification regime for Mercury's core and, hence, is not parsimonious. In summary, further developments of our results to Mercury's dynamo are possible, but the main difficulty is to formulate a model that better explains the observations, while being as parsimonious as existing models.

Part II

Experiments on the fragmentation of a buoyant liquid volume in another immiscible liquid

Most of the material presented in this part of the manuscript is included in a research article that has been submitted to *Journal of Fluid Mechanics* (currently at the revision stage). Movies and their captions can be found at the following link:
http://www.ipgp.fr/ landeau/public/MoviesPhD/MoviesPartII.zip.

Chapter 7

Introduction

Buoyancy-driven fragmentation of one liquid in another immiscible liquid likely occurred on a massive scale during the formation of the terrestrial planets, as already developed in the main introduction (§1.2). Less violent but still dramatic present-day analogs of this phenomenon include sudden releases of petroleum into the ocean through well discharges, such as occurred in 2010 during the Deepwater Horizon disaster (McNutt *et al.*, 2012; Reddy *et al.*, 2012; Camilli *et al.*, 2012).

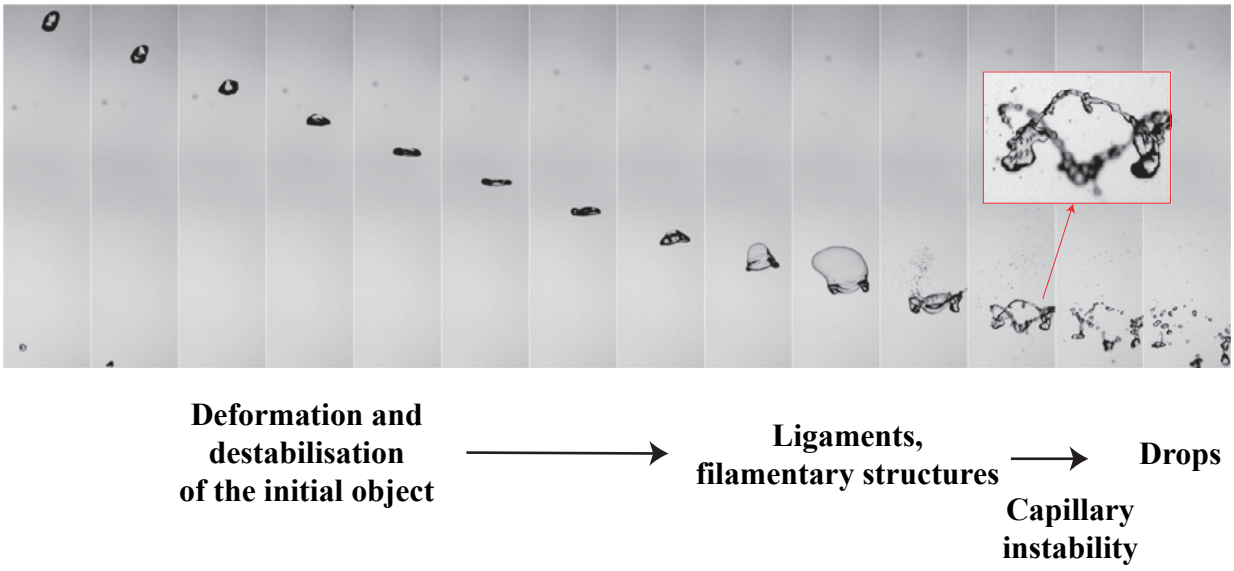

Figure 7.1: Typical sequence of steps involved in a fluid fragmentation process. Water drop falling in an ascending stream of air (modified from Villermaux & Bossa, 2009). The sequence includes deformation of the initial drop which flattens into a pancake shape, formation of liquid ligaments (a toroidal rim collects much of the initial drop mass), destabilization of the rim (highlighted in the inset), leading to disjointed drops distributed in size. Time interval of 4.7 *ms,* $We \approx 600$.

Most fluid fragmentation processes involve a regular sequence of steps (figure 7.1), including deformation or destabilization of the initial mass, formation of filamentary structures called liquid ligaments, breakup of ligaments usually involving capillary instabilities (e.g. Hinze, 1955; Marmottant & Villermaux, 2004; Villermaux & Bossa, 2009). The

destabilizing mechanisms generally set the mean size of the resulting drops, whereas ligament dynamics plays a dominant role in determining the resulting drop size distribution (Marmottant & Villermaux, 2004; Bremond & Villermaux, 2006; Villermaux & Bossa, 2009, 2011). A principal control parameter in any fluid fragmentation process is the Weber number We, which measures the relative importance of the dynamic pressure and the capillary restoring pressure. Breakup, the final fragmentation stage, is usually divided in *primary* and *secondary breakup*. Primary breakup refers to the stage where the initial liquid volume divides into several disconnected blobs or drops. If the Weber number of the resulting blobs (based on the blob size and blob velocity) is larger than the critical value for breakup We_c, secondary breakups occur. The critical Weber number We_c is generally of order 10 but it varies with the flow regime in the surrounding fluid, especially with the Reynolds number (Hinze, 1955). Another main control parameter is the Ohnesorge number Oh, which measures the importance of viscous forces versus interfacial forces and inertia. Very large Weber and Reynolds numbers and Oh much smaller than 1 are the relevant regimes for planetary formation.

Fragmentation of a finite volume of liquid at low Oh has been extensively studied in air (reviewed in Pilch & Erdman, 1987; Faeth *et al.*, 1995; Gelfand, 1996; Guildenbecher *et al.*, 2009; Theofanous, 2011). A rich variety of fragmentation regimes has been identified, including *vibrational breakup*, *bag breakup*, *multimode breakup*, *shear breakup*, *catastrophic breakup* (the terminology varies from one study to the other). Recently, Theofanous *et al.* (2004) and Theofanous & Li (2008) have proposed another categorization based on only two main fragmentation regimes : the *Rayleigh-Taylor (RT) piercing* regime, in which early deformations result from Rayleigh-Taylor instabilities (RTI), which appear when an interface between two fluids of different density is subjected to an acceleration directed towards the lighter fluid, and the *shear-induced entrainment* regime, interpreted as the suppression of RTI due to straining motions associated with the global shear. In general, the Weber number is the main control parameter governing transitions between the different fragmentation regimes.

Fragmentation of a buoyant liquid volume at density ratio of order one (i.e. in a liquid-liquid system) has received less attention. The maximum Weber numbers reached in three dimensional numerical simulations (Ichikawa *et al.*, 2010) of the breakup of drops falling in another immiscible liquid is about $10 - 15$ (figure 7.2(a)). Axisymmetric simulations reach higher Weber numbers and are useful to compute the early deformations of a blob falling under gravity (Han & Tryggvason, 1999; Samuel, 2012; Ohta & Sussman, 2012) or impulsively accelerated (Han & Tryggvason, 2001) in another liquid. However, such simulations do not capture the entire fragmentation process since ligament formation and breakup are inherently non-axisymmetric. Baumann *et al.* (1992) have conducted finite volume experiments in immiscible liquid-liquid systems at Weber numbers ranging from 0.3 to 11000. Oh is of order one or larger in most of their experiments and only two satisfy $We \geq 100$ and $Oh \ll 1$. Baumann *et al.* (1992) focus on viscous immiscible vortex rings (figure 7.2(b), upper panel) that form at $Re \leq 61$. Instabilities developing on these vortex rings are interpreted as RTI (figure 7.2(b), lower panel). Several experimental studies of drop breakup in liquid-liquid systems due to shock-induced flows have reported drag and breakup time measurements, summarized in Pilch & Erdman (1987) and Gelfand (1996). Among those studies, Patel & Theofanous (1981) show that their breakup time data are consistent with drop piercing by RTI. Yang & Yang (1990) identify a regime where the drop volume grows by turbulent entrainment.

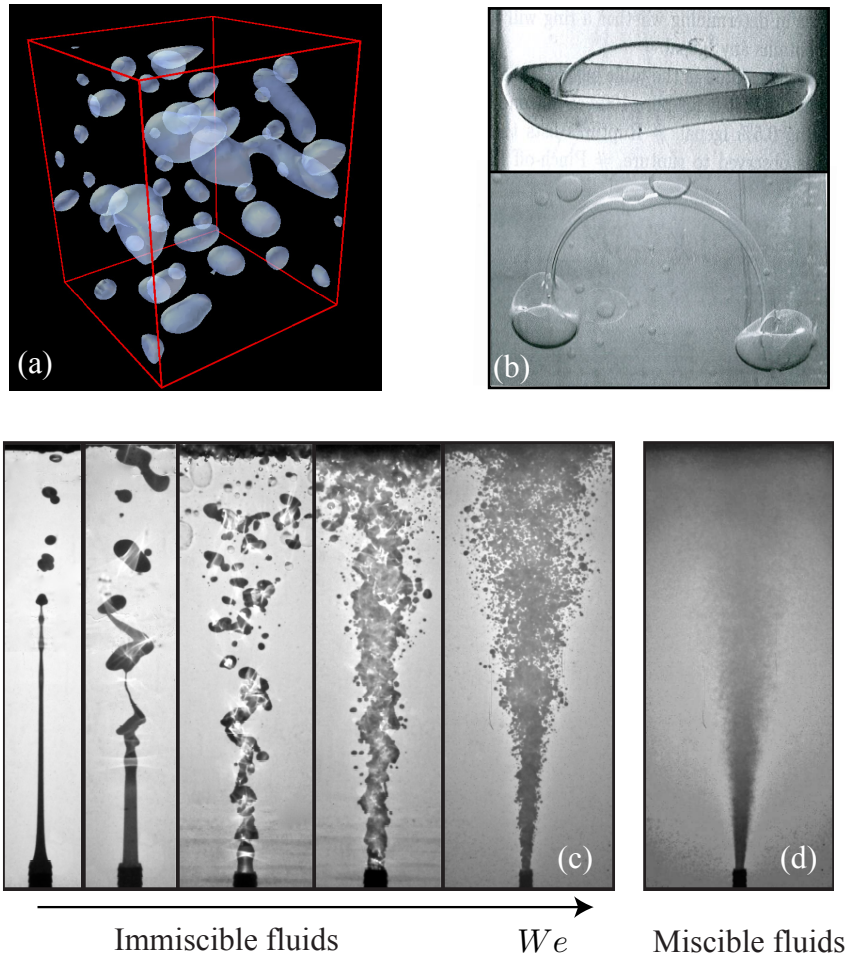

Figure 7.2: Fragmentation in liquid-liquid systems. (a) Falling drops of liquid in another immiscible liquid, numerical simulation, $We \gtrsim 15$ (Ichikawa et al.*, 2010). (b) Immiscible vortex ring (upper panel) and its destabilization (lower panel), $We \approx 570$, (Baumann* et al.*, 1992). (c,d) Forced plumes (Deguen* et al.*, 2011) with (c) immiscible fluids and (d) miscible fluids. The Weber number is progressively increased in (c).*

At large scales, immiscible liquid-liquid plumes (Deguen *et al.*, 2011) and immiscible liquid-liquid coaxial jets (Charalampous *et al.*, 2008), at large Weber and Reynolds numbers, are morphologically similar to their miscible equivalents (figures 7.2(c,d)). This suggests that integral models developed for miscible turbulent flows, including models of *turbulent thermals* and *vortex rings*, can describe the dynamics of immiscible flows.

In miscible fluids, a finite buoyant mass is called a *thermal* when its impulse originates entirely from the buoyancy force, and a *buoyant vortex ring* when an initial momentum is allowed. As pointed out by Turner (1957, 1964), a thermal can be regarded as a special case of a buoyant vortex ring. The more general term *vortex ring* refers to a ring-shaped structure formed by closed-loop vorticity lines. At high Reynolds numbers, the dynamics of turbulent thermals with small or large density differences (Morton *et al.*, 1956; Wang, 1971; Escudier & Maxworthy, 1973; Baines & Hopfinger, 1984; Thompson *et al.*, 2000) and non-buoyant vortex rings (Maxworthy, 1974) is successfully described using the concept of turbulent entrainment, originally proposed by Taylor (1945) and Morton *et al.* (1956),

who hypothesized that the rate of growth of a turbulent buoyant mass is proportional to its velocity and surface area.

The concept of turbulent entrainment has been used to describe the dynamics of two-phase flows in which one phase is dispersed in the other in the form of solid particles (Rahimipour & Wilikinson, 1992; Bush *et al.*, 2003) or air bubbles (Milgram, 1983; Leitch & Baines, 1989; Bettelini & Fannelop, 1993). However, the turbulent entrainment concept applied to immiscible systems that are initially non-dispersed has received less attention. It has been used to describe the dynamics of air jets in liquid (Weimer *et al.*, 1973; Loth & Faeth, 1989, 1990). Epstein & Fauske (2001) apply this concept to various liquid-gas and liquid-liquid flows and they develop an erosion model of a liquid drop immersed in a gas or another liquid with an initial velocity lag. They argue that their model is consistent with published data of total breakup time.

In this part of the manuscript we describe results of a systematic experimental study on the fragmentation of a finite liquid volume into lighter immiscible liquid at low Oh, at large Reynolds numbers ($Re \geq 10^3$ in most experiments) and for Weber numbers up to $\sim 10^3$. Our main objective is to characterize the different fragmentation regimes in parameter space. Two experimental configurations are used. In the first, the velocity of the released fluid originates entirely from the density difference between the two immiscible fluids (immiscible equivalent of thermals). In the second, an initial excess in velocity is introduced (immiscible equivalent of buoyant vortex rings). The experimental apparatus and techniques are described in chapter 8 and the results are presented in chapter 9. In section 9.1 we study the early stages of evolution in terms of velocity and deformation. The different fragmentation regimes are characterized in §9.2 from the study of the subsequent evolution, prior to capillary instabilities and breakup. Results on ligament formation and primary breakup are reported in §9.3. At sufficiently high Weber numbers, the flow reaches a turbulent regime whose dynamics are compared, in §9.4, with predictions from a model based on the concept of turbulent entrainment and on an analogy with miscible thermals and vortex rings. Chapter 10 presents a discussion of experimental results and geophysical implications. Finally, further investigations are suggested in chapter 11.

Chapter 8

Experimental procedure

8.1 Experimental set-up

The experimental set-up is shown in figures 8.1(a,b). A tank of width 25cm and height 50cm is filled with a low viscosity silicone oil, referred to as the ambient fluid in the following. A denser fluid (detailed below), immiscible in oil, is held in a vertically oriented plastic tube that is closed at the lower extremity by a latex membrane. The denser fluid is released by rupturing the membrane with a needle. The rupture lasts less than 0.04s. The volume of released fluid V is such that the height of fluid in the tube is equal to the tube internal diameter D. Six tubes are used, with D ranging from 1.28cm to 7.62cm. In the Immersed configuration (figure 8.1(a)) the tube is initially immersed in the ambient fluid and it is initially held at the surface of the ambient fluid in the Surface configuration (figure 8.1(b)).

The systematic study has been conducted using backlighting as depicted in figure 8.1(d). A blue dye (food coloring) is added in the released fluid. The flow is made visible by backward illumination through a diffusive screen and recorded by a color video camera at 24 frames per second. Other flow visualization images are obtained using a shadowgraph technique (figure 8.1(e)). The released fluid is heated up to about 35°C. A backward collimated light goes through the tank and projects information on a viewing screen, making visible gradients of refractive index which are caused by temperature gradients. Finally, images are also obtained using light-induced fluorescence (figure 8.1(f)). The experimental apparatus is illuminated from the side by a light sheet and a fluorescent dye (rhodamine) is added to the released fluid, imaging a cross section of the falling fluid. The light sheet, whose thickness varies from 5 mm to 7 mm inside the tank, is produced using a flash lamp and a black, opaque screen with a narrow vertical opening of 0.32cm. In the following, the backlighting imaging technique is used unless otherwise.

In order to vary the density ratio between the ambient and released fluids, different oil-immiscible fluids are used: a mixture of ethanol and water, water, a solution of sodium chloride (NaCl) and a solution of sodium iodide (NaI). Their physical properties are given in Table 8.1. NaI solution is of particular interest. First, it provides for large density contrasts between the ambient and released fluids, up to the density of silicone oil, without much increase in viscosity. Second, it can be used to match silicone oil refractive index ($n = 1.384 \pm 0.006$ at 20°C), which is required to obtain satisfactory images with light-

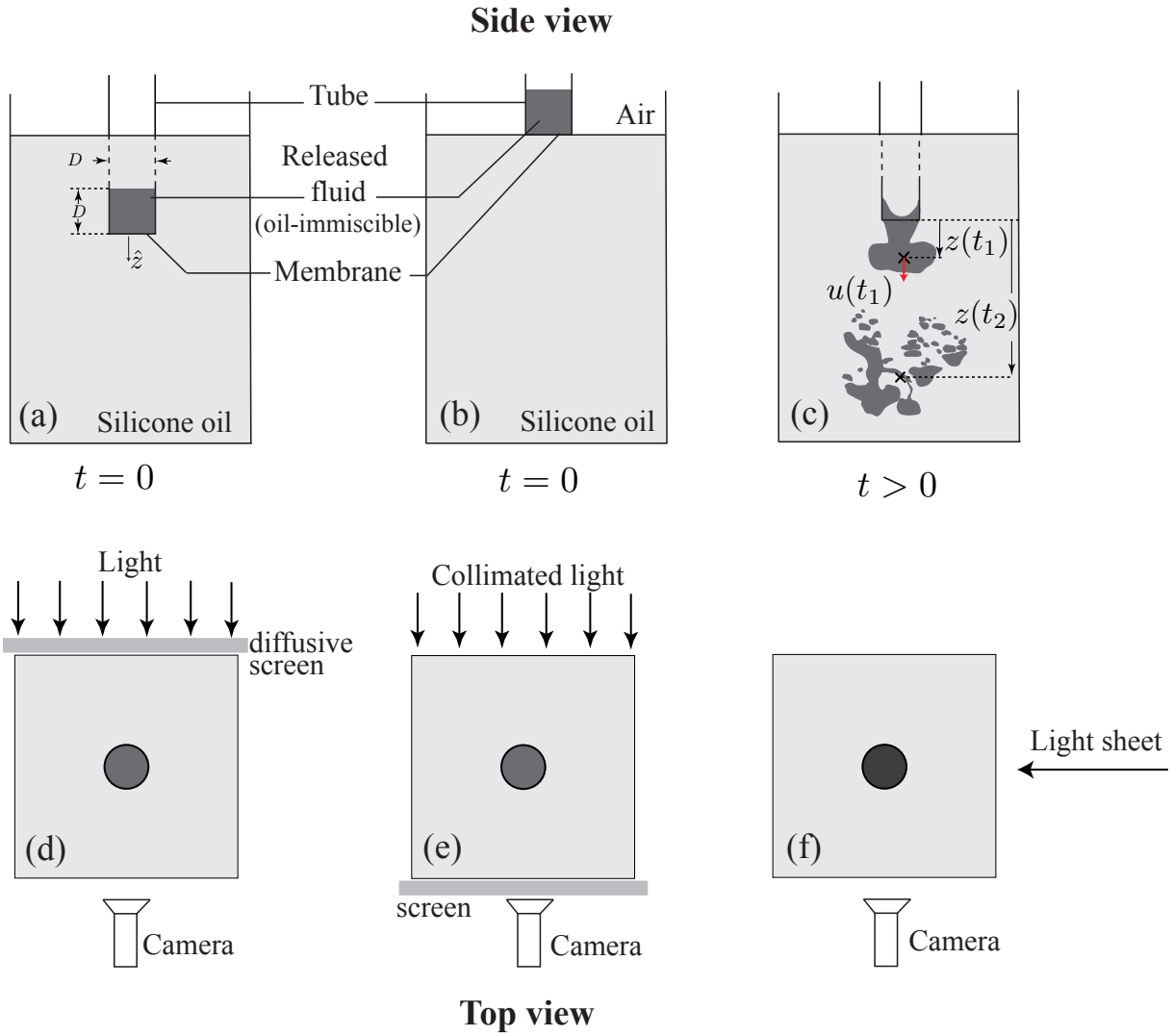

Figure 8.1: Experimental set-up. (a) Side view of the apparatus in the Immersed configuration; (b) side view of the apparatus in the Surface configuration. (c) Sketch of an experiment with variables measured as a function of time. (d,e,f) Visualization techniques.

induced fluorescence. Interfacial tension between silicone oil and the released fluid σ, is measured using a Du Noüy tensiometer.
A non-ionic, oil-insoluble surfactant (trade name "Triton X-100") is added to water and to the NaI solution in several experiments. Equilibrium interfacial tension decreases with surfactant concentration until it reaches the critical micelle concentration, after which it saturates to a constant value. The value given in table 8.1 is used hereafter. The highest possible concentration of surfactant $c \approx 4\text{mL.L}^{-1}$, above which a stable emulsion would be formed in the tank, is used in this study, however, we note that the dynamic interfacial tension may locally be larger than the equilibrium interfacial tension.

In some experiments, water is used in place of silicone oil and a NaCl solution (Table 8.1) is released. Such experiments are used in §9.4 as a reference system.

Fluids	Density ($kg{\cdot}m^{-3}$)	Viscosity ($m^2{\cdot}s$)	Interfacial tension ($mN{\cdot}m^{-1}$)
Silicone oil	$820 \pm 0.2\%$	$1.2 \times 10^{-6} \pm 10\%$	
Ethanol + Water	$843.5 \pm 0.1\%$	$2.6 \times 10^{-6} \pm 10\%$	$2.6 \pm 40\%$
Water	$1000 \pm 0.05\%$	$10^{-6} \pm 10\%$	$31.2 \pm 3\%$
NaCl solution	$1175 - 1192 \pm 0.06\%$	$1.6 \times 10^{-6} \pm 10\%$	$23.3 \pm 4\%$
NaI solution	$1536 - 1607 \pm 0.07\%$	$1.3 \times 10^{-6} \pm 10\%$	$17 - 21 \pm 10\%$
Water + Triton X-100	$1000 \pm 0.1\%$	$10^{-6} \pm 10\%$	$3.3 \pm 15\%$
NaI sol. + Triton X-100	$1260 - 1578 \pm 0.06\%$	$(1.1 - 1.3) \times 10^{-6} \pm 10\%$	$4.4 - 4.8 \pm 10\%$

Table 8.1: Fluid properties.

8.2 Diagnostic techniques

Preprocessing (method detailed in appendix E) is first applied to video images (obtained using backlighting) to get binary images. Then, the centroid and velocity of the released fluid are automatically computed.

We found that the $2D$ centroid obtained from binary images gives too much weight to structures that are located in the rear of the released fluid (membrane of released fluid that remains attached to the tube or wake). Such structures contain a negligible amount of the total released fluid volume whereas they may represent a non-negligible area on a two-dimensional projection. Instead, we measure a vertical position z that takes into account mass distribution in three dimensions:

$$z = \frac{\sum_{i,j} z_{i,j} \log\left(I_{i,j}/I_{0i,j}\right)}{\sum_{i,j} \log\left(I_{i,j}/I_{0i,j}\right)}, \tag{8.1}$$

where the pixels (i, j) form the region occupied by the released fluid in the binary image, $z_{i,j}$ is the pixel vertical position, $I_{i,j}$ is the pixel intensity in the original image and $I_{0i,j}$ the pixel intensity in the back field image. The origin $z = 0$ corresponds to the lower end of the tube. If the light is monochromatic and the two fluids have the same refractive index, according to the Beer-Lambert law, z is then equal to the depth of the real $3D$ centroid of the released fluid. We checked that the dependence of $\log\left(I/I_0\right)$ on the thickness l_y occupied by released fluid in the direction perpendicular to the image is close to linear if the green band of the image is considered in the range relevant for our experiments. When a nonlinear relationship of the form $l_y = a\log\left(I/I_0\right) + b\log\left(I/I_0\right)^2 + c\log\left(I/I_0\right)^3$ with $b = O(a) = O(c)$ is considered, z differs by less than 1% from the value obtained with (8.1). Other sources of discrepancy are due to reflection of light on the immiscible interface. According to Fresnel's equations, the reflectivity of the immiscible interface is less than 4×10^{-4} in our experiments. Given a rough estimation of the number of droplets and their size, we estimate that the fraction of incident energy reflected on the interface is less than 1% in most experiments and less than 5% in the most turbulent

experiments. Finally, curvatures of the immiscible interface act as lenses and concentrate light in some portions of the image when the refractive index of the released fluid does not match the refractive index of the ambient fluid. These effects are probably the main source of discrepancies between z and the real 3D centroid.

From z measurements, we estimate the velocity $u = dz/dt$ of the released fluid as a function of time. Uncertainties on z measurements are mainly due to their sensitivity to the threshold c used in image preprocessing to generate binary images (see appendix E). The frame rate of the video camera also affects uncertainties in u. Uncertainties on z and u measurements are typically less than about 5% and $5 - 10\%$ respectively.

The MATLAB Image Processing toolbox is used to identify the different connected objects and their equivalent radii in binary images. First, the holes in a given connected object are filled. Then, from the $2D$ object, we construct a $3D$ object made of two semi-axisymmetric volumes such that their axis of symmetry is vertically aligned and comprises the centroid of the resulting $3D$ object. The volume of the $3D$ object is given by $V = \sum_{ij} \pi(x_{ij} - \bar{x})S_{ij}$ where x_{ij} and S_{ij} are the pixel horizontal position and pixel surface, and $\bar{x}$ is the horizontal position of the centroid of the resulting 3D volume. The equivalent radius of the connected object r, is defined by $V = \frac{4}{3}\pi r^3$.

In the following sections, errors on systematic experimental results take into account measurement uncertainties and standard deviations obtained in series of experiments conducted at the same input parameter values.

8.3 Input dimensionless numbers

In Immersed experiments, four input dimensionless numbers govern the dynamics:

$$Bo = \frac{\Delta\rho g R^2}{\sigma}, \quad Oh = \frac{\sqrt{\rho_r}\nu_r}{\sqrt{\sigma R}}, \quad P = \frac{\Delta\rho}{\rho_a}, \quad \frac{\nu_r}{\nu_a}. \tag{8.2}$$

Here Bo is the Bond number, Oh the Ohnesorge number, $\Delta\rho$ is the density difference between the ambient and released fluids, g the acceleration due to gravity, R the equivalent spherical radius of the released fluid, ν kinematic viscosity, ρ density. The subscript a and r denote the ambient and released fluid, respectively. Bo measures the importance of the buoyancy force versus interfacial forces. In Surface experiments additional dimensionless numbers are introduced since the released fluid is initially surrounded by air. We are interested in the fragmentation of released fluid in oil and we do not consider interfacial effects involving air. The density and viscosity ratios between air and silicone oil should be added to the above set of dimensionless numbers, however their values remain constant in all the experiments.

Experiments have been conducted for 24 different sets of input dimensionless numbers in the Immersed configuration and 30 sets in the Surface configuration. Bo and P lie in the range $\sim 4 - 1430$ and $\sim 0.029 - 0.96$ respectively, Oh varies from $\sim 10^{-3}$ to $\sim 10^{-2}$ and ν_r/ν_a from 0.8 to 2.2. Since $Oh \ll 1$ we expect viscosity to have little influence on the fragmentation regime in agreement with previous studies on drop fragmentation (Hinze (1955), Pilch & Erdman (1987) and reviews in Gelfand (1996) and Guildenbecher *et al.* (2009)). In this study, we thus concentrate on the effects of Bo and P, which are

independent of viscosity.

Chapter 9

Results

9.1 Early stages of evolution: post-release conditions

In this section we study the velocity and deformation of the released fluid at a short distance from the tube ($z \lesssim 2R$) for the two experimental configurations used.

9.1.1 Weber number scaling: post-release velocity

The definitions of the Weber and Reynolds numbers involve a characteristic velocity U such that

$$We = \frac{\rho_r U^2 R}{\sigma} \; ; \qquad Re = \frac{UR}{\nu_r}. \tag{9.1}$$

In this subsection, we define U and extract a scaling law for We as a function of the input dimensionless numbers Bo and P.

The characteristic velocity classically used at high Reynolds numbers is the terminal velocity, a balance between buoyancy and form drag forces, which gives $U \propto \sqrt{gPR}$. However this scaling is not appropriate for our experiments since fragmentation processes start before the released fluid has reached its terminal velocity (expected between $10 - 20R$). In addition, at fixed Bo and P, the vertical velocity at short distances z is larger in the Surface configuration than in the Immersed configuration. This results from the buoyancy force being initially larger in the Surface configuration since it involves the density difference between the released fluid and the air, rather than $\Delta\rho$. This velocity excess is not accounted for by the terminal velocity scaling which predicts the same characteristic velocity in both configurations.

Another natural scaling, which is adopted here, emerges from a balance between the rate of change in released fluid momentum and buoyancy forces, by assuming that a given portion of the mechanical work generated by buoyancy forces (potential energy) is converted into kinetic energy of the released fluid during its fall.

9.1.1.1 Immersed configuration

In the Immersed configuration, this scaling takes the form

$$\frac{1}{2}\rho_r u^2 \propto \Delta\rho g(z + D/2), \tag{9.2}$$

where the distance to the tube end z is initially equal to $-D/2$. Scaling (9.2) implies that the characteristic velocity U should be defined at a given distance from the tube Z. The choice of Z is partly arbitrary but two conditions have to be met: the released fluid is entirely off the tube at $z = Z$ and drop formation has not yet started. $Z = 2R$ satisfies both conditions in our experiments.

The potential/kinetic energy balance (9.2) implies $We \propto Bo$, which is in agreement with the experimental data shown in figure 9.1(a). We obtain the following least squares best fit:

$$We = a_1 Bo \ , \quad a_1 = 0.76 \pm 0.04, \tag{9.3}$$

where the standard error of the fit is of the order of the experimental errors.

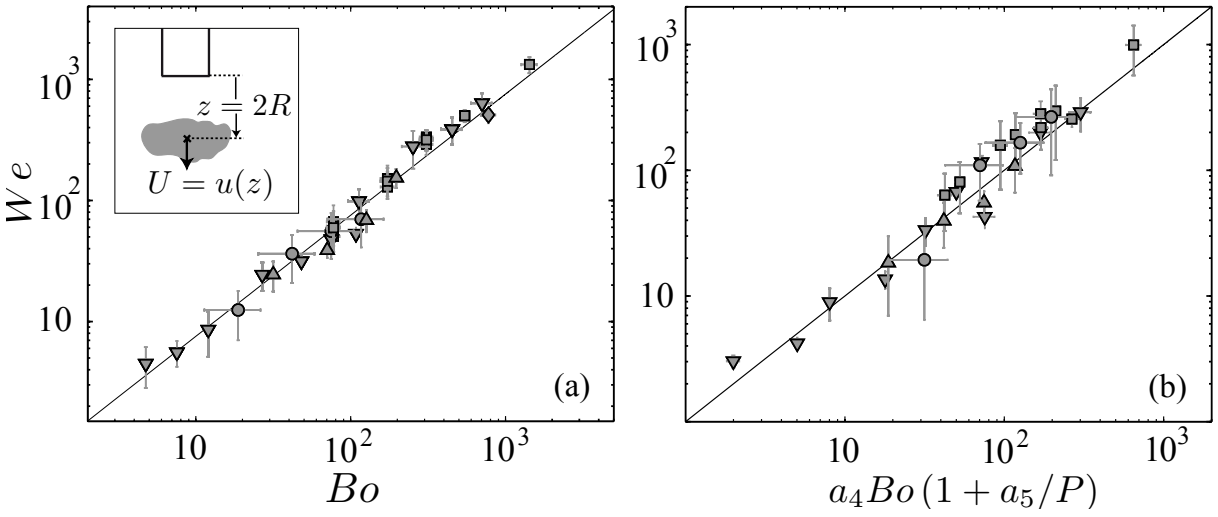

Figure 9.1: (a) Weber number versus Bond number in the Immersed configuration using $U = u(z = 2R)$ as illustrated in the insert. The least squares best fit $We = a_1 Bo$ with $a_1 = 0.76 \pm 0.04$ is shown by the black line. (b) Weber number measured in Surface experiments with $U = u(z = 2R)$ versus Weber number predicted by the least squares best fit $We = a_4 Bo\,(1 + a_5/P)$ (black curve) with $a_4 = 0.51 \pm 0.07$ and $a_5 = 0.07 \pm 0.03$. ■ , $0.82 \leq P \leq 0.96$; ◆ , $P \approx 0.54$; ▲ , $P \approx 0.43$; ▼ , $P \approx 0.22$; ● , $P \approx 0.03$.

9.1.1.2 Surface configuration

In the Surface configuration it is not straightforward to estimate the mechanical work generated by buoyancy forces. For example, the buoyancy force involves the density difference with the surrounding air $\rho_r - \rho_{air} \approx \rho_r$ at initial times, but once the fluid is entirely immersed in the ambient fluid, it depends only on $\Delta\rho$. Assuming that the

mechanical work generated by buoyancy forces can be written as a sum of two independent terms, originating from the former contributions, and assuming that a portion of this work is converted into kinetic energy, we obtain

$$\frac{1}{2}\rho_r U^2 = a_2 \Delta\rho g R + a_3 \rho_r g R, \tag{9.4}$$

where a_2 and a_3 are two constants to be fitted. In terms of dimensionless numbers (9.4) amounts to

$$We = a_4 Bo \left(1 + \frac{a_5}{P}\right), \tag{9.5}$$

where $a_4 = a_2 + a_3$ and $a_5 = \frac{a_3}{a_2+a_3}$. The experimental results are shown in figure 9.1(b). We find the following least squares best-fit values: $a_4 = 0.51 \pm 0.07$ and $a_5 = 0.07 \pm 0.03$. The standard error of the fit is of the order of the experimental errors.

We have found scaling laws for We as a function of the input dimensionless numbers which fit reasonably well with the experimental data. As a consequence, Bo and We can substitute for each other and the physical processes can be studied alternatively in a (Bo, P) or (We, P) diagram. We will mainly concentrate on the (We, P) diagram since, as shown in §9.2, it is well-suited for comparisons between fragmentation regimes in the Immersed and Surface configurations. Re varies from ~ 300 to $\sim 10^4$ in our experiments, with $Re \geq 10^3$ in a large majority of experiments (85%). We do not concentrate on the effect of Re since, as we have already argued in §8, viscosity is expected to have little influence on the fragmentation regime. This is confirmed by estimations of the capillary number $Ca = \nu_r \rho_r U/\sigma$, which measures the ratio of viscous forces to interfacial forces: Ca remains much smaller than 1 in our experiments (in the range $\sim 0.005 - 0.1$).

9.1.2 Early deformations and destabilizations: post-release shape

Once the released fluid exits the tube, it starts to deform and change shape. A wide variety of shapes is observed directly after the release ($z \lesssim 2R$) as illustrated in figures 9.2(a,b,c) and figure 9.4. The present section aims at understanding the physical mechanisms involved.

9.1.2.1 Immersed configuration

Figures 9.2(a,b,c) illustrate the initial deformations of the released fluid in the Immersed configuration at different Weber numbers. At $We \approx 10$ (a) the released fluid flattens into a pancake shape due to dynamic pressure forces while non-axisymmetric perturbations are damped. At $We \approx 50$ (b) non-axisymmetric perturbations grow and at $We \approx 1.5 \times 10^3$ (c) these non-axisymmetric structures develop a mushroom shape, which is morphologically similar to Rayleigh-Taylor instabilities (RTI).

We first compare these with the classical inviscid analysis of the Rayleigh-Taylor instability of a horizontally unbounded interface between two immiscible fluids (Bellman & Pennington, 1954; Chandrasekhar, 1961). Choosing a coordinate system that moves with the released fluid, the governing equations are left unchanged if g is replaced by $g - du/dt$. The uncertainties on du/dt measurements are too large for any scaling law to be extracted

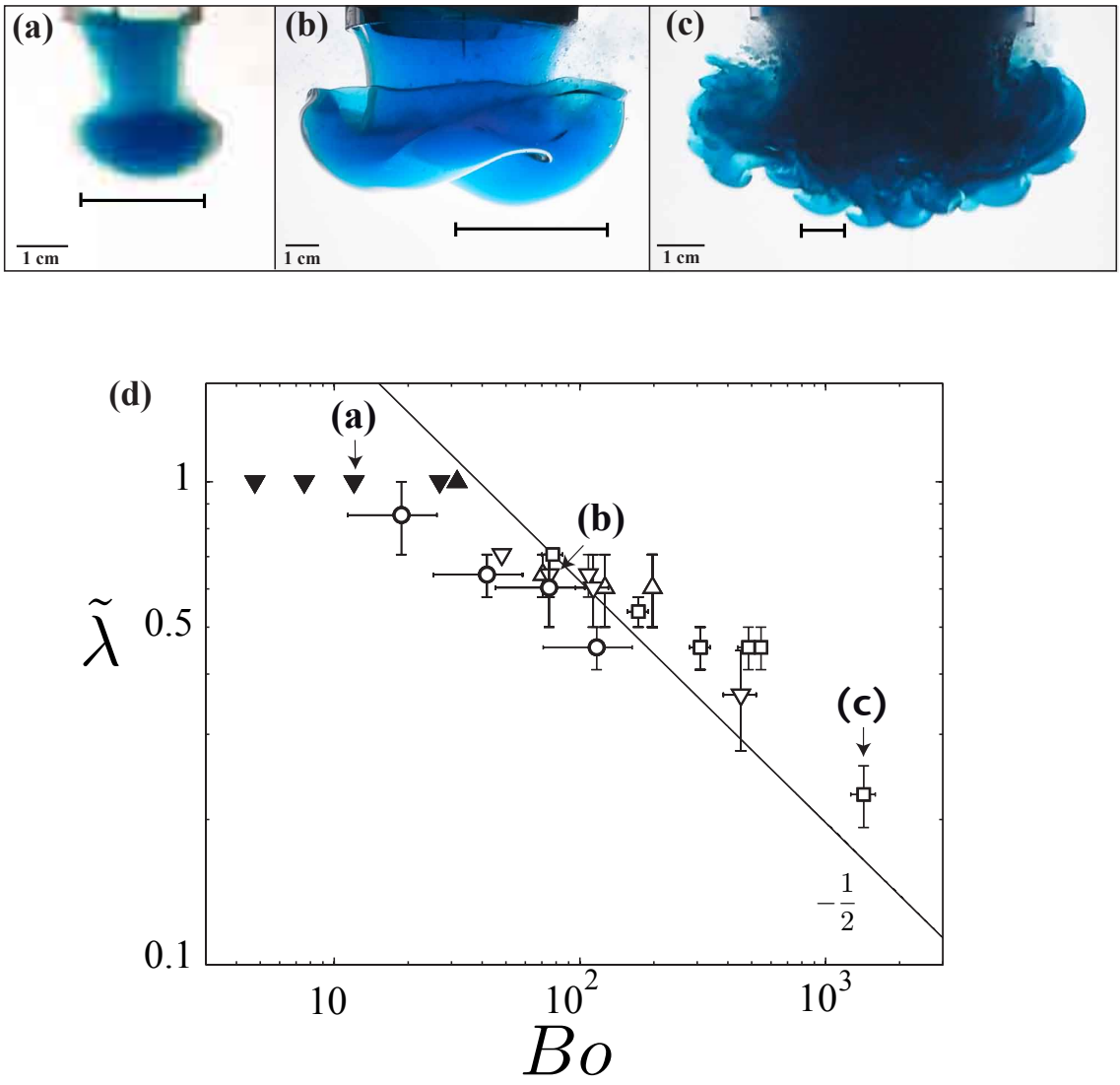

Figure 9.2: (a,b,c) Early deformations of the released fluid in Immersed experiments at $We \approx 10$ *(a),* $We \approx 50$ *(b),* $We \approx 1.5 \times 10^3$ *(c) for* $z \lesssim 2R$*. The black mark in (a) indicates the critical wavelength of RTI deduced from equation (9.10) whereas black marks in (b) and (c) indicate the most amplified wavelength of RTI deduced from equation (9.9). (d) Estimated dimensionless wavelength* $\tilde{\lambda} = 1/\sqrt{n}$ *as a function of Bo in Immersed experiments where n is the number of mushroom-shaped structures.* □ , $0.87 \leq P \leq 0.96$*;* △ , $P \approx 0.43$*;* ▽ , $P \approx 0.22$*;* ○ , $P \approx 0.03$*. The black curve gives the most amplified wavelength predicted by equation (9.9). Filled symbols: experiments in which no RTI grows (*$n = \tilde{\lambda} = 1$*). Symbols (a),(b),(c) denote results obtained from the experiments shown in (a),(b),(c).*

but we estimate that its maximum value is of order $1 - 2$ m·s^{-2} and therefore, as a first order approximation, we neglect du/dt with respect to g. Then, in the case of vertically unbounded layers, the growth rate γ of small perturbations is given by

$$\gamma = \sqrt{\frac{\Delta\rho}{\rho_a + \rho_r} gk - \frac{\sigma}{\rho_a + \rho_r} k^3}, \tag{9.6}$$

where k is the wavenumber of the disturbances at the interface. The most amplified and critical wavenumbers are respectively given by

$$k_m = \sqrt{\frac{\Delta\rho g}{3\sigma}}, \tag{9.7}$$

$$k_c = \sqrt{\frac{\Delta\rho g}{\sigma}}. \tag{9.8}$$

It can be shown that including viscous effects (see equation (113) from Chandrasekhar, 1961, Chap. X) has little effect on the value of k_m and k_c at parameter values relevant for our experiments. In terms of dimensionless wavelength $\tilde{\lambda} = 2\pi/kD$, equations (9.7) and (9.8) take the form

$$\tilde{\lambda}_m = \frac{2\pi\sqrt{3}}{\sqrt{Bo}}\frac{R}{D}, \tag{9.9}$$

$$\tilde{\lambda}_c = \frac{2\pi}{\sqrt{Bo}}\frac{R}{D}. \tag{9.10}$$

The most amplified wavelength predicted by (9.9) matches the size of non-axisymmetric structures in figures 9.2(b,c). In figure 9.2(a) the predicted critical wavelength $\tilde{\lambda}_c D$ is close to the tube diameter which explains why RTI does not develop at the front of the released fluid. The number of mushroom-shaped structures n is evaluated in our experiments and a characteristic wavelength is estimated by $\tilde{\lambda} = 1/\sqrt{n}$. Open symbols in figure 9.2(d) show that experimental data are consistent with prediction (9.9), both in trend and in absolute value, demonstrating that non-axisymmetric perturbations in figures 9.2(b,c) result from RTI. We note that the slopes in figure 9.2(d) at fixed P values are consistent with equation (9.9) but the prefactors slightly vary with P. A regime diagram of the initial deformations is shown in figure 9.3. RTI start to emerge at We_c, which is located between ~ 20 and ~ 30 given the uncertainties on We. From equation (9.10) we estimate that the number of mushroom-shaped structures n is equal to $n_c = 2$ when the Bond number is equal to $Bo_c = 8\pi^2(R/D)^2$, assuming $\tilde{\lambda}_c = 1/\sqrt{n_c}$. Applying the experimental scaling (9.3), we find $We_c \approx 20 \pm 1$, which agrees with the experimental results, despite the simplicity of the above model in which several effects have been neglected.

First, the fluid layers are not vertically unbounded. It can been shown that this effect has a secondary impact in the linear regime given the value of $\tilde{\lambda}/D$ in our experiments and, equations (9.6), (9.7) and (9.9) remain valid at first order. Second, the released fluid is confined in the horizontal direction. Jacobs & Catton (1988) have shown that geometry does not enter in the linear stability analysis of a fluid layer confined in a circular container of diameter D and overlying a gas layer. A similar result holds in the case of two fluid layers so that equation (9.6) remains valid. The circular geometry quantizes the possible values of the wavenumber k: $kD/2$ has to be a zero of the Bessel functions of the first kind. However this effect has little impact on our conclusions since the characteristic dimensionless size of the most amplified waves follows the same general trend $\propto 1/\sqrt{Bo}$ as in (9.9).

Finally, in the analysis leading to equation (9.6), the undisturbed state is at rest in the

moving coordinate system. In our experiments an axisymmetric basic flow develops during the fall of the released fluid, advecting the growing RTI from unstable regions at the front to stable regions at the rim. These effects have been examined in previous studies on the 3D instability of bubbles rising through liquid. Grace *et al.* (1978) proposed a semi-empirical model based on the idea that breakup occurs if the characteristic timescale for RTI growth $t_{RT} = 1/\gamma_m$, where γ_m is the maximum growth rate, is small enough compared to the time available for growth, i.e. the advective timescale, t_a. Batchelor (1987) improved this model by including a basic flow, assumed to be axisymmetric and irrotational, in the stability analysis. He showed that the contractional motion in the direction normal to the interface tends to decrease the amplitude of a disturbance while its wavelength increases exponentially due to the extensional motion parallel to the interface. Because of the latter effect, disturbances do not grow exponentially with a constant growth rate. Similar effects are expected in our experiments, but the axisymmetric basic flow is inherently time-dependent, causing an increase in complexity. For this reason, we treat advection and RTI as if they were two independent mechanisms as in Grace *et al.* (1978).

As a first approximation we use $t_{RT} = 1/\gamma(k_m)$ where γ and k_m are given by equations (9.6) and (9.7). Taking R/U as a characteristic advective timescale t_a we obtain

$$\frac{t_a}{t_{RT}} = d_1 \frac{Bo^{3/4}}{We^{1/2}} \sqrt{\frac{1+P}{2+P}}. \tag{9.11}$$

where $d_1 = \sqrt{2/3^{3/2}}$. Making use of the experimental scaling (9.3), equation (9.11) takes the form (used in figure 9.3)

$$\frac{t_a}{t_{RT}} = \frac{d_1\, We^{1/4}}{a_1^{3/4}} \sqrt{\frac{1+P}{2+P}}, \quad a_1 = 0.76 \pm 0.04. \tag{9.12}$$

According to (9.12), t_a/t_{RT} varies weakly with P (figure 9.3), which is consistent with no observed change in the deformation regime when varying P at a fixed We value. Equation (9.12) predicts that RTI remain the dominant mechanisms when We increases, which is also consistent with experimental observations (figure 9.3). Close to $We = We_c$, $t_a/t_{RT} \sim 1$, indicating that the effect of advection of RTI by the basic flow is probably significant. This may be responsible for a short delay in the emergence of RTI (We_c in figure 9.3) compared to the critical value $We \approx 20$ predicted from equation (9.10).

9.1.2.2 Surface configuration

In the Surface experiments, when $We \gtrsim 8$, a vortex ring forms at the tube end, as a result of the roll-up of a shear layer generated at the tube wall during the release (figures 9.4(a,b,c)). Contraction of the initial ring's diameter is observed in most experiments at $z \sim 2R - 3R$ (figure 9.4(b), see also supplementary video 2). A decrease in the ring diameter after its formation has already been reported in experiments (Didden, 1979) and numerical simulations (Nitsche & Krasny, 1994), and is due to the influence of the tube orifice (Didden, 1979; Sheffield, 1977) or a secondary vortex of opposite circulation formed

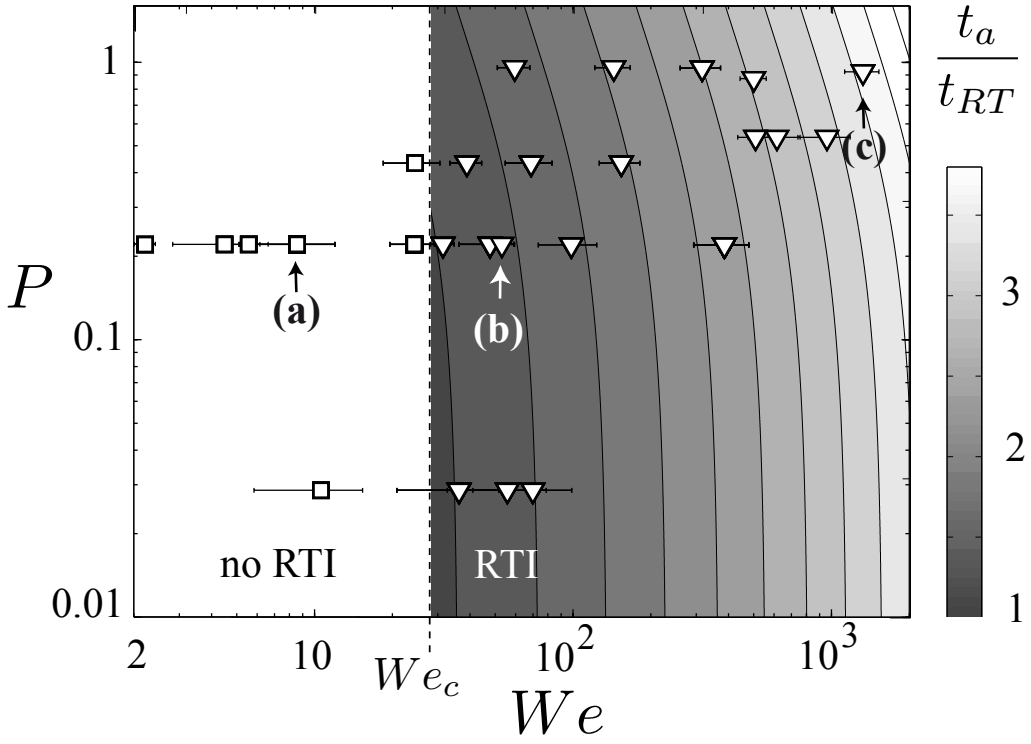

Figure 9.3: (We, P) diagram of the early stage deformation in the Immersed configuration. □ , axisymmetric deformations (no RTI); ▽ , RTI. The ratio of the advective timescale to the RTI timescale t_a/t_{RT} is color coded in regions where RTI are found, at $We \geq We_c$. Symbols (a),(b),(c) denote the experiments shown in figure 9.2.

on the tube end (Didden, 1979). In our experiments, the release process generates a strong wave at the surface of the tank, causing penetration of ambient fluid into the tube after the release is completed, and possibly responsible for the generation of a secondary vortex. Mushroom-shaped structures are observed at the front of the vortex ring in experiments located at the highest P values (figures 9.4(d,e) and figure 9.5).

Using the same argument as in §9.1.2.1, we hypothesize that RTI emerge in Surface experiments when the characteristic time for disturbance growth t_{RT} is small compared to the advective timescale t_a. In previous experimental studies of non-buoyant vortex rings generated by a piston (Gharib *et al.*, 1998) and in the numerical study of the roll-up of a vortex sheet (Moore, 1974), it has been shown that the characteristic timescale for the formation of the vortex ring is few advective times, suggesting that the competition between the growth of perturbations at the front and their advection by the flow is a competition between disturbances growth and the roll-up of the shear layer.

In the Surface configuration, du/dt reaches $0.4g$, larger than in the Immersed configuration because the former case initially involves a density contrast $\rho_r - \rho_{air} \geq \Delta\rho$, implying that the initial effective acceleration $a = g - du/dt$ is smaller in Surface experiments. Therefore, the growth of RTI is reduced by a factor of about 2. In addition, the total circulation of the vortex sheet Γ is larger in the Surface configuration since larger velocities are reached during the early stages of the fall, which tends to further decrease the vortex sheet roll-up time. Thus, we qualitatively expect vortex sheet roll-up to be

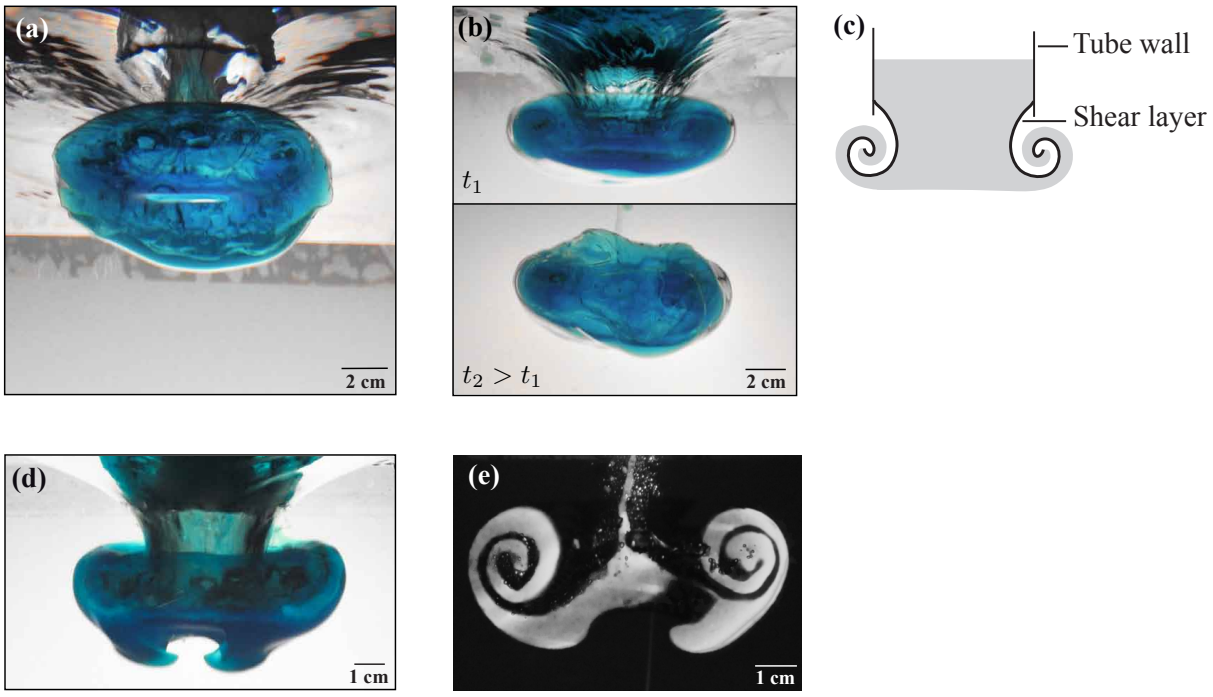

Figure 9.4: (a,b,d,e) Early deformations in the Surface configuration. (a,b) $We \approx 100$, $P \approx 0.22$; $z \lesssim R/4$ and $z \approx 2.5R$ in, respectively, the first and second snapshot of (b); (d) $We \approx 300$, $P \approx 0.96$, $z \approx R$; (e) obtained with light-induced fluorescence, $We \approx 200$, $P \approx 0.54$, $z \approx 2R$. (c) Schematic representation of the generation of a shear layer and its roll-up to form a vortex ring.

favored compared to RTI in the Surface configuration.

Once the released fluid is entirely immersed, the buoyancy force becomes the same as in an equivalent Immersed experiment. At this stage, du/dt is smaller than $\sim 0.2g$ and, with the same assumptions and limitations as in §9.1.2.1, t_a/t_{RT} is given by equation (9.11). Making use of scaling (9.5), we obtain

$$\frac{t_a}{t_{RT}} = \frac{d_1\, We^{1/4}}{a_4^{3/4}\,(1 + a_5/P)^{3/4}} \sqrt{\frac{1+P}{2+P}}, \tag{9.13}$$

where $a_4 = 0.51 \pm 0.07$ and $a_5 = 0.07 \pm 0.03$. Equation (9.13) predicts that, contrary to the Immersed configuration, t_a/t_{RT} strongly depends on P, which explains why the deformation regime changes in Surface experiments when varying P at a fixed We (figure 9.5). Mushroom-shaped structures are found at the largest P and We values, in regions where t_a/t_{RT} reaches its highest values, consistent with the hypothesis that these structures result from RTI.

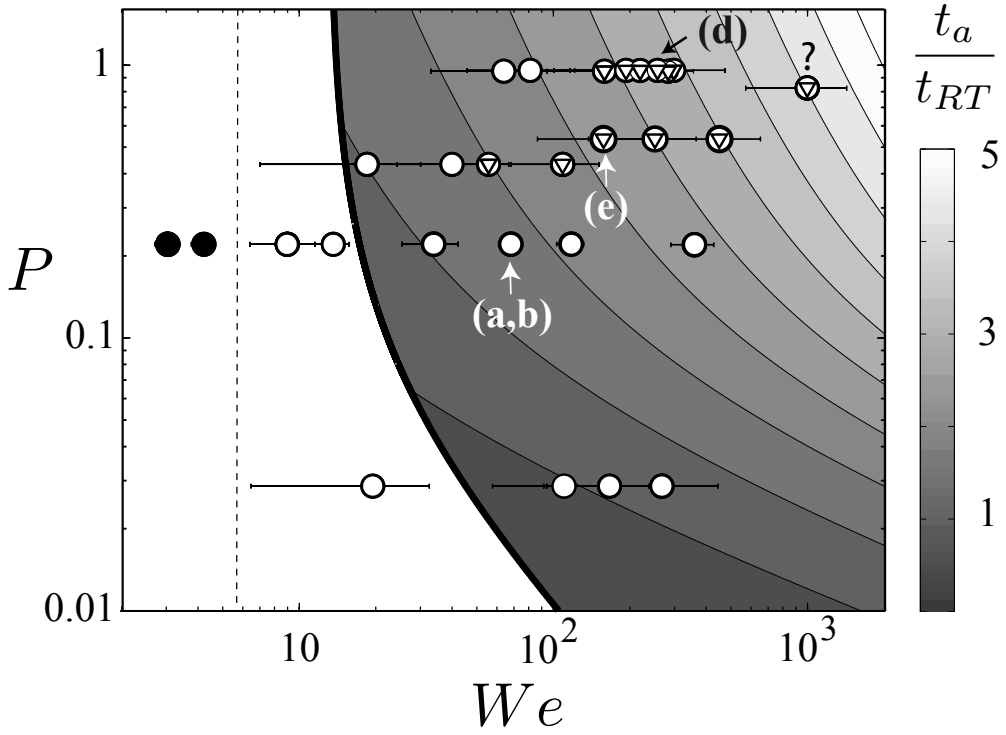

Figure 9.5: (We, P) diagram of the first deformations in the Surface configuration. ● , oblate drops; ○ , vortex rings; ▽ , mushroom-shaped structures, typical of RTI, are observed at the front of a vortex ring. The question mark denotes an experiment in which no clear visualization of mushroom-shaped structures was captured but waves of characteristic size consistent with the predicted wavelength for RTI are observed. The ratio of the advective timescale to the RTI timescale t_a/t_{RT} is color coded in regions where RTI grow in the case of an unbounded interface with no additional basic flow, i.e. for $Bo \geq Bo_c$, making use of scaling (9.5).

9.2 Subsequent evolution : characterization of fragmentation regimes

In §9.1.2 it was shown that the initial deformations and their sensitivity to P and We can be qualitatively accounted for by a competition between growth of RTI and advection by the flow. When the latter effect dominates, a vortex ring is formed. In the present section the different fragmentation regimes are characterized from the evolution following the initial deformations, prior to drop formation. The resulting (P, We) regime diagram, shown in figure 9.6, locates the regimes detailed below.

9.2.1 Low and intermediate Weber numbers : wide variety of regimes

9.2.1.1 $We \lesssim 6$

At the lowest Weber numbers ($We \approx 2-4$) the released fluid takes the form of an oscillating drop. Breakup starts at $We \approx 5$ and the flow reaches a regime where the

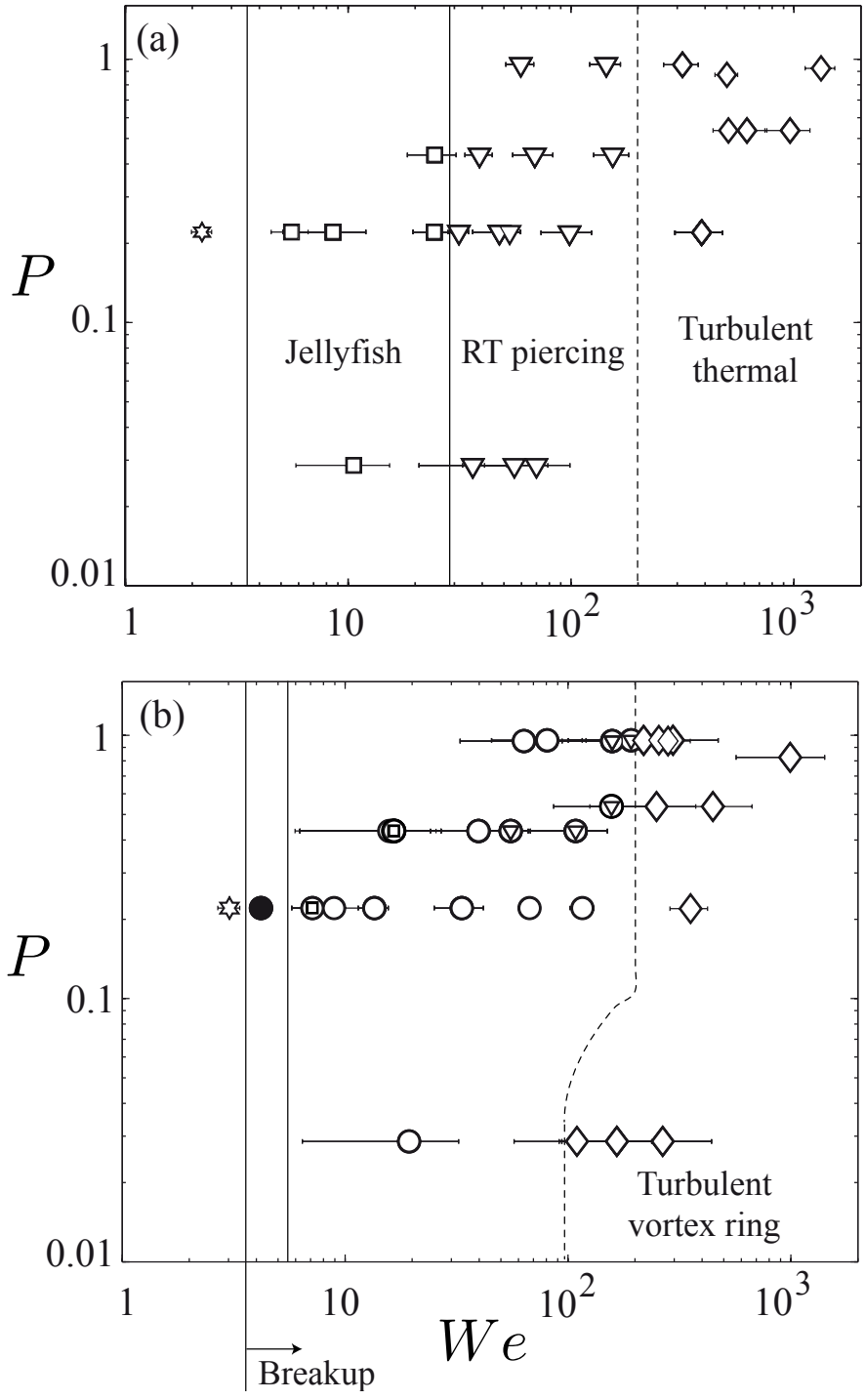

Figure 9.6: Fragmentation regimes in (We, P) space in the Immersed (a) and Surface (b) configurations. Symbols denote: ☆ ,no fragmentation, oscillating drop; ● , vibrational breakup regime; □, jellyfish regime; ▽ , RT piercing regime;◇, turbulent regime; ○, vortex ring destabilization regime;▽ , intermediate regime between vortex ring destabilization and RT piercing (mushroom-shaped structures, typical of RTI, are observed at the front of a vortex ring); ◎ , vortex ring evolving into a jellyfish regime. Plain lines: tentative boundary regime transitions; dashed lines: progressive transitions.

released fluid disintegrates into a few large drops as a consequence of large amplitude oscillations at the natural frequency of the drop. This vibrational breakup regime has been documented previously (e.g. Pilch & Erdman, 1987; Gelfand, 1996).

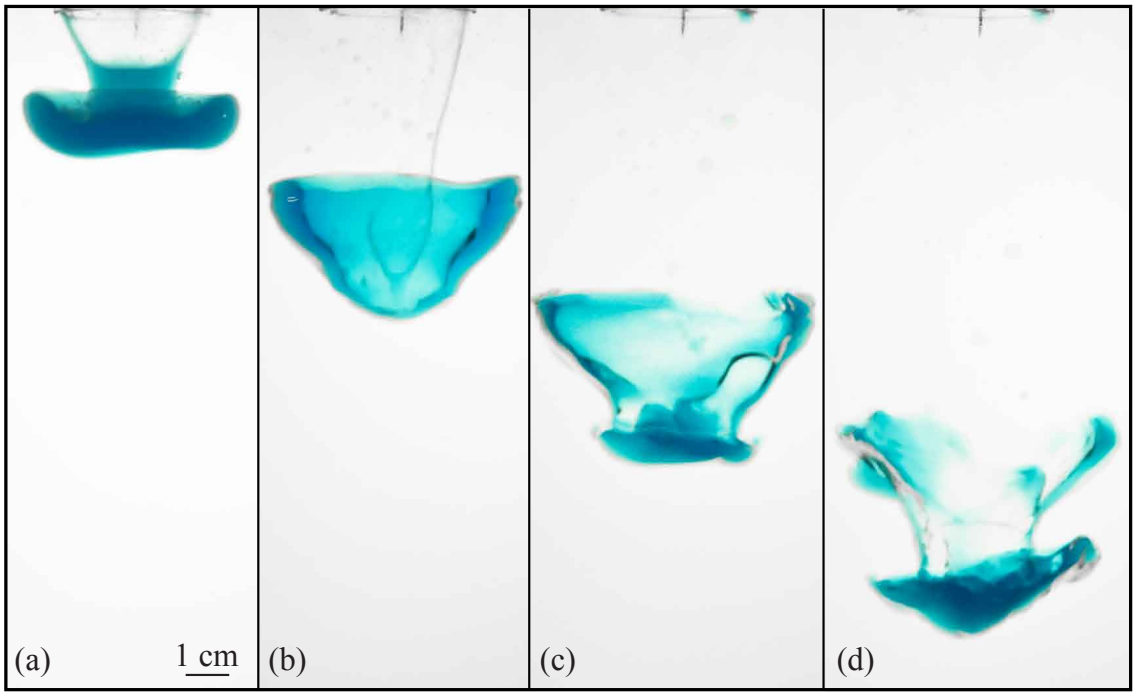

Figure 9.7: Experiment in the jellyfish fragmentation regime, $We \approx 24$, $P \approx 0.22$, Immersed configuration, time intervals of about 0.25 s.

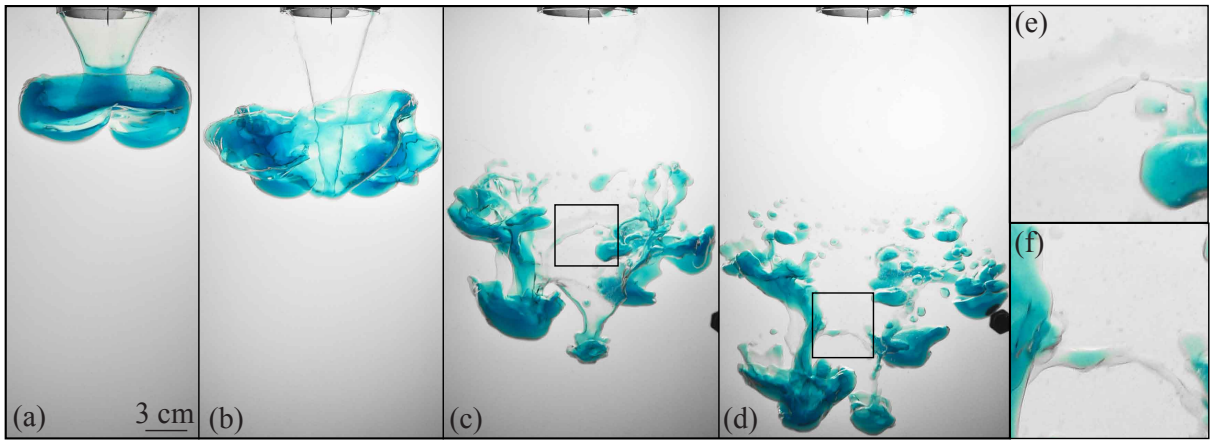

Figure 9.8: Experiment in the RT piercing fragmentation regime, $We \approx 50$, $P \approx 0.22$, Immersed configuration, time intervals of order 0.2 s. (e,f) Close-ups corresponding to the the square boxes in (c) and (d), respectively.

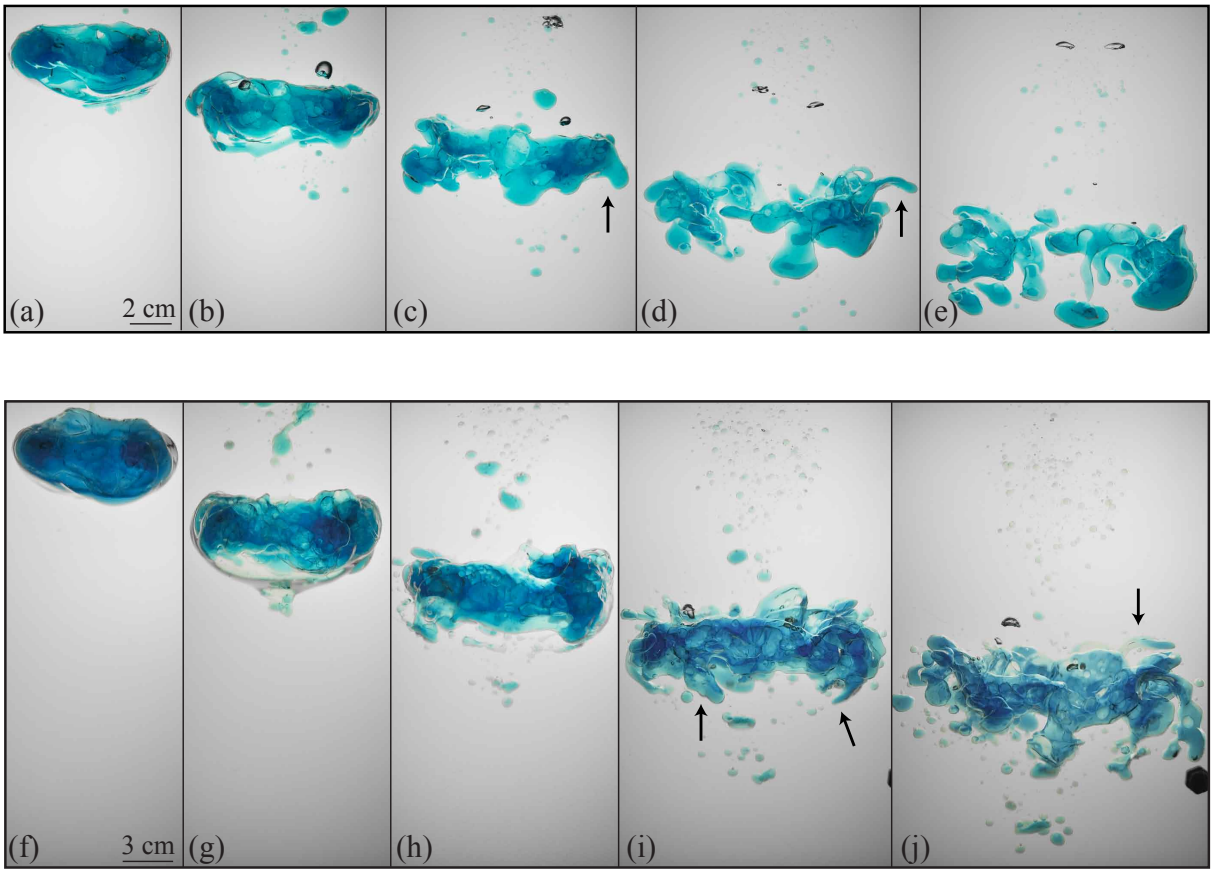

Figure 9.9: Experiments in the vortex ring destabilization regime, Surface configuration. (a-e) $We \approx 30$, $P \approx 0.22$*; (f-j)* $We \approx 70$, $P \approx 0.22$. *Arrows locate elongated structures or filaments. Time intervals are of about* 0.2 *s.*

9.2.1.2 $We \gtrsim 6$; no immiscible ring

For $We \gtrsim 6$, if the released fluid does not roll-up into a ring, the evolution that follows the initial deformation and precedes ligament formation is the continuation of the mechanisms identified in §9.1.2.

The fragmentation regime in experiments located below the onset of RTI, shown in figure 9.7, is named the *jellyfish* regime. In this regime, the absence of growing RTI allows the flow to remain quasi-axisymmetric until the distance from the tube is equal to a few initial diameters. The initial pancake shape (figure 9.7(a)) evolves into a U-shaped membrane (figure 9.7(b)). Then, a portion of released fluid accumulates towards the front, leaving the membrane thinner at the rear (figure 9.7(c,d)), which leads to the formation of sheared filamentary structures near the rear (figure 9.7(d)). Similar structures, categorized as a shear breakup mode, have been found by Han & Tryggvason (1999) in axisymmetric simulations of drop deformation (see their Fig.5). We note that a vortex ring rolls up in experiments with miscible fluids at similar Reynolds number (in the range $300 - 3000$), suggesting that surface tension prevents the roll-up of the shear layer in these experiments.

When the initial deformation is dominated by RTI (figure 9.8 and Movie 1*), the subsequent evolution corresponds to the typical nonlinear evolution of RTI and commonly involves shear instabilities. As a result, the released fluid mass divides into several subvolumes connected by filamentary structures (figure 9.8(c,d)). The flow shares similarities with the multimode breakup regime as described in experiments of aerobreakup and interpreted as a result of RTI (Harper *et al.*, 1972; Simpkins & Bales, 1972; Joseph *et al.*, 1999; Theofanous *et al.*, 2004; Theofanous & Li, 2008; Zhao *et al.*, 2010). Following Theofanous *et al.* (2004) and Theofanous *et al.* (2007), this fragmentation regime is named *RT piercing*. The transition from jellyfish to RT piercing in figure 9.6(a) corresponds to the onset of RTI.

9.2.1.3 $We \gtrsim 6$; with an immiscible ring

When the initial deformation is dominated by the roll-up of a vortex ring, the evolution prior to ligament formation is characterized by the development of additional instabilities on the ring (figure 9.9, Movie 2). This *vortex ring destabilization* regime is morphologically different from the RT piercing regime or the jellyfish regime at similar We values.
A plausible mechanism for the vortex ring destabilization is an elliptical instability, often referred to as the Widnall instability, which has been identified as the mechanism responsible for the destabilization of miscible non-buoyant vortex rings (Widnall & Sullivan, 1973; Widnall *et al.*, 1974; Widnall & Tsai, 1977; Saffman, 1978; Dazin *et al.*, 2006). It results from the parametric resonance of neutrally stable modes of vibration, called Kelvin waves, with an underlying quadrupole strain field induced by the vortex ring on itself. Hattori & Fukumoto (2003) and Fukumoto & Hattori (2005) have shown that a dipole field resulting from the curvature of the vortex ring can also induce a parametric resonance between two Kelvin waves, called the curvature instability. Hattori & Hijiya (2010) have studied the stability of fat vortex rings, which is the relevant regime for our experiments, where the ratio of the core to vortex ring radius is of order 0.4. They found that the Widnall instability dominates over the curvature instability, but the combination of the elliptical deformation and the dipole field initiate a third mode of instability whose growth rate exceeds the Widnall instability near the boundary of the ring.
The centrifugal instability is yet another plausible candidate for the destabilization of our immiscible vortex rings. Finally, the presence of a heavy vortex core can also trigger a RT instability where the centrifugal force plays the role of gravity.

The maximum growth rate of the above instabilities are of the same order of magnitude for miscible rings according to previous theoretical and numerical studies (Widnall & Tsai, 1977; Hattori & Hijiya, 2010; Shariff *et al.*, 1994; Sipp *et al.*, 2005). Thus, one mechanism can not be favored over the others and further investigation, especially accounting for surface tension, would be required to identify the dominant mechanisms in our experiments. Azimuthal waves are seen in our experiments (e.g. figure 9.9(c)) whereas the most unstable waves of RTI are axisymmetric at small density contrast (Sipp *et al.*, 2005).

In Surface experiments, transitions from one of the above regimes to another are often progressive. When RTI grows at the front of a developing vortex ring, the flow is a

*Movies and their captions can be found at the following link: http://www.ipgp.fr/ landeau/public/MoviesPhD/MoviesPartII.zip

combination of RT piercing and vortex ring destabilization regimes (figure 9.6) and, in a few and isolated experiments at $We \leq 20$, a vortex ring forms but finally evolves into a jellyfish fragmentation regime (figure 9.6).

9.2.2 High Weber numbers: turbulent regime

When We is increased above ~ 100, a progressive transition leads to the turbulent regimes illustrated in figure 9.10 (see also Movie 3). The deformations of the immiscible interface are chaotic and exhibit a wide range of length scales (e.g. figures 9.10(c,g)). In the experiment shown in figures 9.10(a-h) initial deformations are dominated by RTI (seen in (a) and (f)) whereas no RTI develops in the experiment shown in figures 9.10(q-w) (Surface configuration, low P). The initial deformations in figure 9.10(i-p) are more ambiguous: the waves in (i) do not have a clear mushroom-shaped structure as in figures 9.10(a,f), but their characteristic size is consistent with the predicted wavelength for RTI and this experiment is located in a region of parameter space where we expect RTI to emerge according to results from §9.1.2. Despite the different initial deformations, the large-scale flow has common features in the three experiments: the released fluid is contained inside a coherent structure whose shape is self-similar during the fall and which grows by entrainment of ambient fluid. This behavior is similar to the case of a fluid mass evolving in another miscible fluid at high Reynolds number, as described by Batchelor (1954) and Scorer (1957) for thermals, Maxworthy (1974) and Glezer & Coles (1990) for non-buoyant vortex rings, and Turner (1957) for buoyant vortex rings. For illustration purposes, figure 9.10 shows a turbulent thermal and a turbulent buoyant vortex ring with miscible fluids obtained using the same experimental set-ups as in figure 9.10.

The geometry of the coherent structure in figure 9.10(q-w) can be approximated by an oblate spheroid of large width to height ratio (≈ 1.8), much like miscible non-buoyant vortex rings. In contrast, the coherent structure in figure 9.10(a-h) can be approximated by a prolate spheroid much like the shape of miscible turbulent thermals.

Figure 9.12 shows experiments conducted using the shadowgraph technique depicted in figure 8.1(e) while the released fluid is initially warmer than the ambient fluid. Regions with high refractive index gradients that are not colored in red or blue correspond to locations of warm ambient fluid that came into contact with released fluid. At low We (figure 9.12(a)) the warm ambient fluid forms a wake as large as the released fluid. On the contrary, in the case of an immiscible thermal (figure 9.12(b)), the warm ambient fluid is mainly located inside the spheroid containing released fluid. This reinforces the analogy with miscible fluids by demonstrating that ambient fluid is indeed entrained inside a growing coherent structure called thermal.

A cross-section of an immiscible thermal is shown in figure 9.13(a). It reveals small-scale intermingling between released and ambient fluids in the entire thermal, even though the two immiscible phases remain continuous. This demonstrates that ambient fluid is entrained in the thermal before the released fluid breaks into fragments. The immiscible interface has a fractal structure as demonstrated in Deguen *et al.* (2013) (reproduced in appendix G of this manuscript). Comparison between figure 9.13(a) and images obtained in equivalent miscible experiments (figure 9.13(b)) demonstrates that the large-scale internal structure of turbulent thermals is morphologically similar in miscible and immiscible experiments.

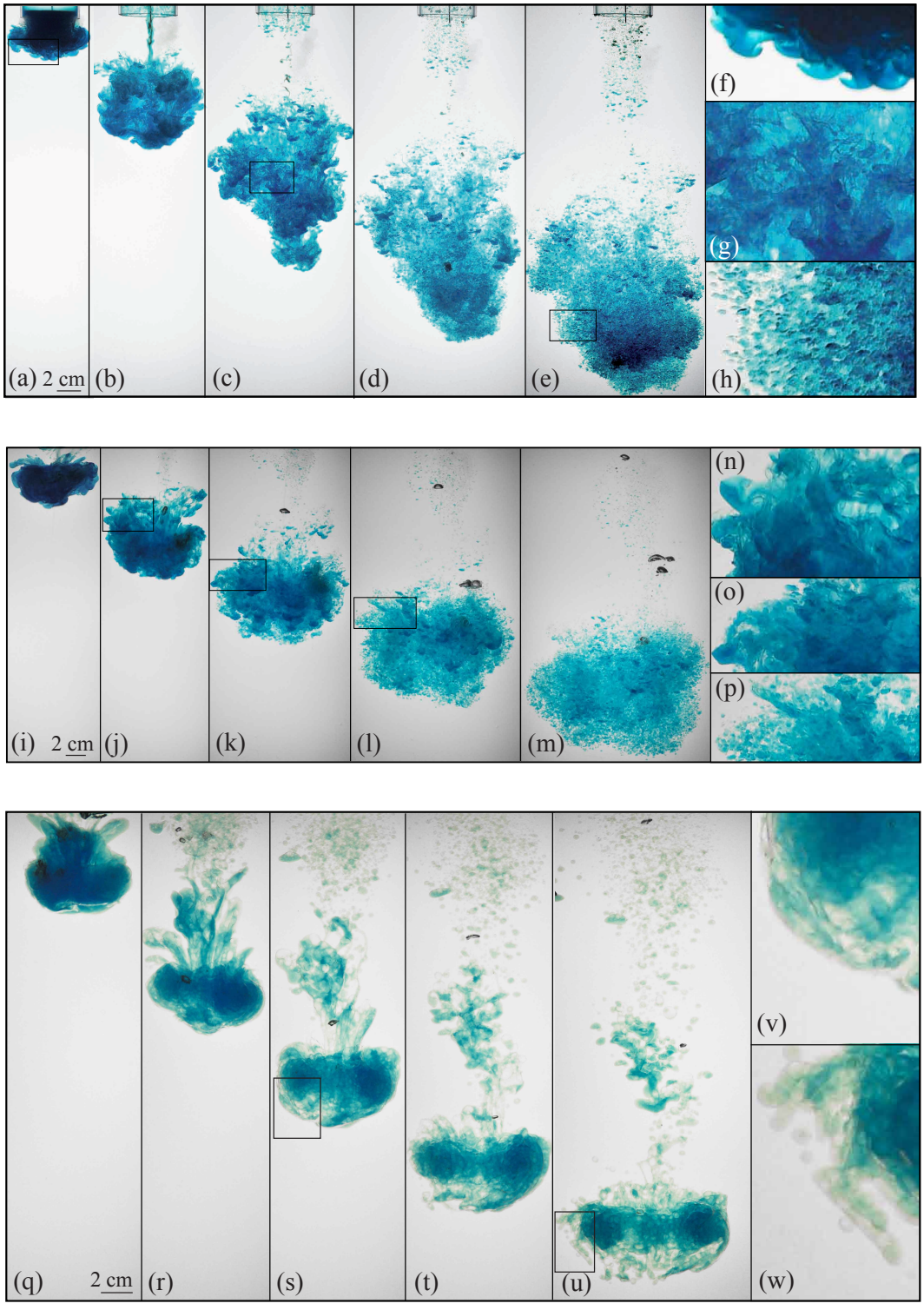

Figure 9.10: Turbulent regime. (a-h) Immiscible turbulent thermal, $We \approx 10^3$, $P \approx 0.92$, Immersed configuration, time intervals of about 0.2 s. (i-w) Immiscible turbulent buoyant vortex rings, Surface configuration. (i-p) $We \approx 10^3$, $P \approx 0.82$, time intervals of about 0.2 s; (q-w) $We \approx 200$, $P \approx 0.03$, time intervals of about 0.4 s. (f,g,h) (n,o,p) (v,w) Close-ups corresponding to the square boxes in (a,c,e), (j,k,l) and (s,u), respectively.

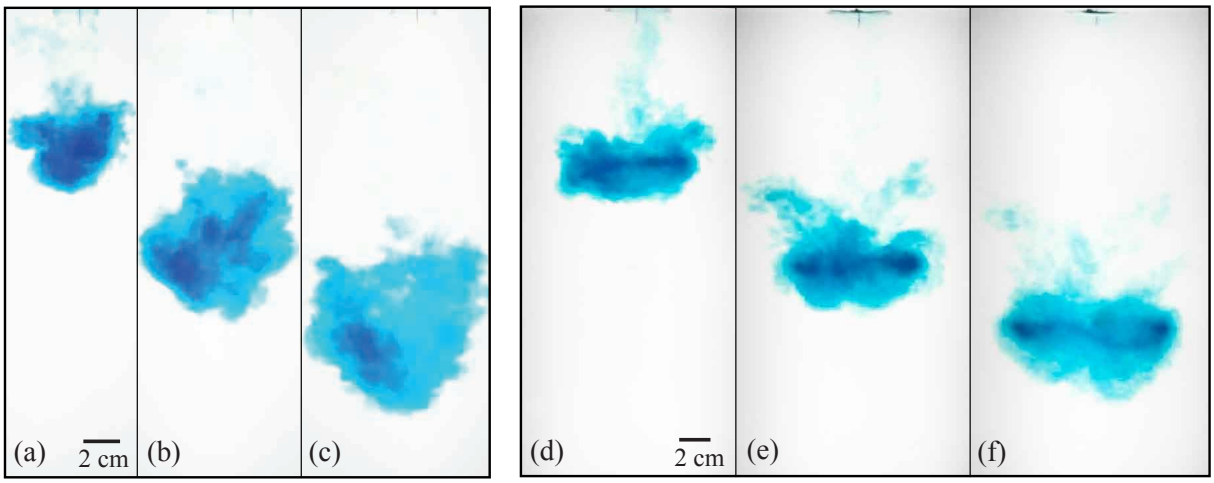

Figure 9.11: Turbulent experiments with miscible fluids. (a-c) Miscible turbulent thermal, $Re \approx 2\times10^3$, $P \approx 0.19$, Immersed configuration, time intervals of about 0.6 s. (d-e) Turbulent buoyant vortex ring, Surface configuration, $Re \approx 4\times10^3$, $P \approx 0.19$, time intervals of about 0.3 s.

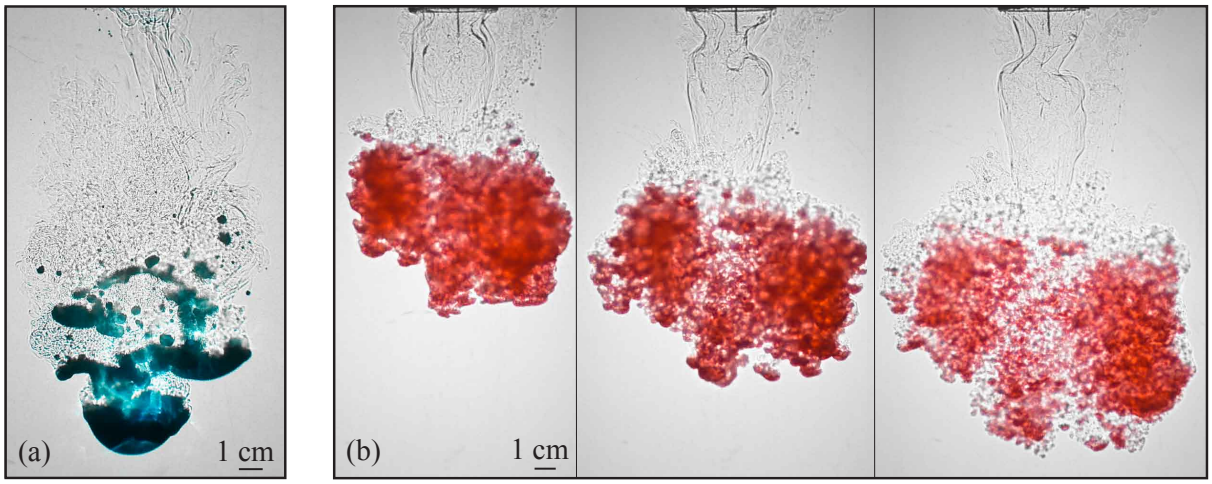

Figure 9.12: Shadowgraphs. (a) Jellyfish regime, $We \approx 30$, $P \approx 0.22$, Immersed; (b) turbulent thermal, $We \approx 600$, $P \approx 0.54$, Immersed.

9.3 Final fragmentation stage: breakup

9.3.1 Description of the physical processes

As in other fluid fragmentation processes (Hinze, 1955), the deformations identified §9.1.2 and §9.2 result in the formation of elongated and filamentary structures, or liquid ligaments, (e.g. figure 9.7(d), 9.8(c,d,e,f), 9.9(d), 9.10(w)) and their destabilization, probably through capillary instabilities, leads to breakup. However the spatial distribution and formation time of these ligaments differ from one fragmentation regime to the other.

In the jellyfish (figure 9.7(d)) or the RT piercing (figure 9.8(c,d,e,f) and Movie 1) regimes thin filamentary structures connect larger blobs of released fluid. In the vortex

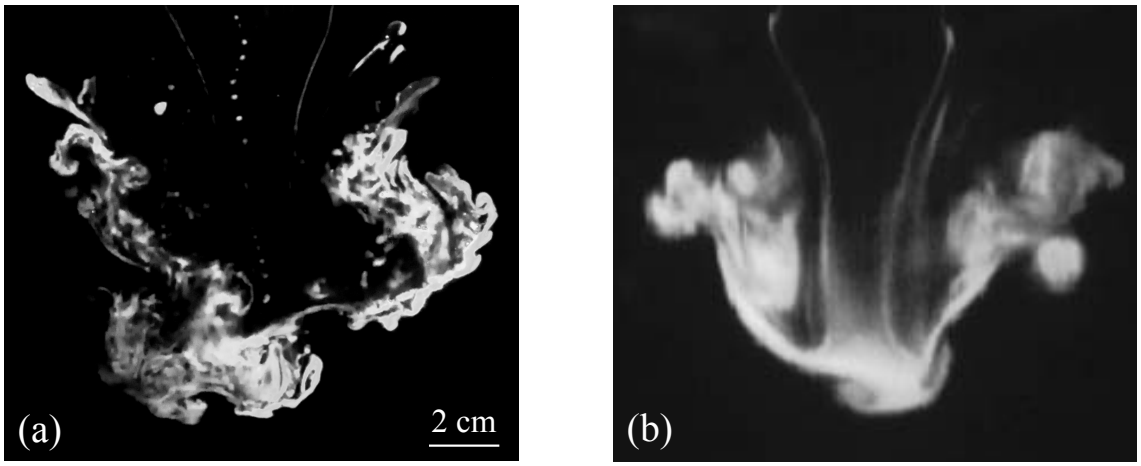

Figure 9.13: (a) Cross-section of an immiscible turbulent thermal, obtained using light-induced fluorescence, $We \approx 10^3$, $P \approx 0.54$, Immersed, $z \approx R$. (b) Turbulent thermal with miscible fluids, picture from Bond & Johari (2010) turned upside down, $Re \approx 5000$, $P \approx 0.05$, $z \approx 3R$.

ring destabilization regime the azimuthal waves result in the formation of thinner portions on the ring (figure 9.9(c)), which eventually break the ring in separated blobs (between figures 9.9(c) and 9.9(d)). In the meantime, the azimuthal disturbances are stretched by the mean shear flow leading to the formation of spiraling filaments located preferentially on the ring boundaries (arrows in figure 9.9, Movie 2).

In the turbulent vortex ring regime at $P \approx 0.03$, ligaments form at the external boundary of the ring (figure 9.10(u,w)). The ligament formation, followed by their breakup, is a multi-step process: the ring is progressively peeled, whereas the primary breakup of the entire released fluid volume occurs in a single and brief event in the turbulent regime for $P \gtrsim 0.2$ (between figures 9.10(d) and 9.10(e), and between figures 9.10(j) and 9.10(l), see also Movie 3). In this case, as can be inferred from figures 9.10(b,c) and from the cross-section in figure 9.13, breakup probably results from capillary instabilities on filamentary structures stretched by the turbulent flow in the entire thermal volume. However, higher temporal and spatial resolution is required to test this interpretation.

9.3.2 Breakup length

The dimensionless breakup length L_B, is defined as the dimensionless distance from the tube at which the number of connected objects in binary images starts to increase (see insert in figure 9.14(a)). It marks the beginning of primary breakup. Drops formed in the rear of the released fluid from the rupture of a membrane that remains attached to the tube (e.g. figures 9.7(b,c), figure 9.8(b)) or from breakup in the wake of turbulent thermals or vortex rings (e.g. figure 9.10) are not taken into account.

In Immersed experiments, the jellyfish, RT piercing and turbulent regimes correspond to specific regions in figure 9.14(a). For a given P value in the jellyfish and RT piercing regimes, the overall trend of the dimensionless breakup length is a decrease with increasing We. In the turbulent regime, the variation of L_B with We is within the experimental error and in the range $4.5 - 7.5$.

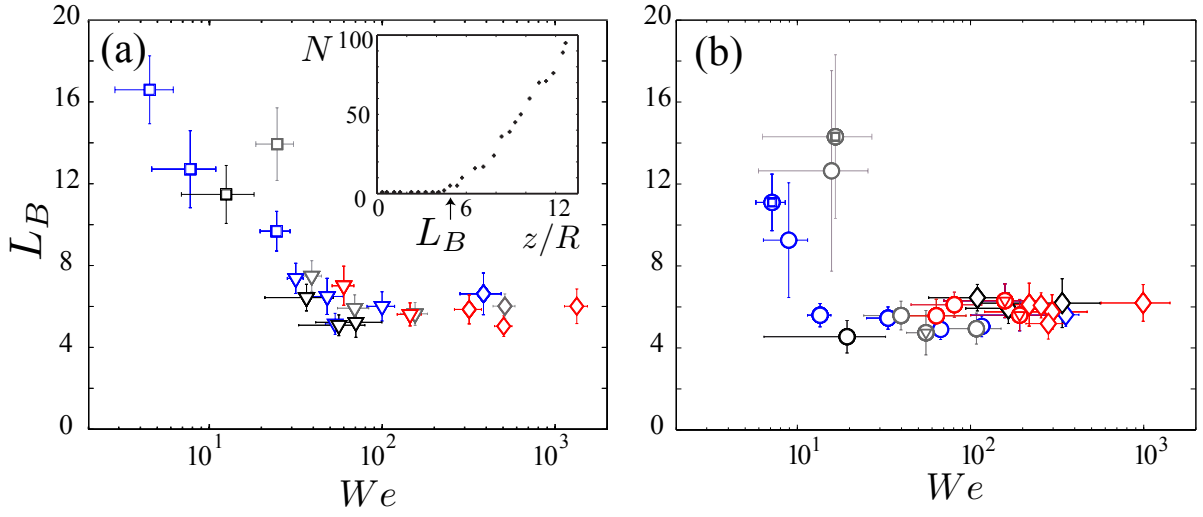

Figure 9.14: Dimensionless breakup length as a function of Weber number in (a) Immersed and (b) Surface experiments. Symbol shapes: as in figure 9.6. Black: $P \approx 0.03$; blue: $P \approx 0.22$; grey: $0.43 \leq P \leq 0.54$; red: $0.83 \leq P \leq 0.96$. Insert in (a): number of connected objects N in binary images as a function of dimensionless distance from the tube in a given experiment.

In Surface experiments (figure 9.14(b)), the different regimes overlap, with no distinctive behavior from one regime to the other, suggesting common destabilizing mechanisms. For $We \lesssim 40$ significant variations of L_B are seen and our data suggest an overall decrease of L_B with We, at fixed P for $We \lesssim 40$. Given experimental errors, no significant variation of L_B is seen for $We \gtrsim 40$: the different fragmentation regimes collapse between $L_B \approx 4.5$ and $L_B \approx 7$.

9.4 Integral model for the turbulent regime

It has been shown in §9.2 that the flow takes the form of turbulent vortex rings (Surface experiments) and turbulent thermals (Immersed experiments) for $We \gtrsim 200$. Following Deguen *et al.* (2011), we assume that immiscibility does not affect the macroscopic behavior of such structures, so that we can apply models that have been developed in the context of miscible fluids (Morton *et al.*, 1956; Maxworthy, 1974; Escudier & Maxworthy, 1973; Thompson *et al.*, 2000) and particle clouds (Bush *et al.*, 2003) at high Reynolds numbers. In the present section we consider the general case of buoyant vortex rings, allowing for initial momentum and large density differences between the ring and the ambient fluid. Re is in the range $4000 - 11000$ in the experiments considered in this section.

9.4.1 Theoretical considerations

Following the turbulent entrainment hypothesis (Taylor, 1945; Morton *et al.*, 1956), we assume that the rate of growth of the vortex ring mass is proportional to its velocity and its surface area:

$$\frac{d}{dt}\left[\frac{4}{3}\pi\rho r^3 c_1\right] = 4\pi r^2 c_2 \alpha \rho_a u, \tag{9.14}$$

where ρ is the mean density of the ring, u is the ring velocity, c_1 and c_2 are shape factors which relate the actual volume V and surface area of the ring to those of an equivalent sphere of radius r, r being a measure of the size of the moving fluid mass, and α the entrainment coefficient as introduced in Taylor (1945) and Morton *et al.* (1956).
Making use of the relations $\rho r^3 = \Delta\rho R^3/c_1 + \rho_a r^3$ and $u = dz/dt$, the mass conservation equation (9.14), in the absence of density stratification, becomes

$$\frac{dr}{dz} = \alpha', \tag{9.15}$$

where $\alpha' = \alpha c_2/c_1$. Equation (9.15) implies that $r \propto z$ at all times whenever the entrainment coefficient α' is constant. This linear relationship between r and z can be derived from dimensional analysis in the special case of a Boussinesq thermal (Batchelor, 1954) or a non-buoyant vortex ring (Maxworthy, 1974).

In the absence of density stratification the total buoyancy $b = (\rho - \rho_a)/\rho_a g V$ of the moving fluid mass is conserved and equal to its initial value B. Then, the impulse conservation equation takes the form

$$\frac{d}{dt}\left[\frac{4}{3}\pi(\rho + k\rho_a) r^3 c_1 u\right] = \rho_a B - \frac{1}{2} C'_D \rho_a u^2 \pi r^2, \tag{9.16}$$

where $C'_D = C_D c_3$, c_3 is another shape factor, C_D is the drag coefficient and the added mass coefficient k accounts for the change in kinetic energy of the surrounding fluid (Saffman, 1992; Escudier & Maxworthy, 1973).

Using the equivalent radius of the released fluid R as a length scale and $R^2\sqrt{(4/3\pi)/B}$ as a time scale, the final set of non-dimensional equations takes the form

$$\left[P + (1+k)c_1\tilde{r}^3\right]\frac{d\tilde{u}}{d\tilde{t}} = 1 - 3\alpha'\left[c_1(1+k) + \frac{C'_D}{8\alpha'}\right]\tilde{r}^2\tilde{u}^2, \tag{9.17}$$

$$\frac{d\tilde{r}}{d\tilde{t}} = \alpha'\frac{d\tilde{z}}{d\tilde{t}}, \qquad \frac{d\tilde{z}}{d\tilde{t}} = \tilde{u}. \tag{9.18}$$

Equation (9.17)-(9.18) can be integrated in time if α', C'_D, k, c_1 and the initial conditions on $\tilde{u}$, $\tilde{r}$ and $\tilde{z}$ are given.

Since $d\tilde{r}/dt = \alpha'\tilde{u}$, (9.17) becomes

$$\frac{\alpha'}{2}\left[P + (1+k)c_1\tilde{r}^3\right]\frac{d\tilde{u}^2}{d\tilde{r}} = 1 - 3\alpha\left[c_1(1+k) + \frac{C'_D}{8\alpha}\right]\tilde{r}^2\tilde{u}^2. \tag{9.19}$$

For constant values of C'_D, k, c_1 and α', the general solution of the first-order linear differential equation (9.19) is

$$\tilde{u}^2 = \frac{2}{\alpha'}\int_{\tilde{r}_0}^{\tilde{r}} \frac{\left(P+(1+k)c_1x^3\right)^{\gamma-1}}{\left(P+(1+k)c_1\tilde{r}^3\right)^{\gamma}}\mathrm{d}x + \tilde{u}_0^2\left[\frac{P+(1+k)c_1\tilde{r_0}^3}{P+(1+k)c_1\tilde{r}^3}\right]^{\gamma}, \tag{9.20}$$

where $\gamma = 2 + C'_D/\left(4\alpha'(1+k)c_1\right)$ and the subscript $_0$ denotes initial conditions. Closed-form solutions for $\tilde{u}$ exist if $C'_D = 0$ or, if the Boussinesq approximation is valid ($P \ll 1$), for arbitrary values of C'_D (given in appendix F).
In the following limit:

$$\tilde{z} - \tilde{z}_0 \gg \frac{\tilde{r}_0}{\alpha'} \text{ and } \tilde{z} - \tilde{z}_0 \gg \frac{\tilde{r}_c}{\alpha'} \text{ where } \tilde{r}_c \text{ satisfies } (1+k)c_1\tilde{r}_c^3 \gg P,$$

the solution (9.20) has an asymptote given by

$$\tilde{u}^2 \approx \frac{2}{\alpha'^3(1+k)c_1(3\gamma-2)}\frac{1}{\left(\tilde{z}-\tilde{z}_0\right)^2}\left[1+\left(\frac{L_M}{\tilde{z}-\tilde{z}_0}\right)^{3\gamma-2}\right], \tag{9.21}$$

where L_M is given by

$$L_M = \left(\frac{1}{2}\alpha'^3(1+k)c_1(3\gamma-2)\tilde{u}_0^2\right)^{1/3\gamma-2}\left(\frac{P+(1+k)c_1\tilde{r_0}^3}{(1+k)c_1\alpha'^3}\right)^{\gamma/3\gamma-2}. \tag{9.22}$$

Since $3\gamma - 2 > 0$, L_M is the distance over which the initial momentum affects the solution, often called the Morton length. If $\tilde{z} - \tilde{z}_0 \gg L_M$ the initial momentum becomes inconsequential and the flow reaches the same asymptotic regime as in thermals, i.e. in terms of dimensional variables

$$u(z) \approx f\frac{\sqrt{B}}{z-z_0}, \tag{9.23}$$

$$\frac{d\left(z-z_0\right)^2}{dt} \approx 2f\sqrt{B}, \tag{9.24}$$

$$\text{where } f = \left\{8/3\pi c_1(1+k)\alpha^3 + C'_D/2\pi\alpha^2\right\}^{-1/2}. \tag{9.25}$$

In miscible turbulent thermals (Scorer, 1957; Richards, 1961; Thompson *et al.*, 2000) or in non-buoyant vortex rings (Maxworthy, 1974; Glezer & Coles, 1990) the size of the structure grows linearly with depth as predicted by (9.15) for a constant α' value. In miscible thermals the entrainment coefficient is usually determined by measuring the growth of the thermal half-width and typically $\alpha_T = 0.25 \pm 0.1$, where α_T is the entrainment coefficient for thermals. The entrainment coefficient of non-buoyant vortex rings, α_V, is commonly determined by measuring the growth of the radius of the vortex ring core and it can be described as $\alpha_V = 0.01 \pm 0.005$. The entrainment coefficients of buoyant vortex rings were not directly reported by Turner (1957) but values ranging from 0.02 to 0.18 can be extracted from his figure 3 and other parameter estimations. These values lie between α_V and α_T, the lowest values being reached when the ratio of initial impulse to buoyancy force is the highest, i.e. when the initial momentum dominates the total momentum.

Given such observations, the entrainment coefficient has to vary with time in a buoyant vortex ring since the flow eventually behaves as a thermal as predicted by (9.23)-(9.25) and α' is equal to α_T in this asymptotic regime. From a theoretical point of view, it is then important to take into account such effects in order to develop a self-consistent model for buoyant vortex rings.

In turbulent buoyant jets the entrainment coefficient varies during the transition from a jet-like to a plume-like behavior (Fisher *et al.*, 1979; Wang & Law, 2002). The parameterization proposed by Fisher *et al.* (1979) is empirical and assumes an exponential dependence of the entrainment coefficient on a local Richardson number that represents the ratio of buoyancy to inertial forces. Other parameterizations, one inspired by the work of Priestley & Ball (1955) and the other developed by Kaminski *et al.* (2005), predict that the entrainment coefficient is a linear function of a local Richardson number. By analogy, we expect a buoyant vortex ring to evolve from a vortex ring-like behavior when the excess in initial momentum dominates the total momentum and to a thermal-like behavior when the initial momentum has become inconsequential and negligible with respect to the buoyancy-induced momentum. During this transition the entrainment coefficient would vary from α_V to α_T depending on a local Richardson number Ri; a possible definition of this parameter being

$$Ri = \frac{\Delta\rho g R^3}{\rho u^2 r^2}. \tag{9.26}$$

According to this definition, Ri varies from 0 in non-buoyant vortex rings to a constant value $Ri_T = 2c_1(1+k)\alpha_T + \frac{3}{8}C'_D$ in boussinesq thermals when $r \gg R$ (asymptotic regime given by equations (9.23)-(9.25)). Turner (1957) showed that the entrainment coefficient of a buoyant vortex ring in which the circulation K remains constant is proportional to B/K^2, which is the ratio of buoyancy to inertial forces, i.e. a Richardson number. The circulation of a buoyant vortex ring is probably not conserved and partly lost to the wake by shedding of vortical structures as observed in non-buoyant vortex rings (Weigand & Gharib, 1994). However Turner's result gives a physical argument in favour of a linear relationship between α' and Ri. In summary, a natural parameterization to account for variations of α' in buoyant vortex rings is

$$\alpha' = \alpha_V + (\alpha_T - \alpha_V)\,\frac{Ri}{Ri_T}. \tag{9.27}$$

Equations (9.17)-(9.18) remain unchanged if α' varies with time. Thus, (9.17)-(9.18) and (9.27) can be coupled and integrated forward in time, giving a self-consistent model for the evolution of a buoyant vortex ring. It is important to emphasize that, once the parameterization between α' and Ri is specified, the above model has one free parameter less than in the case of a constant entrainment coefficient. For instance, in the case of parameterization (9.27), local values of Ri and α' can be experimentally determined, which leads to an estimation of Ri_T. From the estimation of Ri_T we obtain a linear relationship between C'_D and k, whereas these parameters are independent in the case of a constant entrainment coefficient.

	P	α'
Immiscible	0.220 ± 0.001	0.20 ± 0.03
	0.536 ± 0.002	0.25 ± 0.03
	0.954 ± 0.002	0.24 ± 0.05
Miscible	0.192 ± 0.001	0.24 ± 0.05

Table 9.1: Values of the entrainment coefficient α' in Immersed experiments at different density ratios, with miscible and immiscible fluids.

9.4.2 Experimental results - comparison with theory

In this section, the analogy with miscible turbulent thermals and vortex rings is tested by comparing results from immiscible fluid experiments with both theoretical predictions and experimental results obtained with miscible fluids.

9.4.2.1 Entrainment coefficient

Vortex ring equivalent radius and centroid are estimated from video images as described in chapter 8, considering the largest connected object in the image for the equivalent radius. In our immiscible thermals (Immersed experiments), the equivalent radius evolves linearly with the distance traveled, in agreement with equation (9.15) and with the turbulent entrainment hypothesis, as illustrated in figure 9.15. As shown in this figure, experiments with miscible and immiscible fluids have very similar behaviors, supporting the analogy with miscible thermals.

For each experiment an entrainment coefficient α' is estimated. As pointed out in previous studies (Scorer, 1957; Richards, 1961; Thompson *et al.*, 2000; Bush *et al.*, 2003) a large variability in α' between successive realizations is unavoidable and inherent to this turbulent flow, which is not quasi-stationary in the reference frame of the laboratory. The mean values of α' in Immersed experiments are reported in table B.7. Uncertainties take into account both the uncertainty on α' in each experiment and the variability between experiments. Note that the measured entrainment coefficient is $\alpha' = \alpha c_2/c_1$, which depends in principle on the method used to measure the radius and the position of the thermal through the coefficients c_1 and c_2. In our miscible fluid experiments we find $\alpha' = 0.25 \pm 0.05$ (table B.7), in agreement with previously published studies in which the maximal half-width of the thermal (rather than the equivalent radius) is used to estimate r. The use of the equivalent radius is favored in this study because the resulting signal is much smoother than when using the maximal width, which is very sensitive to local deviations from the self-similar behavior. In our immiscible thermals α' is slightly lower at $P \approx 0.22$ but, given the uncertainties, no significant variations of the entrainment coefficients with the density ratio is observed (table B.7). We conclude that the entrainment coefficient in our immiscible thermals, $\alpha' = \alpha_T$, is such that $\alpha_T = 0.23 \pm 0.06$, with no significant deviation from miscible thermals.

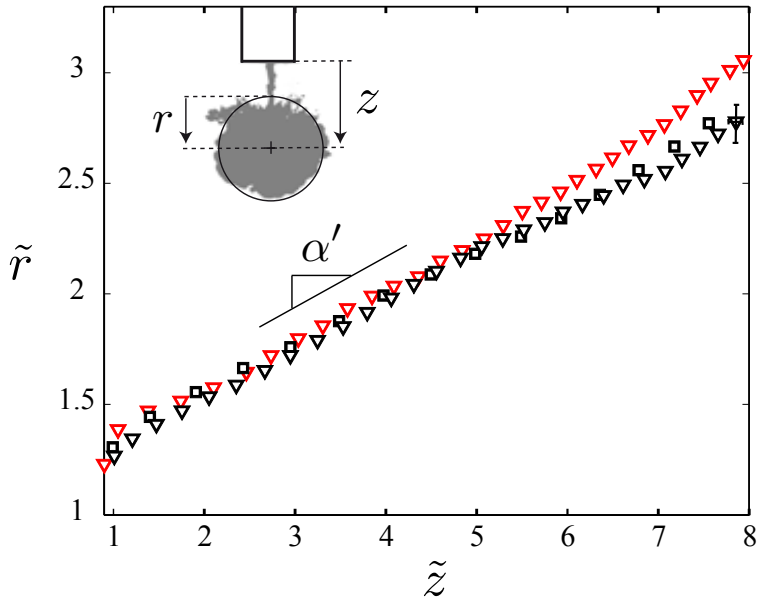

Figure 9.15: Dimensionless equivalent radius as a function of the dimensionless distance between the centroid and the tube in Immersed experiments; □ , $P \approx 0.92$; ▽ , $P \approx 0.22$; ▽ , *miscible fluids,* $P \approx 0.19$.

In Surface experiments, the equivalent radius varies linearly with depth, at least locally, and local values of α' can be estimated. Figure 9.16 shows that a wide range of α' values are found (from ~ 0.05 to ~ 0.25). It also illustrates that the local Richardson number is a control parameter of the entrainment coefficient. By definition, $\alpha' = \alpha_V$ in miscible fluid experiments with no initial buoyancy ($Ri = 0$, bottom-left corner in figure 9.26) and we obtain $\alpha_V = 0.012 \pm 0.003$, in agreement with previous results for non-buoyant vortex rings (Maxworthy, 1974; Glezer & Coles, 1990). The largest α' values are reached for the largest Ri values and correspond to experiments that have reached a turbulent thermal regime, with α' close to α_T and Ri close to Ri_T ($Ri_T = 0.7 \pm 0.2$ in our Immersed experiments). At intermediate Ri values ($\sim 0.4 \pm 0.2$), α' is in the range $0.05 - 0.17$. Figure 9.26 supports a dependence of entrainment on Ri. A best fit of the form $\alpha' = \alpha_V + (\alpha_T - \alpha_V)(Ri/Ri_T)^\beta$ for immiscible experiments yields $\beta = 1.2 \pm 0.2$, which is compatible with $\beta = 1$ and in agreement with (9.27).

9.4.2.2 Descent trajectory

Measured distance $\tilde{z} - \tilde{z}_0$ between vortex ring centroid and initial depth for the turbulent thermals (Immersed configuration) is compared with theoretical predictions obtained by numerical integration of equations (9.17)-(9.18) for a constant α' value, as measured in our experiments. In each experiment, we choose $\tilde{t}_0$ such that $\tilde{z}_0 \approx 1$ in order to ensure that the released fluid is entirely out of the tube at $\tilde{t}_0$. The corresponding initial conditions $\tilde{r}_0$ and $\tilde{u}_0$ are then extracted from each experiment. Squares in figure 9.17(a) illustrates the descent trajectory for a given turbulent thermal in the Immersed configuration. During the last phase, $(\tilde{z} - \tilde{z}_0)^2$ grows linearly with time, in agreement with the expected asymptotic behavior given by equation (9.24). The theoretical evolution fits the data shown in figure

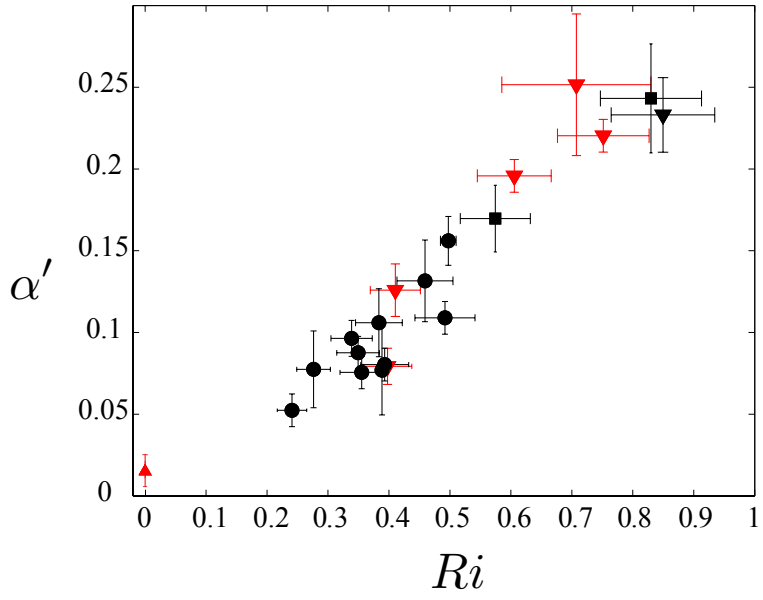

Figure 9.16: Measured turbulent entrainment coefficient as a function of the local Richardson number in Surface experiments. ■ , $P \approx 0.82$; ▼ , $P \approx 0.22$; ● , $P \approx 0.03$; ▼ , *miscible fluids,* $P \approx 0.19$; ▲ , *miscible fluids,* $P = 0$.

9.17(a) for $C'_D = 0.3 \pm 0.1$ if $k = 0$, and $k = 0.18 \pm 0.1$ if $C'_D = 0$ (solid curves). The large uncertainties on C'_D and k for a single experiment comes from the uncertainty on α'. The drag and added mass coefficients, C'_D and k, play a symmetric role in the theoretical solution: an increase in C'_D or k causes a decrease in the slope of $(\tilde{z}-\tilde{z}_0)^2$ in the asymptotic regime (figure 9.17(a)) as expected from equations (9.24)-(9.25). The theoretical solution is also sensitive to c_1 as shown in figure 9.17(a).

The values of C'_D, k and c_1 required to fit the descent trajectory vary between experiments. In 20% of the 20 Immersed experiments, the measured curve is located above the theoretical curve computed with ($c_1 = 1$, $k = 0$, $C'_D = 0$). As negative values for k or C'_D are not physical, these results require $c_1 < 1$. In those experiments, c_1 ranging from 0.8 to 0.9 fits the data, corresponding to an overestimation of the volume of about 20%. In the other Immersed experiments the values of C'_D and k required to fit the observed descent trajectory vary from 0 to about 0.5. Figure 9.17(b) illustrates the large variability in C'_D and k: since the experiments shown have similar α' values, the differences in terminal slope come from differences in C'_D and k. The latter coefficients are similar in our miscible fluid experiments and the descent trajectory is qualitatively very similar with miscible and immiscible fluids (figure 9.17(b)).

In Surface experiments (buoyant vortex rings), our results on the entrainment coefficient (figure 9.16), combined with theoretical predictions, require α' to vary with time, as already argued in 6.1. Thus, a parameterization such as (9.27) is required for a self-

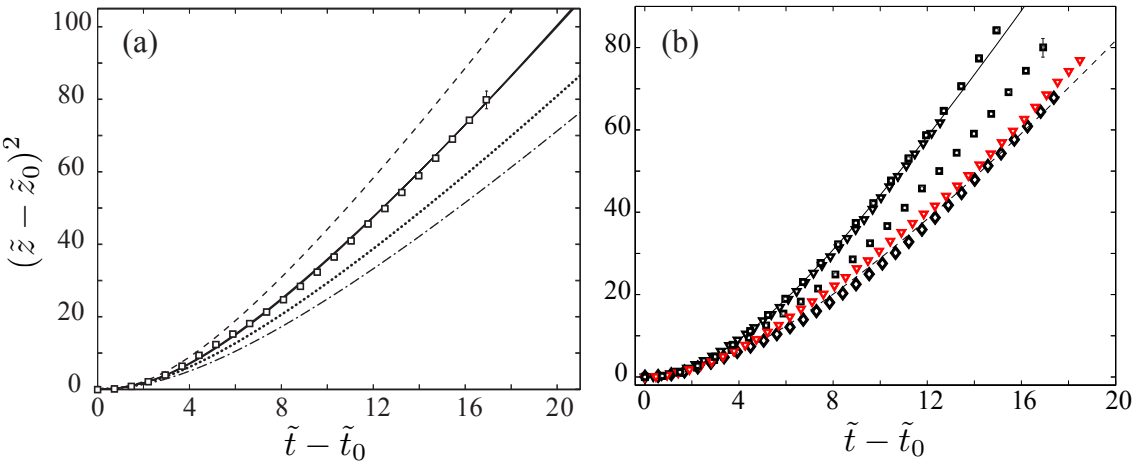

Figure 9.17: Square of dimensionless distance of the vortex ring's centroid from the initial depth as a function of dimensionless time for turbulent thermals in the Immersed configuration. □, $P \approx 0.92$; ◇ , $P \approx 0.54$; ▽ , $P \approx 0.22$; ▽ , *miscible fluids with* $P \approx 0.19$. *Curves are theoretical solutions obtained by numerical integration of equations (9.17)-(9.18) for constant* α' *values. (a) Solid curves: two theoretical solutions (indistinguishable from each other) with* ($c_1 = 1$, $C'_D = 0$, $k = 0.18$) *and* ($c_1 = 1$, $C'_D = 0.3$, $k = 0$). *Dotted curve:* $c_1 = 1$, $C'_D = 1$, $k = 0$. *Dot-dashed curve:* $c_1 = 1$, $C'_D = 0$, $k = 1$. *Dashed curve:* $C'_D = 0$, $k = 0.18$, $c_1 = 0.7$. *Theoretical curves are computed for* $\alpha' = 0.25$, *which is the value measured in the experiment shown in (a). (b) Immersed experiments in which* α' *takes similar values in the range* $0.23 - 0.25$. *Theoretical solutions with* ($c_1 = 1$, $C'_D = 0$, $k = 0$, $\alpha' = 0.24$) *and* ($c_1 = 1$, $C'_D = 0.35$, $k = 0.35$, $\alpha' = 0.24$) *are shown by solid and dashed curves respectively.*

consistent model that predicts the descent trajectory. Theoretical solutions obtained by numerical integration of equations (9.17)-(9.18), coupled with parameterization (9.27), fit the 16 Surface experiments used in this section with $C'_D = 0.6 \pm 0.3$ and $k = 0.4 \pm 0.4$, indicating that this model of buoyant vortex ring is consistent with our measurements. Ri_T, required in parameterization (9.27), is estimated in each experiment from local measurements of α' and Ri. We use the values of α_T and α_V that have been obtained in §9.4.2.1. Figure 9.18 illustrates the agreement between theoretical and experimental results for a single Surface experiment. When using parameterization (9.27), the best-fit theoretical curve is obtained for $C'_D = 0.7 \pm 0.1$ and $k = 0.4 \pm 0.2$ (with $c_1 = 1$, $\alpha_V = 0.012 \pm 0.003$ and $\alpha_T = 0.23 \pm 0.06$). α' varies from 0.04 to 0.14 in this theoretical solution (figure 9.18(b)). The uncertainties on C'_D and k in a single experiment are mainly due to uncertainties on α_T, α' and Ri. Note that the fit between the data and the theoretical solution is also good with a constant α' value (figure 9.18(a)).

The values we have found for (C'_D, k, c_1), as well as their large variability, are also consistent with results from previous studies. Ruggaber (2000) reports negative values for C'_D and k in turbulent particle clouds, which would be explained by $c_1 < 1$ in our formalism. The results by Bush *et al.* (2003) from particle cloud experiments and by Maxworthy (1974) from non-buoyant vortex rings suggest values of C'_D and k small compared to 0.5. Translated into our formalism, results of Gan *et al.* (2012) for non-buoyant vortex rings yield $k \approx 1$ and C'_D of order 0.05. Although Thompson *et al.* (2000) do not include the drag coefficient in their model, they report a mean k value of 0.25 and their data suggest

that k ranges from negative values to values close to 0.8.

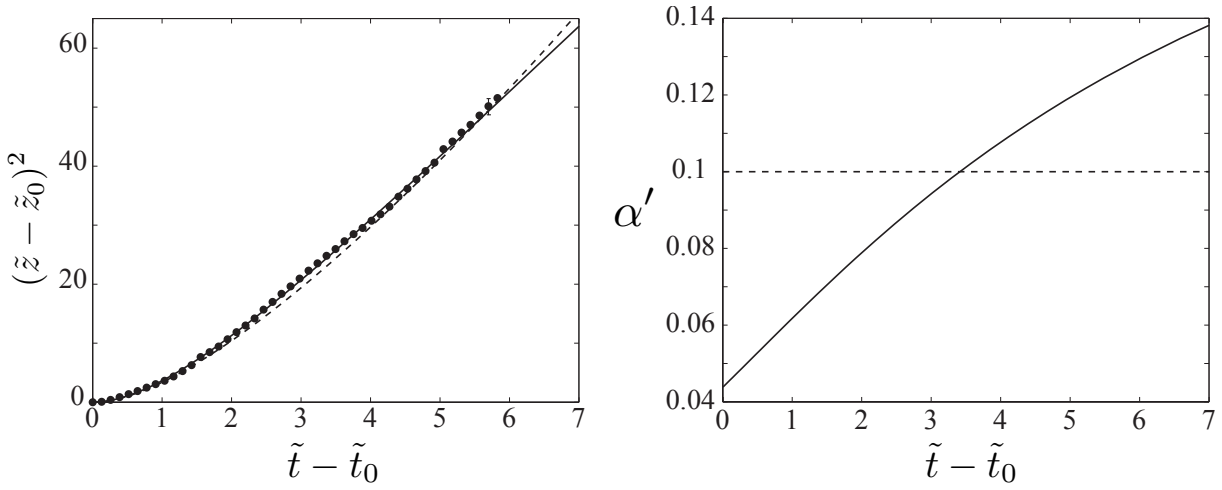

Figure 9.18: (a) Square of dimensionless distance of the vortex ring's centroid from the initial depth as a function of dimensionless time. ●, buoyant vortex ring in the Surface configuration with $P \approx 0.03$. Uncertainties are of the order of the symbol size. Black curves are theoretical solutions obtained by numerical integration of equations (9.17)-(9.18) with either a constant α' value (dashed curve) or α' that varies with time according to (9.27) (solid curve). $\tilde{t}_0$ is chosen such that $\tilde{z}_0 \approx 2$. Dashed curve: $\alpha' = 0.1$, $C'_D = k = 0.34$, $c_1 = 1$. Solid curve: $k = 0.45$, $C_D = 0.68$, $c_1 = 1$. (b) Entrainment coefficient as a function of dimensionless time in the two theoretical solutions shown in (a).

Finally, once the asymptotic regime is reached we expect the slope of the curve $(z-z_0)^2$ as function of time to be equal to $2f\sqrt{B}$ according to equations (9.24)-(9.25). The final value of this slope in each experiment is computed and shown in figure 9.19 as a function of $\sqrt{B}$. The final slope is indeed positively correlated with $\sqrt{B}$ and the data from immiscible fluid experiments are aligned with results from miscible fluid experiments. Two main ingredients explain the large scatter in figure 9.19: first, the asymptotic regime is not perfectly reached in our experiments and, second, the value of α', C'_D and k varies from one experiment to the other, inducing a large variability in the value of the coefficient f according to equation (9.25).

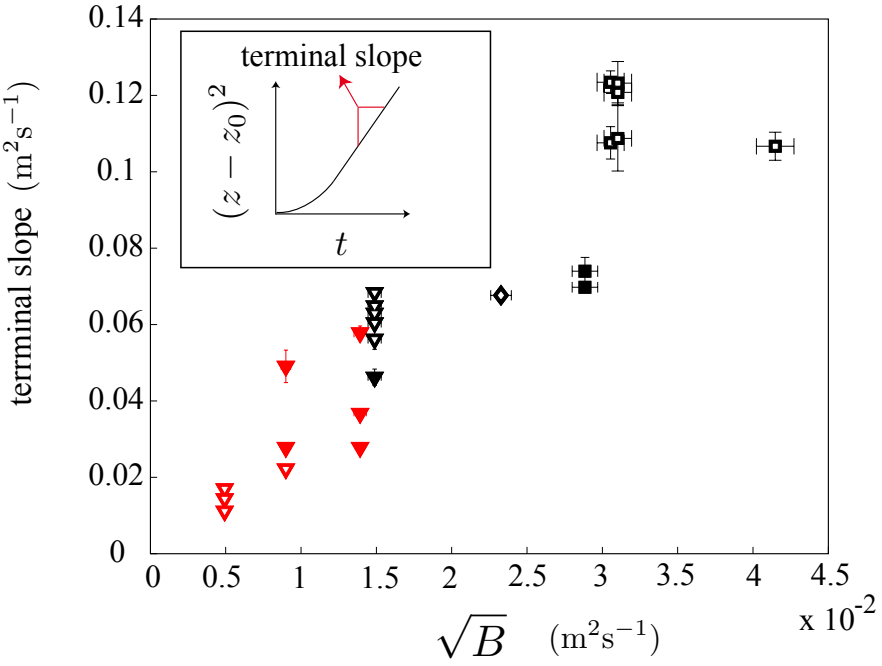

Figure 9.19: Terminal slope of the curve $(z-z_0)^2(t)$ (as depicted in the insert) as a function of the square root of the buoyancy. Open symbols correspond to Immersed experiments, filled symbols to Surface experiments. ■, □ , $0.82 \leq \Delta\rho/\rho_a \leq 0.96$; ◇ , $\Delta\rho/\rho_a \approx 0.54$; ▼ , ▽ , $\Delta\rho/\rho_a \approx 0.22$; ▼ , ▽ , *miscible fluids with* $\Delta\rho/\rho_a \approx 0.19$.

Chapter 10

Discussion and conclusion

10.1 Discussion of experimental results

We find that, in agreement with the literature on fluid fragmentation, and especially on drop breakup at low Oh (Hinze, 1955; Pilch & Erdman, 1987; Gelfand, 1996; Guildenbecher *et al.*, 2009), the Weber number is the control parameter governing regime transitions in our experiments, whereas P has an influence mostly within the fragmentation regime (figure 9.6).

The vortex ring destabilization regime found in this study is morphologically different from the regime observed by Baumann *et al.* (1992). In their study, immiscible vortex rings are rather viscous ($Re \leq 61$) whereas, in the present study, $Re \geq 10^3$ in most immiscible vortex rings, closer to inviscid dynamics. The destabilization of vortex rings in Baumann *et al.* (1992) is interpreted as a manifestation of RTI and is morphologically similar to the instability observed in miscible fluids when a drop of a heavier liquid falls inside a lighter one (Kojima *et al.*, 1984; Arecchi *et al.*, 1989, 1991; Buah-Bassuah *et al.*, 2005). The centrifugal to gravitational acceleration ratio is much smaller than 1 in the vortex rings of Baumann *et al.* (1992), indicating that RTI are mainly driven by gravity. The same ratio (roughly estimated from video images) reaches values of about 0.5 in some of our immiscible vortex rings, demonstrating that the destabilizing mechanisms can not be identical to those in Baumann *et al.* (1992).

A progressive transition leads to a turbulent regime that is observed for $We \gtrsim 100 - 200$ in both Immersed and Surface experiments. We emphasize that in (Bo, P) space the transition to turbulence would occur at different parameter values in Immersed and Surface experiments. For instance, turbulent surface experiments at $P \approx 0.03$ and $We \geq 100$ have a rather low Bo value compared to other turbulent experiments.

In our turbulent experiments, the turbulent entrainment concept describes the large-scale evolution of the released fluid even before breakup occurs, for distances smaller than $4.5 - 7.5$ initial radii. At this stage, both the ambient and released fluids form continuous, non-dispersed phases.

It is not clear whether our turbulent regime corresponds to the regime described by Yang & Yang (1990). In our experiments, the entrainment coefficient decreases when reducing the local Richardson number Ri. Yang & Yang (1990) report that the entrainment coefficient grows as the square root of the Weber number, at similar Bo values. Noting

that $Ri = O(Bo/We)$, their results seem to be at variance with ours, and may indicate that the fully turbulent regime has not been reached in their experiments.

For sufficiently large We, the dimensionless breakup length remains in the range $4.5-7.5$, with no significant variations when increasing further We. These results suggest either that L_B tends towards a constant in the limit of large We, or that it exhibits a weak dependence on We. Further investigations of the turbulent regime at $We \geq 10^3$ are required to test these hypotheses. However, a result shared by all these studies is that, for large enough We and $Oh \ll 1$, the dimensionless breakup time shows no significant dependence on We, which is in agreement with our data.

10.2 Geophysical implications

The migration and fragmentation of liquid metal in fully liquid silicate magma oceans is likely to have played an important role in determining the final composition of Earth's core and Earth's mantle since the small-scale intermingling between metal and silicates allowed for chemical equilibration (Dahl & Stevenson, 2010). Therefore, geophysical and geochemical implications are closely related. Indeed, the only data available in this field of study are geochemical data: Abundances of refractory siderophile (i.e. metal-loving) elements in the Earth's mantle provide information concerning thermodynamic conditions during metal-silicate equilibration (e.g. Wade & Wood, 2005; Siebert *et al.*, 2011), and extinct radioactivity (Hf/W and U/Pb systematics) allows estimations of some characteristic time scales related to core formation (e.g. Lee & Halliday, 1995; Yin *et al.*, 2002; Kleine *et al.*, 2002; Rudge *et al.*, 2010). However, geochemical models are highly underdetermined when partial equilibration between metal and silicates is considered (e.g. Kleine *et al.*, 2004; Halliday, 2004; Rudge *et al.*, 2010) and understanding the involved physical processes may provide additional constraints required for full interpretation of geochemical data. Although the work presented in this manuscript is essentially a fluid mechanic study, it is important to bear in mind such longer-term objectives when discussing geophysical implications.

After an impact between differentiated (i.e. formed of a silicate mantle and metallic core) planetary embryos, the initial radius and post-impact velocity of released metal blobs are expected to be in the range $50-500$ km and $0.1-10$ km·s^{-1}, respectively (Rubie *et al.*, 2003; Canup, 2004; Deguen *et al.*, 2011). The depth of the magma ocean was, at most, of the same order of magnitude as the depth of the present Earth's mantle, i.e. about 3000 km. Thus, the characteristic time scale for the first stages of metal migration in a magma ocean did not exceed a few hours, suggesting that the effects of rotation can be neglected at first order. The density of liquid metal and liquid silicates at magma ocean depths are typically in the range $7000-9000$ kg·m^{-3} (Morard *et al.*, 2013) and $3000-4000$ kg·m^{-3} (Miller *et al.*, 1991), respectively. The interfacial tension between liquid metal and liquid silicates is expected to be of order 1 J·m^{-2} (Chung & Cramb, 2000), although it varies significantly with temperature, light element content and pressure (Terasaki *et al.*, 2012). The viscosity of a fully liquid magma ocean is at most of order 0.1 Pa·s (Liebske *et al.*, 2005; Karki & Stixrude, 2010) while it is likely to be in the range $10^{-3} - 5 \times 10^{-2}$ Pa·s for liquid metal (Funakoshi, 2010; de Wijs *et al.*, 1998). With the above estimates, we expect $We \gtrsim 10^{12}$, $Oh \lesssim 10^{-5}$, $Bo \gtrsim 10^{13}$ and $Re \gtrsim 10^{11}$ following an impact (using the equivalent radius of the metal blob as a length scale), with a density ratio P of order 1

for the metal-silicate system.

Although our laboratory experiments are far from reproducing post-impact conditions that prevailed during planetary formation, they give insights into the flow regime associated with the fragmentation of metal blobs in a fully liquid magma ocean. If we locate proto-planets, including proto-Earth, in the regime diagram of figure 9.6, they would be close to the line $P = 1$ at $We \geq 10^{12}$, indicating that the geophysical flows of interest are located well above the onset of the turbulent regime at $We \sim 200$. Thus, even if the largest We values reached in our experiments are more than 9 orders of magnitude smaller than in the geophysical system (figure 10.1), we have explored the regime that is relevant (at least in terms of large-scale flow) for core formation.

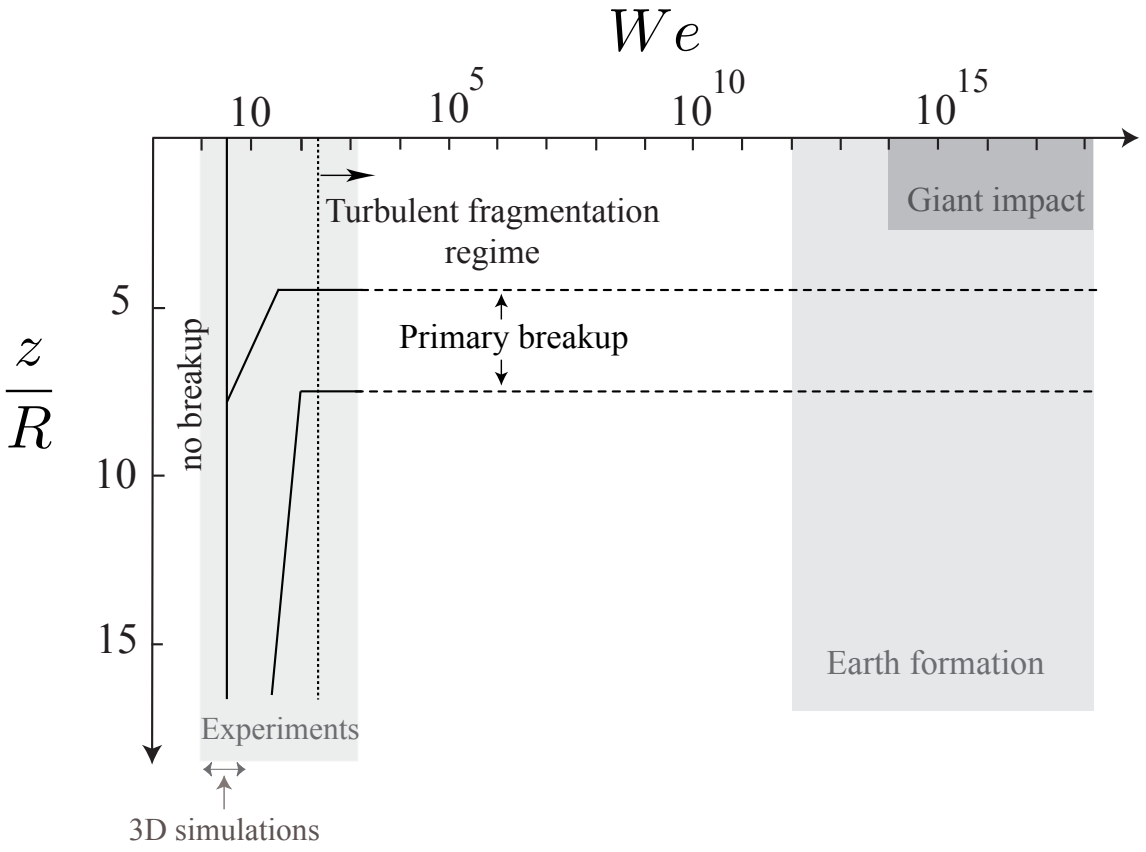

Figure 10.1: Transitions that may be relevant for the geophysical problem in a Weber number versus dimensionless depth diagram. The domains explored by our experiments and during Earth formation are depicted by grey squares. Grey arrows locate the domain explored by 3D-simulations of the fragmentation of liquid metal in a magma ocean (Ichikawa et al.*, 2010). The dark grey square locates the region that can be explored after a giant impact ($R = O(1000)$ km). In this case, the depth z_{MO} of the magma ocean is such that z_{MO}/R is smaller than 4.5, the lower bound for primary breakup in our turbulent experiments.*

Morphologically, the turbulent fragmentation regime is very different from the classic picture found in the literature on planet formation, where a cascade of fragmentation events progressively leads to smaller and smaller fragments (Rubie *et al.*, 2003; Samuel, 2012), eventually resulting in an *iron-rain* falling in a magma ocean (Ichikawa *et al.*, 2010). It is also different from erosion models (Dahl & Stevenson, 2010) where metal-

silicate intermingling occurs only at the metal blob boundary. Our experiments rather suggest that metal fragmentation occurs in a turbulent immiscible vortex ring which grows by entrainment of silicates and where metal and silicates are intimately intermingled in the whole ring volume. Quantitative implications of those findings for mantle and core geochemistry are further discussed in a companion paper (Deguen *et al.*, 2013) (reproduced in appendix G) where a model of chemical equilibration between metal and silicates in a magma ocean is developed. The results of the latter study suggest that efficient chemical equilibration is expected between liquid metal and entrained silicates once the flow is turbulent, and the final signature on geochemical data depends essentially on the amount of silicates that are entrained with metal.

The integral model proposed in §9.4 is expected to apply for the migration of a metal blob in a fully liquid magma ocean. It provides the descent trajectory of the metal-silicate mixture and the amount of silicates that are mixed with metal. The latter can be deduced from equation (9.15) and depends on the value of the entrainment coefficient α'. For distances much larger than the Morton length L_M, the entrainment coefficient is equal to its value in turbulent thermals, i.e. $\alpha_T = 0.23 \pm 0.06$. For distances of the same order of magnitude as L_M or smaller, the value of α' depends on the local Richardson number and it takes values between $\alpha_V = O(0.01)$ and α_T. With $g = 5$ m·s^{-2}, the initial Richardson number for a 100 km sized metal blob can reach values in the range $10^{-3} - 10$ and in the range $10^{-2} - 100$ for a 1000 km sized blob. For initial Richardson numbers equal to 1 or larger, no significant departure from $\alpha' = \alpha_T$ can be caused by Ri variations. For cases where the initial Richardson number is of order $10^{-3} - 10^{-2}$, α' is expected to be initially close to its value in non-buoyant vortex rings, $\alpha_V = O(0.01)$. In such cases, L_M is of about 100 initial radii, which is always larger than the magma ocean depth, suggesting that the entrainment coefficient is influenced by Ri during the entire fall. Thus, a large post-impact velocity can decrease the rate of entrainment by a factor 10, reducing the total volume of silicates mixed with metal during its fall by a factor 10^3. This effect should be taken into account in models of metal-silicate equilibration.

As discussed in the previous section, it is possible that the dimensionless breakup length remains constant when We increases, taking values in the range $4.5 - 7.5$ initial radii. Then, breakup would occur during the fall for blobs with an equivalent radius at least 10 times smaller than the magma ocean depth (figure 10.1). In the case of giant impacts, the size of the impactor core is of the same order of magnitude as the depth of the magma ocean ($O(1000)$km) and it is possible that breakup does not begin before the liquid metal reaches the bottom of the magma ocean (figure 10.1). A secondary impact at the bottom of the magma ocean, with either liquid metal (if the magma ocean depth is equal to the mantle depth) or solid silicates, would then play a major role in the fragmentation process.

10.3 Conclusion

We have described a series of experiments on liquid-liquid fragmentation at low Oh, varying the density ratio ($0.03 \leq P \leq 0.95$) and the Weber number ($1 \lesssim We \lesssim 10^3$). We have shown that the typical stages of any fluid fragmentation process are found in our experiments: from the deformation and destabilization of the released fluid to the formation of liquid filamentary structures that break by capillary instabilities and form

fragments. We have studied the destabilization and macroscopic evolution of the released fluid, from which fragmentation regimes were characterized.

We have found that, at low and intermediate Weber numbers, the fragmentation regime is very sensitive to the release conditions (Immersed vs Surface) and a wide variety of regimes is identified. Most of those fragmentation regimes are influenced by early deformations, which result from a competition between growth of RTI and roll-up of a vortex ring.

At high Weber numbers ($We \gtrsim 200$) a turbulent flow regime is reached and the large-scale flow shares common features in all the experiments: the released fluid is contained inside a coherent structure whose shape is, at first order, self-similar during the fall and which grows by turbulent entrainment of ambient fluid. To our knowledge, we have reported the first visualizations of immiscible turbulent thermals and immiscible turbulent vortex rings in a non-dispersed medium. Previously published models based on the turbulent entrainment concept have been extended to the general case of buoyant vortex rings. Our results indicate a positive correlation between the entrainment coefficient and the local Richardson number. The consistency between experimental and theoretical results, and between results from miscible and immiscible fluid experiments, supports that the turbulent entrainment concept can be applied in the context of non-dispersed immiscible fluids at large Weber and Reynolds numbers.

Chapter 11

Outlook

The results presented in Part II of this manuscript suggest a number of possible investigations. Some of them are listed below.

11.1 Fluid mechanic investigations

In the present study, we have focused on macroscopic behaviors (regime characterization, initial deformations, integral model for the descent trajectory), which is the natural first step when exploring regions of parameter space that have not been reached in previously published studies. A direct development of our study is to focus on small-scale mechanisms leading to breakup and extract drop size distributions. From the study of the fragmentation of various liquid systems in air (drops, sheets, jets), it has been suggested that the breakup of liquid ligaments plays a crucial role in determining the final drop size distribution in the spray (Marmottant & Villermaux, 2004; Bremond & Villermaux, 2006; Villermaux & Bossa, 2009, 2011), with a strong influence of the Gamma distribution resulting from the breakup of each individual ligament (Villermaux *et al.*, 2004). A question that could be investigated is whether similar results hold in the turbulent fragmentation regime that has been identified in the present study (immiscible thermals and vortex rings) or whether drop size distribution is essentially influenced by turbulent energy cascades in this regime.

Buoyant vortex rings, especially with immiscible fluids, have received little attention until now. However, vortex rings are often described as elementary structures of turbulence (Maxworthy, 1974) and understanding the dynamics of buoyant vortex ring is a first step towards more complicated buoyancy-induced turbulent flows as encountered in geophysical contexts. Besides, in the context of core formation, dense metal blobs are expected to have a significant initial velocity and buoyant vortex rings at variable initial Richardson number are well-adapted to study the competing role of initial inertia and buoyancy. Below, possible investigations of buoyant vortex rings are suggested, in addition to the study of the small-scale mechanisms involved in the breakup of immiscible vortex rings, as mentioned above.

First, in the present study, we have identified a vortex ring destabilization regime, but the nature of the involved instability mechanisms remains unclear (Widnall, curvature, centrifugal or RT instability) and requires further investigations. Experiments, using a

piston-cylinder arrangement, and numerical simulations accounting for surface tension effects can be combined.

Second, our results in the turbulent vortex ring regime suggest a positive correlation between the entrainment coefficient and the local Richardson number. A linear relationship, which can be intuited from analogies with turbulent plumes or from Turner (1957)'s theory at constant circulation, is consistent with our preliminary results. A systematic experimental study of miscible buoyant vortex rings (easier to generate in the laboratory than immiscible rings) is required to confirm such a linear relationship.

Third, in the context of core formation, the length to width ratio of initial metal blobs is expected to range between values of order 1 to values much larger than 1 (Dahl & Stevenson, 2010; Canup, 2004) and it is not clear whether the dynamics will be closer to that of a vortex ring or of a jet. When a finite volume of fluid is released through a cylinder by a piston using miscible fluids, its final shape depends on the length to width ratio of the cylinder (Gharib *et al.*, 1998): a single vortex ring forms at small values of this ratio whereas, at larger values, a vortex ring detaches from a trailing jet, whose destabilization is mainly driven by shear instabilities. In addition to distinct destabilization mechanisms, a turbulent vortex ring and a trailing jet have different entrainment rate once they are turbulent, affecting the efficiency of mixing. The transition from vortex ring to trailing jet, and the associated critical aspect ratio, can be characterized experimentally for immiscible systems using a piston-cylinder apparatus.

Turbulent vortex rings are one example of shear flows in which irrotational fluid is entrained into a turbulent flow. Other examples are turbulent wakes, shear layers, jets and plumes. Such flows are encountered in a large number of geophysical and environmental contexts (volcanic eruptions, hydrothermal plumes, core formation, deep-water oil plume, convection in the atmosphere, ...) and characterizing the fundamental mechanisms involved in the turbulent entrainment process has been a long-standing problem in fluid mechanics. The two possible candidates are *nibbling* by viscous processes at the turbulence boundary and *engulfment* of large volumes of irrotational fluid by large-scale eddies in the turbulent region (e.g. Townsend, 1970). The engulfment scenario has first been favored (e.g. Brown & Roshko, 1974) whereas recent studies (Mathew & Basu, 2002; Westerweel *et al.*, 2005; Holzner *et al.*, 2007, 2008) argue that nibbling is the dominant process, contributing to about 90% of the total entrainment (Westerweel *et al.*, 2009). In the case of non-dispersed immiscible flows as those considered in this manuscript, the boundary between rotational and irrotational fluids is initially an immiscible interface and nibbling by viscous eddies is expected to be damped by surface tension. However, we found that the value of the entrainment coefficient in our immiscible vortex rings is similar to that obtained with miscible fluids. How can we reconcile such an observation with the fact that nibbling is found to be the dominant entrainment process in miscible fluids? Investigations of the detailed features of turbulence in immiscible turbulent plumes (better suited than vortex rings since they are quasi-stationary structures) could therefore provide important information concerning the fundamental mechanisms involved in the turbulent entrainment process.

11.2 Core formation

A first possible development suggested by the results reported in Deguen *et al.* (2013) (reproduced in appendix G) is to account for partial equilibration of silicates in geochemical models of core formation, rather than partial equilibration of metal as presently considered (e.g. Kleine *et al.*, 2004; Halliday, 2004; Rudge *et al.*, 2010). A longer-term objective is to develop geochemical models that integrate parameterizations based on robust physical considerations for the volume of entrained silicates. Our experimental results have shown that such an objective is realistic since the concept of turbulent entrainment is valid for immiscible fluids, indicating that the volume of entrained silicates after each impact can be parameterized as a function of only three parameters (as deduced from equation (9.15)): the volume of liquid metal, the entrainment coefficient α and the characteristic length scale of the magma ocean. The main difficulty is to consistently describe α, which may depend on additional parameters such as the Richardson number (discussed in chapter 10) or the Mach number that compares the flow velocity with the sound wave velocity (discussed in Deguen *et al.* 2013, reproduced in appendix G).

Le mot de la fin

Nous finirons avec une citation que j'ai gardée à l'esprit pendant toute cette thèse. Henri Poincaré conclut sur la définition de la masse, après avoir énoncé le principe fondamental de la dynamique :

"Nous sommes acculés à la définition suivante [...] : les masses sont des coefficients qu'il est commode d'introduire dans les calculs."
(Henri Poincaré, *La Science et l'Hypothèse*).

Cette citation souligne l'importance de l'aspect *conventionnel* dans les théories et les modèles en Physique : même les principes fondamentaux de la mécanique sont basés sur certaines conventions. Conventions choisies, parmi d'autres possibles, pour leur *parcimonie*.

Résumé de la thèse en français

Introduction générale

Notions utiles concernant l'objet géophysique

L'objectif de cette section est d'introduire les notions essentielles à la compréhension du contexte géophysique (formation du noyau des planètes telluriques et convection dans des noyaux sans graine) qui a inspiré les deux problèmes présentés dans ce manuscrit. Cette section s'adresse tout particulièrement au lecteur non-familier avec la dynamique interne des planètes.

Les planètes telluriques sont formées de plusieurs enveloppes qui peuvent être divisées en deux grandes unités :

- le manteau formé de roches silicatées ;
- le noyau, situé sous le manteau et formé principalement de fer.

Le noyau peut être (1) entièrement liquide, (2) entièrement solide ou (3) formé d'une graine solide et d'un noyau externe liquide. Le noyau terrestre est actuellement dans cette dernière configuration.

Dans la Terre, la limite graine-noyau externe correspond à un changement de phase associé à la solidification progressive du métal liquide. La température à cette profondeur est donc donnée par la température de fusion du fer, qui est estimée par des expériences de laboratoire sous haute pression et par des calculs ab-initio. Etant donné cette température, il est ensuite possible de calculer le profil de température à travers le noyau externe en supposant que ce dernier est vigoureusement "mélangé" par des mouvements de convection et que son entropie est invariante avec la profondeur. Dans un tel système, le gradient de température est appelé *gradient adiabatique* ; il résulte des variations de pression avec la profondeur et peut être exprimé comme une fonction de différents paramètres connus et de la température (équation (1.1)).

La structure principale (noyau et manteau) des planètes telluriques a été acquise pendant la formation du système solaire (Chambers & Wetherill 1998 ; Agnor *et al.* 1999 ; Yin *et al.* 2002 ; Schersten *et al.* 2006). Les planètes se seraient formées à partir d'une matière initialement contenue dans une *nébuleuse*, un nuage relativement homogène de gaz et de poussières. Ce nuage se serait effondrait pour formé un disque protoplanétaire. Les grains de poussières se seraient agglomérerés (via des mécanismes physiques encore controversés) pour former des corps kilométriques, appelés *planétésimaux*, qui à la suite de collisions successives auraient formé les planètes. Cette période d'accrétion a duré environ $10 - 100$ millions d'années (Chambers & Wetherill 1998 ; Agnor *et al.* 1999), ce qui est très bref comparé au 4.5 milliards d'années du système solaire. Pourtant il s'agit d'une période

cruciale puisque la composition globale du noyau et du manteau a été déterminée pendant l'accrétion. De plus, les planètes et leurs noyaux ont accumulé de la chaleur pendant l'accrétion, provenant (1) de l'énergie libérée pendant les impacts entre planétésimaux, (2) de l'énergie gravitationnelle libérée pendant la différentiation noyau-manteau et (3) de la décroissance radioactive d'éléments à courte durée de vie. Les planètes se sont ensuite progressivement refroidies au cours des temps géologiques par *convection* ou *conduction*, un processus appelé *refroidissement séculaire*. Ainsi, la température à la fin de l'accrétion fixe la condition initiale pour l'évolution thermique des planètes.

Le refroidissement séculaire peut induire des processus de convection dans les noyaux planétaires par deux mécanismes. Premièrement, des instabilités thermiques peuvent être entretenues si le flux de chaleur extrait du noyau par le manteau est plus grand que le flux de chaleur conduit le long du profil de température adiabatique. Deuxièmement, la solidification du noyau externe, plus riche en éléments légers (comme l'oxygène ou le souffre) que la graine, est associée à une décharge continue, à la base du noyau externe, d'un fluide moins dense du fait de sa composition, ce qui génère des instabilités convectives.

La viscosité du fer liquide est très faible (du même ordre que la viscosité de l'eau) et l'échelle de longueur d'un noyau planétaire est très élevée ($\sim 10^3$ km). Par conséquent, les mouvements fluides dans les noyaux externes des planètes telluriques sont associés à des nombres de Reynolds généralement très élevés, correspondant à des régimes d'écoulement turbulents.

Deux sujets indépendants, une approche commune

La figure 11.1 schématise l'histoire typique d'un noyau planétaire et localise les contextes géophysiques qui ont motivé les études présentées en partie I et II de ce manuscrit.

Dans la première partie de ce manuscrit, nous présentons une étude numérique de la convection thermique et de l'effet dynamo, forcés par chauffage interne, dans des sphères en rotation ; une configuration qui a reçu peu d'attention jusqu'à présent et qui est appropriée pour étudier la dynamique d'un noyau planétaire sans graine (figure 11.1). Cette étude a été réalisée à l'Institut de Physique du Globe de Paris avec Julien Aubert.

Dans la seconde partie de ce manuscrit nous remontons dans le temps et nous nous intéressons à la physique des dernières phases de formation de la Terre et de son noyau (figure 11.1), période durant laquelle l'essentiel de la masse de la Terre s'est accrétée lors de gros impacts entre des embryons planétaires déjà différenciés en noyau et en manteau (Melosh 1990 ; Yoshino *et al.* 2003 ; Schersten *et al.* 2006 ; Ricard *et al.* 2009). L'énergie relâchée durant chacun de ces impacts était suffisante pour fondre l'impactant et une partie de la proto-Terre, créant un environnement où le métal liquide de l'impactant migre dans un océan de magma liquide (Tonks & Melosh 1993 ; Pierazzo *et al.* 1997). Comme le métal liquide et les silicates liquides sont des fluides non-miscibles, le métal de l'impactant fragmente en gouttelettes pendant sa chute. Pour mieux comprendre ces processus, nous étudions la fragmentation d'un volume de liquide dans un autre liquide non-miscible et moins dense à l'aide d'expériences analogiques. Les expériences ont été montées et réalisées avec Renaud Deguen et Peter Olson lors d'un séjour de trois mois à

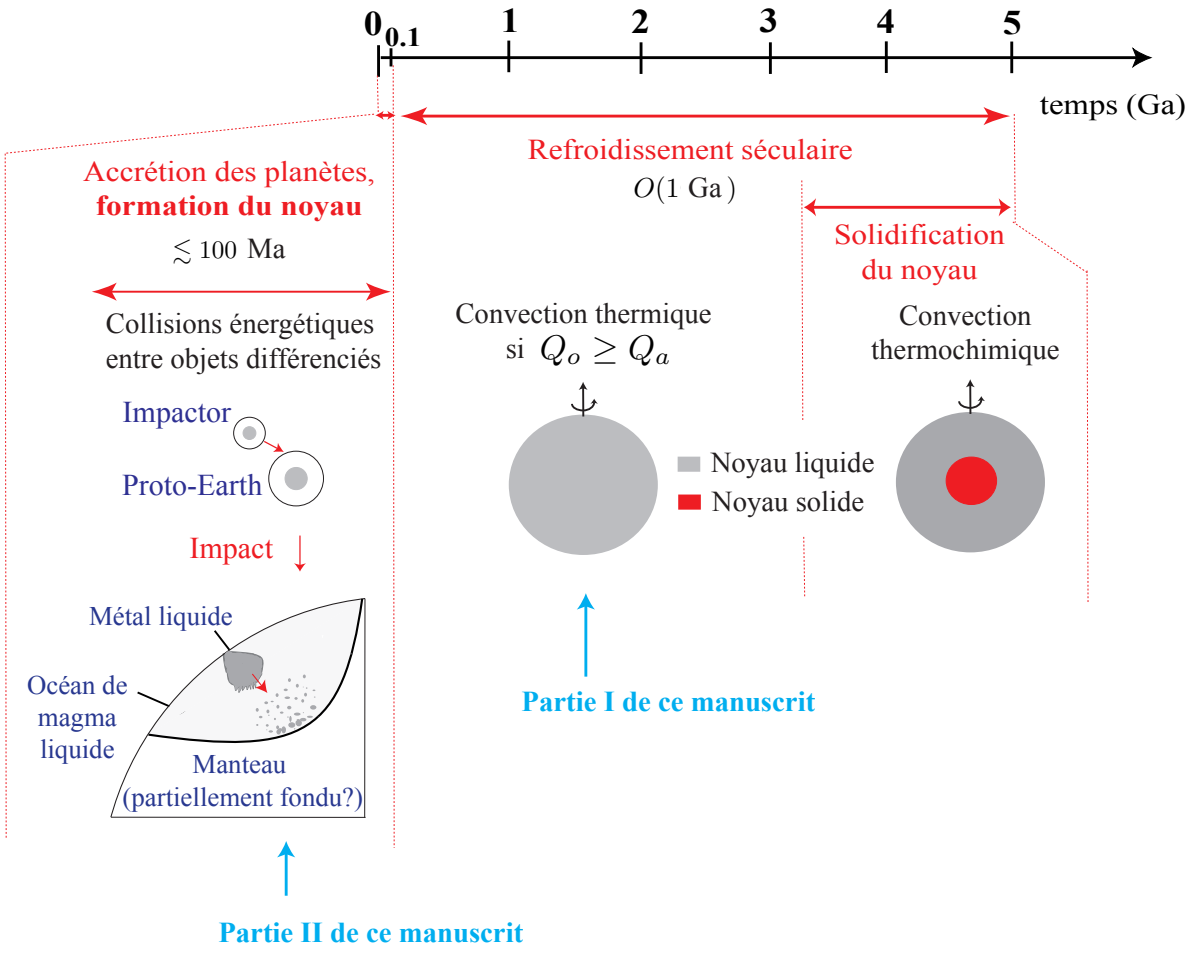

Figure 11.1: Histoire typique d'un noyau planétaire. Q_i et Q_a correspondent respectivement aux flux total et adiabatique à la limite noyau-manteau (ou CMB). L'échelle de temps est seulement indicative et les valeurs absolues peuvent changer d'une planètes à l'autre. Les études présentées en partie I et partie II de ce manuscrit sont inspirées des contextes géophysiques indiqués par des flèches bleues.

l'université Johns Hopkins. Ce séjour a été le résultat d'une initiative personnelle.

Bien que les deux projets présentés dans ce manuscrit traitent tous deux de la dynamique des fluides des noyaux planétaires, leurs motivations spécifiques sont distinctes. Et d'un point de vue de la dynamique des fluides, une autre distinction majeure peut être soulignée : la rotation joue un rôle clé dans la dynamique convective des noyaux planétaires (partie I), tandis qu'elle joue un rôle secondaire sur la fragmentation de métal liquide dans un océan de magma (partie II). Néanmoins, l'approche scientifique, résumée sur la figure 1.5, est très similaire dans ces deux projets.

Tout d'abord, chacun de ces projets démarre d'un problème de dynamique des fluides (boîte 2 dans la figure 1.5) inspiré d'un contexte géophysique (boîte 1 dans la figure 1.5). L'objectif de nos simulations numériques ou de nos expériences analogiques n'est pas de reproduire le contexte géophysique ou d'obtenir des visualisations réalistes du problème géophysique. De tels objectifs ne seraient pas accessibles étant donné la vaste gamme d'échelles de longueur et de temps impliquées dans le système géophysique. Nous

cherchons plutôt à simplifier le système géophysique autant que possible, de sorte à isoler quelques ingrédients clés, afin d'obtenir un problème de dynamique des fluides intelligible. En résumé, le contexte géophysique et le problème de dynamique des fluides sont deux objets distincts dans notre démarche (figure 1.5).

Ensuite, dans chacun de ces projets la problématique de départ peut être résumée ainsi :

- Quels sont les différents régimes d'écoulement et dynamo, caractérisés par des motifs de vitesse ou de champ magnétique, lorsqu'on varie les différents paramètres de contrôle ?
- Peut-on rendre compte de la dynamique observée dans ces régimes par des modèles théoriques (temps caractéristique, longueurs caractéristiques, vitesse, régimes oscillants, évolution temporelle, ...) ?
- Quelles sont les implications pour le système géophysique de départ ? En particulier, peut-on déduire le régime d'écoulement ou le régime dynamo pertinent pour le système géophysique ?

Partie I : Etude numérique de la convection thermique et de l'effet dynamo dans des sphères en rotation

Introduction

Motivations géophysiques

Le champ magnétique mesuré à la surface de la Terre est probablement généré par des mouvements de convection dans le noyau externe, mouvements impliquant des effets à la fois thermiques et compositionnels. L'essentiel des études de convection et d'effet dynamo dans des noyaux planétaires s'est intéressé à des configurations pertinentes pour la Terre actuelle, i.e. dans une coquille sphérique (avec graine) et en imposant un flux de flottabilité non-nul à la graine de sorte à modéliser le relâchement d'éléments légers lors de la cristallisation de la graine (figure 11.2(c)). Les processus de convection et d'effet dynamo dans des noyaux entièrement liquides, avant cristallisation de la graine (figure 11.2(b)), ont eux reçus peu d'attention. Pourtant cette configuration est plus simple, tout d'abord part sa géométrie et ensuite par le forçage de la convection (seulement d'origine thermique, sans effets compositionnels). De plus, plusieurs dynamos de notre système solaire ont opéré dans une configuration de sphère pleine. En effet, les données paléomagnétiques indiquent que la Terre avait une dynamo active il y a ~ 3.4 milliards d'années (Tarduno *et al.* 2010 ; Biggin *et al.* 2011), i.e. avant la nucléation de la graine (comprise entre 0.5 et 3 milliards d'années d'après Labrosse *et al.* (2001)). Le champ magnétique fossile à la surface de Mars indique également que la planète a eu une dynamo active pendant son premier milliard d'années (Acuna *et al.* 1999 ; Milbury & Schubert 2010 ; Milbury *et al.* 2012), alors que le noyau était entièrement liquide (Stewart *et al.* 2007 ; Yoder *et al.* 2003).

Inspirés du contexte géophysique ci-dessus, nous étudions les processus de convection thermique et d'effet dynamo dans des sphères en rotation. Les questions principales sont les suivantes : Quels sont les structure d'écoulement et de champ magnétique qui dominent dans des sphères en rotation ? Sont-elles identiques à celles obtenues dans les études précédentes, i.e. dans une coquille sphérique (en présence d'une graine) ?

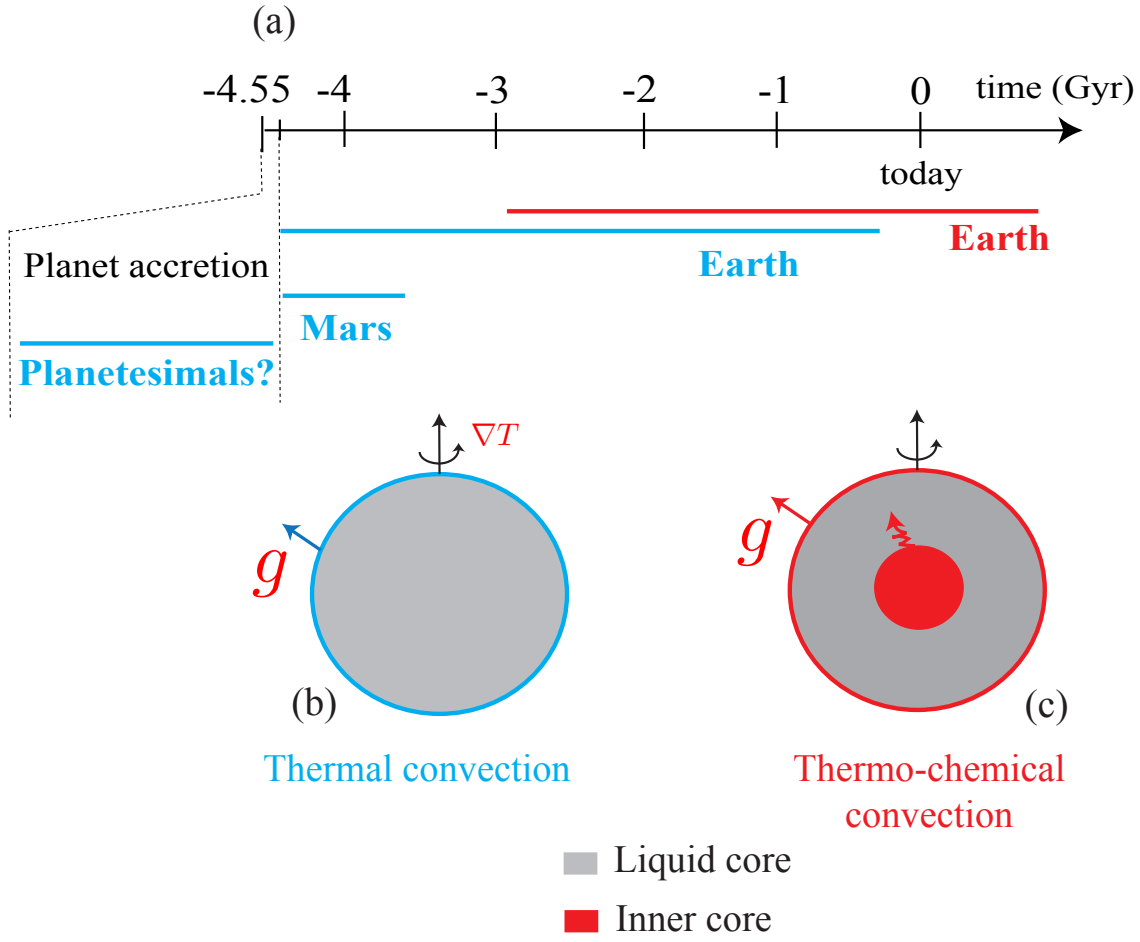

Figure 11.2: (a) Périodes pour lesquelles un effet dynamo forcé par de la convection purement thermique (bleu) ou thermochimique (rouge) est plausible pour le noyau de la Terre ou celui de Mars. De plus, la convection purement thermique et l'effet dynamo sont des processus qui étaient probablement très fréquents durant l'accrétion des planètes, alors que le chauffage dû aux collisions ou à la décroissance radioactive d'éléments à courte durée de vie était suffisant pour induire la fusion du manteau et du noyau. (b) Configuration pertinente pour étudier la convection purement thermique dans un noyau entièrement liquide. Q représente le flux de chaleur total à la CMB. (c) Configuration pertinente pour étudier la dynamique du noyau de la Terre actuelle : convection et effet dynamo forcés par des effets à la fois thermiques et compositionnels (décharge d'éléments légers pendant la cristallisation de la graine).

Structures obtenues dans les études précédentes

Les premières études du seuil de convection dans des sphères en rotation rapide se sont focalisées sur les modes antisymétriques par rapport à l'équateur (Roberts 1965 ; Bisshopp & Niiler 1965 ; Roberts 1968). Busse (1970) est le premier à avoir montré que la convection au seuil s'organise en un écoulement symétrique, qui prend la forme de colonnes alignées avec l'axe de rotation et qui tendent à respecter la contrainte de Taylor-Proudman (invariance de l'écoulement dans la direction axiale). Les modes antisymétriques ont reçu peu d'attention depuis ; ils jouent en effet un rôle secondaire sur l'écoulement total dans toutes les études précédentes de convection non-linéaire dans des coquilles sphériques (i.e. en présence d'une graine), où l'écoulement reste essentiellement symétrique et colonnaire

(e.g. Olson *et al.* 1999 ; Grote & Busse 2001 ; Sakuraba & Roberts 2009). Ces résultats ont joué un rôle important dans la modélisation puisqu'ils ont motivé le développement de modèles *quasi-géostrophiques* qui imposent à l'écoulement horizontal d'être invariant dans la direction axiale, sélectionnant ainsi des écoulements exclusivement symétriques par rapport à l'équateur (e.g. Cardin & Olson 1994 ; Aubert *et al.* 2003 ; Gillet & Jones 2006 ; Gillet *et al.* 2007).

Modèle et méthodes

Un noyau planétaire sans graine est modélisé par une sphère de rayon D, en rotation autour de l'axe $\hat{z}$ à taux constant Ω.

Dans la section 3.2, les équations du problème sont introduites. Nous montrons que le refroidissement séculaire du noyau agit comme un terme de chauffage interne dans l'équation d'évolution des fluctuations de température (fluctuations par rapport à un profil moyen adiabatique de température). Le temps caractéristique de la convection dans le noyau ($\sim O(100)$ ans, Bloxham & Jackson 1991) est petit devant le temps caractéristique du refroidissement séculaire ($\sim O(100)$ millions d'années, Sharpe & Peltier 1978) et cela permet de modéliser les mouvements convectifs dans un noyau planétaire qui se refroidit par un système quasi-stationnaire. Dans le cadre de l'approximation de Boussinesq (détaillée en section 3.1) et de la limite non-relativiste (annexe A), les équations adimensionnés gouvernant l'évolution du champ de vitesse $\mathbf{u}$, du champ magnétique $\mathbf{B}$ et du champ de température T sont :

$$\frac{\partial \mathbf{u}}{\partial t} + \mathbf{u}\cdot\nabla\mathbf{u} = -\nabla P - 2\hat{z}\times\mathbf{u} + Ra_Q\frac{\mathbf{r}}{r_o}T + (\nabla\times\mathbf{B})\times\mathbf{B} + E\Delta\mathbf{u}, \tag{11.1}$$

$$\frac{\partial T}{\partial t} + (\mathbf{u}\cdot\nabla)T = s_T + \frac{E}{Pr}\Delta T, \tag{11.2}$$

$$\frac{\partial \mathbf{B}}{\partial t} + (\mathbf{u}\cdot\nabla)\mathbf{B} = (\mathbf{B}\cdot\nabla)\mathbf{u} + \frac{E}{Pm}\Delta\mathbf{B}, \tag{11.3}$$

$$\nabla\cdot\mathbf{B} = 0, \tag{11.4}$$

$$\nabla\cdot\mathbf{u} = 0. \tag{11.5}$$

Les équations ont été adimensionnées en utilisant les échelles suivantes : D pour l'échelle de longueur, Ω^{-1} pour l'échelle de temps, $\rho D^2\Omega^2$ pour l'échelle de pression avec ρ la masse volumique du fluide, $\sqrt{\rho\mu}\Omega D$ pour l'échelle de champ magnétique avec μ la perméabilité magnétique et $Q/4\pi\rho C_P\Omega D^3$ l'échelle de température avec Q le flux de chaleur total sortant de la sphère et C_P la capacité thermique massique. Le terme s_T dans l'équation (11.2) est un terme source dont la valeur est telle que le bilan de chaleur de la sphère s'annule.

Nous imposons des conditions aux limites de non-glissement et de flux de chaleur fixé. Le milieu extérieur est un isolant électrique.

Les paramètres de contrôle adimensionnés sont :

- le nombre de Rayleigh modifié

$$Ra_Q = \frac{\alpha g_o Q}{4\pi\rho_0 C_P \Omega^3 D^4}, \tag{11.6}$$

- le nombre d'Ekman

$$E = \frac{\nu}{\Omega D^2}, \tag{11.7}$$

- le nombre de Prandtl

$$Pr = \frac{\nu}{\kappa}, \tag{11.8}$$

- le nombre de Prandtl magnétique

$$Pm = \frac{\nu}{\eta}, \tag{11.9}$$

avec α le coefficient de dilatation thermique, g_o l'accélération de la gravité à la surface de la sphère, ν la viscosité cinématique, κ la diffusivité thermique et η la diffusivité magnétique. Avec ce choix pour les paramètres adimensionnés, le nombre de Rayleigh canonique

$$Ra = \frac{\alpha g_o Q D^2}{4\pi\rho_0 C_P \kappa^2 \nu}, \tag{11.10}$$

est donné par $Ra = Ra_Q E^{-3} Pr^2$.

Nous étudions deux types de simulations : des *simulations hydrodynamiques* obtenues en résolvant les équations (11.1), (11.2) et (11.5) avec $\mathbf{B} = \mathbf{0}$, et des *simulations dynamos* obtenues en résolvant les équations (11.1)-(11.5).

Les résultats de nos simulations en sphère pleine sont comparés à des *modèles de référence* réalisés en configuration de coquille sphérique (i.e. avec une graine) et avec un flux de flottabilité non-nul au niveau de la sphère interne.

L'ensemble des paramètres de sortie est défini en section 3.7.

Nous utilisons le code numérique PARODY, initialement développé par Emmanuel Dormy puis par Julien Aubert. Ce code a été validé en géométrie de coquille sphérique dans l'article de Christensen *et al.* (2001). Il est validé en géométrie de sphère pleine dans le présent manuscrit par comparaison aux solutions théoriques obtenues par Bisshopp (1958), Roberts (1965), et Bisshopp & Niiler (1965) pour le seuil de convection axisymétrique (section 3.8.7).

Résultats

Le chapitre 4 contient l'essentiel des résultats de l'article "Equatorially asymmetric convection inducing hemispherical magnetic field in rotating spheres and implications for the past martian dynamo", publié en 2011 dans le journal *Physics of the Earth and Planetary Interiors*. L'analyse a cependant été améliorée dans la version présentée en chapitre 4. Dans ce chapitre, nous caractérisons, dans l'espace des paramètres (E, Ra_Q), l'émergence

systématique de modes antisymétrique par rapport à l'équateur, ainsi que leur effet sur le champ magnétique.

La première partie est dédiée à l'étude de simulations hydrodynamiques (i.e. sans effet dynamo). Le seuil d'émergence Ra_{Qt} des modes antisymétriques dans les simulations non-linéaires est caractérisé dans l'espace (E, Ra_Q) (figure 11.3(a) and figure 4.5) et une loi d'échelle ajustée numériquement est extraite (équation 4.2). Au dessus de Ra_{Qt}, l'énergie antisymétrique augmente rapidement (figure 11.3(a)) et les modes antisymétriques par rapport à l'équateur deviennent plus énergétiques que les modes symétriques pour un forçage suffisamment grand (figure 11.3(a), Table 4.1). Au contraire, dans les simulations de référence (coquille sphérique et flux de chaleur non-nul au niveau de la sphère interne) l'écoulement reste dominé par des modes symétriques par rapport à l'équateur, et cela même si le forçage est nettement supérieur à Ra_{Qt} : les modes symétriques contiennent toujours plus de 70% de l'énergie cinétique totale (figure 11.3(b)). Nous avons vérifié que les simulations fortement asymétriques obtenues en sphère pleine sont localisées dans un régime dominé par la rotation (i.e. géostrophique). L'émergence des modes antisymétriques est associée à des changements morphologiques majeurs de l'écoulement dans une configuration de sphère pleine (figure 11.4). Le changement le plus marquant est l'émergence d'un mode EAA (equatorially antisymmetric and axisymmetric), mode le plus énergétique dans les simulations fortement asymétriques (figure 4.8(b)). Cet écoulement EAA est caractérisé par la présence de forts vents zonaux antisymétriques formant deux vortex contrarotatifs (figure 4.10(d)) et résultant d'un mécanisme de vent thermique (équilibre 4.3 vérifié en figure 4.11).

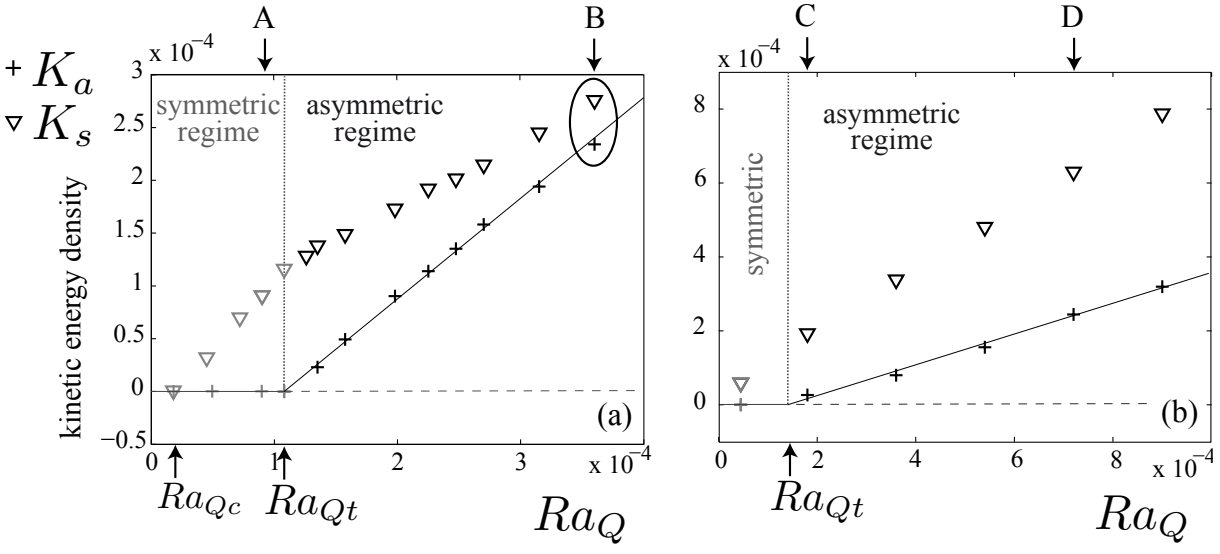

Figure 11.3: Diagramme de bifurcation pour la convection sans effet dynamo : énergie contenue dans l'écoulement antisymétrique par rapport à l'équateur K_a (croix) et énergie contenue dans l'écoulement symétrique par rapport à l'équateur K_s (triangles) en fonction du nombre de Rayleigh Ra_Q, pour $E = 3 \times 10^{-4}$, dans (a) des simulations en sphère pleine (sans graine) et (b) dans des modèles de référence en présence d'une graine. Ra_{Qt} localise l'émergence des modes antisymétriques. Les symboles A, B, C, D renvoient aux simulations A, B, C, D qui sont montrées dans le figures 11.4 et 4.7 (paramètres reportés dans la Table 4.1).

Dans un deuxième temps, une étude similaire est menée avec des simulations dy-

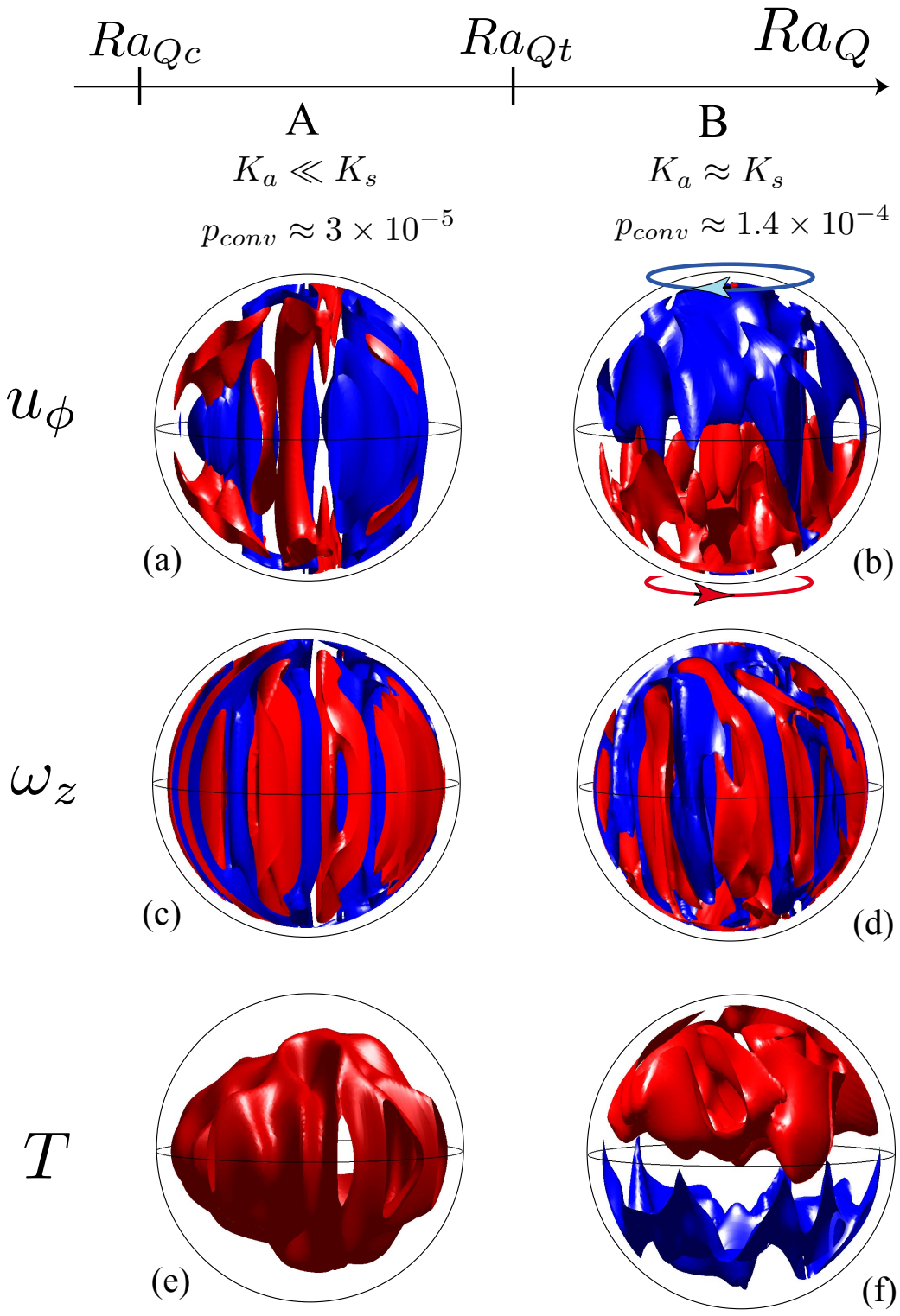

Figure 11.4: Isosurfaces de (a,b) la vitesse longitudinale instantanée, (c,d) de la vorticité axiale et (e,f) de la température pour des simulations de sphère pleine, dénommée A et B (paramètres reportés dans la Table 4.1) et localisées sur le diagramme de bifurcation de la figure 11.3(a). L'axe de rotation est vertical dans cette figure. La couche limite visqueuse a été exclue pour obtenir des visualisations claires. (a,b,c,d) Les couleurs rouge et bleu indiquent respectivement des valeurs positives et négatives. Les isosurfaces suivantes sont montrées : (a) $|u_\phi| = 8.1\times10^{-3}$, (b) $|u_\phi| = 2.4 \times 10^{-2}$, (c) $|\omega_z| = 0.12$, (d) $|\omega_z| = 0.24$, (e) $T = -867$, (f) $T = -667$ (rouge) et $T = -933$ (bleu).

namos. En ce qui concerne l'écoulement, les résultats sont très similaires à ceux obtenus à partir des simulations hydrodynamiques : bien que l'écoulement soit géostrophique, des simulations fortement asymétriques sont obtenues quand le nombre de Rayleigh est suffisamment élevé (figure 4.12) ; l'écoulement est alors fortement influencé par un mode EAA (figure 4.15(b)). La seule différence avec le cas hydrodynamique est l'apparition d'un régime d'écoulement supplémentaire, caractérisé par des oscillations chaotiques de l'énergie cinétique EAA entre des valeurs proche de 0 et des valeurs du même ordre de grandeur que l'énergie totale (figure 4.13). En ce qui concerne les structures magnétiques, nous montrons que la brisure de symétrie équatoriale, associée à l'émergence des modes antisymétriques, contrôle l'hémisphéricité de la dynamo (le caractère hémisphérique est quantifiée par le rapport f_{hem} entre l'énergie contenue dans l'hémisphère le plus énergétique et l'énergie totale, voir la figure 4.20). Dans les simulations où l'écoulement est suffisamment asymétrique, nous obtenons des dynamos hémisphériques telles que 75% (et jusqu'à 90%) de l'énergie magnétique totale est contenu dans un seul hémisphère (Table 4.2, figure 11.5).

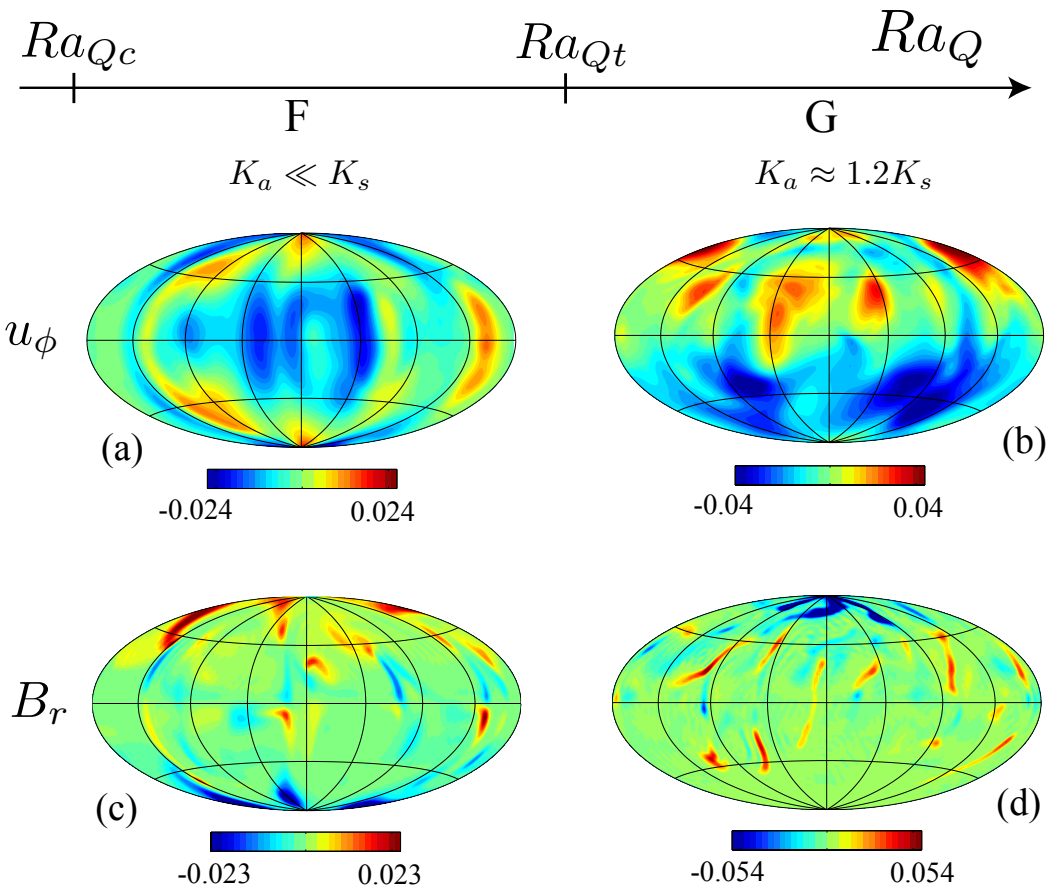

Figure 11.5: (a,b) Vitesse longitudinale instantanée pour un rayon donné égal à la moitié du rayon de la sphère et (c,d) champ magnétique radial instantané à la surface de la sphère dans les simulations dynamos F (gauche, simulation symétrique) et G (droite, simulation fortement asymétrique) (paramètres reportés dans la Table 4.2), réalisés avec les mêmes paramètres de contrôle que les simulations hydrodynamiques A et B.

Discussion et interprétation

Ecoulement asymétrique et contrainte de Taylor-Proudman

Nous avons montré que des simulations fortement asymétriques (dans lesquelles les modes antisymétriques par rapport à l'équateur deviennent aussi énergétiques que les modes symétriques) sont obtenues dans le régime géostrophique d'une sphère en convection. Ce résultat est inattendu et peut sembler en conflit avec la contrainte de Taylor-Proudman. Pourquoi cette contrainte est-elle brisée dans un régime pourtant géostrophique ?

Pour traiter cette question il faut séparer le cas des composantes zonale et non-zonale. Un écoulement non-zonal dans un sphère ou une coquille sphérique brise nécessairement la contrainte de Taylor-Proudman du fait de la condition de non-pénétration. Cependant, cela n'empêche pas cet écoulement de satisfaire, au premier ordre, l'équilibre géostrophique (équilibre entre les forces de pression et la force de Coriolis). Ces remarques valent par exemple au seuil de convection où l'équilibre géostrophique est respecté au premier ordre tandis que les termes visqueux brisent la contrainte de Taylor-Proudman dans l'équation de la vorticité. Dans le cas des modes non-zonaux, la dynamique ci-dessus vaut à la fois pour les modes symétriques et antisymétriques. Les modes symétriques sont favorisés près du seuil car la dissipation visqueuse associée est légèrement plus faible que celle des modes antisymétriques ; cependant cette différence est faible et peut être dépassée pour un forçage suffisamment supercritique.
Dans nos simulations fortement asymétriques l'écoulement non-zonal antisymétrique peut contenir jusqu'à 60% de l'énergie antisymétrique totale. Les remarques ci-dessus indiquent que ces structures ne sont finalement pas si inattendues et certainement pas interdites dans le régime géostrophique.

Contrairement à l'écoulement non-zonal, un écoulement zonal est partout parallèle aux frontières et, par conséquent, n'est pas affecté par la condition de non-pénétration. Dans ce cas, l'écoulement interne (i.e. hors des couches limites) peut être rigoureusement invariant dans la direction de l'axe de rotation. Un tel écoulement respecte parfaitement la contrainte de Taylor-Proudman et est nécessairement symétrique par rapport à l'équateur. Au contraire, un écoulement zonal antisymétrique brise forcément la contrainte de Taylor-Proudman. La dynamique des modes symétriques et antisymétriques est donc distincte quand on considère uniquement les composantes zonales. Dans nos simulations, la contrainte de Taylor-Proudman est brisée par les forces de flottabilité dans l'équation de la vorticité et un fort vent zonal asymétrique est généré en conséquence d'un profil de température nettement asymétrique (figure 4.10(c)). La caractéristique réellement inattendue de nos simulations est donc ce profil de température fortement asymétrique.

Plus généralement, nos résultats rappellent qu'un écoulement fortement asymétrique n'est pas interdit dans le régime géostrophique d'une sphère ou d'une coquille sphérique en convection. Au stade actuel de nos connaissances, il n'y a donc pas de raison immuable d'affirmer que les modes antisymétriques sont de faible amplitude par rapport aux modes symétriques dans la limite $E \to 0$, en particulier pour des nombres de Rayleigh situés très loin du seuil de convection comme c'est le cas dans les noyaux planétaires. Les termes *géostrophique/agéostrophique* et *symétrique/asymétrique* font donc référence à des propriétés qui ne sont pas nécessairement corrélées dans des sphères ou des coquilles sphériques.

Brisure de symétrie de l'écoulement

Dans nos simulations dynamos la brisure de symétrie équatoriale de l'écoulement contrôle l'hémisphéricité du champ magnétique. Plusieurs études publiées précédemment ont montré que la brisure de symétrie de l'écoulement joue un rôle important dans la dynamique des inversions magnétiques (Li *et al.* 2002 ; Nishikawa & Kusano 2008 ; Gissinger *et al.* 2010 ; Monchaux *et al.* 2009). Les résultats présentés dans le chapitre 4 de cette thèse (Landeau & Aubert, 2011), combinés à d'autres résultats récents obtenus dans l'expérience VKS (Gallet *et al.*, 2012), dans des dynamos cinématiques paramétrées (Gallet & Petrelis, 2009) ou dans des dynamos convectives en coquille sphérique avec flux de chaleur asymétrique à la frontière externe (Stanley *et al.* 2008 ; Amit *et al.* 2011 ; Dietrich & Wicht 2013), montrent que la brisure de symétrie de l'écoulement peut également induire des dynamos hémisphériques. De façon plus générale, les résultats cités précédemment convergent vers l'idée que la brisure de symétrie de l'écoulement est un paramètre de contrôle clé du régime dynamo.

Les modèles dits *de basse dimensionnalité*, i.e. basé sur l'interaction entre quelques modes, sont généralement utiles pour rendre compte des effets d'une brisure de symétrie. Gallet & Petrelis (2009) ont introduit un modèle basé sur l'interaction entre deux modes magnétiques et prédisant que la brisure de symétrie équatoriale de l'écoulement peut induire des champs magnétiques hémisphériques. Une comparaison détaillée entre les prédictions de ce modèle et nos simulations (détaillée en section 5.3) illustre à la fois les avantages et les limitations de ce modèle : il permet d'expliquer la dynamique globale observée dans les simulations, bien que les détails quantitatifs ne puissent être reproduits par ce modèle.

Implications géophysiques

Nos résultats suggère le scénario suivant (illustré sur la figure 5.4) pour expliquer le champ magnétique hémisphérique mesuré à la surface de Mars (figure 11.6) : quand la croûte de Mars s'est formée et a acquis son aimantation rémanente, la dynamo était située dans un régime d'écoulement suffisamment asymétrique pour induire un champ magnétique hémisphérique ; ce champ a ensuite été enregistré à la surface de Mars.

Ce scénario est attractif car il satisfait le principe de parcimonie (rasoir d'Ockham) puisque il ne nécessite ni d'asymétrie du flux de chaleur comme supposé par Stanley *et al.* (2008), Amit *et al.* (2011) et Dietrich & Wicht (2013), ni de processus exogène à l'origine d'une démagnétisation de la croûte dans l'hémisphère nord, comme un resurfaçage volcanique (Connerney *et al.*, 2005), de larges impacts (Frey & Schultz, 1988) ou un impact géant unique (Andrews-Hanna *et al.* 2008 ; Marinova *et al.* 2008 ; Nimmo *et al.* 2008 ; Citron & Zhong 2012).

En section 5.4, nous discutons les limitations et l'applicabilité d'un tel scénario.

Perspectives

Il reste à finaliser l'étude détaillée de la circulation EAA dans le régime fortement asymétrique. Tout d'abord il serait utile de quantifier les différentes contributions à la production de

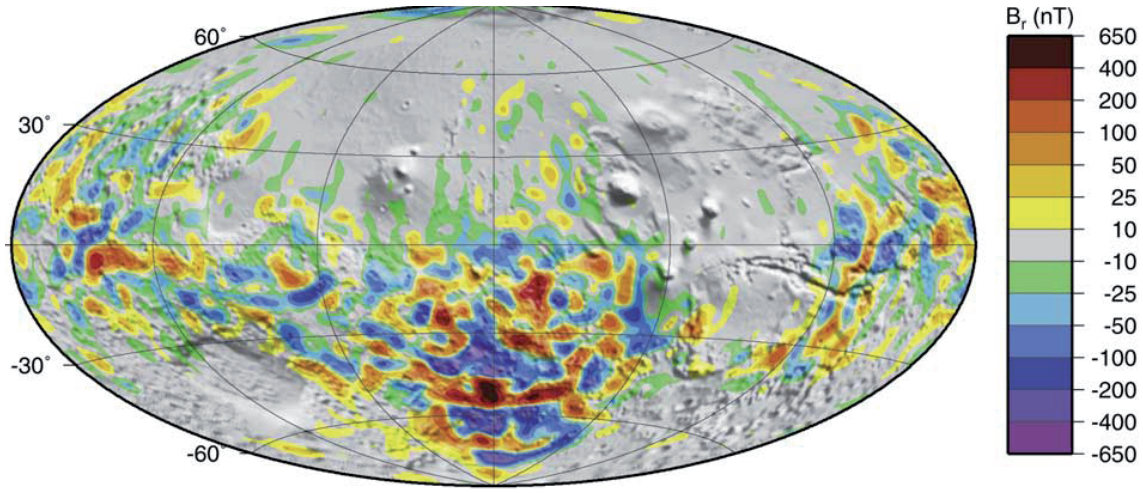

Figure 11.6: Champ magnétique radial à 200 *km d'altitude prédit par le modèle de Langlais* et al. *(2004).*

température EAA, responsable via un mécanisme de vent thermique des deux vortex contrarotatifs dominant l'écoulement. Ensuite, les modes EAA ont les mêmes propriétés de symétrie que les modes émergeant au seuil de convection axisymétrique et étudiés il y a près de 50 ans par Roberts (1965) et Bisshopp & Niiler (1965). Il serait intéressant d'examiner si les modes EAA émergeant dans nos simulations sont en partie hérités des premiers modes axisymétriques instables.

Un autre perspective consiste à étudier de façon systématique l'émergence des modes antisymétriques en variant d'autres paramètres qui nous intéressent pour les planètes, comme par exemple la taille de la graine, le flux de flottabilité à la graine ou le nombre de Prandtl.

L'idée, soutenue par nos résultats et d'autres études, que la brisure de symétrie équatoriale de l'écoulement est un paramètre de contrôle clé du régime dynamo a reçu peu d'attention dans la communauté géophysique et mériterait probablement d'être creusée.

Finalement, des développements possibles pour la Terre primitive peuvent être mentionnés. Les simulations numériques dynamos pourraient être utilisées afin de rechercher des observables paléomagnétiques pouvant être affectées par la nucléation de la graine.

Partie II : Etude expérimentale de la fragmentation d'un volume de liquide dans un autre liquide non-miscible et moins dense

L'essentiel des résultats présentés dans cette partie est inclus dans un article actuellement en révision pour la revue *Journal of Fluid Mechanics*.

Introduction

La fragmentation d'un liquide dans un autre liquide non-miscible a eu lieu à très grande échelle durant la formation des planètes (comme développé dans l'introduction principale). La décharge soudaine de pétrole dans l'océan qui a eu lieu pendant le désastre de 2010 au niveau de la plate-forme *Deepwater Horizon* est un autre exemple de ce phénomène (McNutt *et al.* 2012 ; Reddy *et al.* 2012 ; Camilli *et al.* 2012).

La fragmentation d'un fluide est souvent associée à une séquence bien définie de processus (figure 11.7), incluant la déformation ou déstabilisation du volume initial, la formation de structures filamentaires appelées *ligaments*, et finalement la rupture de ces ligaments par des instabilités capillaires (e.g. Hinze 1955 ; Marmottant & Villermaux 2004 ; Villermaux & Bossa 2009). Le paramètre de contrôle clé des processus de fragmentation est le nombre de Weber We, une mesure de l'importance relative des forces inertielles et des forces superficielles. Un autre paramètre de contrôle clé est le nombre d'Ohnesorge Oh, une mesure de l'importance relative des forces visqueuses par rapport aux forces superficielles et inertielles. Le régime pertinent pour la formation des planètes correspond à des nombres de Weber et des nombres de Reynolds extrêmement élevés et un nombre d'Ohnersorge très faible devant 1.

La fragmentation d'un volume fini de liquide dans le régime $Oh \ll 1$ a été amplement étudiée dans l'air (Pilch & Erdman 1987 ; Faeth *et al.* 1995 ; Gelfand 1996 ; Guildenbecher *et al.* 2009 ; Theofanous 2011), mais beaucoup moins étudiée dans un système liquide-liquide. Les simulations $3D$ de la fragmentation de gouttes dans un autre liquide non-miscible atteignent des Weber de l'ordre de $10 - 15$ (figure 7.2(a)) (Ichikawa *et al.*, 2010) tandis que les simulations axisymétriques (Han & Tryggvason 1999 ; Samuel 2012 ; Ohta & Sussman 2012 ; Han & Tryggvason 2001) atteignent des Weber beaucoup plus élevés mais ne permettent pas d'étudier le processus de rupture qui est essentiellement non-axisymétrique. Baumann *et al.* (1992) ont réalisé des expériences de fragmentation en

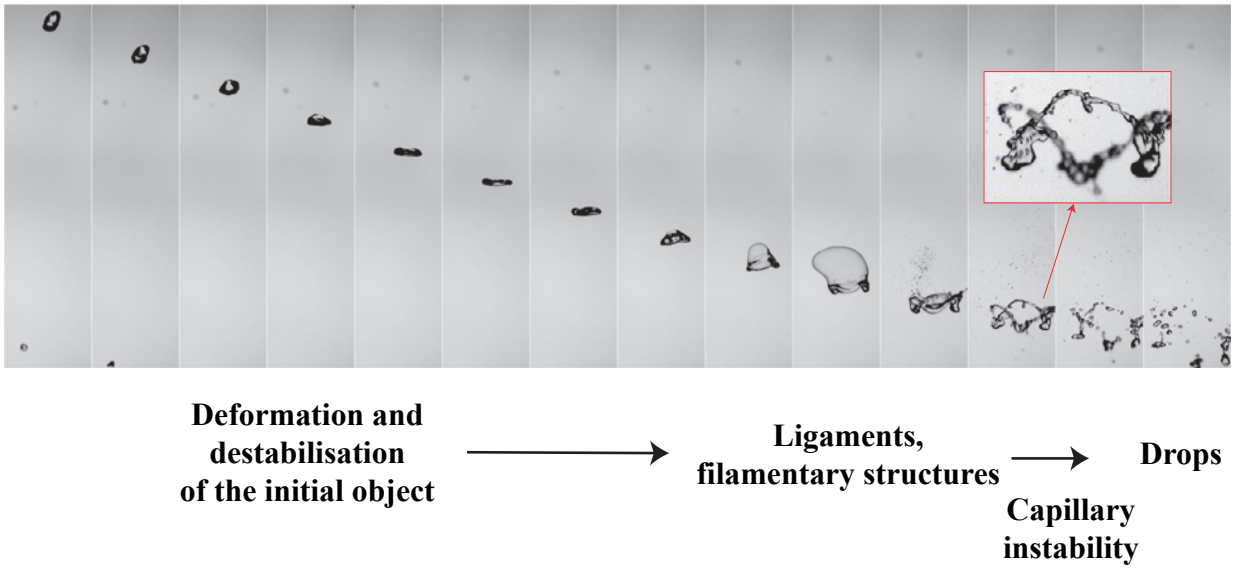

Figure 11.7: Typical sequence of steps involved in a fluid fragmentation process. Water drop falling in an ascending stream of air (modified from Villermaux & Bossa, 2009). The sequence includes deformation of the initial drop which flattens into a pancake shape, formation of liquid ligaments (a toroidal rim collects much of the initial drop mass), destabilization of the rim (highlighted in the inset), leading to disjointed drops distributed in size. Time interval of 4.7 *ms,* $We \approx 600$.

volume fini et pour des systèmes liquide-liquide à des nombres de Weber compris entre 0.3 et 11000. Cependant, les fluides utilisés ont une viscosité élevée et seulement deux de leurs expériences satisfont $We \geq 100$ and $Oh \ll 1$. Dans plusieurs études expérimentales de la fragmentation par ondes de choc d'un liquide dans un autre liquide, des coefficients de trainée et des temps de rupture ont été mesurés. Les valeurs sont résumées dans Pilch & Erdman (1987) et Gelfand (1996).

Aux grands nombres de Reynolds et grands nombres de Weber, le comportement macroscopique d'un panache (Deguen *et al.*, 2011) ou d'un jet (Charalampous *et al.*, 2008) d'un liquide donné dans un autre liquide non-miscible est morphologiquement identique à celui d'un système miscible (figures 7.2(c,d)). Cela suggère que les modèles développés pour des systèmes miscibles turbulents pourraient décrire la dynamique grande échelle des systèmes non-miscibles. Notamment, le concept d'entraînement turbulent permet de décrire la dynamique de nombreux écoulements cisaillants turbulents et il a été considérablement utilisé en miscible pour décrire la dynamique des *thermiques* et des *anneaux de vorticité* (Taylor 1945 ; Morton *et al.* 1956 ; Wang 1971 ; Escudier & Maxworthy 1973 ; Maxworthy 1974 ; Baines & Hopfinger 1984 ; Thompson *et al.* 2000). Ce concept a également été appliqué à des écoulement multiphasiques dans lesquels une phase est initialement dispersée dans une autre sous forme de particules solides (Rahimipour & Wilikinson 1992 ; Bush *et al.* 2003) ou de bulles d'air (Milgram 1983 ; Leitch & Baines 1989 ; Bettelini & Fannelop 1993). L'applicabilité du concept d'entraînement turbulent pour des systèmes non-miscibles non-dispersés a cependant reçu moins d'attention.

Dans cette étude, nous présentons des résultats expérimentaux sur la fragmentation d'un volume de liquide dans un autre liquide non-miscible et moins dense pour de faibles

nombres d'Ohnesorge ($Oh \ll 1$), de grands nombres de Reynolds ($Re \geq 10^3$) et un nombre de Weber variable, atteignant des valeurs de l'ordre de 10^3. Le but principal est de caractériser les régimes d'écoulement dans l'espace des paramètres.

Procédure expérimentale

Dispositif expérimental

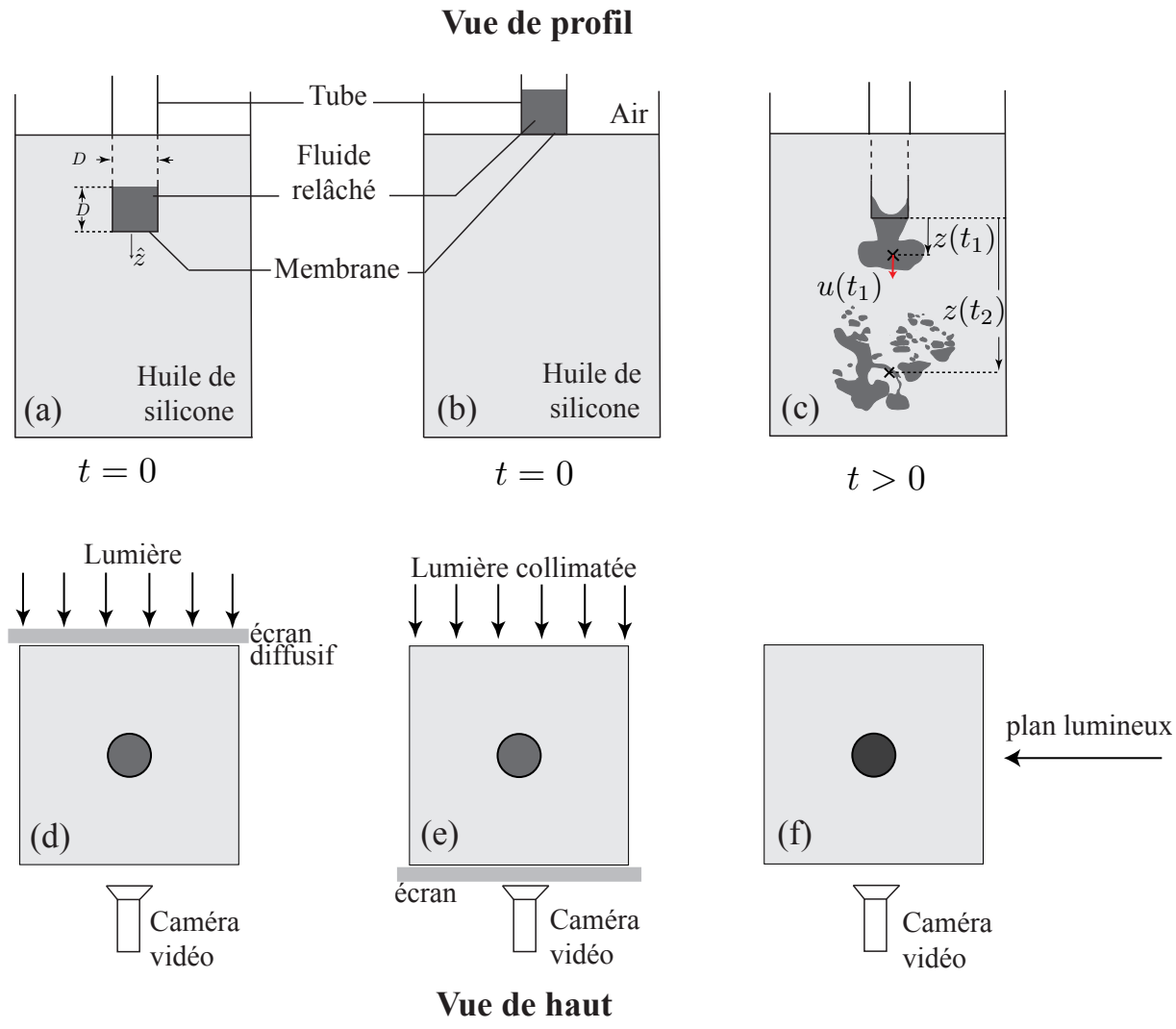

Figure 11.8: Dispositif expérimental. (a) Vue de profil du dispositif en configuration Immergée ; (b) vue de profil du dispositif en configuration Surface. (c) Schéma d'une expérience et des variables mesurées en fonction du temps. (d,e,f) Techniques de visualisations.

Le dispositif expérimental est représenté sur la figure 11.8. Un récipient de 25 cm de large et 50 cm de haut est rempli avec une huile de silicone de faible viscosité, dénommée *fluide ambiant* dans ce qui suit. Un fluide plus dense, non-miscible avec l'huile de silicone, est placé dans un tube de plastique vertical et dont l'extrémité inférieure est fermée par

une membrane en latex. Une aiguille est ensuite utilisée pour briser la membrane en latex et relâcher le fluide dense. La hauteur du fluide dans le tube est égale au diamètre du tube. Dans la configuration *Immergée* (figure 11.8(a)) le fluide est initialement immergé dans le fluide ambiant alors que le tube est placé à la surface du fluide ambiant dans la configuration *Surface* (figure 11.8(b)).

L'étude systématique est conduite en utilisant un éclairage par l'arrière diffus, comme schématisé sur la figure 11.8(d). Un colorant alimentaire bleu est alors ajouté au fluide dense. Une caméra vidéo filme l'écoulement à une vitesse de 24 images par seconde. D'autres images sont obtenues en utilisant une technique d'ombroscopie (figure 11.8(e)). Le fludie dense est chauffé à une température d'environ 35°C. Une lumière collimatée traverse le récipient et projette l'information sur un écran situé à l'avant du récipient. Cette technique rend visible les gradients d'indice de réfraction qui sont induits par des gradients de température. Finalement, des images sont également obtenues en utilisant une technique de fluorescence induite (figure 11.8(f)). Le dispositif est éclairé par le côté par un plan lumineux, alors qu'un colorant fluorescent (la rhodamine) est ajouté au fluide dense, permettant de visualiser une section verticale de l'écoulement. Le plan lumineux, d'épaisseur $5 - 7$ mm, est produit par un flash et une fente de 0.32 cm dans un écran opaque. Dans ce qui suit, la première technique d'éclairage diffus par l'arrière est utilisé, sauf indication contraire.

Pour varier le rapport de densité entre le fluide ambiant et le fluide dense, différents fluides sont relâchés : un mélange eau-éthanol, de l'eau, une solution de chlorure de sodium (NaCl) et une solution d'iodure de sodium (NaI). Les propriétés physiques de ces fluides sont données dans la Table 8.1. La solution de NaI est particulièrement intéressante. Tout d'abord, elle permet d'atteindre de grands rapports de densité entre le fluide ambiant et le fluide dense. De plus, elle permet d'atteindre l'indice de réfraction de l'huile de silicone ($n = 1.384 \pm 0.006$ à 20°C) pour une certaine concentration en NaI, ce qui est nécessaire pour obtenir des images satisfaisantes avec la technique de fluorescence induite. La tension superficielle entre le fluide dense et l'huile de silicone est mesurée avec un tensiomètre Du Noüy.

Un surfactant insoluble avec l'huile de silicone (appelé "Triton X-100" dans le commerce) est ajouté à l'eau et à la solution de NaI dans certaines expériences. La tension superficielle au repos diminue avec la concentration en surfactant jusqu'à ce qu'elle atteigne un concentration critique, à partir de laquelle elle sature à une valeur constante. Cette valeur saturée est celle donnée en Table 8.1. La concentration maximale en surfactant $c \approx 4\text{mL.L}^{-1}$, après laquelle un émulsion stable se formerait dans le récipient, est utilisée dans cette étude. Il est important de souligner que la tension superficielle dynamique peut être localement plus élevée que la tension superficielle au repos.

Dans certaines expériences, de l'eau est utilisé comme fluide ambiant à la place de l'huile de silicone et une solution de NaCl (Table 8.1) est relâchée. Ces expériences sont utilisés comme un système de référence dans la section 9.4.

Variables mesurées

Des étapes de pré-traitement sont appliquées aux images vidéo afin d'obtenir des images binaires (la méthode est détaillée dans l'annexe E). Ensuite, le barycentre z, le rayon équivalent r et la vitesse u du fluide dense sont calculés de façon automatisée (détaillée

en section 8.2). Les incertitudes sur z et u sont respectivement de l'ordre de 5% et 10%. Les barres d'erreur présentées dans les figures qui suivent tiennent compte à la fois des erreurs de mesure et de l'écart type obtenus en reproduisant chaque expérience plusieurs fois.

Nombres sans dimension

Dans la configuration Immergée, quatre nombres sans dimension d'entrée gouvernent la dynamique :

$$Bo = \frac{\Delta\rho g R^2}{\sigma}, \quad Oh = \frac{\sqrt{\rho_r}\nu_r}{\sqrt{\sigma R}}, \quad P = \frac{\Delta\rho}{\rho_a}, \quad \frac{\nu_r}{\nu_a}. \tag{11.11}$$

Dans ce qui précède, Bo est le nombre de Bond, Oh le nombre d'Ohnesorge, $\Delta\rho$ est la différence de densité entre le fluide ambiant et le fluide dense, g est l'accélération de la pesanteur, R le rayon sphérique équivalent du fluide dense, ν la viscosité cinématique, ρ la densité. Les indices a et r renvoient respectivement au fluide ambiant et au fluide dense relâché. Le nombre de Bond est une mesure de l'importance relative des forces de flottabilité et des forces de tension superficielle. Dans la configuration Surface, des nombres sans dimension additionnels sont présents puisque le fluide dense est initialement immergé dans l'air. Dans cette étude nous étudions le fragmentation du fluide dense dans l'huile de silicone est nous ne considérons donc pas les effets de tension superficielle impliquant l'air. Le rapport entre la densité de l'air et celle de l'huile doit être ajouté aux nombres sans dimension ci-dessus. Il en est de même du rapport de viscosité. Cependant ces rapports sont identiques dans toutes les expériences.

Des expériences ont été réalisées dans 24 combinaisons différentes des nombres sans dimension ci-dessus dans la configuration Immergée, et 30 dans la configuration Surface. Bo et P varient respectivement dans la gamme $\sim 4 - 1430$ et $\sim 0.029 - 0.96$, Oh varie de $\sim 10^{-3}$ à $\sim 10^{-2}$ et ν_r/ν_a de 0.8 à 2.2. Puisque $Oh \ll 1$ la viscosité ne doit pas avoir d'influence sur le régime de fragmentation (Hinze 1955 ; Pilch & Erdman 1987) et les revues de Gelfand (1996) et Guildenbecher *et al.* (2009)). Dans cette étude, nous nous concentrons donc sur les effets des deux nombres sans dimension qui sont indépendants de la viscosité : Bo et P.

Résultats

Pendant le processus de fragmentation, nous observons la déformation du fluide dense, la formation de structures filamentaires, et finalement la formation de gouttes. Le chapitre 9 présente les résultats de cette étude dans un ordre essentiellement chronologique.

Dans la section 9.1 nous étudions les premiers stades d'évolution à la sortie du tube en terme de vitesse et de déformation du fluide dense. Cela nous permet notamment d'obtenir des lois d'échelle ajustées expérimentalement pour le nombre de Weber (rapport entre les forces d'inertie et de tension de surface) en fonction des paramètres de contrôle Bo et P.

Le nombre de Weber We est défini par :

$$We = \frac{\rho_r U^2 R}{\sigma}, \tag{11.12}$$

avec U la vitesse du fluide dense à la sortie du tube (à une distance $z = 2R$). Nous montrons également que les premières déformations à la sortie du tube sont le résultat d'une compétition entre des instabilités de Rayleigh-Taylor et la formation d'un anneau de vorticité.

Les différent régimes de fragmentation sont ensuite caractérisés en section 9.2 dans l'espace des paramètres (We, P), à partir de l'étude de l'évolution qui suit les premières phases de déformation. Le diagramme de régime final est présenté sur la figure 11.9. Pour des nombres de Weber suffisamment faibles, le régime de fragmentation est très sensible à la configuration expérimentale (Immergée vs Surface) et une diversité de régime est observée. Le régime de fragmentation dépend alors des premières déformations : dans les expériences où des instabilités de Rayleigh-Taylor se développent à la sortie du tube, le processus de fragmentation correspond à l'évolution non-linéaire de ces instabilités ; dans les expériences où un anneau de vorticité se forme à la sortie du tube, la fragmentation est le résultat d'instabilités additionnelles se développant sur l'anneau. Pour des nombres de Weber suffisamment élevés, le comportement de l'écoulement grande échelle est similaire dans toutes les expériences : le fluide relâché est contenu dans une structure cohérente et autosimilaire qui croit par entraînement de fluide ambiant (figure 11.10).

Les résultats concernant la formation de structures filamentaires et la rupture sont présentés en section 9.3.

Finalement, un modèle basé sur l'hypothèse d'entraînement turbulent, et adapté au cas d'un anneau de vorticité ayant une inertie initial, est présenté en section 9.4. Ce modèle est en accord avec nos résultats expérimentaux pour le régime turbulent ($We \gtrsim 200$), ce qui démontre que le concept d'entraînement turbulent peut être appliqué à une interface séparant des fluides non-miscibles. Le coefficient d'entraînement turbulent prend des valeurs similaires pour des expériences en systèmes miscibles ou non-miscibles. Nous montrons que ce coefficient est corrélé de façon positive avec le nombre de Richardson (rapport entre forces de flottabilité et d'inertie).

Discussion

Discussion des résultats expérimentaux

Le régime de fragmentation caractérisé par le développement d'instabilités de Rayleigh-Taylor est très semblable à des régimes précédemment identifié dans des expériences de fragmentation dans l'air (Harper *et al.* 1972 ; Simpkins & Bales 1972 ; Joseph *et al.* 1999 ; Theofanous *et al.* 2004 ; Theofanous & Li 2008 ; Zhao *et al.* 2010). Au contraire, le régime de fragmentation caractérisé par la déstabilisation d'un anneau de vorticité est morphologiquement différent du régime de déstabilisation d'un anneau identifié par Baumann *et al.* (1992). Nous présentons également les premières visualisations de thermiques et d'anneaux de vorticité turbulents non-miscibles dans un milieu initialement non-dispersé.

Implications géophysiques

Les seules donnés disponibles concernant la formation du noyau sont géochimiques: abondances dans la croûte et le manteau de la Terre en éléments sidérophiles réfractaires et en éléments radiogéniques de systèmes radioactifs éteints. Les premières fournissent des indications concernant les conditions thermodynamiques régnant pendant la différentiation du métal et des silicates tandis que les secondes fournissent un temps caractéristique de formation du noyau. Cependant l'interprétation finale en terme de conditions thermodynamiques ou de temps caractéristique dépend beaucoup du modèle physique utilisé pour inverser les données initiales. Or la physique des processus impliqués dans la formation du noyau reste mal comprise. La présente étude s'inscrit donc dans un effort pour mieux comprendre la physique de la formation du noyau. En particulier, les premières phases de migration et de fragmentation de métal liquide dans un océan de magma après un impact ont joué un rôle crucial sur la composition globale du manteau et du noyau de la Terre. En effet, la formation de gouttelettes de métal augmente la surface de contact entre les silicates et le métal, ce qui favorise les transferts chimiques en éléments sidérophiles.

Le nombre de Weber pertinent pour la fragmentation de métal après un impact est supérieur à 10^{12}. Le système géophysique est donc situé bien au dessus du seuil d'émergence du régime turbulent $We \sim 200$. Le régime de fragmentation turbulent est très différent de l'image classiquement trouvée dans la littérature, où une fragmentation en cascade résulte en une *pluie de fer* dans un océan de magma (Rubie *et al.* 2003 ; Samuel 2012 ; Ichikawa *et al.* 2010). Nos résultats suggèrent plutôt que la fragmentation du métal a lieu dans une structure cohérente et autosimilaire, qui croit par entraînement turbulent de silicates. Dans une étude associée (Deguen *et al.*, 2013) nous proposons un modèle d'équilibrage chimique entre le métal et les silicates dans une telle structure. Les résultats de cette dernière étude suggèrent que l'ensemble du métal s'équilibre efficacement avec les silicates entrainés à partir du moment où l'écoulement devient turbulent ; la signature géochimique finale dépend alors essentiellement de la quantité de silicates entrainés avec le métal.

Le modèle basé sur le concept d'entraînement turbulent proposé en section 9.4 permet de décrire l'évolution macroscopique d'un volume de métal migrant dans un océan de magma infiniment plus grand. Ce modèle fournit l'évolution de la profondeur du métal en fonction du temps et prédit la quantité de silicates entrainés avec le métal. Cette dernière dépend du coefficient d'entraînement, qui est donc un paramètre clé à paramétrer.

Perspectives

Perspectives en dynamique des fluides

Un premier développement consisterait à préciser la corrélation observée entre le coefficient d'entraînement et le nombre de Richardson, à la fois de façon théorique et expérimentale. Un autre développement direct est l'étude des mécanismes petite échelle impliqués dans la fragmentation du régime turbulent. D'un point de vue plus général, les processus d'entraînement turbulent sont impliqués dans un grand nombre d'écoulements géophysiques. Nous pensons que l'étude détaillée de l'entraînement turbulent au niveau

d'une interface non-miscible pourrait aider à décrypter les mécanismes fondamentaux responsables de l'entraînement turbulent.

Perspectives en Sciences de la Terre

D'un point de vue de la formation du noyau, la perspective consiste à insérer des contraintes physiques (déduites de la dynamique des fluides) dans les modèles utilisés pour inverser et interpréter les données géochimiques. Une des difficultés consiste à paramétrer le coefficient d'entraînement turbulent, qui varie en fonction d'autres paramètres du système, comme par exemple le nombre de Richardson ou le nombre de Mach (rapport entre vitesse du métal et vitesse du son ; Deguen *et al.* 2013).

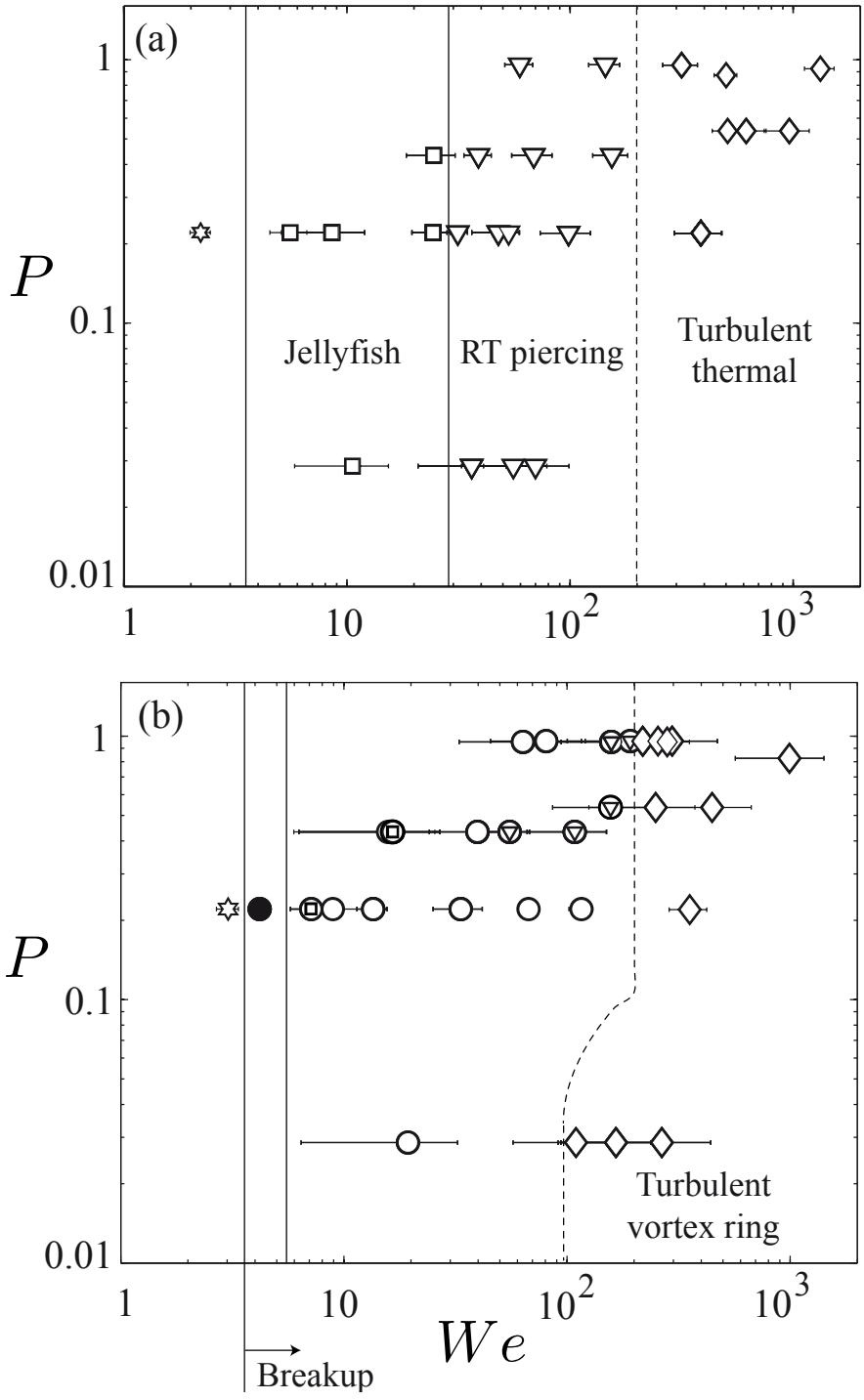

Figure 11.9: Régimes de fragmentation dans un espace (We, P) pour les configurations Immergée (a) et Surface (b). Les symboles signifient : ✩ , pas de fragmentation, gouttes oscillantes ; ● , régime de rupture vibrationnelle ; □, régime méduse ("Jellyfish") ; ▽ , régime de perçage Rayleigh-Taylor ("RT piercing") ;◇, régime turbulent ("turbulent thermal" et "turbulent vortex ring") ; ○, régime de déstabilisation d'un anneau de vorticité ;⊽ , régime intermédiaire entre la déstabilisation d'un anneau et le perçage Rayleigh-Taylor (des structures en forme de champignon, typiques des instabilités de Rayleigh-Taylor, sont observées à l'avant d'un anneau) ; ◎ , anneau de vorticité évoluant en régime méduse. Lignes pleines : transitions de régime abrupte (essai) ; lignes pointillées : transitions progressives.

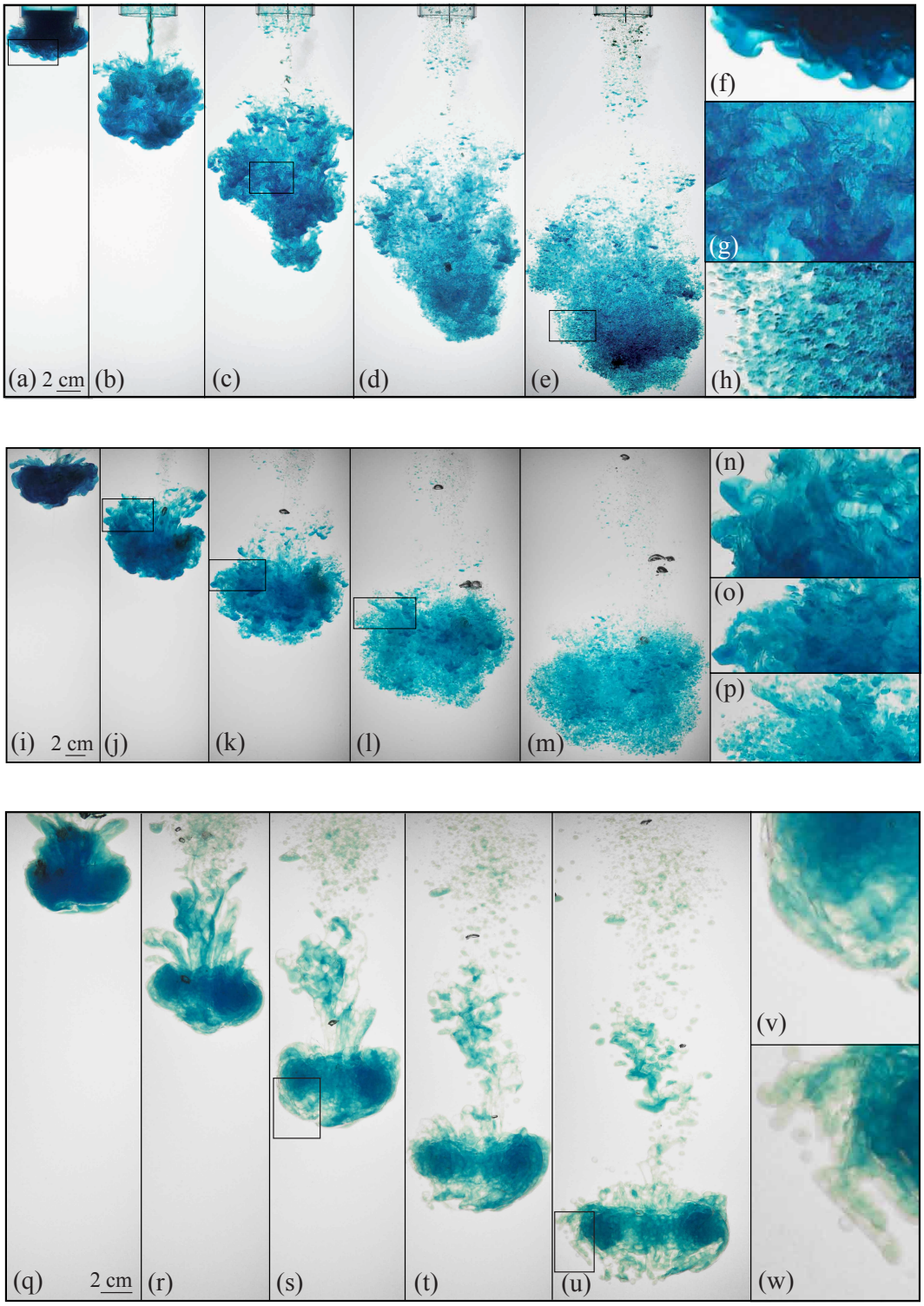

Figure 11.10: Régime de fragmentation turbulent. (a-h) Thermique turbulent non-miscible, $We \approx 10^3$, $P \approx 0.92$, configuration Immergée, intervalle de temps d'environ 0.2 s. (i-w) Anneaux de vorticité turbulents, configuration Surface. (i-p) $We \approx 10^3$, $P \approx 0.82$, intervalle de temps d'environ 0.2 s ; (q-w) $We \approx 200$, $P \approx 0.03$, intervalle de temps d'environ 0.4 s. (f,g,h) (n,o,p) (v,w) Agrandissements des zones localisées respectivement par les carrés des images (a,c,e), (j,k,l) et (s,u).

Bibliography

Acuna, M. H., Connerney, J. E. P., Ness, N. F., Lin, R. P., Mitchell, D., Carlson, C. W., McFadden, J., Anderson, K. A., Reme, H., Mazelle, C., Vignes, D., Wasilewski, P. & Cloutier, P. 1999 Global distribution of crustal magnetization discovered by the Mars Global Surveyor MAG/ER experiment. *Science* **284** (5415), 790–793.

Agnor, C. B., Canup, R M. & Levison, H. F. 1999 On the character and consequences of large impacts in the late stage of terrestrial planet formation. *Icarus* **142** (1), 219–237.

Alfe, D. 2009 Temperature of the inner-core boundary of the Earth: Melting of iron at high pressure from first-principles coexistence simulations. *Phys. Rev. B* **79** (6).

Alfe, D., Gillan, M. J. & Price, G. D. 2003 Thermodynamics from first principles: temperature and composition of the Earth's core. *Mineral. Mag.* **67** (1), 113–123.

Alfe, D., Price, G. D. & Gillan, M. J. 2002 Iron under Earth's core conditions: Liquid-state thermodynamics and high-pressure melting curve from ab initio calculations. *Phys. Rev. B* **65** (16).

Amit, H., Christensen, U. R. & Langlais, B. 2011 The influence of degree-1 mantle heterogeneity on the past dynamo of Mars. *Phys. Earth Planet. Int.* **189** (1-2), 63–79.

Anderson, B. J., Johnson, C. L., Korth, H., Purucker, M. E., Winslow, R. M., Slavin, J. A., Solomon, S. C., McNutt, Jr., Ralph L., Raines, J. M. & Zurbuchen, T. H. 2011 The Global Magnetic Field of Mercury from MESSENGER Orbital Observations. *Science* **333** (6051), 1859–1862.

Andrews-Hanna, J. C., Zuber, M. T. & Banerdt, W. B. 2008 The Borealis basin and the origin of the martian crustal dichotomy. *Nature* **453** (7199), 1212–1216.

Anufriev, A. P., Jones, C. A. & Soward, A. M. 2005 The Boussinesq and anelastic liquid approximations for convection in the Earth's core. *Phys. Earth Planet. Int.* **152** (3), 163–190.

Anzellini, S., Dewaele, A., Mezouar, M., Loubeyre, P. & Morard, G. 2013 Melting of Iron at Earth's Inner Core Boundary Based on Fast X-ray Diffraction. *Science* **340** (6131), 464–466.

Ardes, M., Busse, F. H. & Wicht, J. 1997 Thermal convection in rotating spherical shells. *Phys. Earth Planet. Int.* **99**, 55–67.

Arecchi, F. T., Buah-Bassuah, P. K., Francini, F., Perez-Garcia, C. & Quercioli, F. 1989 An experimental investigation of the break-up of a liquid-drop falling in a miscible fluid. *Europhy. Lett.* **9** (4), 333–338.

Arecchi, F. T., Buah-Bassuah, P. K. & Perez-Garcia, C. 1991 Fragment formation in the break-up of a drop falling in a miscible liquid. *Europhy. Lett.* **15** (4), 429–434.

Arkani-Hamed, J. 2009 Did tidal deformation power the core dynamo of Mars? *Icarus* **201** (1), 31–43.

Aubert, J. 2005 Steady zonal flows in spherical shell dynamos. *J. Fluid. Mech.* **542**, 53–67.

Aubert, J., Aurnou, J. & Wicht, J. 2008 The magnetic structure of convection-driven numerical dynamos. *Geophys. J. Int.* **172**, 945–956.

Aubert, J., Brito, D., Nataf, H.-C., Cardin, P. & Masson, J. P. 2001 A systematic experimental study of spherical shell convection in water and liquid gallium. *Phys. Earth Planet. Int.* **128**, 51–74.

Aubert, J., Gillet, N. & Cardin, P. 2003 Quasigeostrophic models of convection in rotating spherical shells. *Geophys. Geochem. Geosystems.* **4**, doi: 10.1029/2002GC000456.

Aubert, J., Labrosse, S. & Poitou, C. 2009 Modelling the palaeo-evolution of the geodynamo. *Geophys. J. Int.* **179** (3), 1414–1428.

Aubert, J & Wicht, J 2004 Axial vs. equatorial dipolar dynamo models with implications for planetary magnetic fields. *Earth Planet. Sci. Lett.* **221** (1-4), 409–419.

Aurnou, J., Andreadis, S., Zhu, L. & Olson, P. 2003 Experiments on convection in Earth's core tangent cylinder. *Earth Plan. Sci. Lett.* **212**, 119–134.

Aurnou, J. M. & Olson, P. L. 2001 Strong zonal winds from thermal convection in a rotating spherical shell. *Geophys. Res. Lett.* **28** (13), 2557–2559.

Baines, W. D. & Hopfinger, E. J. 1984 Thermals with large density difference. *Atmos. Environ.* **18** (6), 1051–1057.

Batchelor, G. K. 1954 Heat convection and buyoancy effects in fluids. *Quart. J. Roy. Met. Soc.* **80** (345), 339–358.

Batchelor, G. K. 1987 The stability of a large gas bubble rising through liquid. *J. Fluid Mech.* **184**, 399–422.

Baumann, N., Joseph, D. D., Mohr, P. & Renardy, Y. 1992 Vortex rings of one fluid in another in free-fall. *Phys. Fluids A* **4** (3), 567–580.

Beckwith, S. V. W., Sargent, A. I., Chini, R. S. & Gusten, R. 1990 A survey for circumstellar disks around yound stellar objects. *Astron. J.* **99** (3), 924–945.

Bellman, R. & Pennington, R. H. 1954 Effects of surface tension and viscosity on Taylor instability. *Quart. J. Appl. Math.* **12** (2), 151–162.

Bettelini, M. S. G. & Fannelop, T. K. 1993 Underwater plume from an instantaneously started source. *Applied Ocean Research* **15** (4), 195–206.

Biggin, A. J., de Wit, M. J., Langereis, C. G., Zegers, T. E., Voute, S., Dekkers, M. J. & Drost, K. 2011 Palaeomagnetism of Archaean rocks of the Onverwacht Group, Barberton Greenstone Belt (southern Africa): Evidence for a stable and potentially reversing geomagnetic field at ca. 3.5 Ga. *Earth Planet. Sci. Lett.* **302** (3-4), 314–328.

Birch, F. 1952 Elasticity and constitution of the Earth's interior. *J. Geophys. Res.* **57**, 227–286.

Bisshopp, F.E. 1958 On the thermal instability of a rotating fluid sphere. *Philos. Mag.* **3** (36), 1342–1360.

Bisshopp, F.E. & Niiler, P. P. 1965 Onset of convection in a rapidly rotating fluid sphere. *J. Fluid Mech.* **23** (3), 459–469.

Bloxham, J. & Jackson, A. 1991 Fluid flow near the surface of Earth's outer core. *Rev. Geophys.* **29**, 97–120.

Bond, D. & Johari, H. 2010 Impact of buoyancy on vortex ring development in the near field. *Exp. Fluids* **48** (5), 737–745.

Braginsky, S.I. & Roberts, P.H. 1995 Equations governing convection in Earth's core and the geodynamo. *Geophys. Astrophys. Fluid Dyn.* **79** (1-4), 1–97.

Bremond, N. & Villermaux, E. 2006 Atomization by jet impact. *J. Fluid Mech.* **549**, 273–306.

Breuer, D & Moore, W. 2007 Dynamics and thermal history of the terrestrial planets, the moon and io. In *Treatise on Geophysics. Volume 10 - Planets and Moons* (ed. Spohn T.). Elsevier.

Breuer, D. & Spohn, T. 2003 Early plate tectonics versus single-plate tectonics on Mars: Evidence from magnetic field history and crust evolution. *J. Geophys. Res.-Planets* **108** (E7), doi:10.1029/2002JE001999.

Brown, G. & Roshko, A. 1974 On density effects and large structure in turbulent mixing layers. *J. Fluid Mech.* **64** (4), 775–816.

Buah-Bassuah, P. K., Rojas, R., Residori, S. & Arecchi, F. T. 2005 Fragmentation instability of a liquid drop falling inside a heavier miscible fluid. *Phys. Rev. E* **72**, doi: 10.1103/PhysRevE.72.067301.

Buffett, B. 2003 The thermal state of the earth's core. *Science* **299**, 1675–1676.

Buffett, B. A., Huppert, H. E., Lister, J. R. & Woods, A. W. 1996 On the thermal evolution of the Earth's core. *J. Geophys. Res.* **101** (B4), 7989–8006.

Bush, J. W. M., Thurber, B. A. & Blanchette, F. 2003 Particle clouds in homogeneous and stratified environments. *J. Fluid Mech.* **489**, 29–54.

Busse, FH 2002 Convective flows in rapidly rotating spheres and their dynamo action. *Physics of fluids* **14**, 1301–1314.

Busse, F. H. 1970 Thermal instabilities in rapidly rotating systems. *J. Fluid. Mech.* **44** (3), 441–460.

Busse, F. H. 1986 Asymptotic theory of convection in a rotating, cylindrical annulus. *J. Fluid Mech.* **173**, 545–556.

Busse, F. H. & Carrigan, C. R. 1974 Convection induced by centrifugal buoyancy. *J. Fluid Mech.* **62** (3), 579–592.

Busse, F. H. & Or, A. C. 1986 Convection in a rotating cylindrical annulus: thermal rossby waves. *J. Fluid Mech.* **166** (1), 173–187.

Busse, F. H. & Simitev, R. 2004 Inertial convection in rotating fluid spheres. *J. Fluid Mech.* **498** (1), 23–30.

Camilli, R., Di Iorio, D., Bowen, A., Reddy, C. M., Techet, A. H., Yoerger, D. R., Whitcomb, L. L., Seewald, J. S., Sylva, S. P. & Fenwick, J. 2012 Acoustic measurement of the Deepwater Horizon Macondo well flow rate. *Proc. Nati. Acad. Sci. USA* **109** (50), 20235–20239.

Canup, R. M. 2004 Simulations of a late lunar-forming impact. *Icarus* **168** (2), 433–456.

Cao, A. M. & Romanowicz, B. 2004 Constraints on density and shear velocity contrasts at the inner core boundary. *Geophys. J. Int.* **157** (3), 1146–1151.

Cardin, P. & Olson, P. 1992 An experimental approach to thermochemical convection in the Earths core. *Geophys. Res. Lett.* **19** (20), 1995–1998.

Cardin, P. & Olson, P. 1994 Chaotic thermal convection in a rapidly rotating spherical shell: consequences for flow in the outer core. *Phys. Earth Planet. Int.* **82** (3), 235–259.

Cardin, P. & Olson, P. 2007 Experiment on core dynamics. In *Treatise on Geophysics. Volume 8 - Core dynamics* (ed. Olson P.), pp. 319–345. Elsevier.

Carrigan, C. R. & Busse, F. H. 1983 An experimental and theoretical investigation of the onset of convection in rotating spherical shells. *J. Fluid Mech.* **126** (1), 287–305.

Chambers, J. E. 2004 Planetary accretion in the inner Solar System. *Earth Planet. Sci. Lett.* **223** (3-4), 241–252.

Chambers, J. E. & Wetherill, G. W. 1998 Making the terrestrial planets: N-body integrations of planetary embryos in three dimensions. *Icarus* **136** (2), 304–327.

Chandrasekhar, S. 1957*a* The thermal instability of a rotating fluid sphere heated within. *Philos. Mag.* **2** (19), 845–858.

Chandrasekhar, S. 1957*b* The thermal instability of a rotating fluid sphere heated within.2. *Philos. Mag.* **2** (22), 1282–1284.

Chandrasekhar, S. 1961 *Hydrodynamic and Hydromagnetic Stability*. Clarendon Press, Oxford.

Charalampous, G., Hardalupas, Y. & Taylor, A. M. K. P. 2008 Characterisation of instabilities on the interface of coaxial jets of immiscible liquids with Laser Induced Fluorescence. *14th International Symposium on application of Laser Techniques to Fluid Mechanics* .

Chen, B., Li, J. & Hauck, II, Steven A. 2008 Non-ideal liquidus curve in the Fe-S system and Mercury's snowing core. *Geophys. Res. Lett.* **35** (7), doi:10.1029/2008GL033311.

Christensen, U.R. & Aubert, J. 2006 Scaling properties of convection-driven dynamos in rotating spherical shells and application to planetary magnetic fields. *Geophys. J. Int.* **117**, 97–114.

Christensen, U., P., Olson & Glatzmaier, G.A. 1999 Numerical modelling of the geodynamo: a systematic parameter study. *Geophys. J. Int.* **138**, 393–409.

Christensen, U. R. 2001 Zonal flow driven by deep convection in the major planets. *Geophys. Res. Let.* **28**, 2553–2556.

Christensen, U. R. 2002 Zonal flow driven by strongly supercritical convection in rotating spherical shells. *J. Fluid. Mech.* **470**, 115–133.

Christensen, U. R. 2006 A deep dynamo generating Mercury's magnetic field. *Nature* **444** (7122), 1056–1058.

Christensen, U. R., Aubert, J., Busse, F. H., Cardin, P., Dormy, E., Gibbons, S., Glatzmaier, G. A., Honkura, Y., Jones, C. A., Kono, M., Matsushima, M., Sakuraba, A., Takahashi, F., Tilgner, A., Wicht, J. & Zhang, K. 2001 A numerical dynamo benchmark. *Phys. Earth Planet. Int.* **128**, 25–34.

Christensen, U. R., Aubert, J. & Hulot, G. 2010 Conditions for earth-like geodynamo models. *Earth Planet. Sci. Lett.* **296** (3), 487–496.

Christensen, Ulrich R., Holzwarth, Volkmar & Reiners, Ansgar 2009 Energy flux determines magnetic field strength of planets and stars. *Nature* **457** (7226), 167–169.

Christensen, U. R. & Wicht, J. 2007 Numerical dynamo simulations. In *Treatise on Geophysics. Volume 8 - Core dynamics* (ed. Olson P.). Elsevier.

Christensen, U. R. & Wicht, J. 2008 Models of magnetic field generation in partly stable planetary cores: Applications to Mercury and Saturn. *Icarus* **196** (1), 16–34.

Chung, Y. & Cramb, A. W. 2000 Dynamic and equilibrium interfacial phenomena in liquid steel-slag systems. *Metall. Trans. B* **31** (5), 957–971, Geoffrey Belton Memorial Symposium, Sydney, Australia, 2000.

Citron, R. I. & Zhong, S. 2012 Constraints on the formation of the Martian crustal dichotomy from remnant crustal magnetism. *Phys. Earth Planet. Int.* **212**, 55–63.

Connerney, J. E. P., Acuna, M. H., Ness, N. F., Kletetschka, G., Mitchell, D. L., Lin, R. P. & Reme, H. 2005 Tectonic implications of Mars crustal magnetism. *PNAS* **102** (42), 14970–14975.

Connerney, J. E. P. & Ness, N. F. 1988 Merucry's magnetic field and interior. In *Mercury* (ed. F. Vilas, C. R. Chapman & M. S. Matthews). University of Arizona Press.

Cordero, S. 1993 Experiments of convection in a rotating hemispherical shell: transition to chaos. *Geophys. Res. Let.* **20**, 2587–2590.

Cordero, S. & Busse, F. H. 1992 Experiments on convection in rotating hemispherical shells: Transition to a quasi-periodic state. *Geophys. Res. Lett.* **19** (8), 733–736.

Cupal, I., Hejda, P. & Reshetnyak, M. 2002 Dynamo model with thermal convection and free-rotating inner core. *Planet. Space Sci.* **50** (10-11), 1117–1122.

Dahl, T. W. & Stevenson, D. J. 2010 Turbulent mixing of metal and silicate during planet accretion - And interpretation of the Hf-W chronometer. *Earth Plan. Sci. Lett.* **295** (1-2), 177–186.

Dazin, A., Dupont, P. & Stanislas, M. 2006 Experimental characterization of the instability of the vortex ring. Part I: Linear phase. *Exp. Fluids* **40** (3), 383–399.

Deguen, R., Landeau, M. & Olson, P. 2013 Turbulent metal-silicate mixing, fragmentation, and equilibration in magma oceans. *Earth Planet. Sci. Lett.* **(submitted)**.

Deguen, R., Olson, P. & Cardin, P. 2011 Experiments on turbulent metal-silicate mixing in a magma ocean. *Earth and Planetary Science Letters* **310** (3-4), 303–313.

Didden, N. 1979 Formation of vortex rings - rolling-up and production of circulation. *Z. Angew. Math. Phys.* **30** (1), 101–116.

Dietrich, W. & Wicht, J. 2013 A hemispherical dynamo model: Implications for the Martian crustal magnetization. *Phys. Earth Planet. Int.* **217**, 10–21.

Dormy, E. 1997 Modélisation numérique de la dynamo terrestre. *Manuscrit de thèse, IPGP* .

Dormy, E., Cardin, P. & Jault, D. 1998 MHD flow in a slightly differentially rotating spherical shell, with conducting inner core, in a dipolar magnetic field. *Earth Plan. Sci. Let.* **160**, 15–30.

Dormy, E., Soward, A. M., Jones, C. A., Jault, D. & Cardin, P. 2004 The onset of thermal convection in rotating spherical shells. *J. Fluid. Mech.* **501**, 43–70.

Driscoll, P. & Olson, P. 2009 Polarity reversals in geodynamo models with core evolution. *Earth Planet. Sci. Lett.* **282** (1-4), 24–33.

Driscoll, P. & Olson, P. 2011 Superchron cycles driven by variable core heat flow. *Geophys. Res. Lett.* **38** (9), doi:10.1029/2011GL046808.

Dziewonski, A. & Anderson, D. 1981 Preliminary reference earth model. *Phys. Earth Planet. Int.* **25** (4), 297–356.

Dziewonski, A. & Gilbert, F 1971 Solidity of inner core of Earth inferred from normal mode observations. *Nature* **234** (5330), 465–466.

Elkins-Tanton, LT, Zaranek, SE, Parmentier, EM & Hess, PC 2005 Early magnetic field and magmatic activity on Mars from magma ocean cumulate overturn. *Earth Planet. Sci. Lett.* **236** (1-2), 1–12.

Epstein, M. & Fauske, H. K. 2001 Applications of the turbulent entrainment assumption to immiscible gas-liquid and liquid-liquid systems. *Chemical Engineering Research & Design* **79** (A4), 453–462.

Escudier, M. P. & Maxworthy, T. 1973 On the motion of turbulent thermals. *J. Fluid Mech.* **61** (NOV20), 541–552.

Faeth, G. M., Hsiang, L. P. & Wu, P. K. 1995 Structure and breakup properties of sprays. *Int. J. Multiphase Flow* **21** (S), 99–127.

Ferraro, V. C. A. 1937 The non-uniform rotation of the sun and its magnetic field. *Month. Not. Roy. Astr. Soc.* **97**, 458.

Fisher, H. B., List, E. J., Koh, R., Imberger, J. & Brooks, N. 1979 *Mixing in inland and coastal waters*. Academic Press.

Frey, H. & Schultz, R. A. 1988 Large impact basins and the mega-impact origin for the crustal dichotomy on mars. *Geophys. Res. Lett.* **12** (3), 229–232.

Fukumoto, Y. & Hattori, J. 2005 Curvature instability of a vortex ring. *J. Fluid Mech.* **526**, 77–115.

Funakoshi, K. 2010 In situ viscosity measurements of liquid Fe-S alloys at high pressures. *Hi* **30** (1), 60–64, 47th Meeting of the European-High-Pressure-Research-Group (EHPRG 47), Univ Pierre & Marie Curie, Cordeliers Campus, Paris, France, 2009.

Gallet, B., Aumaitre, S., Boisson, J., Daviaud, F., Dubrulle, B., Bonnefoy, N., Bourgoin, M., Odier, Ph., Pinton, J. F., Plihon, N., Verhille, G., Fauve, S. & Petrelis, F. 2012 Experimental Observation of Spatially Localized Dynamo Magnetic Fields. *Phys. Rev. Lett.* **108** (14).

Gallet, B. & Petrelis, F. 2009 From reversing to hemispherical dynamos. *Phys. Rev. E* **80**, dor: 10.1103/PhysRevE.80.035302.

Gan, L., Dawson, J. R. & Nickels, T. B. 2012 On the drag of turbulent vortex rings. *J. Fluid Mech.* **709**, 85–105.

Gelfand, B. E. 1996 Droplet breakup phenomena in flows with velocity lag. *Prog. Energy Comb. Sci.* **22** (3), 201–265.

Gharib, M., Rambod, E. & Shariff, K. 1998 A universal time scale for vortex ring formation. *J. Fluid Mech.* **360**, 121–140.

Gillet, N., Brito, D., Jault, D. & Nataf, H. C. 2007 Experimental and numerical studies of convection in a rapidly rotating spherical shell. *J. Fluid Mech.* **580**, 83.

Gillet, N. & Jones, C. A. 2006 The quasi-geostrophic model for rapidly rotating spherical convection outside the tangent cylinder. *Journal of Fluid Mechanics* **554**, 343–370.

Gissinger, C. 2009 Modèles et simulations numériques de l'effet dynamo. *Manuscrit de thèse, UPMC, ParisVI* .

Gissinger, C., Dormy, E. & Fauve, S. 2010 Morphology of field reversals in turbulent dynamos. *Europhys. Lett.* **90** (4).

Gissinger, C., Petitdemange, L., Schrinner, M. & Dormy, E. 2012 Bistability between Equatorial and Axial Dipoles during Magnetic Field Reversals. *Phys. Rev. Lett.* **108** (23).

Glatzmaier, G. A., Coe, R. S., Hongre, L. & Roberts, P. H. 1999 The role of the Earth's mantle in controlling the frequency of geomagnetic reversals. *Nature* **401** (6756), 885–890.

Glatzmaier, G. A. & Roberts, P. H. 1995 A 3-dimensional self-consistent computer-simulation of a geomagnetic-field reversal. *Nature* **377** (6546), 203–209.

Glatzmaier, G. A. & Roberts, P. H. 1996 An anelastic evolutionary geodynamo simulation driven by compositional and thermal convection. *PHYSICA D* **97** (1-3), 81–94.

Glezer, A. & Coles, D. 1990 An experimental-study of a turbulent vortex ring. *J. Fluid Mech.* **211**, 243–283.

Grace, J. R., Wairegi, T. & Brophy, J. 1978 Break-up of drops and bubbles in stagnant media. *Can. J. Chem. Engng* **56** (1), 3–8.

Greenspan, H. P. 1968 *The theory of rotating fluids*. Breukelen Press.

Grote, E. & Busse, F. H. 2000 Hemispherical dynamos generated by convection in rotating spherical shells. *Phys. Rev. E* **62** (3, Part B), 4457–4460.

Grote, E. & Busse, F. H. 2001 Dynamics of convection and dynamos in rotating spherical fluid shells. *Fluid Dyn. Res.* **28** (5), 349–368.

Gubbins, D., Alfe, D., Masters, G., Price, G. D. & Gillan, M. 2004 Gross thermodynamics of two-component core convection. *Geophys. J. Int.* **157**, 1407–1414.

Gubbins, D., Alfe, D., Masters, G., Price, G. D. & Gillan, M. J. 2003 Can the Earth's dynamo run on heat alone? *Geophys. J. Int.* **155** (2), 609–622.

Gubbins, D, Barber, CN, Gibbons, S & Love, JJ 2000 Kinematic dynamo action in a sphere - II. Symmetry selection. *Proc. R. Soc. A* **456** (1999), 1669–1683.

Gubbins, D. & Roberts, P. H. 1987 Magnetohydrodynamics of the Earth's core. In *Geomagnetism* (ed. J. A. Jacobs), , vol. 2. Academic Press.

Guervilly, C. 2010 Dynamos numériques planétaires générées par cisaillement en surface ou chauffage interne. PhD thesis, Université de Grenoble.

Guildenbecher, D. R., Lopez-Rivera, C. & Sojka, P. E. 2009 Secondary atomization. *Exp. Fluids* **46** (3), 371–402.

Gutenberg, B. 1914 Ueber erdbebenwellen, viia. *Gottingen Nachr.* pp. 125–176.

Halliday, A. N. 2004 Mixing, volatile loss and compositional change during impact-driven accretion of the Earth. *Nature* **427** (6974), 505–509.

Han, J. & Tryggvason, G. 1999 Secondary breakup of axisymmetric liquid drops. I. Acceleration by a constant body force. *Phys. Fluids* **11** (12), 3650–3667.

Han, J. & Tryggvason, G. 2001 Secondary breakup of axisymmetric liquid drops. II. Impulsive acceleration. *Phys. Fluids* **13** (6), 1554–1565.

Harper, E. Y., Grube, G. W. & Chang, I. 1972 On the breakup of accelerating liquid drops. *J. Fluid Mech.* **52** (APR), 565–591.

Hart, J. E., Glatzmaier, G. A. & Toomre, J. 1986 Space-laboratory and numerical simulations of thermal convection in a rotating hemispherical shell with radial gravity. *J. Fluid. Mech.* **173**, 519–544.

Hartmann, W. K. & Neukum, G. 2001 Cratering chronology and the evolution of Mars. *Space Sci. Rev.* **96** (1-4), 165–194, ISSI Workshop on Chronology and Evolution of Mars, Bern, Switzerland, 2000.

Hattori, Y. & Fukumoto, Y. 2003 Short-wavelength stability analysis of thin vortex rings. *Phys. Fluids* **15** (10), 3151–3163.

Hattori, Y. & Hijiya, K. 2010 Short-wavelength stability analysis of Hill's vortex with/without swirl. *Phys. Fluids* **22** (7), doi:10.1063/1.3459956.

Hauck, S. A., Dombard, A. J., Phillips, R. J. & Solomon, S. C. 2004 Internal and tectonic evolution of Mercury. *Earth Planet. Sci. Lett.* **222** (3-4), 713–728.

Hernlund, John W., Thomas, Christine & Tackley, Paul J. 2005 Phase boundary double crossing and the structure of Earth's deep mantle. *Nature* **434**, 882–886, doi:10.1038/nature03472.

Hinze, J. O. 1955 Fundamentals of the hydrodynamic mechanism of splitting in dispersion processes. *AiChE J.* **1** (3), 289–295.

Holzner, M., Liberzon, A., Nikitin, N., Kinzelbach, W. & Tsinober, A. 2007 Small-scale aspects of flows in proximity of the turbulent/nonturbulent interface. *Phys. Fluids* **19** (7), doi: 10.1063/1.274603.

Holzner, M., Liberzon, A., Nikitin, N., Luethi, B., Kinzelbach, W. & Tsinober, A. 2008 A Lagrangian investigation of the small-scale features of turbulent entrainment through particle tracking and direct numerical simulation. *J. Fluid Mech.* **598**, 465–475.

Hori, K. & Wicht, J. 2013 Subcritical dynamos in the early mars' core: Implications for cessation of the past martian dynamo. *Phys. Earth Planet. Int.* .

Huerre, P. & Monkewitz, P. A. 1990 Local and global instabilities in spatially developing flows. *Annu. Rev. Fluid. Mech.* **22**, 473–537.

Ichikawa, H., Labrosse, S. & Kurita, K. 2010 Direct numerical simulation of an iron rain in the magma ocean. *J. Geophys. Res.* **115**, doi:10.1029/2009JB006427.

Ishihara, N. & Kida, S. 2002 Equatorial magnetic dipole field intensification by convection vortices in a rotating spherical shell. *Fluid Dyn. Res.* **31** (4), 253–274.

Jacobs, J. A. 1953 The Earth's inner core. *Nature* **172**, 297–298.

Jacobs, J. W. & Catton, I. 1988 3-dimensional rayleigh-taylor instability .1. weakly nonlinear-theory. *J. Fluid Mech.* **187**, 329–352.

Jeffreys, H. 1926 The rigidity of the Earth's central core. *Mon. Notices R. astr. Soc.* **1**, 371–383.

Jones, CA, Soward, AM & Mussa, AI 2000 The onset of thermal convection in a rapidly rotating sphere. *J. Fluid. Mech.* **405**, 157–179.

Jones, C. A. 2007 Convection-driven geodynamo models. In *Treatise on Geophysics. Volume 8 - Core dynamics*. Olson, P.

Jones, C. A. 2011 Planetary Magnetic Fields and Fluid Dynamos. In *Annual review of fluid mechnaics* (ed. Davis, SH and Moin, P), *Annual Review of Fluid Mechanics*, vol. 43, pp. 583–614. Annual Reviews.

Jones, C. A., Boronski, P., Brun, A. S., Glatzmaier, G. A., Gastine, T., Miesch, M. S. & Wicht, J. 2011 Anelastic convection-driven dynamo benchmarks. *Icarus* **216** (1), 120–135.

Joseph, D. D., Belanger, J. & Beavers, G. S. 1999 Breakup of a liquid drop suddenly exposed to a high-speed airstream. *Int. J. Multiphase Flow* **25** (6-7), 1263–1303.

Kageyama, A., Miyagoshi, T. & Sato, T. 2008 Formation of current coils in geodynamo simulations. *Nature* **454** (7208), 1106–1109.

Kageyama, A. & Sato, T. 1997 Generation mechanism of a dipole field by a magnetohydrodynamic dynamo. *Phys. Rev. E* **55** (4), 4617.

Kaminski, E., Tait, S. & Carazzo, G. 2005 Turbulent entrainment in jets with arbitrary buoyancy. *J. Fluid Mech.* **526**, 361–376.

Karki, B. & Stixrude, L. 2010 Viscosity of MgSiO3 Liquid at Earth's Mantle Conditions: Implications for an Early Magma Ocean. *Science* **328** (5979), 740–742.

King, E. M. & Buffett, B. 2013 Flow speeds and length scales in geodynamo models: The role of viscosity. *Earth Planet. Sci. Lett.* **371-372**, 156–162.

King, E. M., Soderlund, K. M., Christensen, U. R., Wicht, J. & Aurnou, J. M. 2010 Convective heat transfer in planetary dynamo models. *Geochemistry, Geophysics, Geosystems* **11** (6), doi: 10.1029/2010GC003053.

King, E. M., Stellmach, S. & Aurnou, J. M. 2012 Heat transfer by rapidly rotating rayleigh–bénard convection. *J. Fluid Mech.* **691**, 568–582.

King, Eric M., Stellmach, Stephan, Noir, Jerome, Hansen, Ulrich & Aurnou, Jonathan M. 2009 Boundary layer control of rotating convection systems. *Nature* **457** (7227), 301–304.

Kleine, T., Mezger, K., Palme, H. & Munker, C. 2004 The W isotope evolution of the bulk silicate Earth: constraints on the timing and mechanisms of core formation and accretion. *Earth Planet. Sci. Lett.* **228** (1-2), 109–123.

Kleine, T., Munker, C., Mezger, K. & Palme, H. 2002 Rapid accretion and early core formation on asteroids and the terrestrial planets from Hf-W chronometry. *Nature* **418** (6901), 952–955.

Kojima, M., Hinch, E. J. & Acrivos, A. 1984 The formation and expansion of a toroidal drop moving in a viscous-fluid. *Phys. Fluids* **27** (1), 19–32.

de Koker, N., Steinle-Neumann, G. & Vlcek, V. 2012 Electrical resistivity and thermal conductivity of liquid Fe alloys at high P and T, and heat flux in Earth's core. *Proc. Nati. Acad. Sci. USA* **109** (11), 4070–4073.

Kundu, P. K. & Cohen, I. M. 1990 *Fluid mechanics*. Academic Press.

Kutzner, C. & Christensen, U.R. 2002 From stable dipolar to reversing numerical dynamos. *Phys. Earth Planet. Int.* **131**, 29–45.

Labrosse, S. 2003 Thermal and magnetic evolution of the Earth's core. *Phys. Earth Planet. Int.* **140**, 127–143.

Labrosse, S., Poirier, J. P. & Le Mouel, J. L. 2001 The age of the inner core. *Earth Planet. Sci. Let.* **190** (3-4), 111–123.

Landeau, M. & Aubert, J. 2011 Equatorially asymmetric convection inducing a hemispherical magnetic field in rotating spheres and implications for the past martian dynamo. *Phys. Earth Planet. Int.* **185** (3-4), 61–73.

Langlais, B., Purucker, M. E. & Mandea, M. 2004 Crustal magnetic field of Mars. *J. Geophys. Res.-Planets* **109**, doi: 10.1029/2003JE002048.

Lay, Thorne, Hernlund, John & Buffett, Bruce A. 2008 Core-mantle boundary heat flow. *Nature Geosci.* **1** (1), 25–32.

Lee, D. C. & Halliday, A. N. 1995 Hafnium-Tungsten chronometry and the timing of terrestrial core formation. *Nature* **378** (6559), 771–774.

Lehmann, I. 1936 P'. *Union Geodesique at Geophysique Internationale, Serie A, Travaux Scientifiques* .

Leitch, A. M. & Baines, W. D. 1989 Liquid volume flux in a weak bubble plume. *J. Fluid Mech.* **205**, 77–98.

Li, J. H., Sato, T. & Kageyama, A. 2002 Repeated and sudden reversals of the dipole field generated by a spherical dynamo action. *Science* **295** (5561), 1887–1890.

Liebske, C., Schmickler, B., Terasaki, H., Poe, B. T., Suzuki, A., Funakoshi, K., Ando, R. & Rubie, D. C. 2005 Viscosity of peridotite liquid up to 13 GPa: Implications for magma ocean viscosities. *Earth Planet. Sci. Lett.* **240** (3-4), 589–604.

Lister, J. R. 2003 Expressions for the dissipation driven by convection in the Earth's core. *Phys. Earth Planet. Int.* **140** (1-3), 145–158.

Lister, J. R. & Buffett, B. A. 1995 The strength and efficiency of thermal and compositional convection in the geodynamo. *Phys. Earth Planet. Int.* **91** (1-3), 17–30.

Lodders, K & Fegley, B 1997 An oxygen isotope model for the composition of Mars. *Icarus* **126** (2), 373–394.

Longhi, J., Knittle, E., Holloway, J. R. & Waenke, H. 1992 The bulk composition, mineralogy and internal structure of mars. In *Mars* (ed. H. H. Kieffer, B. M. Jakosky, C. W. Snyder & M. S. Matthews), pp. 184–208. The University of Arizona Press.

Lopez, J., Marques, F. & Avila, M. 2013 The boussinesq approximation in rapidly rotating flows. *J. Fluid. Mech.* **(Submitted)**.

Loth, E. & Faeth, G. M. 1989 Structure of underexpanded round air jets submerged in water. *Int. J. Multiphase Flow* **15** (4), 589–603.

Loth, E. & Faeth, G. M. 1990 Structure of plane underexpanded air-jets into water. *AiChE J.* **36** (6), 818–826.

Ma, Y. Z., Somayazulu, M., Shen, G. Y., Mao, H. K., Shu, J. F. & Hemley, R. J. 2004 In situ X-ray diffraction studies of iron to Earth-core conditions. *Phys. Earth Planet. Int.* **143**, 455–467.

Marinova, Margarita M., Aharonson, Oded & Asphaug, Erik 2008 Mega-impact formation of the Mars hemispheric dichotomy. *Nature* **453** (7199), 1216–1219.

Marmottant, P. H. & Villermaux, E. 2004 On spray formation. *J. Fluid Mech.* **498**, 73–111.

Masters, G. & Gubbins, D. 2003 On the resolution of density within the Earth. *Phys. Earth Planet. Int.* **140** (1-3), 159–167.

Mathew, J & Basu, AJ 2002 Some characteristics of entrainment at a cylindrical turbulence boundary. *Phys. Fluids* **14** (7), 2065–2072.

Maxworthy, T. 1974 Turbulent vortex rings. *J. Fluid Mech.* **64**, 227–240.

McNutt, M. K., Camilli, R., Crone, T. J., Guthrie, G. D., Hsieh, P. A., Ryerson, T. B., Savas, O. & Shaffer, F. 2012 Review of flow rate estimates of the Deepwater Horizon oil spill. *Proc. Nati. Acad. Sci. USA* **109** (50), 20260–20267.

Melosh, H. J. 1990 *Giant impacts and the thermal state of the early Earth, Origin of the Earth edited by Newsom H and Jones J*. Oxford University Press Inc.

Milbury, C. & Schubert, G. 2010 Search for the global signature of the Martian dynamo. *J. Geophys. Res.-Planets* **115**, doi: 10.1029/2010JE003617.

Milbury, C., Schubert, G., Raymond, C. A., Smrekar, S. E. & Langlais, B. 2012 The history of Mars' dynamo as revealed by modeling magnetic anomalies near Tyrrhenus Mons and Syrtis Major. *J. Geophys. Res.-Planets* **117**, doi: 10.1029/2012JE004099.

Milgram, J. H. 1983 Mean flow in round bubble plumes. *J. Fluid Mech.* **133**, 345–376.

Miller, G. H., Stolper, E. M. & Ahrens, T. J. 1991 The equation of state of a molten komatiite.1. shock-wave compression to 36 gpa. *J. Geophys. Res.* **96** (B7), 11831–11848.

Miyagoshi, T., Kageyama, A. & Sato, T. 2010 Zonal flow formation in the Earth's core. *Nature* **463** (7282), 793–797.

Moffatt, H. K. 1978 *Magnetic field generation in electrically conducting fluids*. Cambridge University Press.

Monchaux, R., Berhanu, M., Aumaitre, S., Chiffaudel, A., Daviaud, F., Dubrulle, B., Ravelet, F., Fauve, S., Mordant, N., Petrelis, F., Bourgoin, M., Odier, P., Pinton, J.-F., Plihon, N. & Volk, R. 2009 The von Karman Sodium experiment: Turbulent dynamical dynamos. *Phys. Fluids* **21** (3), doi: 10.1063/1.3085724.

Moore, D. W. 1974 Numerical study of roll-up of a finite vortex sheet. *J. Fluid Mech.* **63**, 225–235.

Morard, G., Siebert, J., Andrault, D., Guignot, N., Garbarino, G., Guyot, F. & Antonangeli, D. 2013 The earth's core composition from high pressure density measurements of liquid iron alloys. *Earth Planet. Sci. Lett.* **373**, 169–178.

Morrison, G. & Fearn, D. R. 2000 The influence of rayleigh number, azimuthal wavenumber and inner core radius on 2-12 d hydromagnetic dynamos. *Phys. Earth Planet. Int.* **117** (1), 237–258.

Morton, B. R., Taylor, G. & Turner, J. S. 1956 Turbulent gravitational convection from maintained and instantaneous sources. *Proceedings of the royal society of London Series A - Mathematical and Physical sciences* **234** (1196), 1–23.

Niiler, P. P. & Bisshopp, F. E. 1965 On the influence of coriolis force on onset of thermal convection. *J. Fluid Mech.* **22** (04), 753–761.

Nimmo, F., Hart, S. D., Korycansky, D. G. & Agnor, C. B. 2008 Implications of an impact origin for the martian hemispheric dichotomy. *Nature* **453** (7199), 1220–1224.

Nimmo, F & Stevenson, DJ 2000 Influence of early plate tectonics on the thermal evolution and magnetic field of Mars. *J. Geophys. Res.-Planets* **105** (E5), 11969–11979.

Nishikawa, N. & Kusano, K. 2008 Simulation study of the symmetry-breaking instability and the dipole field reversal in a rotating spherical shell dynamo. *Physics of plasmas* **15** (8), doi: 10.1063/1.2959120.

Nitsche, M. & Krasny, R. 1994 A numerical study of vortex ring formation at the edge of a circular tube. *J. Fluid Mech.* **276**, 139–161.

Ogg, J. 2012 The geomagnetic polarity time scale. In *The Geologic Time Scale* (ed. Elsevier), chap. 5, pp. 85–128. Gradstein, F. and Ogg, J. and Schmitz, M. and Ogg, G.

Ohta, M. & Sussman, M. 2012 The buoyancy-driven motion of a single skirted bubble or drop rising through a viscous liquid. *Phys. Fluids* **24** (11), doi: 10.1063/1.4765669.

Oldham, R. D. 1906 The constitution of the interior of the Earth as revealed by earthquakes. *Quart. J. Geol. Soc.* **62**, 456–475.

Olson, P. 2007 Overview. In *Treatise on Geophysics. Volume 8 - Core dynamics*, pp. 1 – 30. Elsevier.

Olson, P., Christensen, U. & Glatzmaier, G. A. 1999 Numerical modelling of the geodynamo: mechanisms of field generation and equilibration. *J. Geophys. Res.* **104** (B5), 10383–10404.

Olson, P. & Christensen, U. R. 2006 Dipole moment scaling for convection-driven planetary dynamos. *Earth Plan. Sci. Let.* **250** (3-4), 561–571.

Olson, P., Deguen, R., Hinnov, L. A. & Zhong, S. 2013 Controls on geomagnetic reversals and core evolution by mantle convection in the phanerozoic. *Phys. Earth Planet. Int.* **214**, 87–103.

Olson, P. L., Coe, R. S., Driscoll, P. E., Glatzmaier, G. A. & Roberts, P. H. 2010 Geodynamo reversal frequency and heterogeneous core-mantle boundary heat flow. *Phys. Earth Planet. Int.* **180** (1-2), 66–79.

Or, A. C. & Busse, F. H. 1987 Convection in a rotating cylindrical annulus. part 2. transitions to asymmetric and vacillating flow. *J. Fluid Mech.* **174**, 313–326.

Patel, P. D. & Theofanous, T. G. 1981 Hydrodynamic fragmentation of drops. *J. Fluid Mech.* **103** (FEB), 207–223.

Petrelis, F., Besse, J. & Valet, J. P. 2011 Plate tectonics may control geomagnetic reversal frequency. *Geophys. Res. Lett.* **38**, doi: 10.1029/2011GL048784.

Petrelis, F. & Fauve, S. 2008 Chaotic dynamics of the magnetic field generated by dynamo action in a turbulent flow. *J. Phys.: Condens. Matter* **20**, doi: 10.1088/0953–8984/20/49/494203.

Petrelis, F., Fauve, S., Dormy, E. & Valet, J.-P. 2009 Simple Mechanism for Reversals of Earth's Magnetic Field. *Phys. Rev. Lett.* **102** (14), doi: 10.1103/PhysRevLett.102.144503.

Pierazzo, E., Vickery, A. M. & Melosh, H. J. 1997 A reevaluation of impact melt production. *Icarus* **127** (2), 408–423.

Pilch, M. & Erdman, C. A. 1987 Use of breakup time data and velocity history data to predict the maximum size of stable fragments for acceleration-induced breakup of a liquid drop. *Int. J. Multiphase Flow* **13** (6), 741–757.

Poirier, J. P. 1988 Transport-properties of liquid-metals and viscosity of the Earth's core. *Geophys. J.* **92** (1), 99–105.

Poirier, J. P. 1994 Light elements in the Earth's outer core: a critical review. *Phys. Earth Planet. Int.* **85**, 319–337.

Pozzo, M., Davies, C., Gubbins, D. & Alfe, D. 2012 Thermal and electrical conductivity of iron at Earth's core conditions. *Nature* **485** (7398), doi: 10.1038/nature11031.

Price, G. D. 2007 Overview. In *Treatise on Geophysics. Volume 2 - Mineral Physics*. Elsevier.

Priestley, C. H. B. & Ball, F. K. 1955 Continuous convection from an isolated source of heat. *Quart. J. Roy. Met. Soc.* **81** (348), 144–157.

Rahimipour, H. & Wilikinson, D. 1992 Dynamic behavious of particle clouds. *11th Australian Fluid Mech. Conf. University of Tasmania, Hobart, Australia* pp. 743–746.

Reddy, C. M., Arey, J. S., Seewald, J. S., Sylva, S. P., Lemkau, K. L., Nelson, R. K., Carmichael, C. A., McIntyre, C. P., Fenwick, J., Ventura, G. T., Van Mooy, B. A. S. & Camilli, R. 2012 Composition and fate of gas and oil released to the water column during the Deepwater Horizon oil spill. *Proc. Nati. Acad. Sci. USA* **109** (50), 20229–20234.

Ricard, Y., Sramek, O. & Dubuffet, F. 2009 A multi-phase model of runaway core-mantle segregation in planetary embryos. *Earth Planet. Sci. Lett.* **284** (1-2), 144–150.

Richards, J. M. 1961 Experiments on the penetration of an interface by buoyant thermals. *J. Fluid Mech.* **11** (3), 369–384.

Roberts, N. & Piper, D. A. 1989 A description of the behaviour of the earth's magnetic field. In *Geomagnetism* (ed. J. A. Jacobs). Academic Press.

Roberts, P. H. 1965 On the thermal instability of a highly rotating fluid sphere. *Astrophys. J.* **141**, 240–250.

Roberts, P. H. 1968 On the thermal instability of a self gravitating fluid sphere containing heat sources. *Philos. Trans. R. Soc. London, Ser. A* **263**, 93–117.

Rubie, D. C., Melosh, H. J., Reid, J. E., Liebske, C. & Righter, K. 2003 Mechanisms of metal-silicate equilibration in the terrestrial magma ocean. *Earth Planet. Sci. Lett.* **205** (3-4), 239–255.

Rudge, John F., Kleine, Thorsten & Bourdon, Bernard 2010 Broad bounds on Earth's accretion and core formation constrained by geochemical models. *Nat. Geosci.* **3** (6), 439–443.

Ruggaber, G. J. 2000 The dynamics of particle clouds related to open-water sediment disposal. PhD thesis, Department of Civil and Environmental Engineering, MIT.

Saffman, P. G. 1978 Number of waves on unstable vortex rings. *J. Fluid Mech.* **84** (FEB), 625–639.

Saffman, P. G. 1992 *Vortex Dynamics*. Cambridge University Press.

Sakuraba, A. & Roberts, P. H. 2009 Generation of a strong magnetic field using uniform heat flux at the surface of the core. *Nature Geosci.* **2**, 802–805.

Samuel, H. 2012 A re-evaluation of metal diapir breakup and equilibration in terrestrial magma oceans. *Earth Planet. Sci. Lett.* **313**, 105–114.

Sanloup, C, Jambon, A & Gillet, P 1999 A simple chondritic model of Mars. *Phys. Earth Planet. Int.* **112** (1-2), 43–54.

Schersten, A., Elliott, T., Hawkesworth, C., Russell, S. & Masarik, J. 2006 Hf-W evidence for rapid differentiation of iron meteorite parent bodies. *Earth Planet. Sci. Lett.* **241** (3-4), 530–542.

Schmitz, S. & Tilgner, A. 2009 Heat transport in rotating convection without ekman layers. *Physical Review E* **80** (1), doi: 10.1103/PhysRevE.80.015305.

Schmitz, S. & Tilgner, A. 2010 Transitions in turbulent rotating rayleigh-bénard convection. *Geophys. Astrophys. Fluid Dyn.* **104** (5-6), 481–489.

Schubert, G., Turcotte, D. & Olson, P. 2001 *Mantle convection in the Earth and planets*. Cambridge University Press.

Scorer, R. S. 1957 Experiments on convection of isolated masses of buoyant fluid. *J. Fluid Mech.* **2** (6), 583–594.

Shariff, K., Verzicco, R. & Orlandi, P. 1994 A numerical study of 3-dimensional vortex ring instabilities - viscous corrections and early nonlienar stage. *J. Fluid Mech.* **279**, 351–375.

Sharpe, H. N. & Peltier, W. R. 1978 Parameterized mantle convection and the earth's thermal history. *Geophysical Research Letters* **5** (9), 737–740.

Sheffield, J. S. 1977 Trajectories of an ideal vortex pair near an orifice. *Phys. Fluids* **20** (4), 543–545.

Siebert, J., Corgne, A. & Ryerson, F. J. 2011 Systematics of metal-silicate partitioning for many siderophile elements applied to Earth's core formation. *Geochem. Cosmochim. Acta* **75** (6), 1451–1489.

Simitev, R. & Busse, F. H. 2003 Patterns of convection in rotating spherical shells. *New Journal of Physics* **5** (1), doi:10.1088/1367–2630/5/1/397.

Simitev, R. & Busse, F. H. 2005 Prandtl-number dependence of convection-driven dynamos in rotating spherical fluid shells. *J. Fluid. Mech.* **532**, 365–388.

Simpkins, P. G. & Bales, E. L. 1972 Water-drop response to sudden accelerations. *J. Fluid Mech.* **55**, 629–639.

Sipp, D., Fabre, D., Michelin, S. & Jacquin, L. 2005 Stability of a vortex with a heavy core. *J. Fluid Mech.* **526**, 67–76.

Soderlund, Krista M., King, Eric M. & Aurnou, Jonathan M. 2012 The influence of magnetic fields in planetary dynamo models. *Earth Planet. Sci. Lett.* **333**, 9–20.

Sohl, F. & Schubert, G. 2007 Interior structure, composition, and mineralogy of the terrestrial planets. In *Treatise on Geophysics. Volume 10 - Planets and Moons*, , vol. Volume 10, pp. 27 – 68. Elsevier.

Soward, A. M. 1977 On the finite amplitude thermal instability of a rapidly rotating fluid sphere. *Geophys. Astrophys. Fluid Dyn.* **9**, 19–74.

Sreenivasan, B. & Jones, C. A. 2005 Structure and dynamics of the polar vortex in the earth's core. *Geophys. Res. Lett.* **32** (20), doi: 10.1029/2005GL023841.

Sreenivasan, B. & Jones, C. A. 2006*a* Azimuthal winds, convection and dynamo action in the polar regions of planetary cores. *Geophys. Astrophys. Fluid Dyn.* **100** (4-5), 319–339.

Sreenivasan, B. & Jones, C. A. 2006*b* The role of inertia in the evolution of spherical dynamos. *Geophys. J. Int.* **164** (2), 467–476.

Stanley, Sabine, Elkins-Tanton, Linda, Zuber, Maria T. & Parmentier, E. Marc 2008 Mars' paleomagnetic field as the result of a single-hemisphere dynamo. *Science* **321** (5897), 1822–1825.

Starchenko, S. V. & Jones, C. A. 2002 Typical velocities and magnetic field strengths in planetary interiors. *Icarus* **157** (2), 426–435.

Stevenson, D. J., Spohn, T. & Schubert, G. 1983 Magnetism and thermal evolution of the terrestrial planets. *Icarus* **54** (3), 466–489.

Stewart, Andrew J., Schmidt, Max W., van Westrenen, Wim & Liebske, Christian 2007 Mars: A new core-crystallization regime. *Science* **316** (5829), 1323–1325.

Sumita, Ikuro & Olson, Peter 1999 A laboratory model for convection in earth's core driven by a thermally heterogeneous mantle. *Science* **286** (5444), 1547–1549.

Sumita, I. & Olson, P. 2000 Laboratory experiments on high rayleigh number thermal convection in a rapidly rotating hemispherical shell. *Phys. Earth Planet. Int.* **117** (1), 153–170.

Sumita, I. & Olson, P. 2003 Experiments on highly supercritical thermal convection in a rapidly rotating hemispherical shell. *J. Fluid Mech.* **492**, 271–288.

Tarduno, J. A., Cottrell, R. D., Watkeys, M. K., Hofmann, A., Doubrovine, P. V., Mamajek, E. E., Liu, D., Sibeck, D. G., Neukirch, L. P. & Usui, Y. 2010 Geodynamo, solar wind, and magnetopause 3.4 to 3.45 billion years ago. *Science* **327** (5970), 1238–1240.

Taylor, G. I. 1945 Dynamics of a hot mass rising in air. *U.S. Atomic Energy Commission, MDDC-919, LADC-276* .

Terasaki, H., Urakawa, S., Rubie, D. C., Funakoshi, K., Sakamaki, T., Shibazaki, Y., Ozawa, S. & Ohtani, E. 2012 Interfacial tension of Fe-Si liquid at high pressure: Implications for liquid Fe-alloy droplet size in magma oceans. *Phys. Earth Planet. Int.* **202**, 1–6.

Theofanous, T. G. 2011 Aerobreakup of Newtonian and Viscoelastic Liquids. In *Ann. Rev. Fluid Mech.* (ed. Davis, SH and Moin, P), *Annual Review of Fluid Mechanics*, vol. 43, pp. 661–690. Annual Reviews.

Theofanous, T. G. & Li, G. J. 2008 On the physics of aerobreakup. *Phys. Fluids* **20** (5), doi: 10.1063/1.2907989.

Theofanous, T. G., Li, G. J. & Dinh, T. N. 2004 Aerobreakup in rarefied supersonic gas flows. *J. Fluids Engng* **126** (4), 516–527.

Theofanous, T. G., Li, G. J., Dinh, T. N. & Chang, C. H. 2007 Aerobreakup in disturbed subsonic and supersonic flow fields. *J. Fluid Mech.* **593**, 131–170.

Thompson, R. S., Snyder, W. H. & Weil, J. C. 2000 Laboratory simulation of the rise of buoyant thermals created by open detonation. *J. Fluid Mech.* **417**, 127–156.

Tonks, W. B. & Melosh, H. J. 1993 Magma ocean formation due to giant impacts. *J. Geophys. Res.* **98** (E3), 5319–5333.

Townsend, A. A. 1970 Entrainment and the structure of turbulent flow. *J. Fluid Mech.* **41** (1), 13–46.

Turner, J. S. 1957 Buoyant vortex rings. *Proceedings of the royal society of London Series A - Mathematical and Physical sciences* **239** (1216), 61–75.

Vilim, R., Stanley, S. & Hauck, II, S. A. 2010 Iron snow zones as a mechanism for generating Mercury's weak observed magnetic field. *J. Geophys. Res.-Planets* **115**, doi: 10.1029/2009JE003528,.

Villermaux, E. & Bossa, B. 2009 Single-drop fragmentation determines size distribution of raindrops. *Nat. Phys.* **5** (9), 697–702.

Villermaux, E. & Bossa, B. 2011 Drop fragmentation on impact. *J. Fluid Mech.* **668**, 412–435.

Villermaux, E., Marmottant, P. & Duplat, J. 2004 Ligament-mediated spray formation. *Phys. Rev. Lett.* **92** (doi: 10.1103/PhysRevLett.92.074501).

Vocadlo, L., Alfe, D., Price, G. D. & Gillan, M. J. 2000 First principles calculations on the diffusivity and viscosity of liquid Fe-S at experimentally accessible conditions. *Phys. Earth Planet. Int.* **120** (1-2), 145–152.

Wade, J. & Wood, B. J. 2005 Core formation and the oxidation state of the Earth. *Earth Planet. Sci. Lett.* **236** (1-2), 78–95.

Wang, C. P. 1971 Motion of an isolated buoyant thermal. *Phys. Fluids* **14** (8), 1643–1647.

Wang, H. W. & Law, A. W. K. 2002 Second-order integral model for a round turbulent buoyant jet. *J. Fluid Mech.* **459**, 397–428.

Weidenschilling, S. J., Spaute, D., Davis, D. R., Marzari, F. & Ohtsuki, K. 1997 Accretional evolution of a planetesimal swarm .2. The terrestrial zone. *Icarus* **128** (2), 429–455.

Weigand, A. & Gharib, M. 1994 On the decay of a turbulent vortex ring. *Phys. Fluids* **6** (12), 3806–3808.

Weimer, J. C., Faeth, G. M. & Olson, D. R. 1973 Penetration of vapor jets submerged in subcooled liquids. *AiChE J.* **19** (3), 552–558.

Westerweel, J., Fukushima, C., Pedersen, J. M. & Hunt, J. C. R. 2005 Mechanics of the turbulent-nonturbulent interface of a jet. *Phys. Rev. Lett.* **95** (17), doi: 10.1103/PhysRevLett.95.174501.

Westerweel, J., Fukushima, C., Pedersen, J. M. & Hunt, J. C. R. 2009 Momentum and scalar transport at the turbulent/non-turbulent interface of a jet. *J. Fluid Mech.* **631**, 199–230.

Widnall, S. E., Bliss, D. B. & Tsai, C. Y. 1974 Instability of short waves on a vortex ring. *J. Fluid Mech.* **66**, 35–47.

Widnall, S. E. & Sullivan, J. P. 1973 On the stability of vortex rings. *Proc. R. Soc. Lond. A* **332** (1590), 335–353.

Widnall, S. E. & Tsai, C. Y. 1977 The instability of the thin vortex ring of constant vorticity. *Phi. Trans. R. Soc. Lond. A* **287** (1344), 273–305.

de Wijs, G. A., Kresse, G., Vocadlo, L., Dobson, D., Alfe, D., Gillan, M. J. & Price, G. D. 1998 The viscosity of liquid iron at the physical conditions of the Earth's core. *Nature* **392** (6678), 805–807.

Yadav, R., Gastine, T. & Christensen, U. 2013 Scaling laws in spherical shell dynamos with free-slip boundaries. *Icarus* **(In press)**, http://dx.doi.org/10.1016/j.icarus.2013.02.030.

Yang, J. W. & Yang, H. S. 1990 Liquid-liquid mixing for the breakup of accelerating drops. *Korean Journal of Chemical Engineering* **7** (1), 22–30.

Yin, Q. Z., Jacobsen, S. B., Yamashita, K., Blichert-Toft, J., Telouk, P. & Albarede, F. 2002 A short timescale for terrestrial planet formation from Hf-W chronometry of meteorites. *Nature* **418** (6901), 949–952.

Yoder, C. F., Konopliv, A. S., Yuan, D. N., Standish, E. M. & Folkner, W. M. 2003 Fluid core size of mars from detection of the solar tide. *Science* **300** (5617), 299–303.

Yoshino, T., Walter, M. J. & Katsura, T. 2003 Core formation in planetesimals triggered by permeable flow. *Nature* **422** (6928), 154–157.

Zhang, K. 1992 Spiralling columnar convection in rapidly rotating spherical shells. *J. Fluid Mech.* **236**, 535–556.

Zhang, K. 1994 On coupling between the poincaré equation and the heat equation. *J. Fluid Mech.* **268** (1), 211–229.

Zhang, K. 1995 On coupling between the poincaré equation and the heat equation: non-slip boundary condition. *J. Fluid Mech.* **284** (1), 239–256.

Zhao, H., Liu, H., Li, W. & Xu, J. 2010 Morphological classification of low viscosity drop bag breakup in a continuous air jet stream. *Phys. Fluids* **22** (11), doi: 10.1063/1.3490408.

Zhong, Jin-Qiang, Stevens, Richard JAM, Clercx, Herman JH, Verzicco, Roberto, Lohse, Detlef & Ahlers, Guenter 2009 Prandtl-, Rayleigh-, and Rossby-number dependence of heat transport in turbulent rotating Rayleigh-Bénard convection. *Physical review letters* **102** (4), doi: 10.1103/PhysRevLett.102.044502.

Appendixes

Appendix A

Maxwell's equations within the MHD approximation

Maxwell's equations describe the behavior of an electromagnetic field and are given by:

$$\nabla\cdot\mathbf{E} = \frac{\rho_e}{\varepsilon}, \tag{A.1}$$

$$\nabla\cdot\mathbf{B} = 0, \tag{A.2}$$

$$\nabla\times\mathbf{E} = -\frac{\partial\mathbf{B}}{\partial t}, \tag{A.3}$$

$$\nabla\times\mathbf{B} = \mu\mathbf{j} + \frac{1}{c^2}\frac{\partial\mathbf{E}}{\partial t}. \tag{A.4}$$

where ρ_e is the total charge density, $\mathbf{j}$ is the current density, $\mathbf{E}$ is the electric field, $\mathbf{B}$ is the magnetic induction (usually called magnetic field), ε is the permittivity of free space, μ is the magnetic permeability of free space and c is the speed of light in vacuum ($c = 1/\sqrt{\mu\varepsilon}$). We suppose that the characteristic value of the flow velocity is much smaller than the speed of light (called the MHD approximation or non-relativistic limit). The characteristic time for the evolution of the system is determined by advection. Let U be the characteristic value of the flow velocity, then we have:

$$\left|\frac{\frac{1}{c^2}\frac{\partial\mathbf{E}}{\partial t}}{\nabla\times\mathbf{B}}\right| \sim \frac{U^2}{c^2} \ll 1. \tag{A.5}$$

Thus, in the non-relativistic limit, the term $\dfrac{1}{c^2}\dfrac{\partial E}{\partial t}$ can be neglected in equation (A.4) and we obtain:

$$\nabla\times\mathbf{B} = \mu\mathbf{j}. \tag{A.6}$$

In the fluid frame that is moving at velocity $\mathbf{u}$ Ohm's law is given by:

$$\mathbf{j} = \sigma(\mathbf{E} + \mathbf{u}\times\mathbf{B}) + \rho_e\mathbf{u}, \tag{A.7}$$

where σ is the electrical conductivity. Taking the divergence of equation (A.6) and using equation (A.1) and Ohm's law (A.7) the following equation can be obtained:

$$\frac{\varepsilon}{\sigma}\left(\frac{\partial \rho_e}{\partial t} + (\mathbf{u}\cdot\nabla)\rho_e\right) + \rho_e = -\varepsilon\nabla\cdot(\mathbf{u}\times\mathbf{B}). \tag{A.8}$$

The characteristic time of the transient regime ε/σ appears in equation (A.8). The value of ε/σ is in the order of 10^{-17} s for a liquid metal. Thus, this characteristic time is much smaller than the characteristic time of the flow ($\sim L/U$ where L is a typical length scale). For instance, if we consider the flow in the Earth's outer core $L \approx 2.10^6$ m, $U \approx 3.10^{-4}$ m s^{-1} and $L/U \approx 10^{10}$ s. Then, equation (A.8) becomes:

$$\rho_e = -\varepsilon\nabla\cdot(\mathbf{u}\times\mathbf{B}). \tag{A.9}$$

Injecting equation (A.9) in Ohm's law (A.7) we see that $\rho_e\mathbf{u}$ can be neglected in equation (A.7):

$$\left|\frac{\rho_e\mathbf{u}}{\sigma(\mathbf{u}\times\mathbf{B})}\right| = \left|\frac{-\varepsilon\nabla\cdot(\mathbf{u}\times\mathbf{B})\mathbf{u}}{\sigma(\mathbf{u}\times\mathbf{B})}\right| \sim \frac{U\varepsilon}{L\sigma} \ll 1. \tag{A.10}$$

Neglecting $\rho_e\mathbf{u}$ in Ohm's law amounts to assuming that electrical conduction is only due to the motion of electrons. The motion of ions related to the flow is then negligible.

Finally, Maxwell's equations are given by:

$$\begin{aligned}
\nabla\cdot\mathbf{B} &= 0, &\text{(A.11)}\\
\nabla\cdot\mathbf{E} &= \frac{\rho_e}{\varepsilon}, &\text{(A.12)}\\
\nabla\times\mathbf{E} &= -\frac{\partial\mathbf{B}}{\partial t}, &\text{(A.13)}\\
\nabla\times\mathbf{B} &= \mu\mathbf{j} = \mu\sigma(\mathbf{E}+\mathbf{u}\times\mathbf{B}). &\text{(A.14)}
\end{aligned}$$

Taking the curl of (A.14) and injecting it in (A.13), we obtain the induction equation:

$$\frac{\partial\mathbf{B}}{\partial t} = \nabla\times(\mathbf{u}\times\mathbf{B}) + \eta\Delta\mathbf{B}, \tag{A.15}$$

where $\eta = 1/\mu\sigma$ is the magnetic diffusivity.

Appendix B

Mechanisms of magnetic field generation

First, it is important to notice that, for $\eta = 0$, the induction equation (2.6) becomes identical to the equation satisfied by fluid-material lines*. This means that a magnetic field line that initially coincides with a given material line, will remain identical to this material line at later times and, therefore, we can think of the magnetic field as being "frozen" in the fluid. It also follows that stretching of magnetic field lines results in magnetic field amplification, proportionally to the increase in length of the corresponding material line.

The α and ω-effects are two main mechanisms by which a magnetic field can be maintained. The ω-effect is caused by a shear flow and corresponds to the production of magnetic field in the direction of the flow from a magnetic field initially perpendicular to it, as described in figure B.1(a). The α-effect is less intuitive, it corresponds to the generation of mean currents in the mean magnetic field direction by fluctuations of magnetic and velocity fields (Moffatt, 1978).

Both effects can be identified in the induction equation using the so-called mean-field formalism (Moffatt, 1978). The velocity and magnetic fields are separated into fluctuating ($\mathbf{u}'$ and $\mathbf{b}'$) and mean parts:

$$\mathbf{u} = \overline{\mathbf{u}} + \mathbf{u}', \tag{B.1}$$
$$\mathbf{B} = \overline{\mathbf{B}} + \mathbf{b}', \tag{B.2}$$

where the overline denotes an averaging operator. The induction equation is then separated into mean and fluctuating parts:

$$\frac{\partial \overline{\mathbf{B}}}{\partial t} = (\overline{\mathbf{B}}.\nabla)\overline{\mathbf{u}} - (\overline{\mathbf{u}}.\nabla)\overline{\mathbf{B}} + \nabla \times \epsilon + \eta \Delta \overline{\mathbf{B}}, \tag{B.3}$$
$$\epsilon = \overline{\mathbf{u}' \times \mathbf{b}'}, \tag{B.4}$$
$$\frac{\partial \mathbf{b}'}{\partial t} = \nabla \times (\overline{\mathbf{u}} \times \mathbf{b}') + \nabla \times (\mathbf{u}' \times \overline{\mathbf{B}}) + \nabla \times \mathbf{G} + \eta \Delta \mathbf{b}', \tag{B.5}$$
$$\mathbf{G} = \mathbf{u}' \times \mathbf{b}' - \overline{\mathbf{u}' \times \mathbf{b}'}, \tag{B.6}$$

*The same equation is also satisfied by the vorticity field $\boldsymbol{\omega} = \nabla \times \mathbf{u}$.

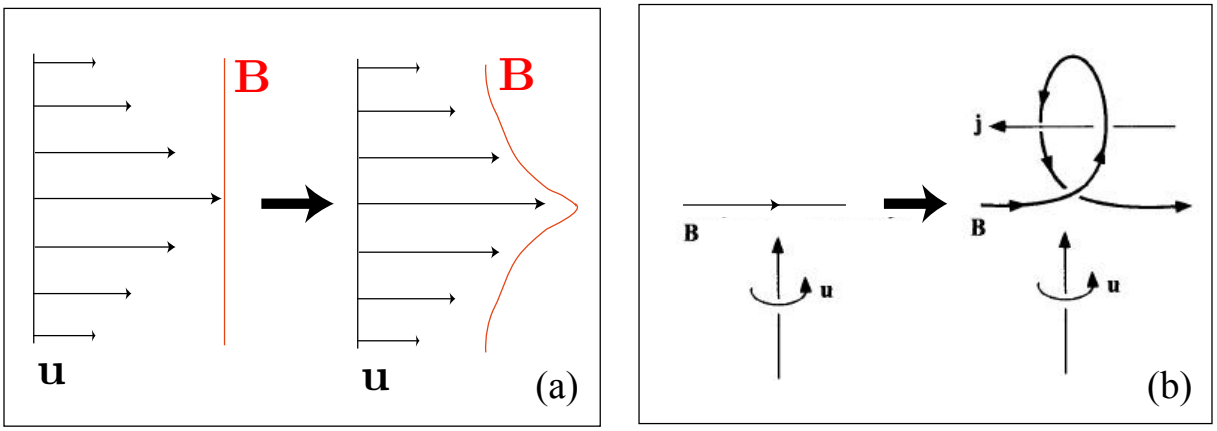

Figure B.1: (a) Schematic representation of the ω-effect. A shear flow stretches a magnetic field line that is "frozen" into the fluid (for sufficiently small magnetic diffusivity), amplifying the magnetic field intensity along the line and generating a net magnetic field component in the direction of the mean flow. (b) Field distortion by a helical localized disturbance inducing currents that are anti-parallel to $\boldsymbol{B}$ (modified from Moffatt, 1978), basic mechanism responsible for an α-effect when averaged in space.

where ϵ is the mean electromotive force. First, the ω-effect can be related to the first term on the RHS in equation (B.3). Then, the linearity in $\overline{\mathbf{B}}$ of equation (B.5) guarantees that $\mathbf{b}'$, and thus ϵ, are linearly related to $\overline{\mathbf{B}}$. In the particular case where all statistical properties of the velocity field are invariant under rotations of the frame of reference, the mean electromotive force ϵ can be written at leading order as (neglecting spatial derivatives of $\overline{\mathbf{B}}$) (Moffatt, 1978):

$$\epsilon = \alpha \overline{\mathbf{B}}. \tag{B.7}$$

This indicates that mean currents are generated in the direction of the mean magnetic field, which corresponds, by definition, to an α-effect. The curl of these currents, represented by the third RHS term in equation B.3, can generate toroidal magnetic field from poloidal magnetic field, and vice versa.

The α-effect is commonly related to helicity which is the scalar product of vorticity and velocity fields. Indeed, the coefficient α is non-zero only if $\mathbf{u}'$ is not invariant under reflexions (when considering localized portions of the spatial domain) and, in such a case, helicity will be in general non-zero. It becomes intuitive that helical flows can induce electric currents in the direction of the mean magnetic field when looking at figure B.1(b): since magnetic field lines are "frozen" into the fluid (for sufficiently small magnetic diffusivity), they are stretched and then twisted by the helical flow, producing currents in the mean field direction.

In rotating spherical shells or spheres, the mean field formalism can be useful to describe the fundamental mechanisms implicated in magnetic field generation when taking the azimuthal average as the averaging operator. Then, the ω-effect becomes the process by which an axisymmetric azimuthal magnetic field is generated as a result of a shear zonal flow, caused by a thermal wind mechanism. Besides, in non-axisymmetric convection columns, a strong axial vorticity is combined with a secondary axial flow, inducing a net

helicity (Olson *et al.*, 1999). Such helical flows are responsible for a macroscopic* α-effect as described by Kageyama & Sato (1997) or by Olson *et al.* (1999) and summarized in figure B.2.

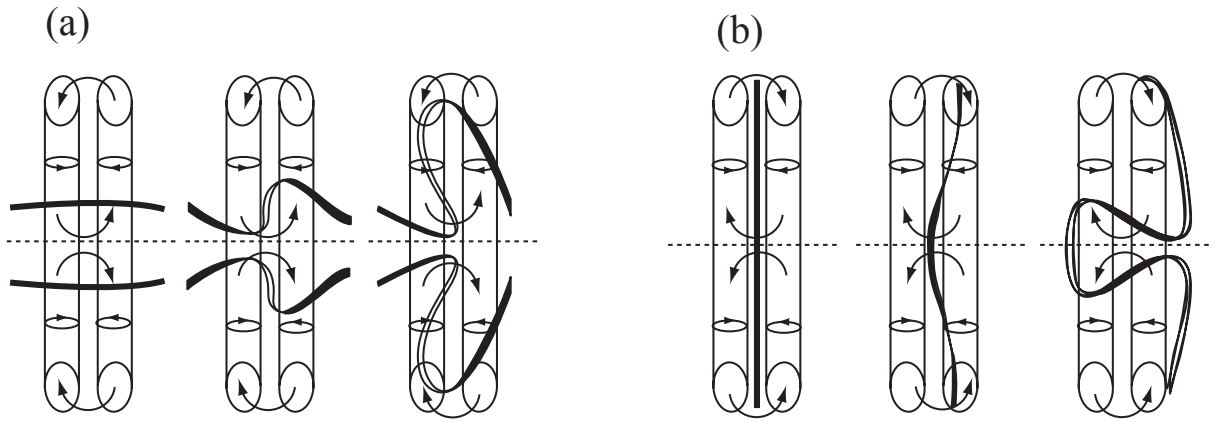

Figure B.2: Cartoons showing, in a time sequence, the generation of (a) axial magnetic field from azimuthal magnetic field and (b) azimuthal magnetic field from axial magnetic field by columnar convection (from Olson et al.*, 1999). Thick solid lines represent magnetic field lines, small arrows indicate the primary columnar flow whereas long arrows indicate the secondary axial flow.*

*The term *macroscopic α-effect* is used here since the convection columns responsible for an α-effect are rather large-scaled in numerical simulations, in contrast to the usual assumption of scale separation in mean-field theory.

Appendix C

Adiabatic reference state

In an isentropic core we can write that

$$\frac{\partial T}{\partial r} = \left(\frac{\partial T}{\partial P}\right)_S \frac{dP}{dr}. \tag{C.1}$$

Assuming hydrostatic equilibrium and making use of Maxwell's relations, equation (C.1) becomes

$$\frac{\partial T}{\partial r} = -\left(\frac{\partial T}{\partial P}\right)_S \rho g = -\frac{1}{\rho^2}\left(\frac{\partial \rho}{\partial S}\right)_P \rho g = -\frac{g}{\rho}\left(\frac{\partial \rho}{\partial T}\right)_P \left(\frac{\partial T}{\partial S}\right)_P = -\frac{\alpha T}{\rho C_p}. \tag{C.2}$$

Appendix D

Article published in Physics of the Earth and Planetary Interiors

The following article is an earlier version of chapter 4. We believe that the analysis has been improved since its publication.

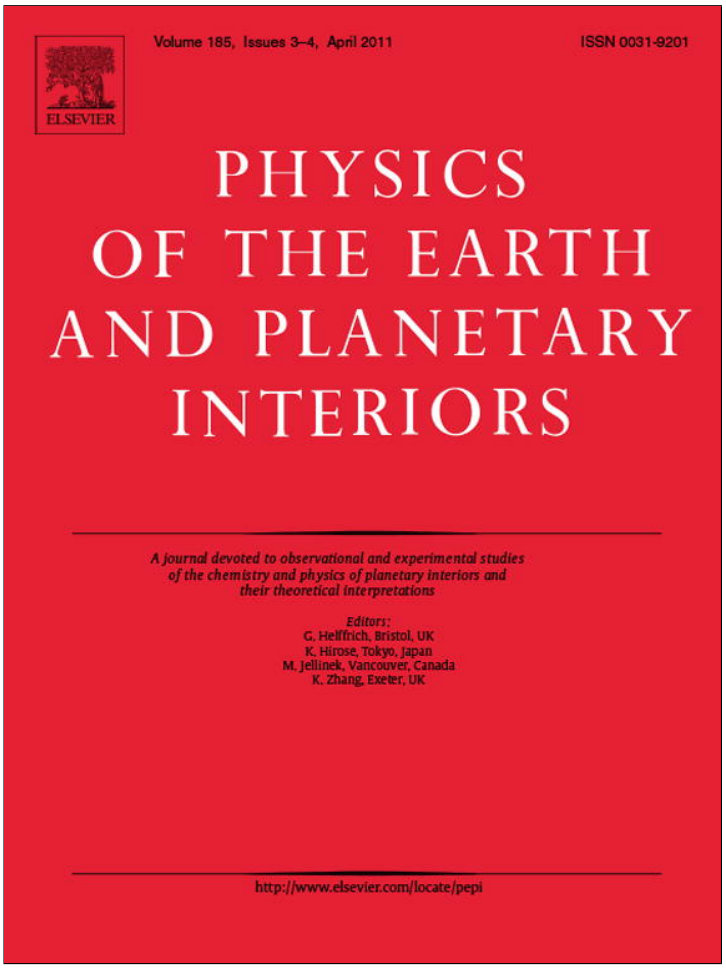

Physics of the Earth and Planetary Interiors 185 (2011) 61–73

Contents lists available at ScienceDirect

Physics of the Earth and Planetary Interiors

journal homepage: www.elsevier.com/locate/pepi

Equatorially asymmetric convection inducing a hemispherical magnetic field in rotating spheres and implications for the past martian dynamo

Maylis Landeau*, Julien Aubert

Dynamique des Fluides Géologiques, Institut de Physique du Globe de Paris, Université Paris-Diderot, PRES Sorbonne Paris Cité, INSU/CNRS UMR 7154, 1 rue Jussieu, 75238 Paris cedex 5, France

ARTICLE INFO

Article history:
Received 23 June 2010
Received in revised form
23 November 2010
Accepted 16 January 2011

Edited by: Keke Zhang.

Keywords:
Rotating convection
Secular cooling
Dynamo
Antisymmetric
Hemispherical
Mars

ABSTRACT

The convective instability in a rapidly rotating, self-graviting sphere sets up in the form of equatorially symmetric, non-axisymmetric columnar vortices aligned with the rotation axis, carrying heat away in the cylindrical radial direction. In this study, we present numerical simulations of thermal convection and dynamo action driven by internal heating (intended to model a planetary core subject to uniform secular cooling) in a rotating sphere where, from the classical columnar convection regime, we find a spontaneous transition towards an unexpected and previously unobserved flow regime in which an equatorially antisymmetric, axisymmetric (EAA) mode strongly influences the flow. This EAA mode carries heat away along the rotation axis and is the nonlinear manifestation of the first linearly unstable axisymmetric mode. When the amplitude of the EAA mode reaches high enough values, we obtain hemispherical dynamos with one single hemisphere bearing more than 75% of the total magnetic energy at the surface of the rotating sphere. We perform the linear analysis of the involved convective modes and the nonlinear study of this hydrodynamic transition, with and without dynamo action, to obtain scaling laws for the regime boundaries. As secular cooling in a full sphere (i.e. without inner core) is a configuration which has probably been widespread in the early solar system in planetary cores, including the core of Mars, we discuss the possible implications of our results for the past martian dynamo.

1. Introduction

Convection in rotating systems has been widely studied because of its numerous geophysical and astrophysical applications. For instance, dynamo processes sustained by convection are an attractive explanation not only for the Sun's magnetic field but also for the magnetic field of the Earth and other planets. Rotationally dominated convection is typically organized into vortices aligned with the rotation axis. These columnar structures tend not to violate the Taylor–Proudman constraint which requires the velocity field to be invariant along any line parallel to the rotation axis and which is approximately valid when the main balance is between the Coriolis force and the pressure gradient force. In the particular case of rotating spheres, the idea of a columnar convection appeared gradually. The first attempts to solve the onset of thermal convection focused on axisymmetric modes. Scaling laws for the threshold of instability of these modes could be extracted from Chandrasekhar (1961), but the asymptotic behavior in the limit of small Ekman numbers was obtained by Roberts (1965) and Busshopp and Niiler (1965) with two different analytical approaches. Roberts (1968) was the first to recognize that the important modes at the onset of thermal convection in rapidly rotating spheres are non-axisymmetric. However, Roberts concentrated his efforts on equatorially antisymmetric modes, in the wake of his 1965 study (Roberts, 1965) where he found that the linearly most unstable axisymmetric mode of convection has this parity. Busse (1970) subsequently showed that the dominant structures at onset are not only non-axisymmetric but also equatorially symmetric, corresponding to the famous illustration of vortices parallel to the axis of rotation and localized in the vicinity of a fixed radius in cylindrical coordinates. The first correct linear asymptotic solution for rapidly rotating full spheres was given by Jones et al. (2000). Nonlinear numerical simulations of convection and dynamo action in spherical shells have subsequently confirmed this columnar flow structure and the secondary influence of equatorially antisymmetric modes (e.g. Olson et al., 1999).

Among the different driving mechanisms which can be imposed in such numerical simulations, secular cooling in full spheres (i.e. without inner core) has been studied little until now. This configuration is appropriate for modeling convection and dynamo action in the Earth's core prior to inner core nucleation (Gubbins et al., 2003; Aubert et al., 2009). Besides, an early dynamo in a convective core subject to secular cooling is the most plausible hypothesis to explain the strong magnetizations measured on Mars' crust by the

* Corresponding author. Tel.: +331 83 95 74 14; fax: +331 83 95 77 02.
E-mail address: landeau@ipgp.fr (M. Landeau).

0031-9201/$ – see front matter © 2011 Elsevier B.V. All rights reserved.
doi:10.1016/j.pepi.2011.01.004

Mars Global Surveyor mission. The timing of the martian dynamo is debated but can be estimated using ages of the different crust regions. Indeed, some large impact basins, believed to be ∼4 Gyr old, are not magnetized (Acuna et al., 1999). Thus, the dynamo would have been active in the early history of Mars, between 4.5 Gyr and 4 Gyr. Several published studies (Lodders and Fegley, 1997; Sanloup et al., 1999) compared sulphur contents of martian meteorites with those of other primitive meteorites and estimated a high sulphur content in Mars' core: from 10.6% to 16.2%. Stewart et al. (2007) performed experiments on iron–sulfur and iron–nickel–sulfur systems at high pressure and obtained the corresponding phase diagrams at fixed pressure. They showed that, considering such high sulphur contents, Mars' core is likely to be presently entirely liquid.

The Mars Global Surveyor mission also revealed a very surprising feature for Mars' crust: intense crustal magnetizations were measured in the Southern hemisphere whereas the Northern hemisphere contains only weak fields. Dynamo models do not easily explain this hemispherical crustal magnetic field. Since Mars is a terrestrial planet with a size comparable to that of the Earth, we could have expected a dipole dominated dynamo regime with similar magnetic field strength in both hemispheres. For this reason it has long been thought that post-dynamo events, such as resurfacing processes or giant impacts, were responsible for the magnetic field asymmetry of the martian crust. It is however possible (Stanley et al., 2008) that hemispherical magnetizations of Mars' surface have been caused by a dynamo process, influenced by a hemispherical pattern in the heat flux extracted by the mantle at the core-mantle boundary (CMB).

Here, we use numerical simulations to model thermal convection and dynamo action driven by secular cooling in rotating full spheres. We find that, in this geometry and with this driving mechanism, an unexpected and previously unobserved flow regime spontaneously emerges through a hydrodynamic bifurcation: from the classical columnar flow regime to a flow regime which is strongly influenced by an equatorially antisymmetric, axisymmetric (EAA) mode and which apparently violates the Taylor–Proudman constraint. This unexpected flow regime, which we will refer to as the asymmetric regime, has never been observed before. The aim of the present study is to investigate the following questions: What is the dynamics of this EAA mode and why does it appear in the particular case of convection driven by secular cooling in rotating spheres? What impact does the EAA mode have on the pattern of magnetic field which can be seen on the planetary surface? In Section 2 we present the model and the equations solved by the numerical code. In Section 3 we introduce the results related to the hydrodynamics of the system. In Section 4 we analyze the effect of the emergence of the EAA mode on magnetic field generation and we show that hemispherical dynamos can be spontaneously induced. Finally, in Section 5, we discuss our numerical results and the possible implications for the past martian dynamo.

2. Model

Fig. 1 illustrates the configuration of the system. We use spherical coordinates (r, θ, ϕ) and cylindrical coordinates (s, ϕ, z). A sphere of radius r_o, which contains a conductive fluid, is rotating at rate Ω around an axis parallel to $\hat{z}$. Because of numerical considerations, for the calculations performed in this study we retained a very small inner sphere of radius $r_i = 0.01 r_o$ at the center of the system. It has already been argued (Aubert et al., 2009) that the presence of the small inner sphere has a negligible impact on the solution. After implementation of a more recent version of our code where the inner sphere is completely removed ($r_i/r_o = 0$), we were able to confirm that this is indeed the case for the results presented here. For this reason, the system will be referred to as a rotating full sphere.

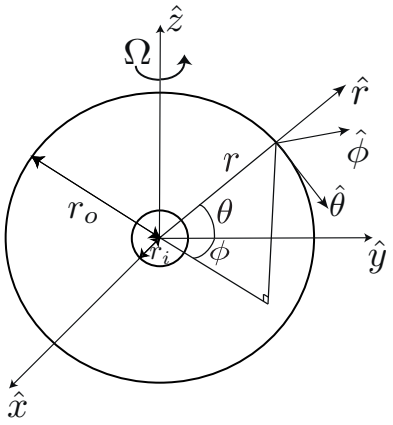

Fig. 1. Schematic representation of the system. $r_i/r_o = 0.01$.

Within the magnetohydrodynamic approximation, the non-dimensionalized governing Boussinesq equations for the velocity field $\mathbf{u}$, the magnetic field $\mathbf{B}$, and the temperature field T, are given by:

$$\frac{\partial \mathbf{u}}{\partial t} + \mathbf{u}.\nabla\mathbf{u} + 2\hat{z} \times \mathbf{u} = -\nabla P + Ra_Q \frac{\mathbf{r}}{r_0} T + (\nabla \times \mathbf{B}) \times \mathbf{B} + E\Delta\mathbf{u} \quad (1)$$

$$\frac{\partial T}{\partial t} + (\mathbf{u}.\nabla)T = \frac{E}{Pr}\Delta T + S_T \quad (2)$$

$$\frac{\partial \mathbf{B}}{\partial t} = \nabla \times (\mathbf{u} \times \mathbf{B}) + \frac{E}{Pm}\Delta\mathbf{B} \quad (3)$$

$$\nabla \cdot \mathbf{B} = 0 \quad (4)$$

$$\nabla \cdot \mathbf{u} = 0 \quad (5)$$

where S_T is a positive source term. The equations have been non-dimensionalized using the following scales: $D = r_o - r_i$ for length scale ($D \approx r_o$), Ω^{-1} for time, ΩD for velocity, $\rho D^2 \Omega^2$ for pressure where ρ is the fluid density, $\sqrt{\rho\mu}\Omega D$ for magnetic field where μ is the magnetic permeability of the fluid and $Q/4\pi\rho C_p \Omega D^3$ for temperature where Q is the total heat flux at the external boundary, or CMB and C_p the specific heat capacity.

Our numerical code solves the Boussinesq equations (1)–(5) for a system which corresponds to fluctuations with respect to an adiabatic reference state. In this framework, we model secular cooling in planetary systems using internal heating in the Boussinesq system. The decrease in the adiabatic (reference) temperature on geological time scales is modeled by a uniform distribution of internal heat sources (S_T) in Eq. (2). As T has to be statistically stationary, S_T is determined such that the heat budget of the sphere vanishes (Aubert et al., 2009).

The mantle dynamics evolves on much longer time scales than the core dynamics and thus, the core provides an isothermal boundary condition for the mantle. The resulting heat flux at the CMB, either related to thermal boundary layers in a convective mantle or to a conductive heat flux in a stagnant mantle, provides the thermal boundary condition for core convection. Thus, we impose a uniform heat flux Q at the surface of the sphere which represents the CMB. The heat flux is equal to zero at r_i. The velocity vanishes on the rigid boundaries. We study hydrodynamic simulations (in which the initial magnetic field is set to zero) and dynamo simulations (in which the initial magnetic field corresponds to a dipole of infinitesimal amplitude).

Non-dimensional control parameters are:

Table 1
Numerical models and results for hydrodynamic simulations. See text for the definitions of input parameters and output quantities. In all simulations we impose $Pr = 1$ and $Pm = 5$. The first column labels *A* and *B* tag runs which are specifically referred to in the text. The last column characterizes the resulting flow regime: 'Sym' and 'Asym' for simulations which are in a symmetric and asymmetric regime respectively (see Section 3.2 for definitions).

	E	Ra_Q	K_s	K_a	K_{0a}	
	0.0001	1.5×10^{-5}	2.56×10^{-5}	3.10×10^{-15}	6.86×10^{-16}	Sym
	0.0001	1.7×10^{-5}	3.01×10^{-5}	1.13×10^{-12}	1.65×10^{-13}	Sym
	0.0001	1.8×10^{-5}	3.24×10^{-5}	1.46×10^{-9}	1.67×10^{-10}	Sym
	0.0001	2×10^{-5}	3.61×10^{-5}	1.45×10^{-6}	2.16×10^{-7}	Asym
	0.0001	2.2×10^{-5}	3.90×10^{-5}	3.98×10^{-6}	7.38×10^{-7}	Asym
	0.0001	2.5×10^{-5}	4.40×10^{-5}	6.44×10^{-6}	1.23×10^{-6}	Asym
	0.0001	4×10^{-5}	6.49×10^{-5}	2.63×10^{-5}	6.81×10^{-6}	Asym
	0.0001	4.5×10^{-5}	7.11×10^{-5}	3.25×10^{-5}	8.48×10^{-6}	Asym
	0.0001	5×10^{-5}	7.76×10^{-5}	3.88×10^{-5}	1.02×10^{-5}	Asym
	0.0001	6×10^{-5}	9.27×10^{-5}	5.15×10^{-5}	1.33×10^{-5}	Asym
	0.0001	7×10^{-5}	1.08×10^{-4}	6.13×10^{-5}	1.52×10^{-5}	Asym
	0.0003	1.8×10^{-5}	6.40×10^{-7}	9.28×10^{-18}	9.20×10^{-18}	Sym
	0.0003	4.5×10^{-5}	3.22×10^{-5}	3.13×10^{-16}	2.55×10^{-16}	Sym
	0.0003	7.2×10^{-5}	6.99×10^{-5}	9.22×10^{-12}	9.80×10^{-13}	Sym
A	0.0003	9×10^{-5}	9.11×10^{-5}	3.69×10^{-11}	7.79×10^{-12}	Sym
	0.0003	1.08×10^{-4}	1.15×10^{-4}	1.41×10^{-10}	1.00×10^{-11}	Asym
	0.0003	1.26×10^{-4}	1.28×10^{-4}	2.07×10^{-5}	6.29×10^{-6}	Asym
	0.0003	1.35×10^{-4}	1.38×10^{-4}	2.30×10^{-5}	6.33×10^{-6}	Asym
	0.0003	1.575×10^{-4}	1.49×10^{-4}	4.93×10^{-5}	1.78×10^{-5}	Asym
	0.0003	1.8×10^{-4}	1.66×10^{-4}	7.20×10^{-5}	2.81×10^{-5}	Asym
	0.0003	1.98×10^{-4}	1.73×10^{-4}	9.04×10^{-5}	3.59×10^{-5}	Asym
	0.0003	2.25×10^{-4}	1.92×10^{-4}	1.14×10^{-4}	4.56×10^{-5}	Asym
	0.0003	2.475×10^{-4}	2.02×10^{-4}	1.35×10^{-4}	5.37×10^{-5}	Asym
	0.0003	2.7×10^{-4}	2.15×10^{-4}	1.58×10^{-4}	6.36×10^{-5}	Asym
	0.0003	3.15×10^{-4}	2.45×10^{-4}	1.94×10^{-4}	7.56×10^{-5}	Asym
B	0.0003	3.6×10^{-4}	2.76×10^{-4}	2.34×10^{-4}	9.00×10^{-5}	Asym
	0.001	6.5×10^{-4}	3.70×10^{-4}	1.88×10^{-7}	7.60×10^{-8}	Asym
	0.001	7×10^{-4}	3.58×10^{-4}	5.98×10^{-5}	3.68×10^{-5}	Asym
	0.01	1.25×10^{-2}	3.40×10^{-5}	0	0	Sym
	0.01	1.3×10^{-2}	8.48×10^{-5}	0	0	Sym
	0.01	1.4×10^{-2}	2.25×10^{-4}	0	0	Sym
	0.01	1.55×10^{-2}	6.00×10^{-5}	2.08×10^{-4}	2.02×10^{-4}	Asym
	0.01	1.57×10^{-2}	1.29×10^{-6}	2.83×10^{-4}	2.83×10^{-4}	Asym
	0.01	1.6×10^{-2}	1.47×10^{-6}	3.35×10^{-4}	3.35×10^{-4}	Asym
	0.01	1.61×10^{-2}	1.60×10^{-6}	3.52×10^{-4}	3.52×10^{-4}	Asym
	0.01	1.62×10^{-2}	1.75×10^{-6}	3.69×10^{-4}	3.69×10^{-4}	Asym
	0.01	1.63×10^{-2}	1.92×10^{-6}	3.87×10^{-4}	3.87×10^{-4}	Asym
	0.01	1.65×10^{-2}	2.32×10^{-6}	4.21×10^{-4}	4.21×10^{-4}	Asym
	0.01	1.7×10^{-2}	3.30×10^{-6}	5.08×10^{-4}	5.08×10^{-4}	Asym
	0.01	1.8×10^{-2}	5.93×10^{-6}	6.80×10^{-4}	6.80×10^{-4}	Asym
	0.01	1.9×10^{-2}	9.30×10^{-6}	8.52×10^{-4}	8.52×10^{-4}	Asym

- the modified Rayleigh number

$$Ra_Q = \frac{\alpha g_0 Q}{4\pi\rho C_p \Omega^3 D^4}, \tag{6}$$

  which has the advantage of being independent of the thermal and viscous diffusivities (Christensen and Aubert, 2006; Aubert et al., 2009),
- the Ekman number

$$E = \frac{\nu}{\Omega D^2}, \tag{7}$$

- the Prandtl number

$$Pr = \frac{\nu}{\kappa}, \tag{8}$$

- the magnetic Prandtl number

$$Pm = \frac{\nu}{\eta}, \tag{9}$$

where α is the thermal expansion coefficient, g_o is the acceleration due to gravity at the outer radius, ν the kinematic viscosity, κ the thermal diffusivity and η the magnetic diffusivity. Using this choice of non-dimensional numbers, the canonical Rayleigh number Ra is given by $Ra = Ra_Q E^{-3} Pr^2$.

The numerical code PARODY is used to solve the entire set of nonlinear equations (1)–(5). More details about this code can be found in Aubert et al. (2008). The parameters of all the nonlinear simulations used in this study are contained in Table 1 (hydrodynamic simulations) and Table 2 (dynamo simulations): we vary the values of E and Ra_Q and set Pr to 1 and Pm to 5 in most simulations. Linear stability results are obtained using a linear version of PARODY. Eqs. (1)–(5) are linearized in order to get the corresponding perturbation equations. The basic state corresponds to a stagnant fluid in which heat is transferred by diffusive processes. The algorithm used here is the same as in Dormy et al. (2004): it does not solve an eigenvalue problem but, for each value of the modified Rayleigh number, it integrates the equations in time until the system converges towards a given eigenfunction of the form $F(\mathbf{r})\exp(\sigma t)\exp i(m\phi - \omega t)$ for each azimuthal wavenumber m. Then, we increase the Rayleigh number until the growth rate of a particular mode with azimuthal wavenumber m_c becomes positive. As for the nonlinear analysis, we set $Pr = 1$ and we vary the Ekman and modified Rayleigh numbers.

As the results presented in this study are rather unexpected, special care has been devoted to testing our numerical implementation PARODY against at least another implementation (the Christensen, Wicht, Glatzmaier MAG/MAGIC code, Christensen et al., 2001) in a case where antisymmetric convection arises in the presence of an inner core, with the following parameters: $E = 10^{-4}$, $Ra_Q = 2 \times 10^{-4}$, $Pr = 1$, $Pm = 7$, and an aspect ratio $r_i/r_o = 0.35$. We have checked that after equilibration, both codes yield the same results, with an equatorially asymmetric temperature profile outside the cylinder tangent to the inner core.

Table 2
Numerical models and results for dynamo simulations. See text for the definitions of input parameters and output quantities. In all simulations we impose $Pr = 1$ and $Pm = 5$, except in simulation H in which $Pm = 1$. The first column labels C to H tag runs which are specifically referred to in the text. The last column characterizes the flow regime: 'Sym', 'Os' and 'Asym' for simulations which are in a symmetric, oscillating and asymmetric regime respectively (see Sections 3.2 and 4.1 for definitions).

	E	Ra_Q	K_s	K_a	K_{0a}	M_{dip}	M_{qua}	
H	3×10^{-5}	4.5×10^{-5}	1.46×10^{-4}	6.07×10^{-5}	8.86×10^{-6}	1.94×10^{-7}	2.16×10^{-7}	Asym
	0.0001	2×10^{-5}	1.79×10^{-5}	3.61×10^{-6}	2.18×10^{-7}	1.65×10^{-5}	9.39×10^{-6}	Os
	0.0001	4×10^{-5}	3.67×10^{-5}	1.03×10^{-5}	6.05×10^{-7}	2.35×10^{-5}	1.66×10^{-5}	Os
	0.0001	6×10^{-5}	5.81×10^{-5}	1.84×10^{-5}	1.43×10^{-6}	2.43×10^{-5}	1.92×10^{-5}	Os
	0.0001	6.5×10^{-5}	6.16×10^{-5}	1.97×10^{-5}	1.47×10^{-6}	2.88×10^{-5}	2.25×10^{-5}	Os
	0.0001	7×10^{-5}	6.61×10^{-5}	2.26×10^{-5}	2.22×10^{-6}	2.85×10^{-5}	2.29×10^{-5}	Os
	0.0001	7.5×10^{-5}	7.26×10^{-5}	2.59×10^{-5}	3.17×10^{-6}	2.69×10^{-5}	2.23×10^{-5}	Os
	0.0001	8×10^{-5}	7.30×10^{-5}	3.44×10^{-5}	7.68×10^{-6}	2.72×10^{-5}	2.43×10^{-5}	Os
G	0.0001	9×10^{-5}	7.79×10^{-5}	5.19×10^{-5}	2.08×10^{-5}	2.54×10^{-5}	2.41×10^{-5}	Os
	0.0001	9.5×10^{-5}	8.11×10^{-5}	6.13×10^{-5}	2.75×10^{-5}	2.23×10^{-5}	2.16×10^{-5}	Asym
	0.0001	1.5×10^{-4}	1.32×10^{-4}	1.27×10^{-4}	5.50×10^{-5}	1.37×10^{-5}	1.40×10^{-5}	Asym
	0.0003	1.8×10^{-5}	6.40×10^{-7}	5.62×10^{-22}	5.57×10^{-22}	7.07×10^{-16}	1.13×10^{-22}	Sym
	0.0003	4.5×10^{-5}	3.26×10^{-5}	1.53×10^{-13}	1.26×10^{-13}	3.30×10^{-10}	7.48×10^{-17}	Sym
	0.0003	7.2×10^{-5}	6.85×10^{-5}	3.56×10^{-11}	1.48×10^{-11}	1.44×10^{-10}	5.17×10^{-14}	Sym
C	0.0003	9×10^{-5}	7.67×10^{-5}	2.33×10^{-6}	1.79×10^{-7}	1.59×10^{-5}	3.13×10^{-6}	Sym
	0.0003	1.08×10^{-4}	8.33×10^{-5}	7.16×10^{-6}	8.03×10^{-7}	2.65×10^{-5}	1.00×10^{-5}	Os
	0.0003	1.35×10^{-4}	1.14×10^{-4}	1.15×10^{-5}	1.27×10^{-6}	3.86×10^{-5}	2.00×10^{-5}	Os
	0.0003	1.8×10^{-4}	1.38×10^{-4}	2.40×10^{-5}	3.11×10^{-6}	2.97×10^{-5}	1.88×10^{-5}	Os
	0.0003	1.98×10^{-4}	1.38×10^{-4}	2.90×10^{-5}	3.73×10^{-6}	4.33×10^{-5}	2.72×10^{-5}	Os
F	0.0003	2.25×10^{-4}	1.58×10^{-4}	4.52×10^{-5}	1.23×10^{-5}	3.84×10^{-5}	2.80×10^{-5}	Os
	0.0003	2.48×10^{-4}	1.58×10^{-4}	4.74×10^{-5}	1.06×10^{-5}	5.59×10^{-5}	4.07×10^{-5}	Os
	0.0003	2.7×10^{-4}	1.48×10^{-4}	8.69×10^{-5}	4.42×10^{-5}	5.88×10^{-5}	5.12×10^{-5}	Os
	0.0003	2.925×10^{-4}	1.49×10^{-4}	1.31×10^{-4}	8.36×10^{-5}	5.05×10^{-5}	4.94×10^{-5}	Asym
	0.0003	3.15×10^{-4}	1.53×10^{-4}	1.65×10^{-4}	1.13×10^{-4}	4.76×10^{-5}	4.89×10^{-5}	Asym
D	0.0003	3.6×10^{-4}	1.75×10^{-4}	2.14×10^{-4}	1.51×10^{-4}	4.28×10^{-5}	4.37×10^{-5}	Asym
	0.0003	4.05×10^{-4}	1.92×10^{-4}	2.83×10^{-4}	2.05×10^{-4}	4.25×10^{-5}	4.43×10^{-5}	Asym
	0.0003	4.5×10^{-4}	2.15×10^{-4}	3.37×10^{-4}	2.40×10^{-4}	3.97×10^{-5}	4.12×10^{-5}	Asym
	0.001	6×10^{-4}	3.25×10^{-4}	2.50×10^{-8}	1.16×10^{-8}	3.34×10^{-11}	4.48×10^{-14}	Sym
	0.001	7×10^{-4}	3.88×10^{-4}	1.95×10^{-5}	9.15×10^{-6}	3.59×10^{-11}	8.83×10^{-12}	Asym
	0.001	7.5×10^{-4}	3.02×10^{-4}	9.33×10^{-5}	6.51×10^{-5}	1.23×10^{-5}	1.00×10^{-5}	Asym
	0.001	7.6×10^{-4}	3.11×10^{-4}	9.44×10^{-5}	6.56×10^{-5}	1.40×10^{-5}	1.12×10^{-5}	Asym
	0.001	7.7×10^{-4}	3.14×10^{-4}	1.10×10^{-4}	7.87×10^{-5}	1.09×10^{-5}	9.27×10^{-6}	Asym
	0.001	8×10^{-4}	3.17×10^{-4}	1.30×10^{-4}	9.29×10^{-5}	1.01×10^{-5}	9.02×10^{-6}	Asym
	0.001	8.2×10^{-4}	3.17×10^{-4}	1.39×10^{-4}	1.00×10^{-4}	1.35×10^{-5}	1.16×10^{-5}	Asym
	0.001	8.5×10^{-4}	3.27×10^{-4}	1.48×10^{-4}	1.05×10^{-4}	1.48×10^{-5}	1.31×10^{-5}	Asym
	0.001	8.7×10^{-4}	3.23×10^{-4}	1.63×10^{-4}	1.18×10^{-4}	1.65×10^{-5}	1.49×10^{-5}	Asym
	0.001	9×10^{-4}	3.25×10^{-4}	1.93×10^{-4}	1.41×10^{-4}	1.48×10^{-5}	1.37×10^{-5}	Asym
	0.001	9.5×10^{-4}	3.29×10^{-4}	2.16×10^{-4}	1.60×10^{-4}	2.15×10^{-5}	1.98×10^{-5}	Asym
	0.001	1×10^{-3}	3.29×10^{-4}	2.24×10^{-4}	1.66×10^{-4}	3.69×10^{-5}	3.41×10^{-5}	Asym
	0.001	3×10^{-3}	7.60×10^{-4}	1.73×10^{-3}	1.34×10^{-3}	7.18×10^{-6}	7.53×10^{-6}	Asym
	0.001	5×10^{-3}	1.31×10^{-3}	2.94×10^{-3}	2.21×10^{-3}	1.46×10^{-5}	1.51×10^{-5}	Asym

The time averaged kinetic energy density K is defined as follows:

$$K = \frac{1}{2V_S}\left\langle \int_{V_S} \mathbf{u}^2 dV \right\rangle \tag{10}$$

where V_S is the shell volume and the angled brackets indicate a time averaging operator. Using this template, we additionally define:

- the time averaged kinetic energy density contained in the equatorially antisymmetric, axisymmetric (EAA) flow component K_{0a},
- the time averaged kinetic energy density contained in equatorially antisymmetric modes K_a,
- the time averaged kinetic energy density contained in equatorially symmetric modes K_s.

In the present study, it is understood that an 'equatorially symmetric' vector field $\mathbf{u}$ is left unchanged by the operator Γ which describes mirror-reflection through the equatorial plane, i.e. $\Gamma\mathbf{u} = \mathbf{u}$, while an 'equatorially antisymmetric' vector field is such that $\Gamma\mathbf{u} = -\mathbf{u}$.

We similarly define a time averaged magnetic energy density M at the external boundary of the model:

$$M = \frac{1}{2S_{\mathrm{cmb}}}\left\langle \int_{S_{\mathrm{cmb}}} \mathbf{B}^2 dS \right\rangle \tag{11}$$

where S_{cmb} is the surface of the sphere (at the CMB). Using this template, we also define:

- the time averaged CMB magnetic energy related to modes of dipole parity (odd $l+m$ in spherical harmonics) M_{dip},
- the time averaged CMB magnetic energy related to modes of quadrupole parity (even $l+m$) M_{qua}.

Another output quantity f_{hem} is used to characterize the hemisphericity of the magnetic field at the CMB:

$$f_{\mathrm{hem}} = \frac{\max[M^S, M^N]}{M}, \tag{12}$$

where M^S and M^N are the time averaged magnetic energy densities contained in the Southern and Northern hemispheres. The hemisphericity factor f_{hem} is equal to 0.5 for a purely dipolar field and has the value 1 for a purely hemispherical field.

3. Results for convection without dynamo action

In this section we introduce the results for secular cooling-driven convection in a rotating sphere without dynamo action. Starting from a non-convective stable state at low Rayleigh number, we introduce the main hydrodynamic transitions found when we progressively increase the forcing.

Table 3
Critical Rayleigh number Ra_{Qc} and azimuthal wavenumber m_c for the most linearly unstable equatorially symmetric convection mode.

E	Ra_{Qc}	m_c
10^{-6}	1.08×10^{-9}	38
3×10^{-6}	6.80×10^{-9}	26
10^{-5}	5.18×10^{-8}	17
3×10^{-5}	3.34×10^{-7}	12
5×10^{-5}	7.98×10^{-7}	10
10^{-4}	2.61×10^{-6}	7
3×10^{-4}	1.72×10^{-5}	5

3.1. Linear stability results: the onset of convection

The first hydrodynamic transition corresponds to the onset of convection and occurs when the modified Rayleigh number reaches a first critical value Ra_{Qc}. We start introducing the onset of convection in our system because it gives the framework for the nonlinear simulations presented in the following parts.

For each value of the azimuthal wavenumber m and each value of the modified Rayleigh number, two growth-rates can be calculated using the linear version of the code PARODY: one for equatorially symmetric modes and one for equatorially antisymmetric modes. Indeed, these two families of modes are not coupled in the linearized equations.

We found that the first unstable modes are equatorially symmetric, non-axisymmetric modes, as expected from previous theoretical studies (Busse, 1970; Jones et al., 2000). Table 3 lists the critical Rayleigh number and azimuthal wavenumber for each studied value of the Ekman number. Fig. 2 shows that $Ra_{Qc}/E^{5/3}$ converges towards an asymptote which is in good agreement with the value 10.3749 (≈10.4) obtained by Jones et al. (2000). It must be pointed out that Jones et al. (2000) used slightly different boundary conditions (fixed temperature and stress-free) at the external boundary, while we presently use a fixed flux condition for geophysical relevance and we consider rigid boundaries. However, as the temperature gradient in the bulk of the fluid is the same in our and their study, we do not expect the asymptote to be shifted by a dramatic amount, as confirmed by our numerical results. The asymptotic behavior of the critical modified Rayleigh number in the limit $E \to 0$ is thus approximated by:

$$Ra_{Qc} \approx 10.4 \cdot E^{5/3} \tag{13}$$

In terms of critical canonical Rayleigh number Ra_c, this corresponds to the following asymptotic behavior: $Ra_c \approx 10.4 \cdot E^{-4/3}$. The exponent value $-4/3$ for the Ekman number dependence of the critical Rayleigh number is a robust feature of the onset of convection in rotating spheres or shells: it is expected from analytical consideration (Busse, 1970; Jones et al., 2000) and has subsequently been found in numerical studies (Dormy et al., 2004) for other geometries and boundary conditions.

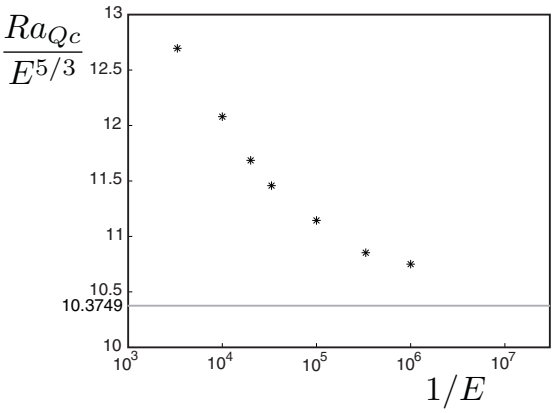

Fig. 2. Convection onset. Stars: $Ra_{Qc}/E^{5/3}$ versus $1/E$ (logarithmic scale). The grey line is the asymptote predicted by the theory of Jones et al. (2000) with slightly different boundary conditions (see text).

As illustrated in Fig. 3, the velocity structures at onset correspond to quasi-geostrophic Rossby waves that vary slowly in z-direction. These waves form a set of non-axisymmetric vortices aligned with the rotation axis as predicted by Busse (1970). The azimuthal wavenumber of the first unstable modes m_c, is expected to vary such that $m_c \propto E^{-1/3}$ (Busse, 1970; Jones et al., 2000). The values we found for m_c are reported in Table 3 and are in agreement with the expected trend.

A second important family of convective modes is the axisymmetric family. At first sight it can seem of secondary importance to study the linear stability of this family into detail since we previously saw that the first unstable modes are non-axisymmetric at high rotation rates (Geiger and Busse, 1981 have shown that axisymmetric modes can be preferred at low rotation rates). However, as announced in Section 1 and developed in Section 3.2, the axisymmetric modes acquire a crucial importance in our nonlinear simulations. We thus compute (Table 4) the linear threshold of instability for the axisymmetric modes Ra_{Qa0}. Indeed, these results will be required in Section 3.2 in order to determine if the emergence of EAA modes in nonlinear simulations is related to their linear instability. Within a margin of error of 20% (which corresponds to the misfit between the results of Roberts (1965) and Bisshopp and Niiler (1965)), our numerical results are compatible

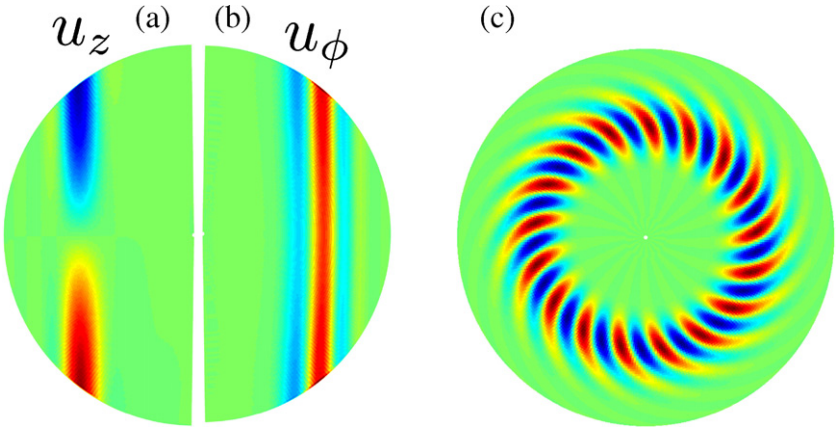

Fig. 3. Velocity structures at onset for $E = 10^{-5}$ and $Pr = 1$. (a) Meridional section of the z-component of velocity. (b) Meridional section of the azimuthal velocity field. (c) Equatorial section ($\theta = \pi/2$) of the z-component of vorticity.

Table 4
Critical Rayleigh numbers Ra_{Qa0} for the linear onset of axisymmetric convection (EAA mode), and Ra_{Qt} for the nonlinear emergence of the EAA mode (see Section 3.2).

E	Ra_{Qa0}	Ra_{Qt}
10^{-4}	8.37×10^{-6}	1.95×10^{-5}
3×10^{-4}	5.00×10^{-5}	1.07×10^{-4}
10^{-3}	3.34×10^{-4}	6.28×10^{-4}
10^{-2}	1.41×10^{-2}	1.41×10^{-2}

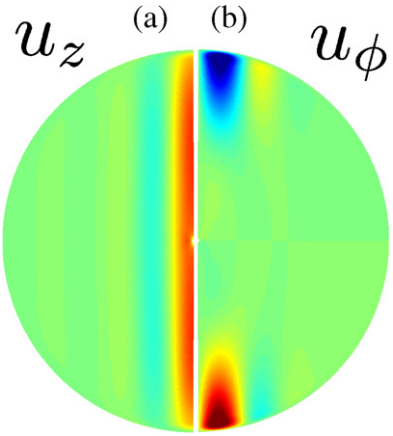

Fig. 4. First unstable axisymmetric convection mode at $E = 3 \times 10^{-4}$ and $Pr = 1$. (a) Meridional section of the z-component of velocity. (b) Meridional section of the azimuthal velocity field.

with both the asymptotes found by Roberts (1965), which yields:

$$Ra_{Qa0} \approx 52.2 \cdot E^{5/3}, \tag{14}$$

and Busse and Niiler (1965), which yields:

$$Ra_{Qa0} \approx 61.3 \cdot E^{5/3}, \tag{15}$$

although the thermal boundary conditions are different and a small inner sphere is present in our study. Unlike the non-axisymmetric modes, the most linearly unstable axisymmetric mode belongs to the equatorially antisymmetric family. Its pattern (Fig. 4) corresponds to a single convection cell carrying heat away in the direction of the rotation axis, whereas the first unstable non-axisymmetric modes convect heat in the cylindrical radial direction. As the axial circulation gets close to the upper and lower boundaries, the flow is diverted and couples with the Coriolis force to give rise to an equatorially antisymmetric, zonal circulation. As in the case of non-axisymmetric convection (Busse, 1970), viscous forces on short length scales of order $E^{1/3}$ are required to overcome the two-dimensional constraint of the Taylor–Proudman theorem. Then, the thickness of the axial cell is of order $E^{1/3}$ (Roberts, 1965) and motion in the cell is quasi-geostrophic, slowly varying in z-direction.

In summary, the linear stability analysis performed in the case of rotating convection driven by secular cooling confirms the theoretical results obtained with slightly different boundary conditions: equatorially symmetric, non axisymmetric vortices are the most linearly unstable modes, and the first linearly unstable axisymmetric modes are equatorially antisymmetric. The critical canonical Rayleigh numbers for both families vary as $E^{-4/3}$ when $E \to 0$. Planetary core dynamos are located largely above the onset of convection and nonlinear simulations are required to go further.

3.2. Nonlinear simulation results: transition towards the asymmetric regime

When we increase the Rayleigh number slightly above onset, we found that non-axisymmetric vortices aligned with the rotation axis (equatorially symmetric structures) remain the main convective features, even though the flow becomes chaotic and small-scale structures appear. This result can be seen in Fig. 5(b) which shows results obtained with simulation A (with $Ra_Q \approx 5Ra_{Qc}$, see Table 1). The columnar structures tend to satisfy the Taylor–Proudman theorem and the flow is said to be in a symmetric regime as indicated in Fig. 5(a) which gives a schematic representation of the main hydrodynamic transitions found when increasing the modified Rayleigh number. Most of the previously studied nonlinear numerical simulations are located in this symmetric regime (see for instance Olson et al., 1999).

By further increasing the forcing, we found that the flow undertakes an unexpected transition when the modified Rayleigh number reaches a second critical value Ra_{Qt} (values reported in Table 4). Fig. 5(a) shows a schematic representation of this transition and Fig. 6 serves as a bifurcation diagram. At the onset of convection ($Ra_{Qc} \approx 0.17 \times 10^{-4}$), the symmetric solution branch ($K_{0a} \ll K_s$) emerges. At $Ra_{Qt} \approx 1.07 \times 10^{-4}$, the symmetric branch looses stability and a new branch of solutions, which is characterized by a rapid increase of K_{0a}, emerges through a supercritical pitchfork bifurcation. This branch of solutions is called asymmetric branch because it characterizes equatorially asymmetric solutions in which the EAA kinetic energy density K_{0a}, and the equatorially symmetric kinetic energy density K_s, become of the same order of magnitude (Fig. 6). The asymmetric regime is unexpected since the amplitude of equatorially antisymmetric modes has always been found to be much smaller than the amplitude of equatorially symmetric modes in previous numerical simulations (Olson et al., 1999; Christensen and Aubert, 2006; Sakuraba and Roberts, 2009). The EAA mode is the dominant equatorially antisymmetric mode since almost half of K_a is contained in this mode ($K_{0a} \approx 0.44K_a$). Equa-

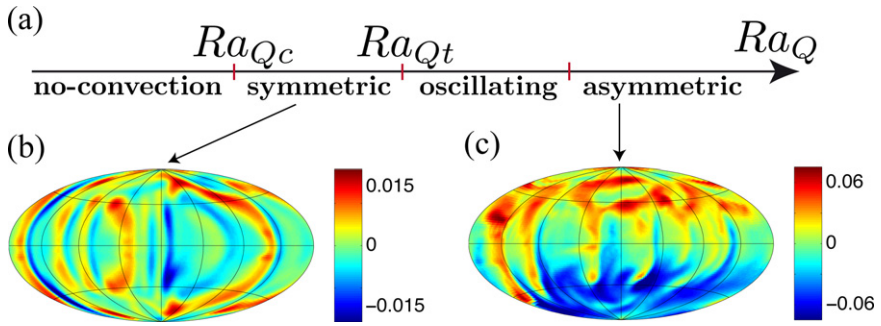

Fig. 5. (a) Schematic representation of the two main hydrodynamic transitions found when increasing the modified Rayleigh number: from a non-convective state to the classical symmetric regime at Ra_{Qc} (onset of convection) and then, at Ra_{Qt}, from the symmetric regime to the asymmetric regime (characterized by the emergence of an EAA mode). (b) and (c) Snapshots of azimuthal velocity field at radius $r = 0.88$ (Hammer projection), hydrodynamic simulations. (b) Simulation A. (c) Simulation B (parameters reported in Table 1).

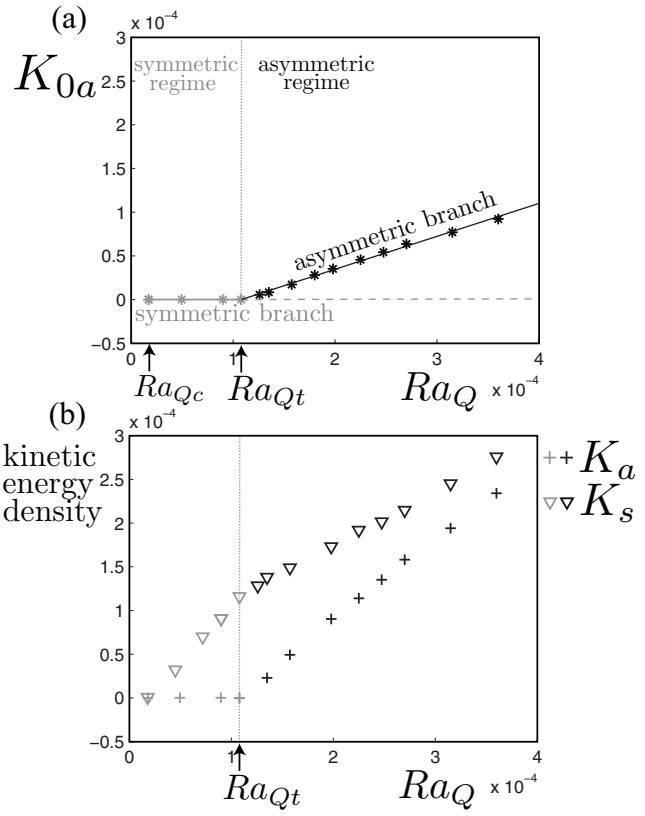

Fig. 6. Bifurcation diagram showing K_{0a} (stars), K_a (crosses) and K_s (triangles) versus Ra_Q at $E = 3 \times 10^{-4}$. Solution branches are identified in (a) since K_{0a} is the energy contained in the mode which emerges at the transition of interest. Solid and dashed curves refer to linearly stable and unstable solutions respectively. Ra_{Qt} locates the emergence of the asymmetric solution branch. To estimate the value of Ra_{Qt} we look for Ra_{Qt} and the constant a such that K_{0a} is best scaled (in the sense of the least squares) by $a(Ra_Q - Ra_{Qt})$ on the asymmetric branch.

torially antisymmetric, non-axisymmetric modes also emerge at Ra_{Qt}, with an energy density equal to $K_a - K_{0a}$. However, we find that these modes do not emerge spontaneously, contrary to the EAA mode, but result from nonlinear interactions between the EAA mode and equatorially symmetric modes. The spatial structure of these modes is indeed strongly correlated with that of equatorially symmetric, non-axisymmetric modes. Thus, in the asymmetric regime, the dominant (and dynamically important) structures correspond to a superposition of columnar, equatorially symmetric modes and an EAA mode (Fig. 5(c)).

We found that, at low Ekman numbers ($E \leq 10^{-3}$), Ra_{Qt} is located above the linear threshold of instability of EAA modes Ra_{Qa0} (Table 4). This result means that the emergence of an EAA mode in our nonlinear simulations can not be explained by linear stability analysis if $E \leq 10^{-3}$. Thus, the asymmetric branch emerges from the equatorially symmetric, columnar convection which has to be seen as the new basic state. We checked numerically that Ra_{Qt} corresponds indeed to the threshold of linear instability of EAA modes with respect to a purely equatorially symmetric basic state. The bifurcation at $E = 10^{-2}$ is a very isolated case since $Ra_{Qt} = Ra_{Qa0}$ (Table 4). In this case the bifurcation can be described in terms of interactions between two linearly unstable modes: an equatorially symmetric mode of order $m = 1$ and an EAA mode. Since we are looking for asymptotic behaviors in the limit $E \to 0$, we will not consider the slowly rotating cases $E \geq 10^{-2}$ for the determination of the regime boundaries.

Fig. 7 gives a schematic view of the EAA mode which emerges in the asymmetric regime: the azimuthal velocity field is organized into two large equatorially antisymmetric vortices, one in each

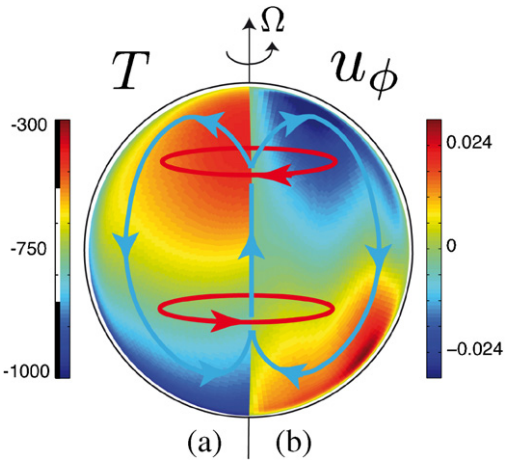

Fig. 7. Arrows: schematic representation of the time-averaged EAA mode (azimuthal and meridional flows) which emerges in the asymmetric regime. (a) Meridional section (arbitrary azimuth) of the time-averaged temperature field in asymmetric simulation B (parameters reported in Table 1). (b) Same as (a) for the time-averaged azimuthal velocity field.

hemisphere. Contrary to the two-cell meridional circulation of the symmetric regime (Olson et al., 1999), the time-averaged meridional circulation induced by the EAA mode is organized in only one cell. The fluid goes from one pole to the other passing through the center of the sphere. As a consequence of this equatorially antisymmetric meridional circulation, the temperature profile has a considerable equatorially antisymmetric component (Fig. 7(a)).

The dynamics of the asymmetric regime is strongly influenced by rotation since the local Rossby number (Christensen and Aubert, 2006) remains inferior to 0.08 in all our asymmetric simulations. We find that the equatorially asymmetric azimuthal velocity field results from meridional variation of the asymmetric temperature field through a thermal wind mechanism, which is characterized by a balance between the Coriolis, pressure gradient and buoyancy forces. Taking the ϕ-component of the curl of the momentum equation, and retaining only the above forces, we have:

$$\frac{\partial u_\phi}{\partial z} = \frac{Ra_Q}{2r_0}\frac{\partial T}{\partial \theta} \tag{16}$$

Fig. 8 shows a high degree of similarity between the right-hand side and left-hand side terms of Eq. (16), thus confirming that Eq. (16) captures the flow dynamics inside the shell (except near the

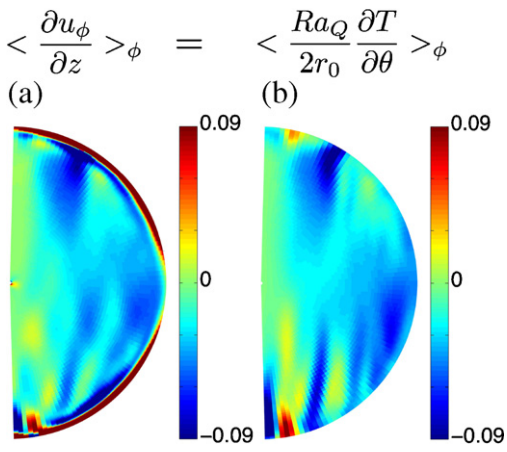

Fig. 8. Comparison between (a) a snapshot of the ϕ-average of the left-hand side term of Eq. (16), and (b) a snapshot of the ϕ-average of the right-hand side term of the same equation. Results obtained using asymmetric simulation B (parameters indicated in Table 1).

boundaries where the viscous term in Eq. (1) is not negligible). The term $\partial T/\partial\theta$ is globally negative in the whole shell as a consequence of the equatorially antisymmetric component of the temperature profile shown in Fig. 7(a). Then, according to Eq. (16), $\partial u_\phi/\partial z$ is also negative, and this is coherent with an antisymmetric azimuthal flow organized in two vortices as we find in our asymmetric simulations (Fig. 7(b)).

The time-averaged zonal velocity field is also in equilibrium with the time-averaged convective axial velocity field. In our nonlinear simulations, we have found that this equilibrium arises through Ekman pumping. In the Southern hemisphere in Fig. 7, the fluid is rotating faster than the external boundary, inducing a meridional flow that converges towards the center of the vortex. Conversely, the time-averaged meridional flow diverges from the center of the vortex in the Northern hemisphere. The axial velocity v_z is then related to the vertical vorticity ω_z by $v_z = O(E^{1/2}\omega_z)$. To check this hypothesis we computed the ratio

$$r_E = \frac{\max|\langle\langle v_z\rangle\rangle_\phi|}{E^{1/2}\max|\langle\langle\omega_z\rangle\rangle_\phi|}, \tag{17}$$

where $\langle\rangle_\phi$ and $\langle\rangle$ denote the azimuthal and time averaging operators. Considering only the equatorially antisymmetric part of the velocity and vorticity fields, we find a mean value $\bar{r}_E = 3.52$ and a standard deviation 1.6, meaning that this ratio remains of order 1, as expected in the case of an Ekman pumping mechanism, even though our configuration is far from being the ideal case of a unique rotating plate for which the classical Ekman pumping formula is derived.

Eqs. (1), (2) and (5), and the boundary conditions have equatorial reflection symmetry. Consequently, if $A(t)$ is the amplitude of the EAA mode $\mathbf{u}_a$, then $A\mathbf{u}_a$ and $-A\mathbf{u}_a$ are two dynamically equivalent solutions. This means that the solution for the EAA mode which is represented in Fig. 7 is dynamically equivalent to the solution which can be obtained by reversing the arrows in Fig. 7. In our simulations we indeed found both solutions. The system chooses one of the two and does not reverse towards the other. Thus, the EAA mode should emerge through a pitchfork bifurcation. As it would be in a canonical supercritical pitchfork bifurcation, K_{0a} is proportional to $(Ra_Q - Ra_{Qt})$ in our numerical simulations (Fig. 6(a)).

Considering the possible relationship between the emergence of a strong EAA mode and the smallness (or absence) of the inner core, we found the same hydrodynamic transition towards the asymmetric regime in a shell with aspect ratio $r_i/r_o = 0.35$, provided the driving mode is the same (secular cooling with zero heat flux at the inner core). The critical value Ra_{Qt} is larger when $r_i/r_o = 0.35$ than when $r_i/r_o = 0.01$ (results not reported here) but the transition occurs at about the same static temperature difference in both cases. However, no transition to the EAA state has been found when a non-zero homogeneous heat flux or fixed temperature was imposed at the inner core boundary, suggesting that the presence of a thermal boundary layer with a positive incoming heat flux at the inner core boundary prevents the EAA mode from emerging. We presume that the EAA hydrodynamic transition is favored in our numerical simulations because the buoyancy driving allows for EAA convection carrying heat away in the direction perpendicular to the equatorial plane.

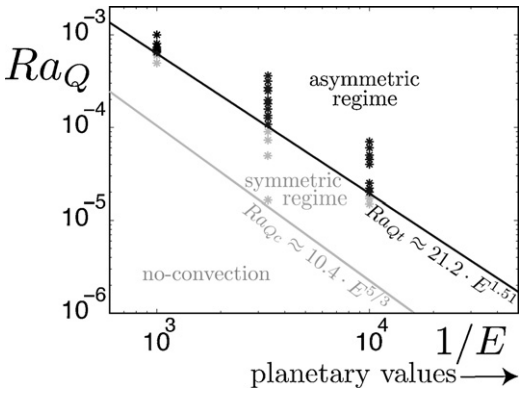

Fig. 9. Phase diagram of the two main hydrodynamic transitions in the absence of dynamo action: from a non-convective state to the symmetric regime (light grey curve corresponds to the asymptotic behavior of Ra_{Qc} at low Ekman numbers according to Eq. (13)) and from the symmetric regime to the asymmetric regime (black curve). Light grey symbols: symmetric simulations. Black symbols: asymmetric simulations.

The different transitions found are represented in a $(1/E, Ra_Q)$ parameter space (Fig. 9). The transition between the symmetric and asymmetric regimes occurs at Ra_{Qt}, which is best scaled (in the sense of the least squares) by:

$$Ra_{Qt} \approx 21.2 \cdot E^{1.51} \tag{18}$$

4. Results for convective dynamos

We now turn to the study of the EAA mode in the presence of dynamo action. We first introduce the different hydrodynamic transitions found when allowing dynamo action and compare them with the transitions found in hydrodynamic simulations (Section 3). Then we present the changes in magnetic field generation which are related to these hydrodynamic transitions.

4.1. Hydrodynamic transitions

Fig. 10(a) gives a schematic representation of the different hydrodynamic transitions found when increasing the modified Rayleigh number and allowing dynamo action. The results for the linear onset of convection at Ra_{Qc} are identical to what we found in

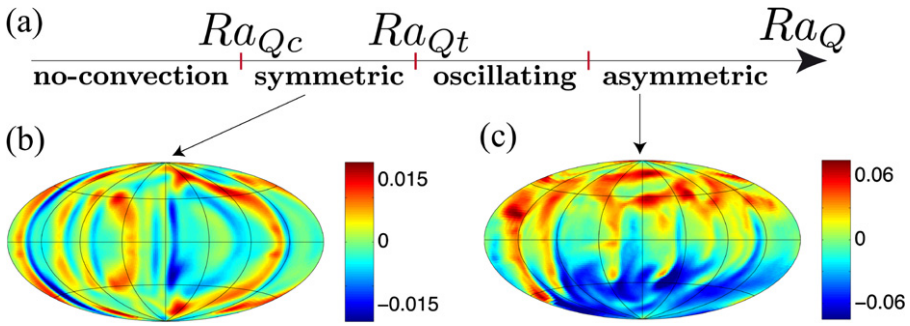

Fig. 10. (a) Schematic representation of the main hydrodynamic transitions found when increasing the modified Rayleigh number and allowing dynamo action: from a non-convective state to the classical symmetric regime at Ra_{Qc} (onset of convection) and then, from the symmetric regime to the oscillating regime at Ra_{Qt} and finally from the oscillating regime to the asymmetric regime. (b) and (c) Snapshots of azimuthal velocity field at radius $r = 0.88$ (Hammer projections). (b) Simulation *C*. (c) Simulation *D* (parameters reported in Table 2).

Section 3.1 (without dynamo action) since the Lorentz force (third term in the right-hand side of Eq. (1)) is a nonlinear term. Increasing the modified Rayleigh number above onset we found a symmetric regime dominated by columnar, equatorially symmetric vortices as illustrated in Fig. 10(b), similarly to the non-magnetic case.

By further increasing the forcing, the flow undertakes successive changes of regime which can be identified in the bifurcation diagram of Fig. 11(a). When Ra_Q reaches the value Ra_{Qt} (previously computed in Section 3.2), the symmetric solution branch ($K_{0a} \ll K_s$) becomes unstable and the instantaneous value of K_{0a} starts oscillating in a chaotic manner between low values much smaller than K_s (symmetric regime), and larger values of order K_s (asymmetric regime). The flow is said to be in an oscillating regime, illustrated in Fig. 12. Finally, when the forcing is strong enough ($Ra_Q \approx 3 \times 10^{-4}$), the flow reaches the asymmetric regime: the instantaneous value of K_{0a} remains large and does not reach the symmetric solution branch anymore. Similarly to the hydrodynamic case, the dominant (and dynamically important) modes in the asymmetric regime are the columnar, equatorially symmetric modes and the EAA mode (Fig. 10(c)).

We found a similar bifurcation diagram (with a symmetric, oscillating and asymmetric regime) at $E = 10^{-4}$. However we did not find any oscillating simulations at $E \geq 10^{-3}$ because the dynamo onset has not been overcome when Ra_Q reaches Ra_{Qt} at such Ekman numbers. Therefore, the bifurcation diagrams are similar to the ones obtained in hydrodynamic simulations if $E \geq 10^{-3}$. Since we are looking for asymptotic behaviors in the limit $E \to 0$, we will not consider cases in which $E \geq 10^{-3}$ for the determination of the regime boundaries.

The appearance of the oscillating regime when allowing dynamo action can be seen as a consequence of Ferraro's law of corotation (Ferraro, 1937): the axisymmetric magnetic field lines tend to follow the isocontours of $\langle u_\phi/s \rangle_\phi$ where s is the cylindrical radius. At the beginning of an oscillation towards the asymmetric regime, the EAA flow component emerges because it is linearly unstable with respect to the symmetric regime (because $Ra_Q \geq Ra_{Qt}$). Then, the EAA mode distorts the isocontours of $\langle u_\phi/s \rangle_\phi$ which no longer follow the magnetic field lines. Consequently, an axisymmetric azimuthal magnetic field is created from stretching of the axisymmetric poloidal magnetic field by the EAA azimuthal flow through an ω-effect, which increases the magnetic tension along the meridional field lines. In agreement with Lenz law, the resulting Lorentz force tends to oppose the motion that increases the magnetic tension, i.e. reduces the EAA flow component. If the Lorentz force becomes strong enough, the flow returns its symmetric regime.

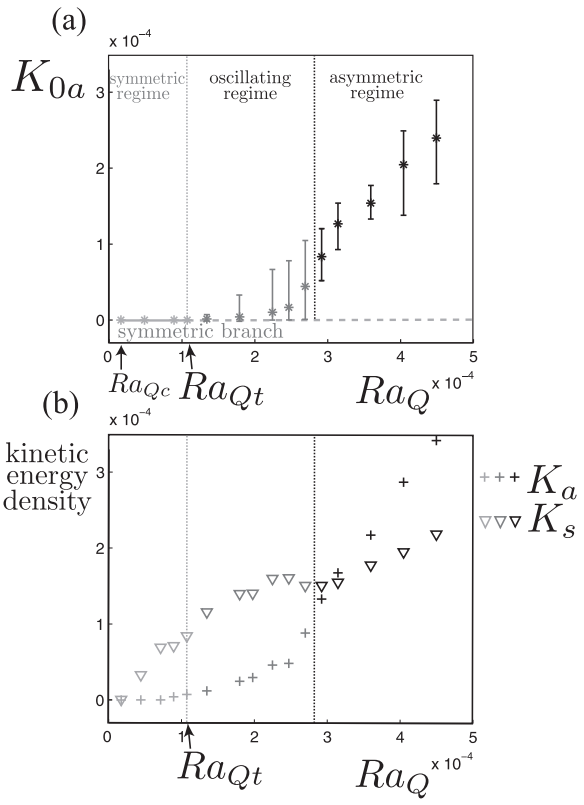

Fig. 11. Bifurcation diagram at $E = 3 \times 10^{-4}$ (when allowing dynamo action) showing K_{0a} (stars), K_a (crosses) and K_s (triangles) versus Ra_Q. Vertical bars in (a) show the range of values taken by the instantaneous values of K_{0a}. Ra_{Qt} corresponds to the emergence of the asymmetric branch introduced in the hydrodynamic study (computed in Section 3.2). Light grey, medium grey and black symbols correspond to symmetric, oscillating and asymmetric simulations respectively (see text). Note that K_{0a} is not exactly equal to zero in the symmetric regime but very small compared to the scale of the figure.

Thus, the closer we get to Ra_{Qt} in the oscillating regime, the smaller the growth-rate value of the EAA flow component becomes and the faster the Lorentz force will be able to restore the symmetric state. As a consequence, for Rayleigh numbers located just above Ra_{Qt}, we observe rather bursts towards the asymmetric regime than oscillations (Fig. 12(a)).

The EAA mode forms one axisymmetric vortex in each hemisphere, one cyclone and one anticyclone. The geometry of the

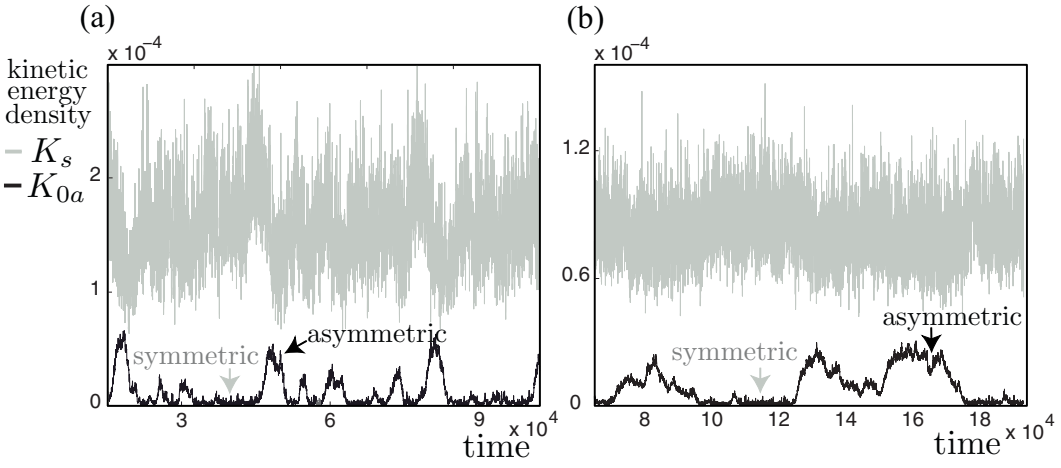

Fig. 12. Instantaneous values for K_{0a} (black curve) and K_s (light grey curve) versus time for oscillating simulations F ((a), Ra_Q close to Ra_{Qt}) and G ((b), Ra_Q further away from Ra_{Qt}) (Table 2).

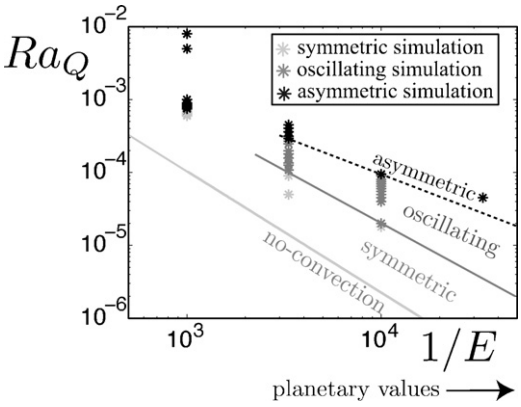

Fig. 13. Phase diagram of the main hydrodynamic regimes when allowing dynamo action. Each symbol corresponds to one numerical simulation. Light grey, medium grey and black symbols correspond to symmetric, oscillating and asymmetric simulations respectively. The light grey curve corresponds to the asymptotic behavior of Ra_{Qc} given by Eq. (13). The medium grey curve corresponds to the best fit (in the sense of the least squares) for Ra_{Qt}. The black dashed line corresponds to a tentative boundary regime between the oscillating and asymmetric regime.

time-averaged EAA mode in Fig. 7 remains unchanged when dynamo action is present.

Similarly to Fig. 9, Fig. 13 summarizes the regime boundaries in a $(1/E, Ra_Q)$ parameter space when dynamo action is allowed. We emphasize here again that the boundary between symmetric and oscillating regimes is set by $Ra_Q = Ra_{Qt}$, where Ra_{Qt} is the forcing at which the transition from the symmetric to the asymmetric regime occurs in the hydrodynamic case. Its location is thus given by Eq. (18).

4.2. Magnetic field structures: effects of the emergence of the EAA mode

Fig. 14 shows the qualitative effects of the transition from the symmetric to the asymmetric hydrodynamic regime on the dynamo-generated magnetic field. Fig. 14(a) shows the results obtained with symmetric simulation *C* (Table 2): the magnetic field is dipole dominated similarly to previously described numerical dynamos. In contrast, in asymmetric simulation *D* (Table 2), the magnetic field is hemispherical with high intensities in one hemisphere and weaker in the other (Fig. 14(b)), not only at the CMB (top) but also at the surface of the planet (bottom). Thus,

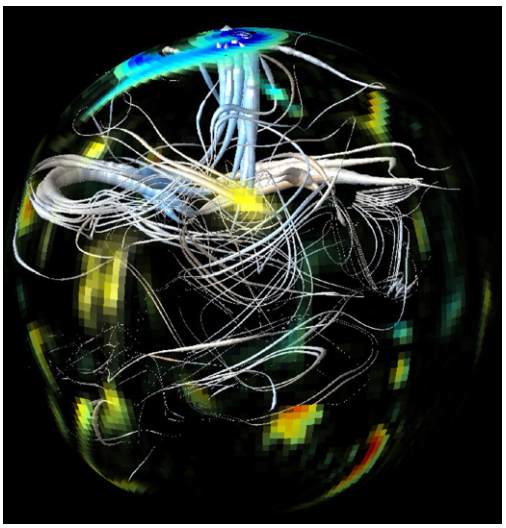

Fig. 15. DMFI visualization of asymmetric simulation *D* (Table 2). The outer boundary of the model is color-coded with the radial magnetic field. In addition, the outer boundary is made selectively transparent, with a transparency level that is inversely proportional to the local radial magnetic field. Field lines are displayed in grey, their thickness is proportional to $\mathbf{B}^2$ (for details see Aubert et al., 2008).

the hydrodynamic asymmetric regime can induce hemispherical dynamos.

The reason why the radial magnetic field becomes hemispherical in the asymmetric hydrodynamic regime can be qualitatively captured looking at the corresponding DMFI visualization (Aubert et al., 2008) (Fig. 15). The surface magnetic flux is collected in the hemisphere where the EAA meridional flow converges. Near the pole, the converging EAA meridional flow is converted into flow downwellings. The ambient radial magnetic field is amplified by stretching within these downwellings, forming magnetic downwellings which are similar to the magnetic upwellings described in Aubert et al. (2008). In the other hemisphere, magnetic flux is dispersed by the divergent EAA flow and is thus much weaker.

In order to quantify this result, we computed the hemisphericity factor f_{hem} (Fig. 16(a)). A dynamo is said to be hemispherical if $f_{\mathrm{hem}} \geq 0.75$ which means that one hemisphere contains at least 75% of the CMB magnetic energy. The ratio K_a/K_s, which measures the equatorial symmetry breaking of the flow, is a control parameter of the hemisphericity factor f_{hem}, as shown by the univariate behavior in Fig. 16(a). In symmetric simulations the flow is domi-

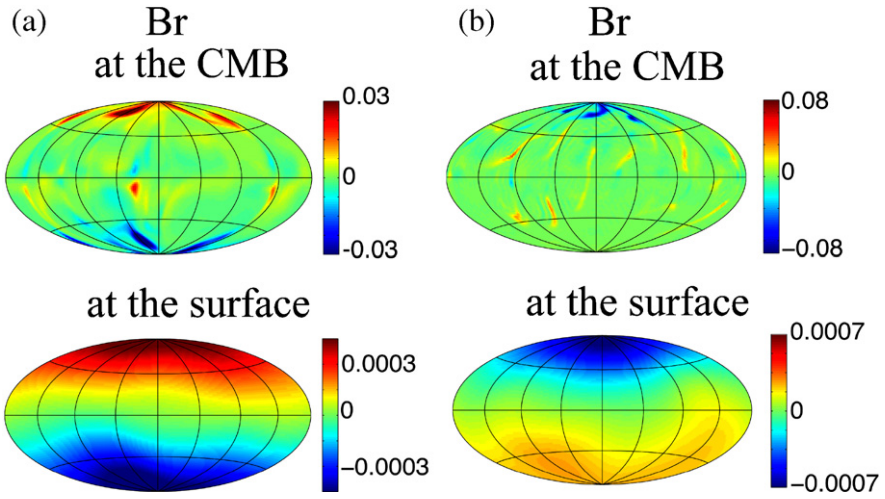

Fig. 14. Snapshots of the radial magnetic field at the CMB (top) and at the surface of a Mars-like planet (bottom) (Hammer projections). (a) Symmetric simulation *C*. (b) Asymmetric simulation *D*.

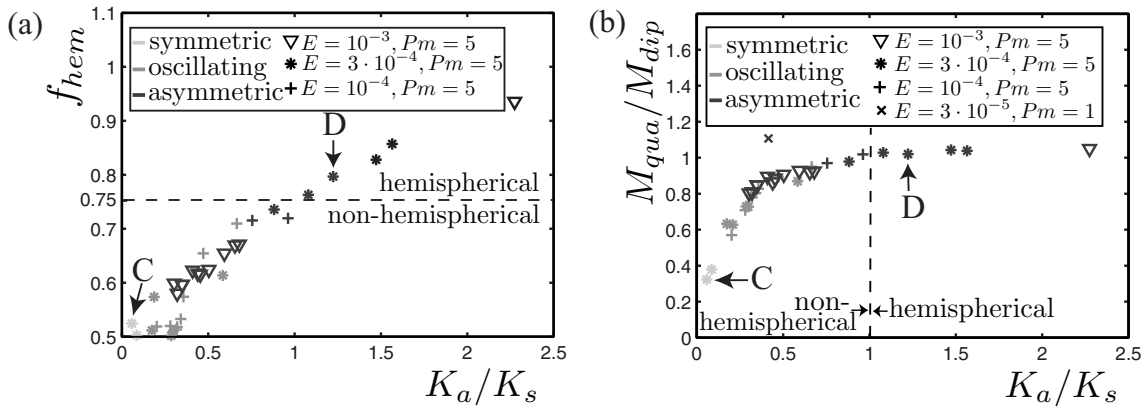

Fig. 16. (a), Hemisphericity factor f_{hem} versus K_a/K_s. (b), Magnetic energy parity ratio $M_{\text{qua}}/M_{\text{dip}}$ versus K_a/K_s. Light grey, medium grey and black symbols correspond to symmetric, oscillating and asymmetric simulations respectively. The dashed black line locates the transition from non-hemispherical to hemispherical dynamos at $f_{\text{hem}} = 0.75$. The symbols *C* and *D* indicate the results obtained with simulations *C* and *D* respectively, which are illustrated in Fig. 14.

nated by equatorially symmetric modes and K_a/K_s has low values. In these symmetric simulations the hemisphericity factor is very close to 0.5 which means that these dynamos are not hemispherical, as illustrated with Fig. 14(a). In asymmetric and oscillating simulations the ratio K_a/K_s increases progressively from low values ($\sim$0.2) to large values ($\sim$2.3) due to the progressive emergence of the EAA mode. Fig. 16(a) shows that the hemisphericity factor f_{hem} increases almost linearly with K_a/K_s and the transition from non-hemispherical to hemispherical dynamos is gradual. The hemisphericity factor reaches 0.75 when $K_a/K_s \approx 1$ (at $Pm = 5$). Several hemispherical dynamos ($f_{\text{hem}} \geq 0.75$) are obtained, including the simulation of Fig. 14(b). The reader may have expected the use of K_{0a}/K_s rather than K_a/K_s in Fig. 16(a) since the equatorial symmetry breaking of the flow is caused by the emergence of the EAA mode in our simulations. However, we find a less univariate behavior if we plot f_{hem} as a function of K_{0a}/K_s rather than K_a/K_s. This result suggests that equatorially antisymmetric, non-axisymmetric modes play a non-negligible role in the transition towards hemispherical dynamos. However, these non-axisymmetric modes remain a consequence of the spontaneous emergence of the EAA mode.

Fig. 16(b) shows that the equatorial symmetry breaking of the flow K_a/K_s, is also a control parameter of the magnetic field parity $M_{\text{qua}}/M_{\text{dip}}$ at fixed *Pm*. Indeed, all the simulations are aligned on the same curve (with the exception of one simulation which has been obtained at a different value of *Pm*). At fixed *Pm*, $M_{\text{qua}}/M_{\text{dip}}$ increases when K_a/K_s increases (due the emergence of the EAA mode in the oscillating and asymmetric regimes). When K_a/K_s reaches $\sim$0.75, $M_{\text{qua}}/M_{\text{dip}}$ saturates and remains close to 1: there is equipartition between magnetic energy contained in modes of dipole parity and magnetic energy contained in modes of quadrupole parity. We underline that several simulations have reached the equipartition of magnetic energy even though they are not hemispherical (for instance, multipole-dominated simulations). Note that we use K_a/K_s rather than K_{0a}/K_s for the same reasons as in Fig. 16(a).

5. Discussion

5.1. Discussion of the numerical results

At onset, convection driven by secular cooling (modeled by internal heating) in rapidly rotating spheres is very similar to what has been obtained for other geometries and boundary conditions: the first unstable modes are equatorially symmetric, non-axisymmetric vortices aligned with the rotation axis. By increasing the modified Rayleigh number above onset we found a flow regime which remains dominated by equatorially symmetric modes. These modes are in agreement with the Taylor–Proudman constraint. The flow is said to be in a symmetric regime and it is very similar to flows already described in previous numerical studies (Olson et al., 1999).

By further increasing the forcing, we found a transition towards a new flow regime, called the asymmetric regime. We have shown that the asymmetric regime is characterized by the emergence of an EAA mode (at $Ra_Q = Ra_{Qt}$), with an amplitude which becomes of the same order of magnitude as those of equatorially symmetric modes. This transition is unexpected. First, because the amplitude of equatorially antisymmetric modes has always been found to be much smaller than the amplitude of equatorially symmetric modes in previous studies (Olson et al., 1999; Christensen and Aubert, 2006; Sakuraba and Roberts, 2009). Second, because bifurcations are often related to symmetry breaking. Even though the emergence of the EAA mode breaks the equatorial symmetry, this mode has gained axisymmetry with respect to the columnar basic state on which it emerges. The occurrence of this transition highlights the need to study secondary instability mechanisms, especially for planetary systems which are far above the onset of primary instability.

The dynamics of the asymmetric regime is strongly influenced by rotation. The EAA mode comprises strong azimuthal thermal winds which induce two large-scale axial vortices: a cyclone in one hemisphere and an anticyclone in the other hemisphere. The related time-averaged meridional circulation is organized in only one cell. The EAA mode is the nonlinear manifestation of the first linearly unstable axisymmetric mode (considering a static basic state) studied by Roberts (1965) and Busshopp and Niiler (1965). We underline that the EAA mode is an alternative way of carrying heat away while complying with the Taylor–Proudman constraint. As shown by Eqs. (14) and (15), the critical modified Rayleigh number for axisymmetric convection is proportional to $E^{5/3}$, as is the critical Rayleigh number for non-axisymmetric convection (Eq. (13)). The Rayleigh number Ra_{Qt} for the nonlinear emergence of the EAA mode scales with the power 1.51 of the Ekman number (Eq. (18)), which is rather close to 5/3.

For the EAA mode to emerge and become a dynamically meaningful mode, two conditions must be met: the buoyancy flux must vanish at the inner boundary and Ra_Q has to exceed Ra_{Qt}. The reason why the asymmetric regime has not been previously observed stems from the fact that one of these two conditions was not met in earlier studies. The size of the inner core appears not to have effect on the transition towards the asymmetric regime. However, in a geophysical context, the presence of an inner core implies a non-zero buoyancy flux at the inner boundary. For that reason, the asymmetric regime is only expected in planetary systems that

Table 5
Plausible parameter values for Mars' core, after Nimmo and Stevenson (2000) and references for the first five parameters. The last parameter value is an estimation of ν in the terrestrial core.

Parameters	Plausible values for Mars
Acceleration due to gravity at the CMB, g_0 ($m\,s^{-2}$)	~3
Core radius, r_o (km)	1300–1700
Density, ρ ($kg\,m^{-3}$)	6600–8300
Thermal expansion coefficient, α (K^{-1})	$\sim 10^{-5}$
Heat capacity, C_p ($J\,kg^{-1}\,K^{-1}$)	820–860
Rotation rate (present), Ω (s^{-1})	7.1×10^{-5}
Kinematic viscosity, ν ($m^2\,s^{-1}$)	$\sim 10^{-6}$

have not nucleated an inner core yet, and where convection is thus powered only by secular cooling (or radiogenic heating).

We have shown that the emergence of the EAA mode in the asymmetric hydrodynamic regime breaks the equatorial symmetry which controls the hemisphericity of the dynamo. Indeed, if the energy contained in the EAA mode is strong enough (i.e. the equatorial symmetry breaking of the flow K_a/K_s is larger than ~1), then we obtain hemispherical dynamos in which at least 75% of the total magnetic energy at the CMB is contained in one hemisphere. The fact that an equatorial symmetry breaking of the flow can lead to hemispherical dynamos is a universal result related to fundamental symmetries in the governing equations, and can be captured using simple kinematic α^2-dynamo models (Gallet and Petrelis, 2009). The equatorial symmetry breaking of the flow, due to the emergence of the EAA mode, leads to an equipartition between magnetic energy contained in modes of dipole parity and magnetic energy contained in modes of quadrupole parity in agreement with the low dimensional model proposed by Gallet and Petrelis (2009).

Hemispherical dynamos have been previously found in numerical simulations of convection and dynamo action in rotating shells (Grote and Busse, 2000; Simitev and Busse, 2005; Stanley et al., 2008). Fixed temperature and stress-free boundary conditions have been imposed in Grote and Busse (2000) and in Simitev and Busse (2005). Their hemispherical dynamos do not result from the same mechanism as ours. Indeed, we found that the antisymmetric kinetic energy remains at low values in their dynamo simulations ($K_a/K_s \approx 0.01$ at $Pr = 1$, $Pm = 2$, $E = 2 \times 10^{-4}$ and $Ra = 6.5 \times 10^5$) and it is exactly equal to zero in the corresponding hydrodynamic simulations. In Stanley et al. (2008), hemispherical dynamos result from the emergence of an EAA mode, as in our simulations, but this mode is forced by thermal boundary conditions in Stanley et al. (2008) while it spontaneously emerges in our study.

5.2. Implications for the past martian dynamo

The EAA mode of convection could be an attractive explanation for the asymmetry of Mars' crustal magnetic field without requiring any post-dynamo mechanism or any heat flux heterogeneity at the CMB. In the following we discuss first, whether the past martian dynamo could have been in an asymmetric hydrodynamic regime and, second, whether the asymmetric regime may generate hemispherical dynamos at Ekman numbers close to planetary values.

The past martian dynamo may have reached the asymmetric regime if Ra_Q was at least larger than Ra_{Qt} when the dynamo was active. One may use the scaling law (18) to estimate Ra_{Qt} in Mars' core: considering plausible parameter values given in Table 5, we find that E is roughly within the range 5×10^{-15} to 8×10^{-15} in Mars' core and Ra_{Qt} within the range 5×10^{-21} to 10^{-20}. The past martian CMB heat flux depends on the mechanism of heat transfer which is considered. Considering a stagnant lid mantle convection the maximum heat flux is expected to be about $60\,mW\,m^{-2}$ (Nimmo and Stevenson, 2000; Breuer and Spohn, 2003; Stevenson et al., 1983) whereas if we consider an overturn after magma ocean crystallization it is about $600\,mW\,m^{-2}$ (Elkins-Tanton et al., 2005). Plate tectonics has been suggested for Mars but is not coherent with little remixing of crust and mantle as indicated by geochemistry. In addition Breuer and Spohn (2003) have shown that it is difficult to reconcile crust production required by geological constraints and the presence of a core-dynamo using a model that includes plate tectonics. We note that, in the case of plate tectonics, the maximum heat flux at the CMB would be of the same order as in the case of a stagnant lid regime (~$100\,mW\,m^{-2}$, Nimmo and Stevenson, 2000). It is important to underline that Ra_Q has to be estimated using the superadiabatic heat flux (the total heat flux minus the adiabatic heat flux). The adiabatic heat flux for Mars' core is estimated to be in the range 5–$19\,mW\,m^{-2}$ (Nimmo and Stevenson, 2000).

Using the parameter values given in Table 5, one can estimate a plausible range of values for the maximum modified Rayleigh number Ra_{Qm}, in Mars' core. Considering convection underneath a single plate, Ra_{Qm} is within the range 2×10^{-13} to 4×10^{-13} whereas with a model that supposes an overturn after magma ocean crystallization (Elkins-Tanton et al., 2005), Ra_{Qm} is within the range 3×10^{-12} to 4.5×10^{-12}. These values are larger than Ra_{Qt}. This suggests that Mars' core could have been in the hydrodynamic asymmetric regime.

In the previous section we saw that the CMB magnetic field is hemispherical in our simulations if the equatorial symmetry breaking of the flow K_a/K_s is larger than 1. The equatorial symmetry breaking which may have been due to the EAA flow component of the asymmetric regime can be roughly estimated for the past martian dynamo. Considering fixed heat flux boundary conditions, Aubert et al. (2009) have obtained a scaling law which gives the non-dimensional mean kinetic energy K, as a function of the dimensionless convective power p. In the particular case of secular cooling $p = 3/5 Ra_Q$ and their scaling law becomes: $K \approx 0.56 Ra_Q^{0.84}$. Since the EAA mode results from a thermal wind mechanism, we expect the kinetic energy density related to the zonal EAA flow to be proportional to Ra_Q at forcings far above Ra_{Qt} (Aurnou et al., 2003; Aubert, 2005). Supposing that the amplitude of the meridional circulation is, at most, of the same order of magnitude as the amplitude of the zonal circulation (as it is in the first linearly unstable axisymmetric mode analytically computed by Roberts (1965) and in our nonlinear numerical simulations) then, $K_{0a} \propto Ra_Q$. Considering this scaling law (roughly satisfied in our numerical simulations) and the plausible values listed above for Ra_{Qm}, we estimate that the ratio K_{0a}/K induced by the asymmetric regime would not have been larger than 0.05 in Mars' core. This result means that the EAA mode was of much weaker amplitude than the equatorially symmetric, non-axisymmetric modes and it suggests that the equatorial symmetry breaking of the flow due to the EAA mode was not large enough to induce a hemispherical dynamo in Mars' core. However such a conclusion may be hasty. First of all, we have noticed that the spontaneous emergence of the EAA mode gives birth to equatorially antisymmetric, non-axisymmetric modes as a consequence of nonlinear interactions between the EAA mode and the symmetric columnar structures. These modes might saturate with a different scaling law from the EAA mode and become of much higher amplitude than the EAA mode at planetary parameters. In such a case, the equatorial symmetry breaking might have reached higher values in Mars' core. Second, the transition between non-hemispherical and hemispherical dynamos occurs at $K_a/K_s \approx 1$ in our simulations when $Pm = 5$. However, there is no reason to suppose that the transition would occur at the same K_a/K_s value if $Pm \neq 5$. Indeed, the simulation at $Pm = 1$ in Fig. 16(b) is the only one located above the general trend, which suggests that Pm may have a considerable impact on the quantitative effects of the equatorial symmetry breaking of the flow on magnetic field. Recalling that Pm is expected to be of the

order of 10^{-6} in Mars' core, the transition towards hemispherical dynamos may occur at much lower K_a/K_s-values in planetary cores. The results obtained in Gallet and Petrelis (2009) suggest that this last point is not completely speculative: they show that even very weak equatorial symmetry breaking of the flow may lead to hemispherical dynamos. Thus, the Pm-dependence of f_{hem} could be studied in order to determine if the asymmetric regime is able to explain the asymmetry of Mars' crustal magnetic field.

A heterogeneous CMB heat flux is plausible for the past martian dynamo (Stanley et al., 2008) and would make the emergence of hemispherical dynamos easier. Indeed, a strong EAA heat flux heterogeneity would directly set the amplitude of the EAA temperature contribution to $\partial T/\partial\theta$ and thus the amplitude of the EAA mode according to Eq. (16) (which is probably what fixes the amplitude of the EAA mode in the simulations of Stanley et al. (2008)). Thus, larger K_a/K_s-values could have been reached in Mars' core due to heterogeneous boundary conditions.

Acknowledgements

We wish to thank D. Jault and F. Pétrélis for discussions. This work was supported by program SEDIT and PNP/SEDI-TPS of French *Institut National des Sciences de l'Univers* (INSU), a division of CNRS. Numerical computations were performed at S-CAPAD, IPGP, France and at HPC resources from GENCI-CINES and GENCI-IDRIS (Grants 2009-042122 and 2010-042122). This is IPGP contribution 3086.

References

Acuna, M., Connerney, J., Ness, N., Lin, R., Mitchell, D., Carlson, C., McFadden, J., Anderson, K., Reme, H., Mazelle, C., Vignes, D., Wasilewski, P., Cloutier, P., APR 30 1999. Global distribution of crustal magnetization discovered by the Mars Global Surveyor MAG/ER experiment. Science 284 (5415), 790–793.

Aubert, J., 2005. Steady zonal flows in spherical shell dynamos. J. Fluid Mech. 542, 53–67.

Aubert, J., Aurnou, J., Wicht, J., 2008. The magnetic structure of convection-driven numerical dynamos. Geophys. J. Int. 172, 945–956.

Aubert, J., Labrosse, S., Poitou, C., DEC 2009. Modelling the palaeo-evolution of the geodynamo. Geophys. J. Int. 179 (3), 1414–1428.

Aurnou, J., Andreadis, S., Zhu, L., Olson, P., 2003. Experiments on convection in Earth's core tangent cylinder. Earth Plan. Sci. Lett. 212, 119–134.

Bisshopp, F., Niiler, P., 1965. Onset of convection in a rapidly rotating fluid sphere. J. Fluid Mech. 23 (Part 3), 459–469.

Breuer, D., Spohn, T., 2003. Early plate tectonics versus single-plate tectonics on Mars: Evidence from magnetic field history and crust evolution. J. Geophys. Res. Planets 108 (July (E7)), 13.

Busse, F.H., 1970. Thermal instabilities in rapidly rotating systems. J. Fluid Mech. 44 (3), 441–460.

Chandrasekhar, S., 1961. Hydrodynamic and Hydromagnetic Stability. Clarendon Press, Oxford.

Christensen, U., Aubert, J., 2006. Scaling properties of convection-driven dynamos in rotating spherical shells and application to planetary magnetic fields. Geophys. J. Int. 117, 97–114.

Christensen, U.R., Aubert, J., Busse, F.H., Cardin, P., Dormy, E., Gibbons, S., Glatzmaier, G.A., Honkura, Y., Jones, C.A., Kono, M., Matsushima, M., Sakuraba, A., Takahashi, F., Tilgner, A., Wicht, J., Zhang, K., 2001. A numerical dynamo benchmark. Phys. Earth Planet. Int. 128, 25–34.

Dormy, E., Soward, A., Jones, C., Jault, D., Cardin, P., 2004. The onset of thermal convection in rotating spherical shells. J. Fluid Mech. 501 (February), 43–70.

Elkins-Tanton, L., Zaranek, S., Parmentier, E., Hess, P., 2005. Early magnetic field and magmatic activity on Mars from magma ocean cumulate overturn. Earth Planet. Sci. Lett. 236 (July (1–2)), 1–12.

Ferraro, V.C.A., 1937. The non-uniform rotation of the sun and its magnetic field. Month. Not. R. Astron. Soc. 97, 458.

Gallet, B., Petrelis, F., SEP 2009. From reversing to hemispherical dynamos. Phys. Rev. E 80 (3, Part 2).

Geiger, G., Busse, F., 1981. On the onset of thermal convection in slowly rotating fluid shells. Geophys. Astrophys. Fluid Dyn. 18 (1–2), 147–156.

Grote, E., Busse, F., 2000. Hemispherical dynamos generated by convection in rotating spherical shells. Phys. Rev. E 62 (September (3, Part B)), 4457–4460.

Gubbins, D., Alfe, D., Masters, G., Price, G., Gillan, M., 2003. Can the Earth's dynamo run on heat alone? Geophys. J. Int. 155 (November (2)), 609–622.

Jones, C., Soward, A., Mussa, A., 2000. The onset of thermal convection in a rapidly rotating sphere. J. Fluid Mech. 405 (February), 157–179.

Lodders, K., Fegley, B., 1997. An oxygen isotope model for the composition of Mars. Icarus 126 (April (2)), 373–394.

Nimmo, F., Stevenson, D., 2000. Influence of early plate tectonics on the thermal evolution and magnetic field of Mars. J. Geophys. Res. Planets 105 (May (E5)), 11969–11979.

Olson, P., Christensen, U., Glatzmaier, G.A., 1999. Numerical modelling of the geodynamo: mechanisms of field generation and equilibration. J. Geophys. Res. 104 (B5), 10383–10404.

Roberts, P.H., 1965. On the thermal instability of a highly rotating fluid sphere. Astrophys. J. 141, 240–250.

Roberts, P.H., 1968. On the thermal instability of a self gravitating fluid sphere containing heat sources. Philos. Trans. R. Soc. London, Ser. A 263, 93–117.

Sakuraba, A., Roberts, P.H., 2009. Generation of a strong magnetic field using uniform heat flux at the surface of the core. Nature Geosci. 2, 802–805.

Sanloup, C., Jambon, A., Gillet, P., 1999. A simple chondritic model of Mars. Phys. Earth Planet. Int. 112 (March (1–2)), 43–54.

Simitev, R., Busse, F., 2005. Prandtl-number dependence of convection-driven dynamos in rotating spherical fluid shells. J. Fluid Mech. 532 (June), 365–388.

Stanley, S., Elkins-Tanton, L., Zuber, M.T., Parmentier, E.M., 2008. Mars' paleomagnetic field as the result of a single-hemisphere dynamo. Science 321 (September (5897)), 1822–1825.

Stevenson, D.J., Spohn, T., Schubert, G., 1983. Magnetism and thermal evolution of the terrestrial planets. ICARUS 54 (3), 466–489.

Stewart, A.J., Schmidt, M.W., van Westrenen, W., Liebske, C., 2007. Mars: A new core-crystallization regime. Science 316 (June (5829)), 1323–1325.

Appendix E

Preprocessing of experimental images

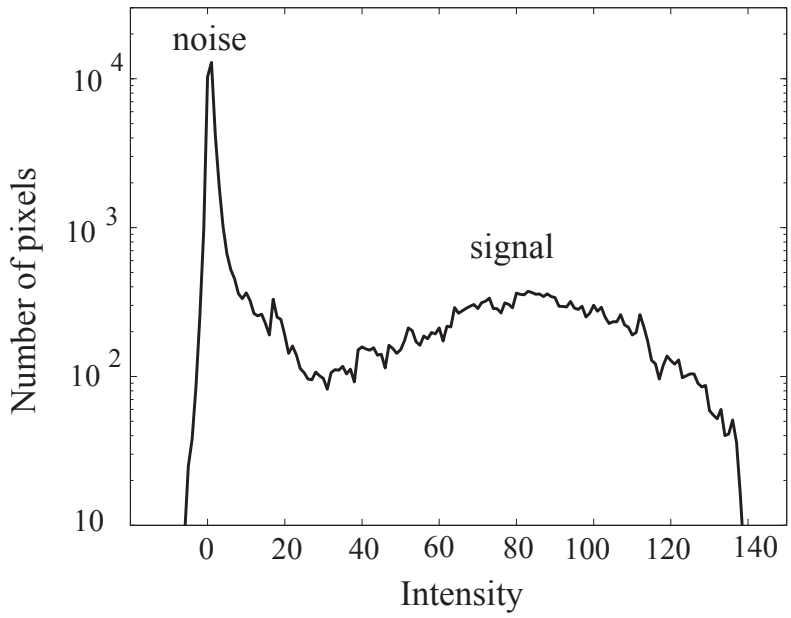

Figure E.1: Number of pixels as a function of intensity after subtraction of the back field image.

Binary images are obtained by subtracting the back field image, taken before the release of dyed fluid, to each video frame. Figure E.1 shows the number of pixels as a function of intensity for a given image after such an operation. The peak near zero intensity corresponds to the noise of the back field and the signal on the right is due to pixels that contain released fluid. Then, we select an appropriate pixel intensity threshold I_c, above which the pixel intensity is set to 1, and 0 otherwise. The threshold is chosen as $I_c = c \cdot I_{noise}$ where c is a constant specified by the operator and I_{noise} the standard deviation to 0 of the back field noise. If X is the set of pixels with negative intensity

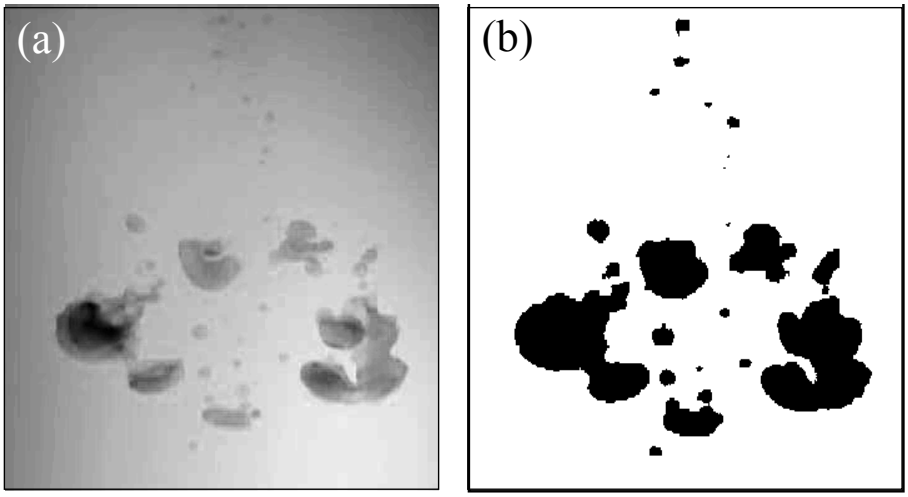

Figure E.2: (a) Initial image. (b) Binary image ($c = 10$).

values after subtraction of the back field, I_{noise} is given by

$$I_{noise} = \sqrt{\frac{1}{N_X} \sum_{(i,j)\in X} I_{i,j}^2} \tag{E.1}$$

where N_X is the number of pixels in X. We use images in which the absorption of light by the released fluid is the largest (i.e. red images for blue-dyed fluid). The value of c is chosen such that the output variables that are eventually obtained from binary images (z, u, r, L_B, α' defined in §8, §8, §8, §9.3, §9.4, respectively) do not vary significantly with c. Sensitivity of output variables to c are included in measurement uncertainties. Coefficient c is held constant for a particular group of experiments (same lighting conditions and same fluids). Figure E.2 gives an example of binary image obtained with such a method.

Appendix F

Turbulent entrainment model: closed-form solutions

In the Boussinesq limit $P \to 0$, the solution (9.20) to equation (9.19) takes the following closed-form expression:

$$\tilde{u}^2 = \frac{\tilde{r}_0^{3\gamma}}{\tilde{r}^{3\gamma}} \left\{ \tilde{u}_0^2 - \frac{1}{2\alpha'} \left[\frac{3C_D'}{16\alpha'} + (1+k)c_1 \right]^{-1} \left[\frac{1}{\tilde{r}_0^2} - \frac{\tilde{r}^{3\gamma-2}}{\tilde{r}_0^{3\gamma}} \right] \right\} \tag{F.1}$$

where $\tilde{r} = \tilde{r_0} + \alpha'(\tilde{z} - \tilde{z}_0)$.

A closed-form solution also exists for $C_D' = 0$ and is given by

$$\tilde{u}^2 = \left[\frac{P + (1+k)c_1\tilde{r}_0^3}{P + (1+k)c_1\tilde{r}^3} \right]^2 \left[\tilde{u}_0^2 + \frac{2P(\tilde{r} - \tilde{r}_0)}{\alpha'(P + (1+k)c_1\tilde{r}_0^3)^2} + \frac{c_1(1+k)(\tilde{r}^4 - \tilde{r}_0^4)}{2\alpha'(P + (1+k)c_1\tilde{r}_0^3)^2} \right] \tag{F.2}$$

where $\tilde{r} = \tilde{r_0} + \alpha'(\tilde{z} - \tilde{z}_0)$. The first term within the second brackets in equation (F.2) is due to the initial momentum of the vortex ring, the second term to departures from the Boussinesq approximation and the third term is related to buoyancy forces.

Appendix G

Article submitted to Earth and Planetary Science Letters

The following article Deguen *et al.* (2013) has been submitted to Earth and planetary Science Letters.

Turbulent metal-silicate mixing, fragmentation, and equilibration in magma oceans

Renaud Deguen[a,*], Maylis Landeau[b], Peter Olson[a]

[a]*Department of Earth and Planetary Sciences, Johns Hopkins University, Baltimore, MD 21218, USA*
[b]*Dynamique des Fluides Géologiques, Institut de Physique du Globe de Paris, Université Paris-Diderot, INSU/CNRS, 1 rue Jussieu, 75238, Paris cedex 05, France.*

Abstract

Much of the Earth was built by high-energy impacts of planetesimals and embryos, many of these impactors already differentiated, with metallic cores of their own. Geochemical data provide critical information on the timing of accretion and the prevailing physical conditions, but their interpretation depends critically on the degree of metal-silicate chemical equilibration during core-mantle differentiation, which is poorly constrained. Efficient equilibration requires that the large volumes of iron derived from impactor cores mix with molten silicates down to scales small enough to allow fast metal-silicate mass transfer. Here we use fluid dynamics experiments to show that large metal blobs falling in a magma ocean mix with the molten silicate through turbulent entrainment, with fragmentation into droplets eventually resulting from the entrainment process. In our experiments, fragmentation of the dense fluid occurs after falling a distance equal to 3-4 times its initial diameter, at which point a sizable volume of ambient fluid has already been entrained and mixed with the dense falling fluid. Contrary to what has usually been assumed, we demonstrate that fragmentation of the metallic phase into droplets may not be required for efficient equilibration: turbulent mixing, by drastically increasing the metal-silicate interfacial area, may result in fast equilibration even before fragmentation.

Keywords:
core formation, magma ocean, fragmentation, turbulent mixing, chemical equilibration

1. Introduction

The formation of Earth's core produced chemical and isotopic fractionations which have been used to constrain the timing of differentiation (Yin et al., 2002; Kleine et al., 2002) and the physical conditions (Wood et al., 2006; Corgne et al., 2008) that prevailed early in Earth's history. Hafnium-Tungsten (Hf-W) systematics in particular provide constraints on the timing of accretion, but their interpretation depends critically on the degree to which the metal portion of the impactors equilibrates isotopically with Earth's mantle silicates (Halliday, 2004; Kleine et al., 2004; Nimmo et al., 2010; Rudge et al., 2010). Assuming full equilibration after each impact, Hf-W chronometry implies an exponential accretion timescale of about 10 My (Yin et al., 2002; Rudge et al., 2010), whereas relaxing this assumption can increase this timescale by several tens of My, or even render it indeterminate (Rudge et al., 2010).

Partial equilibration is usually modeled by assuming that a fraction k of the metal phase re-equilibrates with the whole mantle, the remaining metal fraction $1-k$ reaching the Earth's core without chemical interaction with the mantle (Halliday, 2004; Kleine et al., 2004; Nimmo et al., 2010; Rudge et al., 2010). However, the compositional transfer between metal and silicate also depends on the quantity of silicates the metal phase equilibrates with. For example, the amount of radiogenic Tungsten extracted from the silicates by the metal will be insignificant if the volume of interacting silicate is small. We thus define a more general measure of equilibration, the equilibration efficiency $\mathscr{E}_i$, as the total mass of element i exchanged between metal and silicates normalized by its maximum possible value, had all the metal re-equilibrated with an infinitely larger silicate reservoir. If a fraction k of the metal phase equilibrates with a mass of silicates equal to Δ times the mass of equilibrated metal, the equilibration efficiency of an element i with a metal/silicate partition coefficient D_i is, from mass balances,

$$\mathscr{E}_i = \frac{k}{1 + D_i/\Delta} \tag{1}$$

(see Appendix A), with the metal dilution Δ defined as

$$\Delta = \frac{\text{mass of equilibrated silicates}}{\text{mass of equilibrated metal}}. \tag{2}$$

$\mathscr{E}_i$ approaches k when $\Delta \gg D_i$, which is the usual assumption of disequilibrium core formation models. Importantly, $\mathscr{E}_i$ is element-dependent, with efficient equilibration of an element i requiring a metal dilution Δ similar or larger than its distribution coefficient. Tungsten, for example, has $D_W \simeq 30$, so that equilibration is efficient only if the metal mixes and equilibrates with more than about 30 times its mass of silicates.

Previous disequilibrium geochemical models assuming infinite dilution can be corrected for the effect of finite metal dilution by substituting $\mathscr{E}_i$ in place of k (Appendix A), which

*Corresponding author
Email address: renaud.deguen@imft.fr (Renaud Deguen)

means that previously determined constraints on k would actually apply to $\mathscr{E}_i$. In particular, Hf-W systematics imply that the Tungsten equilibration efficiency $\mathscr{E}_W$ must have been larger than about 0.36 on average during Earth's accretion (Rudge et al., 2010), which requires that on average $k \geq 0.36$ and $\Delta \geq 17$. The Hf-W accretion timescale becomes unbounded when $\mathscr{E}_i$ approaches 0.36 (Rudge et al., 2010), so that additional constraints on metal-silicate equilibration are needed to properly interpret the data.

During accretion, dissipation of the gravitational and kinetic energies associated with large impacts inevitably results in widespread melting (Melosh, 1990; Tonks and Melosh, 1993; Pierazzo et al., 1997), implying that part of the separation of the core-forming metal phase from the silicates occurred in low-viscosity magma oceans. Under these conditions, efficient chemical equilibration would be expected if the Earth had formed through the accretion of undifferentiated bodies with the metal phase already finely dispersed within a silicate matrix. However, it is now recognized that much of the Earth was accreted from already differentiated bodies with sizes ranging from a few tens of kilometers in diameter to objects the size of Mars (Yoshino et al., 2003; Baker et al., 2005; Bottke et al., 2006; Ricard et al., 2009). It is usually assumed that efficient chemical equilibration between the cores of these impactors and the proto-Earth's mantle requires fragmentation of the metal down to scales of 1 cm to 1 m where efficient metal-silicate chemical equilibration can occur (Stevenson, 1990; Karato and Murthy, 1997; Rubie et al., 2003; Ulvrová et al., 2011), implying a scale reduction by a factor of $10^4 - 10^8$. Smooth Particle Hydrodynamics (SPH) simulations of the Moon-forming impact suggest some degree of disruption of the impactor core into 100-1000 km sized iron blobs (Canup, 2004), but the current resolution of these models is too coarse to give any information about smaller scale mixing and fragmentation. Hence the fate of these large iron blobs, while critical for the interpretation of geochemical data, remains uncertain.

2. Non-dimensional parameters

We consider the evolution of an iron blob, which can be either the core of an impactor or a fragment of an impactor core, falling in a magma ocean. Its dynamics are characterized by the following set of non-dimensional numbers :

$$Re = \frac{\rho_m\, w\, d}{\eta_m}, \qquad We = \frac{\rho_m\, w^2 d}{\sigma}, \qquad Bo = \frac{\Delta\rho\, g\, d^2}{\sigma},$$
$$M = \frac{w}{c}, \qquad \mathsf{P} = \frac{\rho_m}{\rho_s}, \qquad \mathsf{H} = \frac{\eta_m}{\eta_s},$$

where w and d are the velocity and diameter of the falling metal volume, ρ is density, η is the dynamic viscosity, g the acceleration of gravity, σ the iron-silicate interfacial tension, and c the sound wave velocity in the dominant phase. Subscripts "m" and "s" refer to metal and silicate, respectively, and $\Delta\rho = \rho_m - \rho_s$. The Reynolds number Re compares the magnitude of inertia to viscous forces, the Weber and Bond numbers, We and Bo, are measures of the relative importances of inertia and buoyancy to interfacial tension at the lengthscale d, and the Mach number M compares the velocity of the flow to the sound wave velocity.

Typical values for these parameters for a metal blob 100 km in diameter falling in a magma ocean with an initial velocity of 1 km.s^{-1} are $Re \sim 10^{14}$, $Bo \sim 10^{14}$, $We \sim 10^{14}$, with $\mathsf{P} \simeq 2$ and $\mathsf{H} \sim 0.1-1$. Note that Re, We, Bo and M are all time-dependent.

The huge value of Re implies that the flow must have been extremely turbulent. The Weber and Bond numbers are large as well, which implies that interfacial tension effects were unimportant except at the smallest scales of the flow (Dahl and Stevenson, 2010; Deguen et al., 2011). M is typically larger than 1 (supersonic flow) just after the impact and decreases with time as the metal decelerates.

3. Turbulent entrainment

Given the extreme values of We and Bo, it is appropriate to first consider the limiting case of miscible fluids, for which We and Bo are formally infinite. Numerous experimental and theoretical studies have shown that the evolution of a turbulent buoyant fluid falling or rising under the action of gravity - what is called a *turbulent thermal* in fluid mechanics - is governed by turbulent entrainment of ambient fluid (Batchelor, 1954; Morton et al., 1956; Turner, 1986). As an illustration, Fig. 1a shows snapshots from an experiment in which a volume of a dense solution is released into a larger volume of pure water. A small amount of fluorescent dye has been added to the solution. The volume of dyed fluid is seen to increase as it falls, which indicates that the negatively buoyant fluid entrains and incorporates ambient fluid, resulting in its gradual dilution (Batchelor, 1954; Morton et al., 1956).

This effect is quantified using the *entrainment hypothesis* of Morton et al. (1956), which states that the rate of entrainment of ambient fluid is proportional to the mean velocity of the buoyant turbulent fluid, and predicts that the radius $r = d/2$ of the buoyant fluid evolves as

$$r = r_0 + \alpha\, z, \tag{3}$$

where α is the entrainment coefficient and $r_0 = d_0/2$ the initial radius of the dense blob. The velocity of the mixture can be calculated from the equations of conservation of momentum and mass (Appendix B), a general expression being given in Eq. (B.12). The velocity law (B.12) has a useful large-z asymptote given by

$$w = \left(\frac{r_0^3 g}{2\,\alpha^3}\frac{\Delta\rho}{\rho_s}\right)^{1/2}\left(1 + K + \frac{3}{16}\frac{C_d}{\alpha}\right)^{-1/2}\frac{1}{z}, \tag{4}$$

where C_d is the drag coefficient, and K the coefficient of added mass, which accounts for the momentum imparted to the surrounding fluid. These laws have been verified in a wide variety of physical settings, from laboratory experiments using thermally or compositionally buoyant fluids to large scale geophysical flows including explosive volcanic plumes (Terada and Ida, 2007; Yamamoto et al., 2008), underwater gas plumes (Bettelini and Fanneløp, 1993), and atmospheric convective bursts

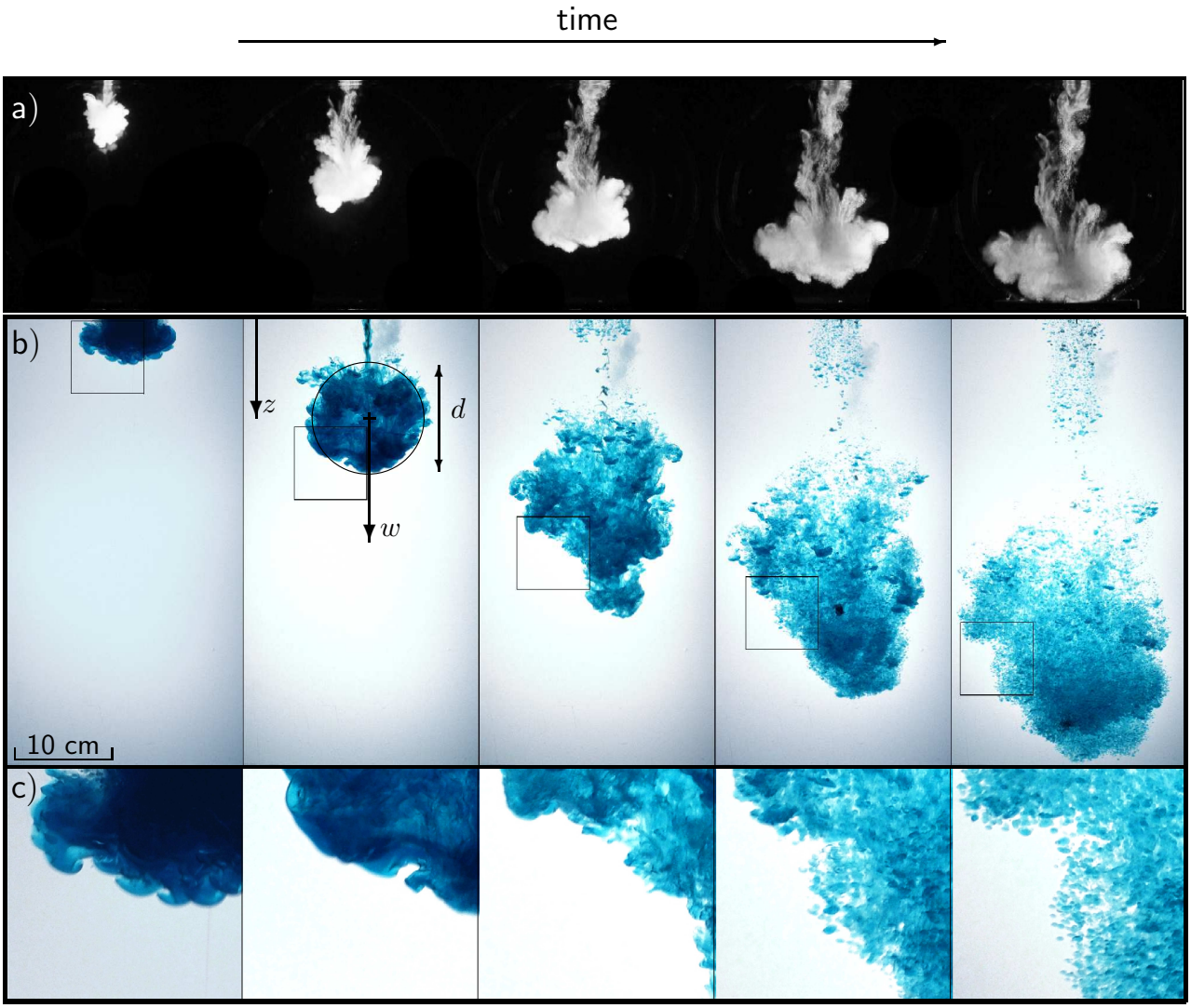

Figure 1: Analog fluid dynamics experiments on metal-silicate mixing and fragmentation. **a)** Growth of a negatively buoyant thermal by turbulent entrainment at $Re = 2 \times 10^3$. Here the buoyancy of the falling fluid is due to very fine dense particles in suspension (modified from Deguen et al. (2011)). A small amount of fluorescent dye (fluoresceine) is added to the particle-laden fluid, which appears white in the pictures. **b)** Fragmentation of a volume of aqueous solution of NaI salt (dyed in blue) released in silicone oil, at $We = 3 \times 10^3$, $Re = 2 \times 10^4$, P = 1.9, H = 2.1. Fragmentation of the aqueous volume into droplets occurs between the third and fourth snapshots. **c**) Close-ups corresponding to the squares in **b)**. Small scale Rayleigh-Taylor instabilities are apparent in the first close-up.

(known as *thermals* - hence the name - by sailplane pilots (Woodward, 1959)).

Turbulent entrainment results from a combination of *engulfment* of ambient fluid by large scale, inviscid eddies, which draws large volumes of surrounding fluid into the turbulent region, and *nibbling*, which denotes small scale viscous processes (vorticity diffusion) (Turner, 1986; Mathew and Basu, 2002; Westerweel et al., 2009). The rate at which the ambient fluid is entrained is thought to be controlled by large scale process (Brown and Roshko, 1974; Turner, 1986), while nibbling is responsible for eventually imparting vorticity to the entrained fluid. The entrainment coefficient appears to be independent of *Re* (Turner, 1969), which is consistent with the rate of turbulent entrainment being controlled by the largest inviscid eddies rather by the small scale viscous effects. In two-fluids systems we would expect that these large-scale eddies remain unaffected by interfacial tension if the Weber number is large enough, in which case turbulent entrainment should still occur, at a rate similar to the case of miscible fluids. We therefore argue here that the concept of turbulent entrainment is also applicable to immiscible fluids like molten metal and silicate, provided *Re* and *We* are large. This is demonstrated below in a series of experiments with two immiscible fluids.

4. Experimental set-up

Molten silicate is modeled by a low viscosity silicone oil (density $\rho_s = 820$ kg.m^{-3}, viscosity $\eta_s = 1$ mPa s) enclosed in a 25.5 cm $\times$ 25.5 cm $\times$ 47 cm container. A volume of NaI aqueous solution (density $\rho_m = 1580$ kg.m^{-3}, viscosity $\eta_m = 2$

mPa s), representing a metal blob falling into a magma ocean, is held in a vertically oriented tube whose lower extremity is sealed using a thin latex diaphragm, which is ruptured at the beginning of the experiment. A surfactant (Triton X-100) is added to the NaI solution, lowering the interfacial tension of the silicone oil/NaI solution system to about 5 mJ m^{-2}. A small amount of $Na_2S_2O_3$ is added to the NaI solution to avoid a yellowish coloration of the solution. In experiments where induced fluorescence is used to image cross-sections (Fig. 3), we use a concentration of the NaI solution for which the refractive index of the NaI solution matches that of the silicone oil, which is necessary to avoid optical distortions. At this concentration, its density is $\rho_m = 1260$ kg.m^{-3}. The exact values of the densities, viscosities and interfacial tension are measured before each series of experiments. The experiments are recorded with a color video camera at 24 frames per second. Using a pixel intensity threshold method, we estimate on each video frame the location of the center of mass z of the oil/NaI solution mixture and the apparent area A of the mixture, from which its equivalent radius is estimated as $r = \sqrt{A/\pi}$.

The dense fluid is released from rest and its vertical velocity is set by the conversion of its gravitational potential energy into kinetic energy, which implies that the vertical velocity initially scales as $w \sim \sqrt{(\Delta\rho/\rho_m) g\, r}$. Using this scaling for w implies that $We \sim Bo$, using the equivalent diameter of the NaI solution volume as the length scale. The Weber and Reynolds numbers that characterize the experiments are defined using as a velocity scale the vertical velocity of the dense fluid after it has travelled a distance equal to its initial diameter. With this definition, we found that $We \simeq 0.43\, Bo$ in our experiments. Our choice of experimental fluids plus the use of a surfactant to reduce the interfacial tension allows us to reach values of Re larger than 10^4 and We up to 3×10^3, making our experiments far more dynamically similar to planetary accretion than current numerical simulations (Ichikawa et al., 2010; Samuel, 2012).

5. Experimental validation of the turbulent entrainment model

Snapshots from an experiment with $Bo = 6.9 \times 10^3$, $We = 3 \times 10^3$, $Re = 2 \times 10^4$, $\mathsf{P} = 1.9$, and $\mathsf{H} = 2.1$ are shown in Fig. 1b and c. After release, the dense fluid (dyed in blue) undergoes small scale Rayleigh-Taylor instabilities (apparent on the first snapshot) which, together with shear induced by the global motion of the fluid, generate turbulence. The volume of the falling fluid increases with time much like the miscible fluids case shown in Fig. 1a, indicating that entrainment is occurring in spite of immiscibility.

Fig. 2 shows that the equivalent radius of the NaI solution-silicone oil mixture increases linearly with the distance travelled, in agreement with the turbulent entrainment model predictions (Eq. (3)). The entrainment coefficient α is in the range 0.2-0.3 in our experiments, similar to turbulent thermals in miscible fluids (Morton et al., 1956; Turner, 1969), which suggests that we have indeed reached a regime for which the large scales of the flow are unaffected by interfacial tension effects.

The predicted descent trajectory also compares favorably with the experimental results. Once integrated in time, the asymptotic velocity law Eq. (4) yields

$$\left(\frac{z}{r_0}\right)^2 = \left(\frac{2\,\Delta\rho\, g}{\alpha^3 \rho_s\, r_0}\right)^{1/2} \left(1 + K + \frac{3}{16}\frac{C_d}{\alpha}\right)^{-1/2} t. \qquad (5)$$

Fig. 2b shows that after a short acceleration phase the experiments agree well with the prediction of Eq. (5) that $z^2 \propto t$, although there is some variability in the magnitude of the slope. The full evolution of our experiments can be explained by the model described in Appendix B. Although the drag and virtual mass coefficients are uncertain, the model (black curves in Fig. 2) fits very well the experimental measurements for reasonable values of these coefficients, with the observed variability in our experiments attributable to imperfect control of initial conditions plus natural variability inherent in turbulent flows.

The agreement between our experiments and the entrainment prediction strongly supports our contention that the turbulent entrainment concept can be applied to immiscible fluids when We and Re are large, and offers a simple way [Eq. (3), (4), and Appendix B] to model the evolution of large metal masses in a magma ocean. In particular, the linear increase of the buoyant mixture radius provides a measure of metal-silicate mixing, with the metal dilution [Eq. (2)] given by

$$\Delta = \frac{\rho_s}{\rho_m}\left[\left(1 + \alpha\frac{z}{r_0}\right)^3 - 1\right]. \qquad (6)$$

We have so far ignored the effects of compressibility on the entrainment process, which are negligible in our experiments but may be significant if the post-impact flow is supersonic or nearly supersonic. The fact that the flow velocity is similar to the sound velocity has an important qualitative consequence for the structure of the flow: the finite speed of sound introduces a time delay in the transmission of pressure signals from one point to another, which makes it impossible for large turbulent eddies to remain coherent when the local Mach number (based on the eddy velocity scale) is of order one (Breidenthal, 1992; Freund et al., 2000; Pantano and Sarkar, 2002). Because the rate of entrainment is thought to be controlled by the process of engulfment of ambient fluid by large scale eddies (Brown and Roshko, 1974; Turner, 1986; Mathew and Basu, 2002), mixing is expected to decrease when $M \to 1$. Experiments on compressible turbulent jets and mixing layers show that the entrainment rate indeed decreases significantly with increasing M, before saturating at a value about five times smaller than for incompressible flows (Brown and Roshko, 1974; Freund et al., 2000) when $M \gtrsim 1$.

6. Fragmentation

Fig. 1b-c reveals that the dense NaI solution entrains and incorporates silicone oil *before* it fragments into droplets. Fragmentation occurs relatively late in the descent process (between the third and fourth pictures in the experiment shown in Fig. 1b-c), at a time when a sizable volume of ambient fluid has already

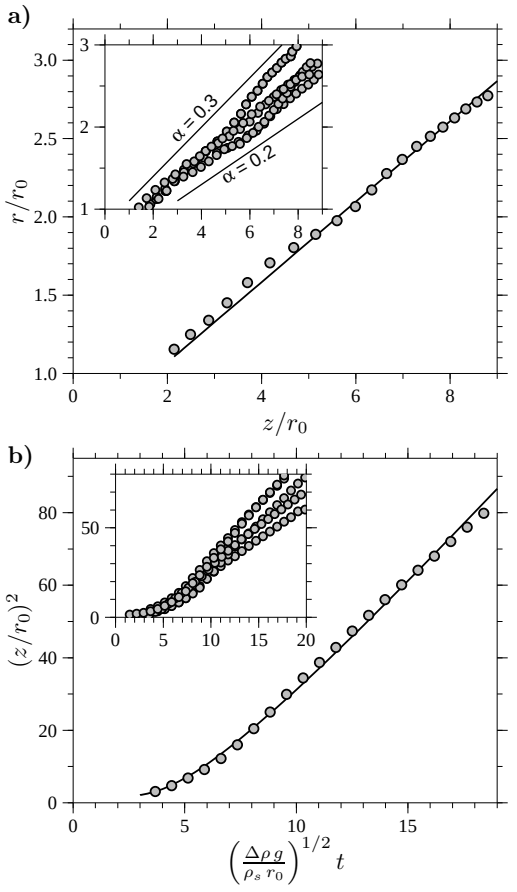

Figure 2: Time evolution of the mean radius and position of the falling fluid, in experiments where a volume of NaI solution is released into silicone oil (P = 1.9). **a)** Mean radius r (normalized by r_0) of the aqueous solution/oil mixture as a function of the position z (normalized by r_0) of its center of mass. **b)** Square of the normalized position z of the center of mass of the aqueous solution/oil mixture as a function of time (normalized by $(\Delta\rho\, g/\rho_s\, r_0)^{-1/2}$). The results of one experiment are compared with the predictions of our model based on the entrainment assumption shown with black lines in **a)** and **b)**. For this experiment, the model [Eqs. (B.8), (B.9) and (B.10)] best fits the data with $\alpha = 0.26$, a drag coefficient $C_d = 0.53$, and a virtual mass coefficient $K = 0.5$ (see Appendix B for details on the model). The experimental results shown in the inserts illustrate the natural variability seen in our experiments, with α varying between 0.2 and 0.3.

been entrained. Droplets appear in a single global fragmentation event, which is at variance with previously suggested "cascade" processes, in which a succession of fragmentation events lead to the final stable drop size (Rubie et al., 2003; Samuel, 2012), and "erosion" processes, in which metal-silicate mixing occurs predominantly on the boundary with the ambient fluid (Dahl and Stevenson, 2010).

Adding a small amount of fluorescent dye to the NaI solution and illuminating the experiment with a thin light sheet reveals cross-sections of the NaI solution/silicone oil mixture, one example being shown in Fig. 3. Small scale mixing of the phases is evident in this picture, demonstrating that oil has been entrained into the NaI solution and that the two phases are already intimately mixed *before* fragmentation occurs. This striking observation suggests that fragmentation is a consequence

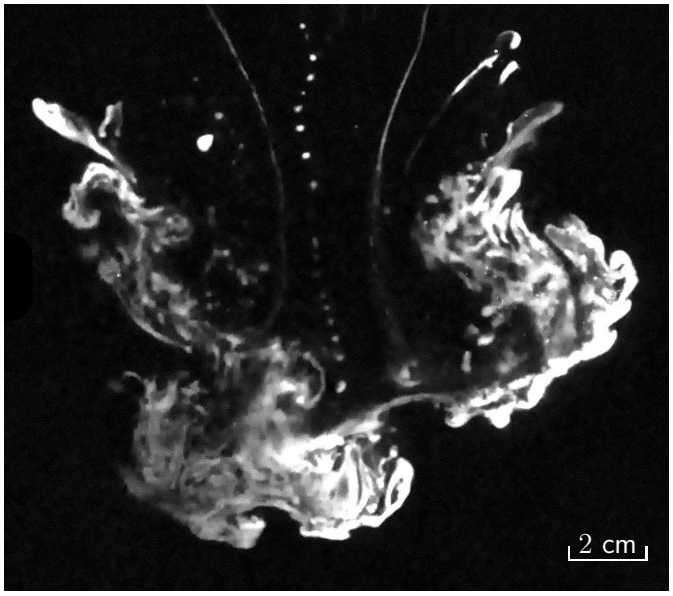

Figure 3: Cross-section of the NaI solution/silicone oil mixture at a distance $\sim 2\,d_0$ from the origin. The experiment is illuminated with a thin light sheet exciting a fluorescent dye (Rhodamine B) added to the NaI solution, which appears white in the picture. In this experiment $Bo = 4.6 \times 10^3$, $We = 2 \times 10^3$, P = 1.54, H = 2.1, and $Re = 2 \times 10^4$.

of mixing associated with turbulent entrainment of the ambient fluid, with fragmentation into drops ultimately resulting from small scale instabilities, plausibly capillary instabilities developed on filaments stretched by the turbulent flow (Villermaux et al., 2004; Shinjo and Umemura, 2010).

In all our experiments in this turbulent regime, fragmentation into drops is observed to occur after the dense liquid falls a distance equal to 3 to 4 times its initial diameter, with no clear trend observed in the explored range of parameters. At this point the volume fraction of the dense fluid in the mixture is of order 5-10 %. It is possible that the fragmentation distance becomes independent of *Re* and *We* when these two numbers are large, but the maximum value of *We* obtained in our experiments (3000) is only 6 times larger than its observed critical value for this turbulent regime ($\sim$ 500), making the explored range of *We* too small to test this possibility.

7. Chemical equilibration before fragmentation - a fractal model

Fragmentation of the metal phase into drops is an important facet of the problem of metal-silicate interactions, because drop formation is an efficient way of increasing the interfacial area between metal and silicate, thus enhancing chemical transfer and equilibration. However, it may not be necessary for chemical equilibration. The small scale mixing observed in our experiments (Fig. 3) results in a highly convoluted interface, which should drastically decrease the timescale of equilibration with the entrained silicate.

To illustrate this point, we consider a model of metal-silicate equilibration prior to drop formation based on the observation

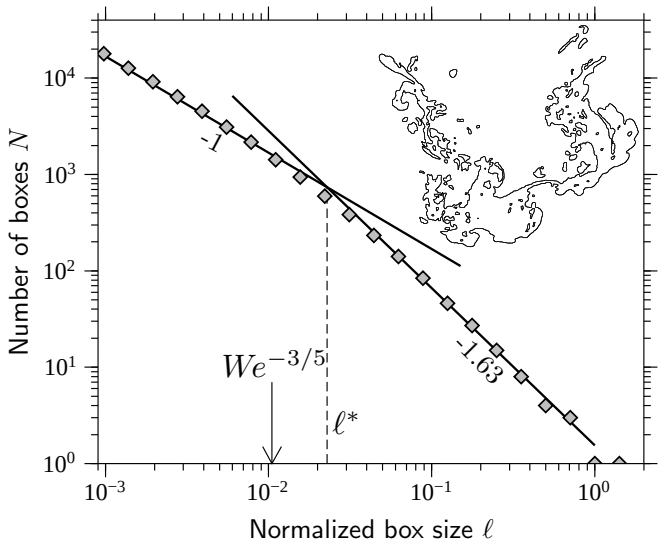

Figure 4: The fractal dimension of the oil/aqueous solution interface shown in Fig. 3, determined using a box counting algorithm. Shown here is the number $N(\ell)$ of square boxes of size ℓ required to cover the oil/aqueous solution interface as a function of the box size ℓ, here normalized by the size of the smallest box fully enclosing the interface. The slope of the resulting curve is $1 - D$, where D is the fractal dimension of the 3D interface. A slope of -1 is expected for a non-fractal surface, as found here for small ℓ. The interface is fractal at scales above $\ell^* \simeq 2.3\times10^{-2}$, which is of the same order of magnitude as $We^{-3/5} \simeq 1.05 \times 10^{-2}$. Fitting the data for $\ell > \ell^*$ (thick black line) gives a slope of -1.63 ± 0.03 ($\pm 1\,\sigma$), which implies a fractal dimension of 2.63 ± 0.03, slightly smaller than $D = 8/3 = 2.67$.

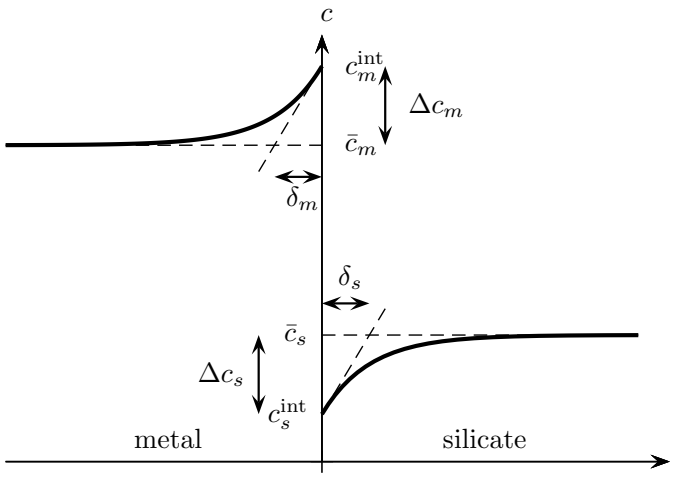

Figure 5: A sketch of the composition profiles in the vicinity of the metal-silicate interface. The situation depicted here is that of a siderophile element in excess in the silicate phase.

that the interface separating the two fluids has a fractal nature once turbulence is well-developed. Theory (Mandelbrot, 1975; Constantin et al., 1991; Constantin and Procaccia, 1994) and experiments (Sreenivasan et al., 1989; Constantin et al., 1991) show that isosurfaces of transported quantities (composition, temperature) in well-developed turbulent flows are fractal – a consequence of the self-similarity of the turbulent flow – with a fractal dimension predicted to be $D = 8/3$ for homogeneous turbulence with Kolmogorov scaling.

It is to be expected that the interface between immiscible fluids in a turbulent flow shares this property over the range of scales in which interfacial tension is unimportant. Experimental support for this assumption is given in Fig. 4, where the interface between the oil and aqueous solution is shown to have a fractal nature with a fractal dimension at scales larger than a cut-off length ℓ^*. For miscible fluids, Sreenivasan et al. (1989) assumed that the inner cut-off length is the Kolmogorov scale for isovorticity surfaces, and the Batchelor scale for isocompositional surfaces for high Schmidt number fluids. For a surface separating two immiscible fluids, we expect that the inner cut-off length will be the largest of the Kolmogorov scale $\ell_K = d\,Re^{-3/4}$ and the scale $\ell_\sigma = d\,We^{-3/5}$ at which interfacial tension balances local dynamic pressure fluctuations estimated assuming a Kolmogorov cascade [(Kolmogorov, 1949; Hinze, 1955), and see section 8 for more details]. Typically $\ell_\sigma \gg \ell_K$, and we expect that $\ell^* \sim \ell_\sigma$. In our experiments, ℓ^* and ℓ_σ are numerically close (within a factor of 2, Fig. 4) and the measured fractal dimension is only slightly smaller than the theoretical value of $8/3$. Note that the observed fractal nature of the interface is indicative of self-similarity in the flow, and that the measured fractal dimension is consistent with Kolmogorov type turbulence and a $k^{-5/3}$ kinetic energy spectrum.

Assuming that the metal-silicate interface has a fractal nature offers a convenient way of estimating its area A_T, which according to fractal geometry is $A_T = A_0(\ell^*/d)^{2-D}$, where $A_0 = \pi d^2$ is the area measured at the scale d. Using $\ell^* \sim \ell_\sigma$, the predicted surface area is $A_T \sim A_0 We^{\frac{3}{5}(D-2)}$. With $D = 8/3$ and $We = 10^{14}$, this implies an increase in interfacial area by five orders of magnitude. A timescale for chemical equilibration, $\tau_{\rm eq}$, can then be found by coupling the estimate for A_T with a local scaling for turbulent mass flux at the metal-silicate interface.

We denote by κ_c the diffusivity of the chemical element of interest. The Schmidt number $Sc = \nu/\kappa_c$, where ν is the kinematic viscosity, is assumed to be large in both phases. Fig. 5 shows a sketch of the composition profiles in the vicinity of the metal-silicate interface, with definitions of the main variables. Thermodynamic equilibrium is assumed at the metal/silicate interface, so that the concentrations by mass $c_m^{\rm int}$ and $c_s^{\rm int}$ at the interface are linked by the partition coefficient $D_i = c_m^{\rm int}/c_s^{\rm int}$, but the bulk compositions $\bar{c}_m$ and $\bar{c}_s$ are out of thermodynamic equilibrium, *i.e.* $\bar{c}_m/\bar{c}_s \neq D_i$. The resulting compositional boundary layers have thicknesses $\delta_{m,s}$, and we denote by $\Delta c_{m,s}$ the composition difference across the boundary layers. The local diffusive compositional flux across the interface scales as $\kappa_c \Delta c/\delta$ and the total mass flux F_c is

$$F_c \sim \rho_m A_T \kappa_c^m \frac{\Delta c_m}{\delta_m} \sim \rho_s A_T \kappa_c^s \frac{\Delta c_s}{\delta_s}. \qquad (7)$$

Continuity of the mass flux across the interface implies that

$$\gamma_{m/s} = \frac{\Delta c_m}{\Delta c_s} = \frac{\rho_s}{\rho_m}\frac{\kappa_c^s}{\kappa_c^m}\frac{\delta_m}{\delta_s}. \qquad (8)$$

We now relate the compositional jumps Δc_s and Δc_m to the

mean composition $\overline{c}_m$ and $\overline{c}_s$ of the metal and silicate phases. Using Eq. (8) together with the assumption of local thermodynamic equilibrium ($D_i = c_m^{\rm int}/c_s^{\rm int}$), we obtain the following expressions for Δc_s and Δc_m :

$$\Delta c_s = -\frac{\overline{c}_m - D_i\overline{c}_s}{\gamma_{m/s} + D_i}, \quad \Delta c_m = -\gamma_{m/s}\frac{\overline{c}_m - D_i\overline{c}_s}{\gamma_{m/s} + D_i}. \tag{9}$$

Using $(\pi/6)\overline{\rho}\, d^3$ for the mass of the metal-silicate mixture, the evolution of composition in the metal and silicate phases are given by

$$\phi\frac{\pi}{6}\overline{\rho}\, d^3\frac{d\overline{c}_m}{dt} = -F_c, \tag{10}$$

$$(1-\phi)\frac{\pi}{6}\overline{\rho}\, d^3\frac{d\overline{c}_s}{dt} = F_c, \tag{11}$$

where ϕ is the mass fraction of the metal phase in the mixture. Combining Eqs. (10) and (11) and using the metal dilution $\Delta = (1-\phi)/\phi$, we obtain

$$\frac{d}{dt}\ln(\overline{c}_m - D_i\overline{c}_s) = -\frac{(1+\Delta)(D_i+\Delta)}{\Delta(D_i+\gamma_{m/s})}\frac{\rho_s}{\overline{\rho}}\frac{6\kappa_c^s}{d\,\delta_s}\, We^{\frac{3}{5}(D-2)}, \tag{12}$$

from which we obtain an equilibration timescale $\tau_{\rm eq}$ given by

$$\tau_{\rm eq} = f(\Delta, D_i, \gamma_{m/s})\,\frac{\overline{\rho}}{\rho_s}\,\frac{d\,\delta_s}{\kappa_c^s}\, We^{-\frac{3}{5}(D-2)}, \tag{13}$$

where the factor 6 in Eq. (12) has been omitted, and

$$f(\Delta, D_i, \gamma_{m/s}) = \frac{\Delta(D_i+\gamma_{m/s})}{(1+\Delta)(D_i+\Delta)}. \tag{14}$$

The function f is $O(1)$ for intermediate values of Δ (with a maximum always smaller than 1), but $f \to 0$ if Δ is small compared to $\min(1, D_i)$ or large compared to $\max(1, D_i)$.

We now estimate the boundary layers thicknesses δ in the metal and silicate phases (the subscript m and s will be omitted in what follows, with the understanding that the analysis applies to both phases). Denoting by ℓ the smallest scale of the flow in the vicinity of the interface, then the smallest scale δ of the compositional field is found by balancing the strain rate at scale ℓ with the diffusion rate at the scale δ, *i.e.* $u_\ell/\ell \sim \kappa_c/\delta^2$. Assuming a Kolmogorov type velocity spectrum, the velocity at scale ℓ is $u_\ell \sim w(\ell/d)^{\frac{1}{3}}$, where w is the large scale velocity. With these assumptions, we obtain

$$\delta = d\, Sc^{-\frac{1}{2}} Re^{-\frac{1}{2}}\left(\frac{\ell}{d}\right)^{\frac{1}{3}}. \tag{15}$$

At this stage, further progress requires some assumptions on the small scale structure of the turbulence in the vicinity of the metal-silicate interface :

1. If we assume that the turbulence structure is not affected by the presence of the interface and interfacial tension effects, then ℓ should be the Kolmogorov scale. Eq. (15) with $\ell = \ell_K = dRe^{-3/4}$ gives

$$\delta = d\, Sc^{-\frac{1}{2}} Re^{-3/4}, \tag{16}$$

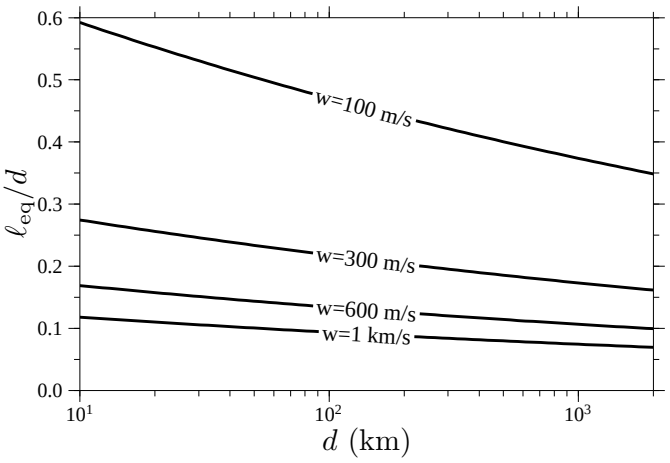

Figure 6: Equilibration distance $\ell_{\rm eq}/d$ as functions of the metal-silicate mixture diameter d, for $w = 100, 300, 600$ and 1000 m.s^{-1}, calculated using Eq. (23) with $f(\Delta, D_i) = 0.5$, $\kappa_c^s \sim 10^{-8}$ m.s^{-1}, $\sigma = 1$ J.m^{-2} and $\rho_s = 3500$ kg.m^{-3}.

which is the Batchelor scale ℓ_B. With this estimate for δ, we obtain

$$\gamma_{m/s} = \left(\frac{\rho_s}{\rho_m}\right)^{5/4}\left(\frac{\kappa_c^s}{\kappa_c^m}\right)^{1/2}\left(\frac{\eta_s}{\eta_m}\right)^{1/4} \tag{17}$$

and

$$\tau_{\rm eq} = f(\Delta, D_i, \gamma_{m/s})\,\frac{\overline{\rho}}{\rho_s}\,\frac{d^2}{\kappa_c^s}\, Sc^{-1/2} Re^{-3/4} We^{-\frac{3}{5}(D-2)}. \tag{18}$$

2. Alternatively, one might argue that the turbulent motion in the vicinity of the interface is damped by interfacial tension at scales smaller than ℓ_σ. In this case the smallest scale of the flow is $\ell_\sigma \sim d\, We^{-3/5}$ and the boundary layer thickness is

$$\delta = d\, Sc^{-\frac{1}{2}} Re^{-\frac{1}{2}} We^{-\frac{1}{5}}, \tag{19}$$

giving

$$\gamma_{m/s} = \left(\frac{\rho_s}{\rho_m}\right)^{6/5}\left(\frac{\kappa_c^s}{\kappa_c^m}\right)^{1/2} \tag{20}$$

and an equilibration timescale

$$\tau_{\rm eq} = f(\Delta, D_i, \gamma_{m/s})\,\frac{\overline{\rho}}{\rho_s}\,\frac{d^2}{\kappa_c^s}\, Sc^{-\frac{1}{2}} Re^{-\frac{1}{2}} We^{-\frac{3}{5}D+1}. \tag{21}$$

Choosing between the two models Eqs. (18) or (21) would require detailed measurement of the small scale structure of the flow, or alternatively, measurements of a tracer concentration in both phases, which are beyond the scope of our current experimental set-up. We therefore choose the more conservative estimate of the equilibration timescale Eq. (21) which assumes that turbulent motions in the vicinity of the interface are damped at scales smaller than ℓ_σ. For comparison, the model assuming no effect of the interface on the turbulence structure would yield an equilibration timescale a factor $We^{1/5}Re^{-1/4}$ smaller (typically a factor of 5 or more smaller).

With $\rho_s/\rho_m \simeq 0.5$, assuming that κ_c^s and κ_c^m are of the same order of magnitude implies that $\gamma_{m/s} = O(1)$. Since it only appears in $f(\Delta, D_i, \gamma_{m/s})$ as a sum with D_i which is $\gg 1$ for siderophile elements, the exact value of $\gamma_{m/s}$ should be of little importance. The factor $\overline{\rho}/\rho_s$ is also $O(1)$, and ignoring it as well in Eq. (21) yields the simplified equilibration timescale

$$\tau_{\rm eq} = f(\Delta, D_i)\,\frac{d^2}{\kappa_c^s}\,Sc^{-\frac{1}{2}}Re^{-\frac{1}{2}}We^{-\frac{3}{5}D+1}. \quad (22)$$

From Eq. (22), the equilibration distance $\ell_{\rm eq} = w\,\tau_{\rm eq}$ is

$$\ell_{\rm eq} = f(\Delta, D_i)\,d\,Sc^{\frac{1}{2}}Re^{\frac{1}{2}}We^{-\frac{3}{5}D+1}. \quad (23)$$

Fig. 6 shows $\ell_{\rm eq}$ as a function of d for various values of w between 100 m.s^{-1} and 1 km.s^{-1}, calculated with $f(\Delta, D_i) = 0.5$, $\kappa_c^s \sim 10^{-8}$ m.s^{-1}, $\sigma = 1$ J.m^{-2} and $\rho_s = 3500$ kg.m^{-3}. The equilibration distance is always a fraction of the metal-silicate mixture diameter, and is usually smaller than plausible magma ocean depths.

8. Prediction for the stable drop size after fragmentation

After fragmentation, the metal-silicate equilibration timescale depends mostly on the resulting fragments size (Karato and Murthy, 1997; Rubie et al., 2003; Ulvrová et al., 2011). In a fully turbulent flow, the stable drop size d_d after fragmentation, as well as the cut-off length scale ℓ^* before fragmentation, are expected to depend only on the dissipation rate ϵ, the interfacial tension σ, the densities and viscosities of both phases, and the metal volume fraction :

$$\ell^* = \mathcal{F}_1(\epsilon, \sigma, \rho_m, \rho_s, \nu_s, \nu_m, \phi). \quad (24)$$

The Buckingham-π theorem then indicates that ℓ^* must be the solution of an equation of the form

$$\mathcal{F}_2\left[\mathsf{P}, \mathsf{H}, \phi, \frac{\ell^*}{\ell_K}, \frac{\ell^*}{\ell_\sigma}\right] = 0. \quad (25)$$

where we have introduced two length scales,

$$\ell_K = \left(\frac{\nu_s^3}{\epsilon}\right)^{1/4}, \quad \ell_\sigma = \left(\frac{\sigma}{\rho_s}\right)^{3/5}\epsilon^{-2/5}. \quad (26)$$

ℓ_K is the Kolmogorov scale, at which turbulent kinetic energy is dissipated into heat by the action of viscous forces; ℓ_σ can be shown to be the length scale at which interfacial tension (Laplace pressure) balances turbulent pressure fluctuations and stresses if a Kolmogorov type turbulence is assumed (Kolmogorov, 1949; Hinze, 1955). With $\epsilon \sim w^3/r$ (Tennekes and Lumley, 1972),

$$\ell_K \sim Re^{-3/4}d, \quad \ell_\sigma \sim We^{-3/5}d. \quad (27)$$

Two end-member cases are possible, depending on the relative values of ℓ_K and ℓ_σ. Let us first compare the magnitude of the viscous stress and Laplace pressure at a given scale ℓ. Assuming a Kolmogorov type turbulence cascade, the velocity fluctuations u_ℓ at scale ℓ is $u_\ell \sim w(\ell/d)^{1/3}$. Using this estimate for u_ℓ, we find that the ratio of the viscous stress to the Laplace pressure at the scale ℓ is

$$\frac{\text{Viscous stress at scale } \ell}{\text{Laplace pressure at scale } \ell} \sim \frac{\eta_s u_\ell/\ell}{\sigma/\ell} \sim \left(\frac{\ell_K}{\ell_\sigma}\right)^{4/3}\left(\frac{\ell}{\ell_\sigma}\right)^{1/3}. \quad (28)$$

Two options are possible :

1. First, if $\ell_K \gg \ell_\sigma$, all the energy input is dissipated at the Kolmogorov scale, at which scale the ratio of viscous stress and Laplace pressure is $\sim (\ell_K/\ell_\sigma)^{5/3} \gg 1$ according to Eq. (28). In this case interfacial tension is unimportant, and ℓ^* scales as
$$\ell^* = \mathcal{F}_3(\mathsf{P}, \mathsf{H}, \phi)\left(\frac{\nu_s^3}{\epsilon}\right)^{1/4} \sim \mathcal{F}_3(\mathsf{P}, \mathsf{H}, \phi)\,d\,Re^{-3/4}. \quad (29)$$
2. Alternatively, if $\ell_K \ll \ell_\sigma$, then interfacial tension balances turbulent pressure and stress fluctuations at the scale ℓ_σ, with further smaller scale deformation of the interface inhibited by the interfacial tension. According to Eq. (28), the ratio of viscous stress and Laplace pressure is $\sim (\ell_K/\ell_\sigma)^{4/3} \ll 1$ at this scale, which implies that viscous effects are unimportant. As a consequence, the stable drop size does not depend on the viscosity of either phase, nor on the viscosity ratio H, and thus the cut-off length scale follows a scaling law of the form:
$$\ell^* = \mathcal{F}_4(\mathsf{P}, \phi)\left(\frac{\sigma}{\rho_s}\right)^{3/5}\epsilon^{-2/5} \sim \mathcal{F}_4(\mathsf{P}, \phi)\,d\,We^{-3/5}. \quad (30)$$

The ratio $\ell_K/\ell_\sigma \sim We^{3/5}Re^{-3/4}$ following an impact is found to be typically smaller than 10^{-2}, which suggests that the drop size or cut-off length will be set by interfacial tension rather than viscosity, and will obey the scaling given by Eq. (30). When ϕ is small, its effect should be negligible, as indeed observed in experiments with dilute dispersions (Hinze, 1955; Chen and Middleman, 1967).

From analysis of Clay (1940)'s data, Hinze (1955) found that the maximum drop size $d_{\rm max}$ in a turbulent flow with $\ell_\sigma \gg \ell_K$ is given by

$$d_{\rm max} \simeq 0.725\left(\frac{\sigma}{\rho_s}\right)^{3/5}\epsilon^{-2/5}. \quad (31)$$

Effects of changing the density ratio was not investigated in this study, which focused on fluids with density ratios $\mathsf{P} \simeq 1$. Theory (Levich, 1962) and experiments (Hesketh et al., 1987) argue for a dependence on the density ratio of the form $d_{\rm max} \propto \mathsf{P}^{-1/5}$. For the metal-silicate system, which has $\mathsf{P} \simeq 2$, this would predict a maximum drop size about 13 % smaller than what Eq. (31) predicts, a minor discrepancy in light of the other uncertainties.

Clearly, the size of the drops produced by fragmentation of the metal blob must depend on the details of the fragmentation mechanism, which are not elucidated yet, and the drop size just after fragmentation does not have to match the prediction of Eq. (31) (although a similar scaling is expected). Nevertheless,

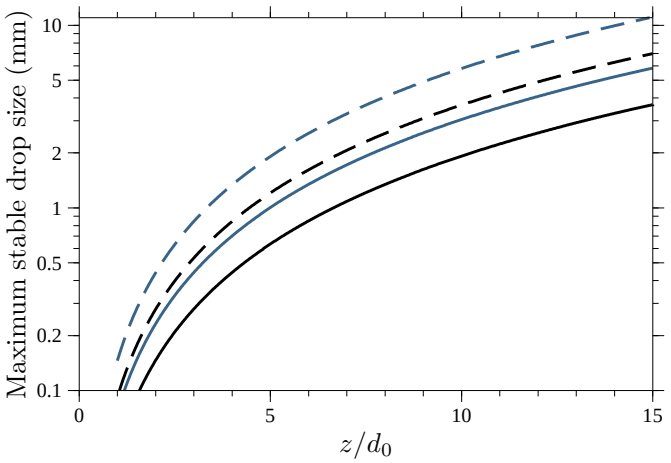

Figure 7: Maximum stable drop size after fragmentation according to Eq. (34), as a function of the distance travelled (normalized by the initial metal blob diameter d_0), for metal blobs with initial diameter 100 km (blue curves) and 1000 km (black curves) with $f = 0.5$ (solid curves) and $f = 0.1$ (dashed curves). Assumed parameters values are : $\alpha = 0.25$, $K + 3\,C_d/16\,\alpha = 1$, $\Delta\rho = 4000$ kg m^{-3}, $\rho_s = 3500$ kg m^{-3}, $g = 5$ m s^{-2}, $\sigma = 1$ J m^{-2}.

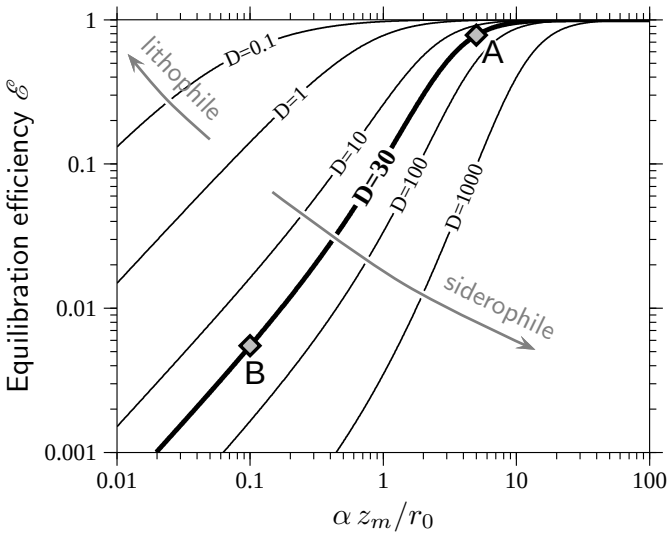

Figure 8: Equilibration efficiency $\mathscr{E}_i$ as a function of $\alpha z_m/r_0$ (where z_m is the depth of the magma ocean) and various values of the partition coefficient D, estimated for metal-silicate mixing in a magma ocean as predicted by the turbulent entrainment model (Eq. (6)). Point A corresponds to the case of a metal blob falling through a magma ocean of depth ten times its diameter, with $\alpha = 0.25$. Point B corresponds to the case of a giant impact with $r_0 = 0.5\,z_m$ and $\alpha = 0.05$.

Eq. (31) should give a reasonable upper bound for the fragment size, since it predicts that larger drops would be disrupted by turbulent dynamic pressure fluctuations.

In a system in statistical steady state, the dissipation rate ϵ must equal the total energy input in the system $e_{\rm in}$, which here is the rate of work of the buoyancy forces. However, since the metal-silicate mixture is not in statistical steady state (it can be shown using the self-similar regime velocity (Eq. (4)) that the total kinetic energy of the system evolves with time), dissipation does not equal the rate of energy input, but is some fraction f of the work done by the buoyancy forces. The rate of work of the buoyancy forces,

$$e_{\rm in} = \bar{\phi}\,\frac{\Delta\rho}{\bar{\rho}}\,g\,w, \tag{32}$$

tends towards

$$e_{\rm in} = 2\left[1 + K + \frac{3}{16}\frac{C_d}{\alpha}\right]^{-1/2}\frac{\rho_s}{\bar{\rho}}\left[\frac{\Delta\rho\,g\,r_0^{1/3}}{2\alpha^3\rho_s}\right]^{3/2}\left(\frac{r_0}{z}\right)^4, \tag{33}$$

in the self-similar regime, for which w is given by Eq. (4). Using Eq. (33) for $e_{\rm in}$ and writing the dissipation as $\epsilon = f\,e_{\rm in}$, we find that

$$\frac{d_{\rm max}}{d_0} \simeq \frac{3}{f^{2/5}}\left[1 + K + \frac{3}{16}\frac{C_d}{\alpha}\right]^{1/5}\left(\frac{\bar{\rho}}{\rho_s}\right)^{2/5}\frac{\alpha^{9/5}}{Bo_0^{3/5}}\left(\frac{z}{d_0}\right)^{8/5} \tag{34}$$

when the mixture has reached the self-similar regime. Here $Bo_0 = \Delta\rho\,g\,d_0^2/\sigma$. The value of f is difficult to estimate precisely, but shouldn't be much smaller than 1. Fig. 7 shows $d_{\rm max}$ from Eq. (34) for metal blobs with initial diameter 100 km (blue curves) and 1000 km (black curves) with $f = 0.5$ (solid curves) and $f = 0.1$ (dashed curves), and $\alpha = 0.25$. Smaller values of α would result in smaller drop sizes. Eq. (34) predicts submillimeter-to-centimeter maximum stable drop sizes, which is small enough to ensure fast re-equilibration with the surrounding silicates (Karato and Murthy, 1997; Rubie et al., 2003; Ulvrová et al., 2011).

9. Implications for planetary core formation

Efficient chemical re-equilibration requires that two necessary conditions are met [see Eq. (1)] : (i) that the metal phase is capable of equilibrating with the silicates it has mixed with (*i.e.* that the parameter k in Eq. (1) is of order 1), and (ii) that the metal phase equilibrates with a silicate mass at least a factor D_i larger (*i.e.* that the metal dilution $\Delta \gtrsim D_i$).

With w in the range 0.1-1 km.s^{-1} and $d > 10$ km, our model predicts that $\ell_{\rm eq}$ is always smaller than about $0.6\,d$ (Fig. 6). For example, Eq. (23) yields $\ell_{\rm eq} \simeq 50$ km for $d = 100$ km and $w = 100$ m.s^{-1}, and $\ell_{\rm eq} \simeq 75$ km for $d = 1000$ km and $w = 1$ km.s^{-1}, assuming $\kappa_c = 10^{-8}$ m^2.s^{-1}, $\rho_s = 3500$ kg.m^{-3}, $\sigma = 1$ J.m^{-2}, and $f(\Delta, D_i) = 0.5$. The corresponding equilibration timescales are $\tau_{\rm eq} \simeq 8$ min and $\simeq 75$ s, respectively. Since $\ell_{\rm eq}$ is smaller than the metal-silicate mixture diameter, and small compared with the typical depth of a magma ocean, the metal phase and the entrained silicate should readily equilibrate once turbulence is fully developed, which typically requires one advection time $\sim d/w$, or a distance of fall $\sim d$. Re-equilibration should be efficient as well once the metal phase is fragmented : the maximum stable size of the resulting fragments is expected to scale as $d\,We^{-3/5}$ (Kolmogorov, 1949; Hinze, 1955; Risso, 2000), which predicts submillimeter-to-centimeter size drops, small enough for fast re-equilibration (Karato and Murthy, 1997; Rubie et al., 2003; Ulvrová et al., 2011). This suggests that once turbulence is well-developed,

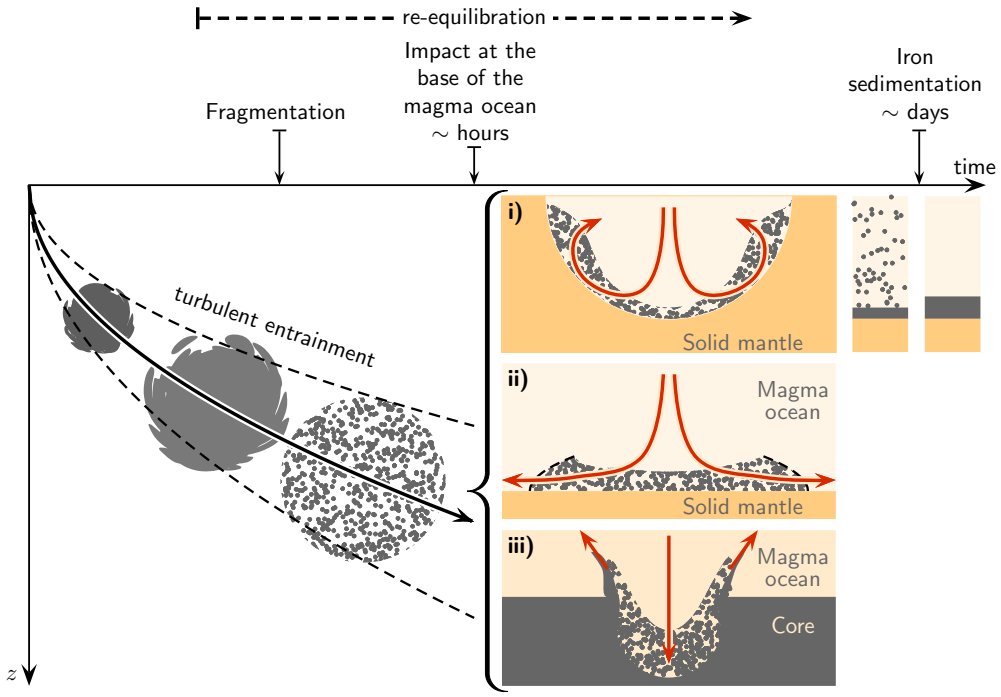

Figure 9: Possible scenarios for metal-silicate mixing and segregation following a large impact involving a previously differentiated impactor. The metal is shown in grey, molten silicate in light orange, and solid silicate in dark orange. The metal phase gradually mixes with the silicates through turbulent entrainment, with efficient chemical equilibration resulting from small-scale mixing. Additional mixing may be caused by the impact of the metal-silicate mixture at the base of the magma ocean.

most of the metal indeed equilibrates with the surrounding silicates and k should be close to 1. Whether or not metal-silicate equilibration has a significant geochemical fingerprint then depends on the ratio Δ/D_i. Assuming that metal-silicate mixing occurs through turbulent entrainment, Fig. 8 shows that the equilibration efficiency $\mathscr{E}_i$, calculated using Eqs. (1) and (6) with $k = 1$, depends strongly on the quantity $\alpha\, z_m/r_0$, where z_m is the depth of the magma ocean.

The above considerations suggest that efficient metal-silicate equilibration should have been the norm for impacts in which the magma ocean is much deeper than the impactor core diameter. As an example, Eq. (6) predicts that a molten iron blob falling through a magma ocean of depth ten times its diameter mixes with about 100 times its mass of silicate, assuming $\alpha = 0.25$ (a relevant value here because the large value of z_m/r_0 ensures deceleration of the metal phase to subsonic velocity, irrespectively of the initial conditions). The large value of z_m/r_0 also ensures well-developed turbulence and fast equilibration. The resulting Tungsten equilibration efficiency is $\mathscr{E}_W \simeq 0.78$ (point A in Fig. 8), assuming $D_W = 30$.

The cases of impacts for which z_m/r_0 is not much larger than one, which includes the Moon-forming event, are not as clear. First, it is not obvious that the time needed for the impactor core material to reach the base of the magma ocean would allow enough turbulence to develop and the metal-silicate interfacial area to increase sufficiently for fast equilibration. Second, the effect of compressibility on α may significantly reduce the entrainment rate, allowing only a small mass of silicate to mix with the metal. Assuming, as for turbulent jets, a five-fold decrease of the entrainment rate due to compressibility, $\alpha = 0.25/5 = 0.05$, the core of an impactor with $\simeq$ 10% the mass of the proto-Earth ($r_0 \simeq 0.5\, z_m$) would mix with only about 17 % its mass of silicate before it reaches the proto-Earth's core, giving $\mathscr{E}_W \simeq 5.5\ 10^{-3}$ (point B in Fig. 8). However, the actual equilibration efficiency may depend on the details of the impact dynamics. SPH simulations of the Moon-forming impact suggest that in the likely case of an oblique impact, a fraction of the impactor including most of its core would be sheared past the planet before re-impacting Earth's mantle (Canup, 2004). Some degree of disruption of the impactor core during this process might be sufficient to allow subsequent metal-silicate equilibration by increasing the value of $\alpha\, z_m/r_0$ for individual blobs.

Lastly, we point out that core-mantle segregation is a complex, multi-step process and additional equilibration is possible at other stages. In particular, the velocity of the metal-silicate mixture may easily exceed hundreds of m.s^{-1}, implying an energetic "secondary impact" when it reaches the bottom of the magma ocean, which, as sketched in Fig. 9, could cause additional metal-silicate mixing (Deguen et al., 2011). (i) In the case of an impact forming its own semi-spherical magma pool, the inertia of the mixture drives an upward flow, re-suspending iron fragments (Deguen et al., 2011) which, in spite of likely vigorous convection, sediment out on a timescale similar to the Stokes' sedimentation time (Martin and Nokes, 1988; Lavorel and Le Bars, 2009). (ii) In a pre-existing global magma ocean with a horizontal lower boundary, the metal-silicate mixture will rather spread laterally as a turbulent gravity current - analo-

gous to a pyroclastic flow - with possibly significant additional entrainment of molten silicate (Hallworth et al., 1993). (iii) If the mantle is fully molten, the metal-silicate mixture directly impacts the proto-Earth's core, with splashing and entrainment of mantle material into the core (Storr and Behnia, 1999) providing additional metal-silicate mixing.

Acknowledgement

This research was supported by NSF grants EAR-110371 and EAR-1135382 (FESD).

Appendix A. Equilibration efficiency

Definition. Let c_m and c_s denote the concentrations (in weight %) of element i in either the metal or silicate phases, respectively. The metal and silicate are fully equilibrated when the two phases have reached thermodynamic equilibrium, for which the equilibrium concentration $c_m^{\rm eq}$ and $c_s^{\rm eq}$ are linked through the metal/silicate partition coefficient D_i by $c_m^{\rm eq} = D_i\, c_s^{\rm eq}$.

Consider a mass M_m of metal, in which we assume that a fraction $k\,M_m$ has been mixed and equilibrated with a mass M_s of silicates. We define the metal dilution Δ as the ratio of the mass of equilibrated silicate over the mass of equilibrated metal,

$$\Delta = \frac{M_s}{kM_m}. \tag{A.1}$$

Given initial values c_m^0 and c_s^0 of the concentration in the metal and silicate phases, the concentration in the equilibrated metal $c_m^{\rm eq}$ and equilibrated silicate $c_s^{\rm eq}$ are found from mass conservation,

$$c_m^{\rm eq} + \Delta\, c_s^{\rm eq} = c_m^0 + \Delta\, c_s^0, \tag{A.2}$$

which, together with the assumption of thermodynamic equilibrium, $c_m^{\rm eq} = D_i\, c_s^{\rm eq}$, gives

$$c_m^{\rm eq} = \frac{c_m^0 + \Delta\, c_s^0}{1 + \Delta/D_i}, \quad c_s^{\rm eq} = \frac{c_m^0 + \Delta\, c_s^0}{D_i + \Delta}. \tag{A.3}$$

The net mass exchange $\mathcal{M}_i$ of element i between the metal and silicate phases can be written as

$$\mathcal{M}_i = k\,M_m|c_m^{\rm eq} - c_m^0| = M_s|c_s^{\rm eq} - c_s^0| \tag{A.4}$$

$$= k\,M_m \frac{|c_m^0 - D_i c_s^0|}{1 + D_i/\Delta}. \tag{A.5}$$

$\mathcal{M}_i$ reaches a maximum value $\mathcal{M}_i^{\rm max} = M_m|c_m^0 - D_i c_s^0|$ when all the metal phase is equilibrated ($k = 1$) and is infinitally diluted in the silicate phase ($\Delta \to \infty$). We thus define the equilibration efficiency $\mathscr{E}_i$ of element i as the actual mass exchange $\mathcal{M}_i$ normalized by the maximum possible mass exchange $\mathcal{M}_i^{\rm max}$. From Eq. (A.5) and the value of $\mathcal{M}_i^{\rm max}$, the equilibration efficiency is found to be

$$\mathscr{E}_i = \frac{k}{1 + D_i/\Delta}, \tag{A.6}$$

which reduces to k when $\Delta/D_i \gg 1$, the limit that is usually assumed in continuous accretion models (*e.g.* Rudge et al., 2010).

As shown by Eq. (A.6), the equilibration efficiency $\mathscr{E}_i$ depends critically on the ratio Δ/D_i, and is small, even when $k = 1$, if Δ is small compared to D_i. Efficient re-equilibration requires the metal dilution to be similar to or larger than the partition coefficient of the element considered. For Tungsten, which has $D_W \simeq 30$, efficient re-equilibration thus requires that the metal re-equilibrates with at least 30 times its mass of silicate.

Use of $\mathscr{E}_i$ in geochemical models. We demonstrate here that geochemical models assuming partial equilibration of the metal phase but infinite dilution can be generalized by using the equilibration efficiency $\mathscr{E}_i$ in place of k. We consider the case of continuous accretion, according to the formulation of Rudge et al. (2010) (see their Supplementary Information). Discontinuous accretion can be treated in the same way.

We note $c_m(t)$ and $c_s(t)$ the concentration in Earth's mantle and core at time t, and $c_m^{\rm imp}(t)$ and $c_s^{\rm imp}(t)$ the composition of the metal and silicate phase of the impacting bodies. The mass of the Earth is denoted by $M(t)$, and, using F for the mass fraction of metal in the Earth (assumed constant), then the masses of the core and mantle are $FM(t)$ and $(1-F)M(t)$, respectively. We assume for simplicity that all impactors have the same metal mass fraction F.

Conservation of mass of element i in Earth's core implies that

$$\frac{d}{dt}\left[FMc_m\right] = \underbrace{(1-k)Fc_m^{\rm imp}\frac{dM}{dt}}_{\text{Flux of non-equilibrated metal}} + \underbrace{kFc_m^{\rm eq}\frac{dM}{dt}}_{\text{Flux of equilibrated metal}} \tag{A.7}$$

where $c_m^{\rm eq}$ is the concentration in the re-equilibrated fraction of the impactor core. One complication is that the metal of the impactor may equilibrate with silicates from both the impactor mantle and Earth's mantle, in unknown proportion. If $\tilde{c}_s$ denotes the mean composition of the equilibrated silicate, Eq. (A.3) yields

$$c_m^{\rm eq} = \frac{c_m^{\rm imp} + \Delta\,\tilde{c}_s}{1 + \Delta/D_i}. \tag{A.8}$$

For siderophile elements such as Tungsten, $\tilde{c}_s$ can be approximated by $c_s(t)$. As discussed above in Appendix A, the effect of re-equilibration is significant only if the metal re-equilibrates with a mass of silicates about D_i times larger (*e.g.* about 30 times larger for Tunsten). Since the mass of the impactor mantle is only about twice the mass of its core, efficient re-equilibration of siderophile elements requires that the impactor metal equilibrates with a mass of Earth's mantle significantly larger than the impactor's mantle. This implies that, in cases where equilibration is efficient, the mean concentration of the equilibrated silicate is close to $c_s(t)$. The approximation $\tilde{c}_s \simeq c_s(t)$ is not valid if the equilibration efficiency is small, but in that situation it has little effect on the results.

Substituting Eq. (A.8) into Eq. (A.7) yields the following equation for the compositional evolution of the core :

$$\frac{d}{dt}\left(Mc_m\right) = \left[\mathscr{E}_i D_i \tilde{c}_s + (1-\mathscr{E}_i)c_m^{\rm imp}\right]\frac{dM}{dt}, \tag{A.9}$$

while conservation of element i in the mantle yields the following equation for the mantle :

$$\frac{d}{dt}\left(Mc_s\right) = \left[c_s^{\rm imp} + \mathscr{E}_i \frac{F}{1-F}(c_m^{\rm imp} - D_i\tilde{c}_s)\right]\frac{dM}{dt}. \qquad \text{(A.10)}$$

If $\tilde{c}_s$ is taken to be equal to $c_s(t)$, equations (A.9) and (A.10) are the same as used by Rudge et al. (2010) for stable species if $\mathscr{E}_i$ is substituted for k (see their equations A.3 and A.4 in the Supplementary Information). The equivalence also holds if radioactive or radiogenic species are considered (see the Supplementary Information of Rudge et al. (2010) for a detailed derivation of the relevant equations). Results of previous accretion models, including the bounds on Earth's accretion derived by Rudge et al. (2010) from Hf-W and U-Pb systematics, can therefore be generalized to include the effect of finite dilution by using $\mathscr{E}_i$ in place of k.

Implications. Previous studies (Kleine et al., 2004; Nimmo et al., 2010; Rudge et al., 2010) have shown that Hf-W systematics can be used to infer a lower bound for the mean degree of re-equilibration during Earth's accretion. Assuming infinite dilution of the metal phase, (Rudge et al., 2010) found that Hf-W systematics constrains the fraction of equilibrated metal k to be larger than about 0.36 on average during Earth's accretion. If finite metal dilution is considered, the implication is that $\mathscr{E}_W \geq \mathscr{E}_W^{\rm min} = 0.36$, which requires that $k > 0.36$ and, assuming $D_W \simeq 30$, $\Delta \geq \Delta^{\rm min} = D_W/(1/\mathscr{E}_W^{\rm min} - 1) \simeq 17$.

A possibly important implication for modeling the abundance of siderophile elements in the mantle is that the equilibration efficiency $\mathscr{E}_i$ is element-dependent. One consequence is that constraints on the equilibration efficiency from Hf-W systematics do not apply directly to other elements. The equilibration efficiency of an element i with partition coefficient D_i differs from the Tungsten equilibration efficiency $\mathscr{E}_W$ according to

$$\mathscr{E}_i = g(D_W, D_i, \Delta)\,\mathscr{E}_W, \qquad \text{(A.11)}$$

where

$$g(D_W, D_i, \Delta) = \frac{1 + D_W/\Delta}{1 + D_i/\Delta}.$$

In Eq. (A.11), the function g is an increasing function of Δ if $D_i > D_W$, and a decreasing function of Δ if $D_i < D_W$. Thus the lower bounds on k and Δ deduced from Hf-W systematics imply the following lower bound on the equilibration efficiency of an element i :

$$\mathscr{E}_i \geq \mathscr{E}_i^{\rm min} = \begin{cases} \frac{1+D_W/\Delta^{\rm min}}{1+D_i/\Delta^{\rm min}}\mathscr{E}_W^{\rm min} & \text{if } D_i \geq D_W, \\ \mathscr{E}_W^{\rm min} & \text{if } D_i \leq D_W. \end{cases} \qquad \text{(A.12)}$$

The constraint on the equilibration efficiency becomes weaker for elements that are more siderophile. For example, the lower bound on the equilibration efficiency is $\mathscr{E}_i^{\rm min} \simeq 0.14$ for an element with $D_i = 100$, and only $\mathscr{E}_i^{\rm min} \simeq 0.017$ for an element with $D_i = 10^3$. Thus low equilibration efficiency should be considered when modeling the core/mantle partitioning of highly siderophile elements (*e.g.* Wood et al., 2006; Corgne et al., 2008).

Appendix B. Turbulent entrainment model

Integral relationships. We consider a buoyant spherical mass of initial radius r_0 and density $\rho_m = \rho_s + \Delta\rho$ released with an initial (downward) velocity w_0 in a fluid of density ρ_s. Owing to entrainment, the mean density of the metal-silicate mixture evolves with time according to

$$\bar{\rho}(t) = \rho_s + (\rho_m - \rho_s)\phi = \rho_s\left[1 + \frac{\Delta\rho}{\rho_s}\phi\right], \qquad \text{(B.1)}$$

where $\phi = r_0^3/r^3$ is the metal phase volume fraction. The buoyancy of the metal-silicate mixture,

$$B = g\frac{\bar{\rho} - \rho_s}{\rho_s}V = g\,\frac{\Delta\rho}{\rho_s}\,\phi\,V, \qquad \text{(B.2)}$$

is conserved in absence of density stratification in the ambient fluid. Here V is the volume of the turbulent fluid and r is its mean radius.

We adopt the standard entrainment assumption of (Morton et al., 1956) for which the local inward entrainment velocity u_e is proportional to the magnitude of the mean vertical velocity w of the mixture,

$$u_e = \alpha\,|w|, \qquad \text{(B.3)}$$

where α is the entrainment coefficient. With this assumption, the equation of conservation of mass becomes

$$\frac{4\pi}{3}\frac{d(\bar{\rho}r^3)}{dt} = 4\pi r^2\rho_s\alpha|w|, \qquad \text{(B.4)}$$

while conservation of momentum becomes (*e.g.* Bush et al., 2003)

$$\frac{4\pi}{3}\frac{d}{dt}\left[(\bar{\rho} + K\rho_s)r^3 w\right] = \rho_s B - \frac{1}{2}C_d\rho_s\pi r^2 w^2. \qquad \text{(B.5)}$$

Here K is the coefficient of added mass, which accounts for the momentum imparted to the surrounding fluid (Escudier and Maxworthy, 1973). The second term on the right hand side of equation (B.5) is the hydrodynamic drag F_d, with C_d the drag coefficient.

Using Eq. (B.1) to write $\bar{\rho}$ as a function of ϕ, Eqs. B.4 and B.5 become

$$\frac{dr}{dt} = \alpha|w|, \qquad \text{(B.6)}$$

$$\left[(1+K)r^3 + \frac{\Delta\rho}{\rho_s}\,r_0^3\right]\frac{dw}{dt} = g\,\frac{\Delta\rho}{\rho_s}\,r_0^3 - 3\alpha\left[1 + K + \frac{C_d}{8\alpha}\right]r^2w^2. \qquad \text{(B.7)}$$

Noting that $w = dz/dt$, Eq. (B.6) implies that $dr/dz = \alpha$.

We now non-dimensionalize lengths by r_0, time by $[\rho_s\,r_0/(\Delta\rho\,g)]^{1/2}$, and velocity by $(r_0\,g\,\Delta\rho/\rho_s)^{1/2}$. In non-dimensional form, equations (B.6)-(B.7) then become

$$\frac{d\tilde{r}}{d\tilde{t}} = \alpha|w|, \qquad \text{(B.8)}$$

$$\left[(1+K)\tilde{r}^3 + \frac{\Delta\rho}{\rho_s}\right]\frac{d\tilde{w}}{d\tilde{t}} = 1 - 3\alpha\left[1 + K + \frac{C_d}{8\alpha}\right]\tilde{r}^2\tilde{w}^2. \qquad \text{(B.9)}$$

where the tilde ('∼') denotes non-dimensional variables. The initial conditions are

$$\tilde{r} = 1,\ \tilde{z} = 0,\ \text{and}\ \tilde{w} = \frac{w_0}{\left(r_0\, g\, \frac{\Delta\rho}{\rho_s}\right)^{1/2}} \quad \text{at} \quad \tilde{t} = 0. \qquad \text{(B.10)}$$

In Fig. 2, we use a least-square inversion procedure to find the values of α, K and C_d for which the model described by Eqs. (B.8-B.10) best fits our experimental data on the position of the center of mass $\tilde{z}$ and radius of the mixture $\tilde{r}$ as a function of time.

Analytical solutions. Using $d\tilde{r}/d\tilde{t} = \alpha\, d\tilde{z}/d\tilde{t} = \alpha\,\tilde{w}$, Eq. (B.9) can be re-written as

$$\left[(1+K)\tilde{r}^3 + \frac{\Delta\rho}{\rho_s}\right]\frac{\alpha}{2}\frac{d\tilde{w}^2}{dr} = 1 - 3\alpha\left[1 + K + \frac{C_d}{8\alpha}\right]\tilde{r}^2\tilde{w}^2, \quad \text{(B.11)}$$

the solution of which is

$$\tilde{w}^2 = \frac{2}{\alpha}\int_1^{\tilde{r}} \frac{\left(\frac{\Delta\rho}{\rho_s} + (1+K)x^3\right)^{\gamma-1}}{\left(\frac{\Delta\rho}{\rho_s} + (1+K)\tilde{r}^3\right)^{\gamma}} dx + \left(\frac{\frac{\Delta\rho}{\rho_s} + 1 + K}{\frac{\Delta\rho}{\rho_s} + (1+K)\tilde{r}^3}\right)^{\gamma} \tilde{w}_0^2, \qquad \text{(B.12)}$$

where

$$\gamma = 2 + \frac{C_d}{4(1+K)\alpha} = \frac{2}{1+K}\left(1 + K + \frac{C_d}{8\alpha}\right). \qquad \text{(B.13)}$$

The integral on the RHS of Eq. (B.12) can be calculated analytically if $C_d = 0$, or if $\Delta\rho/\rho_s \to 0$ (for arbitrary K and C_d).

The solution (B.12) has a large-z asymptote given by

$$\tilde{w} = \left[2\left(1 + K + \frac{3}{16}\frac{C_d}{\alpha}\right)\alpha^3\right]^{-1/2}\frac{1}{\tilde{z}}, \qquad \text{(B.14)}$$

which corresponds to the self-similar regime of a turbulent thermal, consistent with the form given in Eq. (2) of the paper. Once integrated, Eq. (B.14) yields

$$\tilde{z}^2 = \left[\left(1 + K + \frac{3}{16}\frac{C_d}{\alpha}\right)\frac{\alpha^3}{2}\right]^{-1/2}\tilde{t}. \qquad \text{(B.15)}$$

K and C_d act in exactly the same way in the self-similar regime. Furthermore, $3/(16\alpha) \sim 1$ if $\alpha \simeq 0.25$, which implies that K and C_d have a quantitatively similar effect.

References

Baker, J., Bizzarro, M., Wittig, N., Connelly, J., Haack, H., 2005. Early planetesimal melting from an age of 4.5662 Gyr for differentiated meteorites. Nature 436, 1127–1131.

Batchelor, G., 1954. Heat convection and buoyancy effects in fluids. Quart. J. R. Met. Soc. 80, 339–358.

Bettelini, M., Fanneløp, T., 1993. Underwater plume from an instantaneously started source. Applied Ocean Research 15, 195 – 206.

Bottke, W.F., Nesvorný, D., Grimm, R.E., Morbidelli, A., O'Brien, D.P., 2006. Iron meteorites as remnants of planetesimals formed in the terrestrial planet region. Nature 439, 821–824.

Breidenthal, R., 1992. Sonic eddy-a model for compressible turbulence. AIAA journal 30, 101–104.

Brown, G.L., Roshko, A., 1974. On density effects and large structure in turbulent mixing layers. Journal of Fluid Mechanics 64, 775–816.

Bush, J.W.M., Thurber, B.A., Blanchette, F., 2003. Particle clouds in homogeneous and stratified environments. J. Fluid Mech. 489, 29–54.

Canup, R., 2004. Simulations of a late lunar-forming impact. Icarus 168, 433–456.

Chen, H., Middleman, S., 1967. Drop size distribution in agitated liquid-liquid systems. AIChE Journal 13, 989–995.

Clay, P., 1940. The mechanism of emulsion formation in turbulent flow. Proceedings of the Section of Sciences 43, 852–965.

Constantin, P., Procaccia, I., 1994. The geometry of turbulent advection: Sharp estimates for the dimensions of level sets. Nonlinearity 7, 1045.

Constantin, P., Procaccia, I., Sreenivasan, K.R., 1991. Fractal geometry of isoscalar surfaces in turbulence: theory and experiments. Physical review letters 67, 1739–1742.

Corgne, A., Keshav, S., Wood, B.J., McDonough, W.F., Fei, Y., 2008. Metal silicate partitioning and constraints on core composition and oxygen fugacity during Earth accretion. Geochimica and Cosmochimica Acta 72, 574–589.

Dahl, T., Stevenson, D., 2010. Turbulent mixing of metal and silicate during planet accretion — and interpretation of the Hf–W chronometer. Earth Planet. Sci. Lett. 295, 177–186.

Deguen, R., Olson, P., Cardin, P., 2011. Experiments on turbulent metal-silicate mixing in a magma ocean. Earth Planet. Sci. Lett. 310, 303–313.

Escudier, M., Maxworthy, T., 1973. On the motion of turbulent thermals. Journal of Fluid Mechanics 61, 541–552.

Freund, J.B., Lele, S.K., Moin, P., 2000. Compressibility effects in a turbulent annular mixing layer. part 1. turbulence and growth rate. J. Fluid Mech. 421, 229 267.

Halliday, A., 2004. Mixing, volatile loss and compositional change during impact-driven accretion of the earth. Nature 427, 505–509.

Hallworth, M., Phillips, J., Huppert, H., Sparks, R., 1993. Entrainment in turbulent gravity currents. Nature 362, 829–831.

Hesketh, R., Fraser Russell, T., Etchells, A., 1987. Bubble size in horizontal pipelines. AIChE journal 33, 663–667.

Hinze, J., 1955. Fundamentals of the hydrodynamic mechanism of splitting in dispersion processes. AIChE Journal 1, 289–295.

Ichikawa, H., Labrosse, S., Kurita, K., 2010. Direct numerical simulation of an iron rain in the magma ocean. J. Geophys. Res. 115, B01404.

Karato, S., Murthy, V.R., 1997. Core formation and chemical equilibrium in the earth—I. physical considerations. Phys. Earth Planet. Inter. 100, 61–79.

Kleine, T., Mezger, K., Palme, H., Münker, C., 2004. The W isotope evolution of the bulk silicate earth: constraints on the timing and mechanisms of core formation and accretion. Earth Planet. Sci. Lett. 228, 109–123.

Kleine, T., Münker, C., Mezger, K., Palme, H., 2002. Rapid accretion and early core formation on asteroids and the terrestrial planets from Hf-W chronometry. Nature 418, 952–955.

Kolmogorov, A., 1949. On the breakage of drops in a turbulent flow, in: Dokl. Akad. Navk. SSSR, pp. 825–828.

Lavorel, G., Le Bars, M., 2009. Sedimentation of particles in a vigorously convecting fluid. Physical Review E 80, 046324.

Levich, V., 1962. Physicochemical Hydrodynamics, Prentice-Hall, Englewood Cliffs, NJ. Chap. VI 60, 355.

Mandelbrot, B., 1975. On the geometry of homogeneous turbulence, with stress on the fractal dimension of the iso-surfaces of scalars. Journal of Fluid Mechanics 72, 401–416.

Martin, D., Nokes, R., 1988. Crystal settling in a vigorously converting magma chamber. Nature 332, 534–536.

Mathew, J., Basu, A.J., 2002. Some characteristics of entrainment at a cylindrical turbulence boundary. Physics of Fluids 14, 2065–2072.

Melosh, H.J., 1990. Giant impacts and the thermal state of the early Earth. pp. 69–83.

Morton, B.R., Taylor, G., Turner, J.S., 1956. Turbulent gravitational convection from maintained and instantaneous sources. Proceedings of the Royal Society of London. Series A, Mathematical and Physical Sciences 234, 1–23.

Nimmo, F., O'Brien, D., Kleine, T., 2010. Tungsten isotopic evolution during late-stage accretion: Constraints on earth–moon equilibration. Earth Planet. Sci. Lett. .

Pantano, C., Sarkar, S., 2002. A study of compressibility effects in the high-speed turbulent shear layer using direct simulation. Journal of Fluid Mechanics 451, 329–371.

Pierazzo, E., Vickery, A.M., Melosh, H.J., 1997. A reevaluation of impact melt

production. Icarus 127, 408–423.
Ricard, Y., Šrámek, O., Dubuffet, F., 2009. A multi-phase model of runaway core–mantle segregation in planetary embryos. Earth Planet. Sci. Lett. 284, 144–150.
Risso, F., 2000. The mechanisms of deformation and breakup of drops and bubbles. Multiphase Science and Technology 12.
Rubie, D., Melosh, H., Reid, J., Liebske, C., Righter, K., 2003. Mechanisms of metal–silicate equilibration in the terrestrial magma ocean. Earth Planet. Sci. Lett. 205, 239–255.
Rudge, J., Kleine, T., Bourdon, B., 2010. Broad bounds on earth's accretion and core formation constrained by geochemical models. Nature Geoscience 3, 439–443.
Samuel, H., 2012. A re-evaluation of metal diapir breakup and equilibration in terrestrial magma oceans. Earth and Planetary Science Letters 313, 105–114.
Shinjo, J., Umemura, A., 2010. Simulation of liquid jet primary breakup: Dynamics of ligament and droplet formation. International Journal of Multiphase Flow 36, 513 – 532.
Sreenivasan, K.R., Ramshankar, R., Meneveau, C., 1989. Mixing, entrainment and fractal dimensions of surfaces in turbulent flows. Royal Society of London Proceedings Series A 421, 79–107.
Stevenson, D.J., 1990. Origin of the Earth. Oxford University Press. chapter Fluid dynamics of core formation. pp. 231–249.
Storr, G., Behnia, M., 1999. Experiments with large diameter gravity driven impacting liquid jets. Experiments in fluids 27, 60–69.
Tennekes, H., Lumley, J.L., 1972. First Course in Turbulence. MIT Press.
Terada, A., Ida, Y., 2007. Kinematic features of isolated volcanic clouds revealed by video records. Geophys. Res. Lett. 34, L01305.
Tonks, W.B., Melosh, H.J., 1993. Magma ocean formation due to giant impacts. J. Geophys. Res. 98, 5319–5333.
Turner, J., 1969. Buoyant plumes and thermals. Annual Review of Fluid Mechanics 1, 29–44.
Turner, J.S., 1986. Turbulent entrainment - The development of the entrainment assumption, and its application to geophysical flows. Journal of Fluid Mechanics 173, 431–471.
Ulvrová, M., Coltice, N., Ricard, Y., Labrosse, S., Dubuffet, F., Velímskỳ, J., Šrámek, O., et al., 2011. Compositional and thermal equilibration of particles, drops and diapirs in geophysical flows. Geochemistry Geophysics Geosystems 12, 1–11.
Villermaux, E., Marmottant, P., Duplat, J., 2004. Ligament-mediated spray formation. Physical review letters 92, 74501.
Westerweel, J., Fukushima, C., Pedersen, J.M., Hunt, J.C.R., 2009. Momentum and scalar transport at the turbulent/non-turbulent interface of a jet. Journal of Fluid Mechanics 631, 199–230.
Wood, B., Walter, M., Wade, J., 2006. Accretion of the earth and segregation of its core. Nature 441, 825–833.
Woodward, B., 1959. The motion in and around isolated thermals. Quarterly Journal of the Royal Meteorological Society 85, 144–151.
Yamamoto, H., Watson, M., Phillips, J.C., Bluth, G.J., 2008. Rise dynamics and relative ash distribution in vulcanian eruption plumes at Santiaguito Volcano, Guatemala, revealed using an ultraviolet imaging camera. Geophys. Res. Lett. 35, L08314.
Yin, Q., Jacobsen, S.B., Yamashita, K., Blichert-Toft, J., Telouk, P., Albarede, F., 2002. A short timescale for terrestrial planet formation from Hf/W chronometry of meteorites. Nature 418, 949–952.
Yoshino, T., Walter, M.J., Katsura, T., 2003. Core formation in planetesimals triggered by permeable flow. Nature 422, 154–157.